

THE UNIVERSITY OF MANITOBA

STUDY OF THE RELATIONSHIP BETWEEN  
FRACTURE TOUGHNESS AND LOADING RATE  
UNDER TENSILE LOADING  
USING COMPACT TENSION SPECIMENS

BY

DAVID KIN-MING SHUM

A Thesis

Submitted to the Faculty of Graduate Studies in  
Partial Fulfillment of the Requirements  
for the Degree of  
Master of Science in Mechanical Engineering

Department of Mechanical Engineering

Winnipeg, Manitoba



June 1985

Permission has been granted to the National Library of Canada to microfilm this thesis and to lend or sell copies of the film.

The author (copyright owner) has reserved other publication rights, and neither the thesis nor extensive extracts from it may be printed or otherwise reproduced without his/her written permission.

L'autorisation a été accordée à la Bibliothèque nationale du Canada de microfilmer cette thèse et de prêter ou de vendre des exemplaires du film.

L'auteur (titulaire du droit d'auteur) se réserve les autres droits de publication; ni la thèse ni de longs extraits de celle-ci ne doivent être imprimés ou autrement reproduits sans son autorisation écrite.

ISBN 0-315-33592-0

STUDY OF THE RELATIONSHIP BETWEEN FRACTURE TOUGHNESS  
AND LOADING RATE UNDER TENSILE LOADING USING  
COMPACT TENSION SPECIMENS

BY

DAVID KIN-MING SHUM

A thesis submitted to the Faculty of Graduate Studies of  
the University of Manitoba in partial fulfillment of the requirements  
of the degree of

MASTER OF SCIENCE

© 1985

Permission has been granted to the LIBRARY OF THE UNIVER-  
SITY OF MANITOBA to lend or sell copies of this thesis, to  
the NATIONAL LIBRARY OF CANADA to microfilm this  
thesis and to lend or sell copies of the film, and UNIVERSITY  
MICROFILMS to publish an abstract of this thesis.

The author reserves other publication rights, and neither the  
thesis nor extensive extracts from it may be printed or other-  
wise reproduced without the author's written permission.

Roll back the curtain of memory now and then,  
Show me where you brought me from  
and where I could have been;  
Remember I'm human,  
and humans forget,  
So remind me, remind me,  
dear Lord.

## ABSTRACT

A study of the fracture behavior of materials at loading rates ranging from quasi-static to stress wave was undertaken. More specifically, a testing procedure was designed and implemented for the determination of a characterizing fracture energy parameter, similar to the  $J$ -integral in quasi-static loading, using standardized compact tension specimens. This testing procedure utilizes tensile loading and stress triaxiality to characterize quasi-static to stress wave induced fracture. Its main feature is the use of a dynamic tensile test assembly that adapts an existing compression Split Hopkinson bar for dynamic tensile testing of compact tension specimens. Simplicity in design, assembly and calibration are the main features of this dynamic tensile test assembly.

Specifically, standard ASTM compact tension specimens are loaded in simple tension, at rates ranging from quasi-static to stress wave loadings, using a standard servo-hydraulic test frame and a stress wave loading arrangement. The load during testing is monitored by a load cell for the servo-hydraulic test frame case and by instrumented loading grips in the stress wave loading arrangement. Crack initiation and load-line displacement at all speeds are determined using a specimen face-mounted high frequency crack opening displacement gage.

Fracture toughness based on this testing procedure is expressed in terms of a characterizing fracture energy parameter,  $J_Q$ , derivable from either the load/load-line

displacement test record or from a microscopic examination of the fracture surface's stretch zone using scanning electron microscopy. The loading rate during testing is expressed in terms of  $\dot{J}_Q$ , the fracture energy parameter divided by the crack initiation time.

A study of the variation of fracture toughness,  $J_Q$ , of an AISI 1045 steel in the annealed condition, with loading rate ranging from quasi-static to stress wave loading, was undertaken using compact tension specimens of three different  $a/w$  ratios (0.5, 0.6, 0.7). The experimental results based on stretch zone measurements and load/load-line displacement records both indicate a significant decrease in fracture toughness for this steel at high loading rate. In addition, fracture toughness is seen to decrease with increasing  $a/w$  ratio for these two methods of fracture toughness determination. However, fracture toughness based on stretch zone measurements indicates a lesser dependence on specimen  $a/w$  ratio than the method of load/load-line displacement records.

Specifically, the fracture toughness,  $J_Q$ , of this steel based on load/load-line displacement records decreases in a concave, bilinear fashion with increasing  $\log(\dot{J}_Q)$ . Similarly, the fracture toughness of this steel based on stretch zone measurements decreases bilinearly with increasing  $\log(\dot{J}_Q)$ , though in a convex fashion. This slight discrepancy in results in terms of concavity/convexity can be explained in terms of the variability in both specimen  $a/w$  ratio dependence and

experimental errors associated with each method of  $J_Q$  determination.

Correlation of the fracture toughness obtained between these two methods of  $J_Q$  determination indicates that the fracture toughness-loading rate relationship of this steel can be further simplified to a linearly decreasing function of the loading rate that spans eight orders of  $\dot{J}_Q$ . Specifically,  $J_Q$  is seen to range from  $69 \text{ kJ/m}^2$  (quasi-static) to  $5 \text{ kJ/m}^2$  (dynamic) while  $\dot{J}_Q$  ranges from  $10^{-1} \text{ kJ/m}^2\text{s}^{-1}$  (quasi-static) to  $10^7 \text{ kJ/m}^2\text{s}^{-1}$  (dynamic).

## ACKNOWLEDGEMENTS

The author would like to express his sincere appreciation to his advisor Dr. M.N. Bassim for the suggestion of the problem and for his invaluable advice, guidance, discussions and criticism throughout this work.

Sincere thanks are also extended to Dr. T.R. Hsu for his making possible the use of his laboratory and equipments for the dynamic portion of this work.

Sincere appreciation is gladly extended to Dr. M.C. Chaturvedi for making available his computer system at his home for the printing of this thesis.

Thanks are due to Dr. M.R. Bayoumi for his invaluable assistance and discussions throughout all phases of this work. Without his help and warm friendship throughout the past two years this thesis work would not have been possible. Special thanks are also due Mr. G.G.Chen for his warm friendship and patience in explaining the principles of Solid Mechanics that the author needed.

Special thanks are due to Mr. D. Mardis, Mr. J. Van Dorp and Mr. R. Hartle in the metallurgical sciences laboratory for their invaluable help in the practical application of engineering principles to laboratory experimentation. Without their putting up with the author for the last two years this work would not be possible. Thanks are also extended to Mr. D. Kuss for this invaluable help during the dynamic portion of this work, and to Mr. L. Wilkins and Mr. J. Shewchuk in the machine shop for their

excellent technical help and for their warmth and friendship.

The author would like to extend his deepest gratitude to the Koinonia Fellowship for their continual physical and spiritual support throughout the author's university years. In particular, thanks is due Dr. Y. Hoh for her friendship and spiritual guidance in helping the author to keep a proper perspective on academic achievements, and for the constant encouragement to strive for one's personal best. Similarly, thanks is due Miss B. Wong who has proved to be invaluable in providing personal support in times of difficulty and frustration.

Finally, the author gratefully acknowledge the financial support provided by the National Sciences and Engineering Research Council of Canada in the form of a post-graduate scholarship.

## TABLE OF CONTENTS

	Page
Abstract .....	i
Acknowledgements .....	iv
Table of Contents .....	vi
List of Figures .....	ix
List of Tables .....	xiii
Chapter 1 Introduction .....	1
Chapter 2 Literature Review .....	5
2.1 Linear Elastic Fracture Mechanics .....	7
2.1.1 Continuum Mechanics Approach of LEFM .....	7
2.1.2 Energy Approach of LEFM .....	8
2.1.3 Plastic Zone Correction .....	12
2.2 Elastic Plastic Fracture Mechanics ....	15
2.2.1 Crack Opening Displacement and Stretch Zone Width .....	15
2.2.2 J-integral .....	20
2.2.2.1 J-integral Theory .....	20
2.2.2.2 J-integral Determination	24
2.2.3 Strain Energy Density Factor ...	25
2.3 Specimen Geometry and Fracture Toughness	29
2.3.1 Overall Specimen Shape .....	31
2.3.2 Specimen Thickness .....	31
2.3.3 Crack Length or a/w Ratio .....	33
2.4 Stress Wave Analysis .....	36
2.5 Theoretical Dynamic Crack Considerations	38
2.6 Loading Rates and Fracture Toughness ..	43
2.7 Historical Development of Dynamic Fracture Toughness Parameters .....	46
2.7.1 Qualitative Dynamic Fracture Toughness Parameters .....	47
2.7.2 Quantitative Dynamic Fracture Toughness Parameters .....	48
2.8 Conclusions .....	58

	Page
Chapter 3 Experimental Procedures .....	60
3.1 Material .....	61
3.2 Specimen .....	61
3.3 Reference Fracture Toughness Testing ( $J_{IC}$ ) .....	61
3.4 Quasi-Static to Dynamic Fracture Testing ( $J_Q$ ) .....	64
3.4.1 Instron Speeds Tests .....	66
3.4.2 Impact Loading by Modified Split Hopkinson Bar .....	72
3.4.2.1 Rationale for Design ..	78
3.4.2.2 Theory of Operation ...	79
3.4.2.3 Theory of Analysis ....	82
3.5 Stretch Zone Measurement .....	90
Chapter 4 Experimental Results .....	93
4.1 Fracture Toughness ( $J_{IC}$ ) from Compliance Method .....	94
4.2 Instron Speeds Fracture Toughness ( $J_Q$ ) .	94
4.2.1 Quasi-Static Instron Tests .....	97
4.2.2 Slow Speed Instron Tests .....	97
4.2.3 High Speed Instron Tests .....	106
4.3 Impact Loading Fracture Toughness ( $J_Q$ ) .	112
4.4 Stretch Zone Measurement .....	123
Chapter 5 Discussion .....	137
5.1 Macroscopic $J_Q$ Results .....	138
5.2 Microscopic $J_Q$ Results .....	141
5.3 Agreement of Macroscopic/Microscopic $J_Q$ Results .....	143
5.4 General Test Methodology .....	145
5.4.1 Crack Initiation Detection using COD Gage .....	145
5.4.2 Dynamic Load/Load-line Displacement Interpretation ..	148
5.4.3 Stretch Zone Measurement .....	152

	Page
5.5 Relevance and Application of $J_Q$ to Fracture Mechanics .....	153
Chapter 6 Conclusions .....	156
References .....	159
Appendix A Slow Speed Instron Test Results	
Appendix B High Speed Instron Test Results	
Appendix C Stress Wave Loading Results	
Appendix D Scanning Electron Micrographs	

## LIST OF FIGURES

	Page
Figure 2.1	The three modes of fracture. .... 9
Figure 2.2	Coordinate system and stress components ahead of crack tip. .... 10
Figure 2.3	Graphical representation of the Irwin plastic zone correction. .... 14
Figure 2.4	Graphical representation of the Dugdale plastic zone correction. .... 14
Figure 2.5 (a)-(b)	Mathematical Models of CTOD. .... 17
Figure 2.6	Portions of fracture surface relief with a stretched-zone. .... 19
Figure 2.7	Illustration of the stretch zone width based on a diagonal definition. .... 19
Figure 2.8	Graphical Definition of the J-integral. .. 22
Figure 2.9	J around contour at a crack tip. .... 22
Figure 2.10	Illustration and diagrammatic details for J-integral R-curve technique..... 26
Figure 2.11	Graphical definition of the strain energy density function. .... 28
Figure 2.12	Crack growth in elastic portion of elastic-plastic stress field. .... 28
Figure 2.13	Crack growth with yielding along the path. 28
Figure 2.14 (a) - (c)	Schematic of resistance curves for changes in specimen size, loading rate and material toughness based on strain energy density factor. .... 30
Figure 2.15 (a) - (c)	Relationship between fracture toughness and specimen thickness. .... 32
Figure 2.16	$K_{ID}$ vs $a/w$ . .... 32
Figure 2.17	COD and $a/w$ vs temperature. .... 35
Figure 2.18	Relationship between specimen dependence of fracture toughness and relative size of plastic zone and crack length. .... 35

	Page
Figure 2.19	Definition of rectangular pulse in bar. .. 39
Figure 2.20	Notation for discussing energy flux to a mathematically sharp, structureless crack tip. .... 41
Figure 2.21	Diagramic details of line integral by Kishimoto. .... 41
Figure 2.22	$K$ vs $\dot{K}$ for the case of ductile fracture. . 45
Figure 2.23	Wedge loaded compact tension setup. .... 52
(a) - (c)	
Figure 2.24	Modified wedge loaded compact tension setup. .... 53
Figure 2.25	Instrumentation on Split Hopkinson Bar for dynamic fracture test using WLCT. ....56
Figure 2.26	Crack initiation detection on WLCT using strain gage. ....56
Figure 3.1	Compact tension specimen geometry and dimensions. .... 63
Figure 3.2	Photographs of Instron speeds test setup. . 68
(a) - (c)	
Figure 3.3	COD gage mounted on CTS. .... 71
Figure 3.4	Ideal COD gage response to crack blunting. .... 71
Figure 3.5	Instrumentation and close-up drawing of dynamic tensile test. .... 73
Figure 3.6	Experimental set-up drawing of dynamic tensile test. .... 74
Figure 3.7	Photographs of dynamic tensile test setup.. 75
(a) - (e)	
Figure 3.8	Dynamic load overestimation due to proximity of strain gages to CTS. .... 87
Figure 4.1	Experimental J-Resistance curve. .... 95
Figure 4.2	COD-t, load-t and $J_Q$ results for test #INST14. .... 98
(a)-(c)	
Figure 4.3	COD-t, load-t and $J_Q$ results for test #INST7. .... 101
(a)-(c)	

	Page
Figure 4.4 (a)-(c)	COD-t, load-t and $J_Q$ results for test #INST12. .... 103
Figure 4.5	Load-t curves as a function of a/w for slow speed Instron tests. .... 105
Figure 4.6 (a)-(c)	COD-t, load-t and $J_Q$ results for test #INST2. .... 107
Figure 4.7 (a)-(c)	COD-t, load-t and $J_Q$ results for test #INST3. .... 109
Figure 4.8	Load-t curves as a function of a/w for high speed Instron tests. .... 111
Figure 4.9	Relationship between fracture toughness ( $J_Q$ ) and loading rate ( $\dot{J}_Q$ ) for Instron tests. .... 114
Figure 4.10 (a)-(b)	COD-t, load-t results for test #SHB4. .... 115
Figure 4.11	Smooth loading pulse from WLCT Split Hopkinson Bar Test. .... 118
Figure 4.12 (a)-(b)	Location of digitally expanded regions for test #SHB4. .... 119
Figure 4.13 (a)-(b)	Expanded COD-t, load-t results for test #SHB4. .... 120
Figure 4.14	Doubly expanded load-t result for test #SHB4. .... 124
Figure 4.15	Fracture toughness ( $J_Q$ ) determination for test #SHB4. .... 125
Figure 4.16	Relationship between stretch zone width and nominal strain rate. .... 128
Figure 4.17 (a)-(b)	Representative stretch zone micrographs for Instron speeds tests illustrating ductile fracture mode (from #INST1). .... 129
Figure 4.18 (a)-(b)	Stretch zone micrographs for dynamic test #SHB1 illustrating ductile fracture mode. . 131
Figure 4.19 (a)-(b)	Stretch zone micrographs for dynamic test #SHB4 illustrating brittle fracture mode. . 132

Figure 4.20	Relationship between the load/load-line displacement method and the stretch zone method of determining fracture toughness ( $J_Q$ ). . . . .	133
Figure 4.21	Relationship between fracture toughness ( $J_Q$ ) and nominal strain rate based on stretch zone measurements. . . . .	135
Figure 4.22	Relationship between fracture toughness ( $J_Q$ ) and loading rate ( $J_Q$ ) based on stretch zone measurements. . . . .	136
Figure 5.1	Relationship between fracture toughness ( $J_Q$ ) and loading rate based on load/load-line displacement curves. . . . .	140
Figure 5.2	Comparison of macroscopic and microscopic methods of fracture toughness ( $J_Q$ ) determination. . . . .	144
Figure 5.3	Underestimation of $J_Q$ based on digitized load/load-displacement curve. . . . .	149

## LIST OF TABLES

	Page
Table 3.1 Chemical composition of 1045 steel .....	62
Table 3.2 Mechanical properties of annealed 1045 steel.	62
Table 4.1 Instron speeds tests' experimental results ..	96
Table 4.2 Dynamic tensile tests' experimental results .	113
Table 4.3 Stretch zone measurement results .....	127

CHAPTER ONE

INTRODUCTION

With the advent of technology comes more stringent demands on material performance and application. One persistent problem is a metal's increased tendency toward catastrophic cleavage fracture at tensile loading rates approaching the stress wave regime. Survey of the literature indicates that there have been much theoretical and experimental investigations into the use of dynamic fracture toughness parameters for characterization of this loading rate effect. The establishment of a dynamic fracture toughness parameter would be the logical first step to a systematic investigation and subsequent control of dynamic material properties.

However, the same survey would also indicate that current experimental research efforts into dynamic fracture toughness characterization are on the whole disjointed, with tests results from one experimenter not immediately correlatable to others'. This disjointness is due, on the most part, to the fact that there is at present no agreed upon test procedures, specimen configuration or interpretation of experimentally obtained values. Also, much of the present experimental research efforts is directed at high speed compression testing, while engineering failures of interest are mostly tensile in nature. In addition, most test conditions do not include stress triaxiality, a serious test deficiency in view of the presence of cracks in all engineering structures.

Consequently, there is a clear and present need for an experimental fracture toughness testing procedure that

utilizes tensile loading and stress triaxiality to characterize quasi-static to stress wave induced fracture.

This study attempts to address this fundamental need through a testing procedure based on an author designed dynamic test set-up and state-of-the-art fracture toughness measurement methods. This original experimental set-up involves the adaptation of an existing compression Split Hopkinson Bar to simulate stress wave loading under tension, using compact tension specimens to incorporate their associated stress triaxiality. Simplicity in design, assembly and data interpretation are the main features of this new design. This testing procedure yields a fracture toughness parameter  $J_Q$ , which is proposed as a candidate to characterize the loading rate effects of fracture toughness for metals.

Experimental procedures, described in Chapter Three, were adopted to investigate the loading rate dependence of fracture toughness of AISI 1045 steel in the annealed condition. Fracture toughness testing using an Instron servo-hydraulic tester at quasi-static, slow and high speeds were performed. In the stress wave loading regime, tests were performed at two additional loading rates using the author designed apparatus. Fracture toughness in terms of  $J_Q$  at these five loading rates were evaluated using the experimental load/load-line displacement curves. Compact tension specimens of three different crack lengths ( $a/w$  ratios) were used to evaluate specimen dependence of  $J_Q$ . In

addition, a standard ASTM E813  $J_{IC}$  fracture toughness test was performed to establish a baseline quasi-static fracture toughness value for comparison purposes. Stretch zone measurements of fracture surfaces were performed using scanning electron microscopy.  $J_Q$  values evaluated based on stretch zone measurements were used as reference fracture toughness values for all remaining test speeds.

Experimental results for the five loading rates are presented in Chapter Four. These results include the variation of  $J_Q$  with loading rates, the dependence of  $J_Q$  on specimen geometry and stretch zone measurement results.

Discussions on the experimental results and the various assumptions and models used in data interpretation are presented in Chapter Five. In addition, an evaluation of the general test methodology is also included.

Finally, general conclusions derived from this work are presented in Chapter Six.

CHAPTER TWO  
LITERATURE REVIEW

Current interests in dynamic fracture toughness characterization represent one of the newest and least understood branches of fracture mechanics. However, the fundamental objective of dynamic fracture analysis, similar to the general field of fracture mechanics, is still the desire to quantitatively and qualitatively assess the process of fracture with the ultimate goal to control the fracture process. Similar birthpains were experienced by Linear Elastic Fracture Mechanics (LEFM) and Elastic-Plastic Fracture Mechanics (EPFM), with the eventual standardization of  $K_{IC}$  and  $J_{IC}$  test procedures to characterize the quasi-static fracture process.

In this chapter, the concepts of LEFM are briefly described, and the three most promising EPFM techniques are discussed. A review of the current understanding of fracture toughness dependence on specimen geometry is also given. Following these quasi-static crack considerations is a brief discussion on the fundamentals of stress wave analysis. This in turn is followed by some theoretical dynamic crack considerations, and the current understanding of fracture toughness dependence on loading rate. Finally, attention is directed at the historical development of dynamic fracture toughness testing techniques. It will be shown that the author designed dynamic fracture test setup represents a natural extension of past efforts, and therefore distinguishes itself as the latest experimental technique in dynamic fracture toughness characterization.

## 2.1 Linear Elastic Fracture Mechanics

Linear Elastic Fracture Mechanics (LEFM) is the earliest attempt at applying continuum mechanics principles to the solution of fracture problems. The solution methodology is essentially that of identifying the field variables (stress, strain and displacement) as a function of the distance ahead of a crack tip. The major shortcoming of LEFM is that the solutions are only valid at distances moderately far away from the crack tip where the material response is basically elastic.

### 2.1.1 Continuum Mechanics Approach of LEFM

Fundamental to the analytic solution of all fracture problems is the formulation of an appropriate stress function, a concept originated with Airy. Given the well known equilibrium and compatibility equations, the problem faced by Airy was to find a suitable function,  $\phi$ , in two dimensions which satisfies these conditions from continuum mechanics, and thereby enabling the stresses to be related to the applied loads. Airy first demonstrated that such a function existed in 1862 [1], and he proceeded to use this function to solve for the problem of an infinite plate (plane stress) with a hole in the center.

Some 50 years later, Inglis in 1913 [2] applied the Airy stress function principle to the solution of an elliptical hole in a uniformly stressed plate. It was observed that, by increasing the ratio between the major and minor axes of an ellipse, one would approach the solution to

a crack in an infinite plate.

Westergaard in 1939 [3] was able to do precisely the above and provided the first vigorous solution for the case of a crack in an infinite plate. Westergaard's solution consisted of specifying the stress state ahead of a crack in terms of the nominal stress and crack length in the form:

$$\sigma_{ij} = \sigma \sqrt{\frac{a}{2r}} f_{ij}(\theta) \quad (2.1)$$

By convention, the Stress Intensity Factor, SIF, is denoted

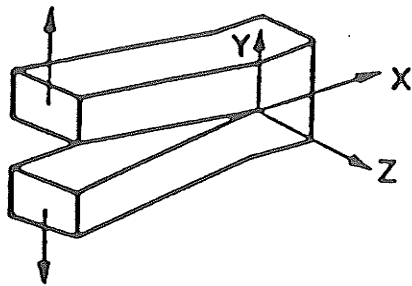
$$K = \sigma \sqrt{\pi a}$$

and therefore 
$$\sigma_{ij} = \frac{K}{\sqrt{2\pi r}} f_{ij}(\theta) \quad (2.2)$$

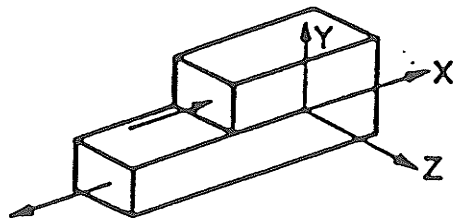
As can be seen, the SIF is used to represent the intensity of the stress field in front of a crack where LEFM applies, and exhibits the well known singularity property ( $1 / \sqrt{r}$ ). As a material fracture toughness parameter, a critical value of  $K$ ,  $K_C$ , represents the limiting conditions of applied stress and crack size at the onset of brittle failure. In general, there are three separate modes of failures and therefore three values of  $K_C$ :  $K_{IC}$ ,  $K_{IIC}$  and  $K_{IIIC}$ . Figure 2.1 shows the three modes of failure and Fig. 2.2 lists the associated field functions.

### 2.1.2 Energy Approach Of LEFM

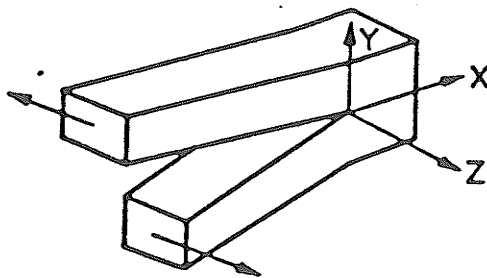
Aside from the progress of a continuum stress analysis that seeks to identify the field variables in the vicinity of a crack tip, a parallel development in terms of understanding the basic energetic requirements for crack



(a)

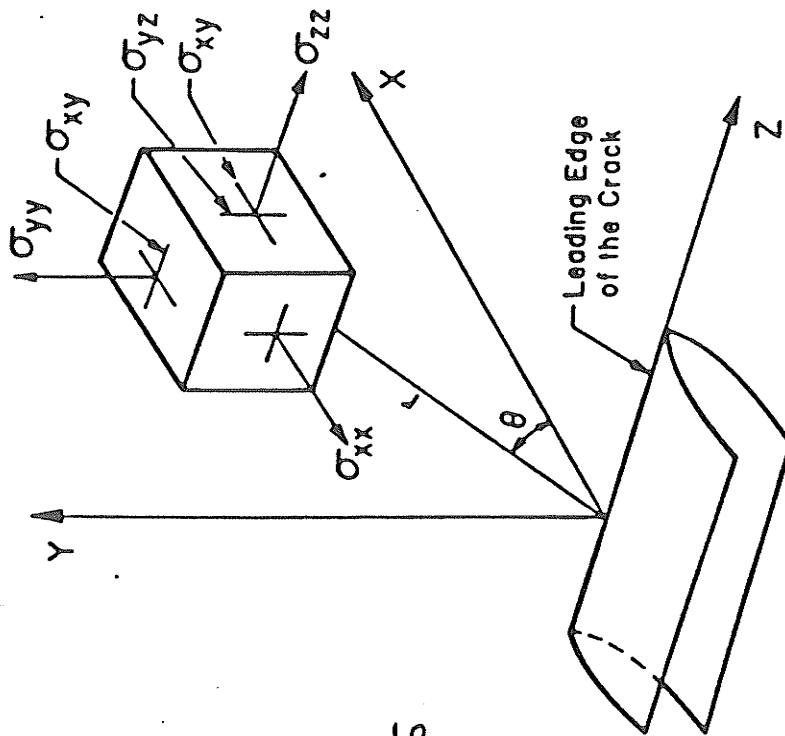


(b)



(c)

Figure 2.1 The three modes of fracture. (after Ref. 10)  
(a) Mode I, (b) Mode II, (c) Mode III.



Fracture Mode	Stress Components
Mode I	$\sigma_{xx} = \frac{K_I}{(2\pi r)^{1/2}} \cos \frac{\theta}{2} \left[ 1 - \sin \frac{\theta}{2} \sin \frac{3\theta}{2} \right]$ $\sigma_{yy} = \frac{K_I}{(2\pi r)^{1/2}} \cos \frac{\theta}{2} \left[ 1 + \sin \frac{\theta}{2} \sin \frac{3\theta}{2} \right]$ $\sigma_{xy} = \frac{K_I}{(2\pi r)^{1/2}} \sin \frac{\theta}{2} \cos \frac{\theta}{2} \cos \frac{3\theta}{2}$ $\sigma_{zz} = \nu(\sigma_{xx} + \sigma_{yy}), \sigma_{xz} = \sigma_{yz} = 0$ $U = \frac{K_I}{G} \left[ \frac{r}{2\pi} \right]^{1/2} \cos \frac{\theta}{2} \left[ 1 - 2\nu + \sin^2 \frac{\theta}{2} \right]$ $V = \frac{K_I}{G} \left[ \frac{r}{2\pi} \right]^{1/2} \sin \frac{\theta}{2} \left[ 2 - 2\nu - \cos^2 \frac{\theta}{2} \right], W = 0$
Mode II	$\sigma_{xx} = \frac{K_{II}}{(2\pi r)^{1/2}} \sin \frac{\theta}{2} \left[ 2 + \cos \frac{\theta}{2} \cos \frac{3\theta}{2} \right]$ $\sigma_{yy} = \frac{K_{II}}{(2\pi r)^{1/2}} \sin \frac{\theta}{2} \cos \frac{\theta}{2} \cos \frac{3\theta}{2}$ $\sigma_{xy} = \frac{K_{II}}{(2\pi r)^{1/2}} \cos \frac{\theta}{2} \left[ 1 - \sin \frac{\theta}{2} \sin \frac{3\theta}{2} \right]$ $\sigma_{zz} = \nu(\sigma_{xx} + \sigma_{yy}), \sigma_{xz} = \sigma_{yz} = 0$ $U = \frac{K_{II}}{G} \left[ \frac{r}{2\pi} \right]^{1/2} \sin \frac{\theta}{2} \left[ 2 - 2\nu + \cos^2 \frac{\theta}{2} \right]$ $V = \frac{K_{II}}{G} \left[ \frac{r}{2\pi} \right]^{1/2} \cos \frac{\theta}{2} \left[ -1 + 2\nu + \sin^2 \frac{\theta}{2} \right], W = 0$
Mode III	$\sigma_{xz} = \frac{K_{III}}{(2\pi r)^{1/2}} \sin \frac{\theta}{2}, \sigma_{yz} = \frac{K_{III}}{(2\pi r)^{1/2}} \cos \frac{\theta}{2}$ $\sigma_{xx} = \sigma_{yy} = \sigma_{zz} = \sigma_{xy} = 0$ $W = \frac{K_{III}}{G} \left[ \frac{2r}{\pi} \right]^{1/2} \sin \frac{\theta}{2}, u = v = 0$

Figure 2.2 Coordinate system and stress components ahead of crack tip.

propagation and failures was undertaken by Griffith in 1920 [4].

The conventional statement of Griffith's thermodynamic crack propagation criterion is as follow:

- 1) an existing crack will propagate if this leads to a reduction of the total energy of the system
- or 2) the incremental elastic energy loss ( $W_e$ ) due to the propagation of a crack should be  $\geq$  the work needed to develop a new crack surface ( $W_s$ )

By taking into account the plastic work needed to create a new surface in a real material, Irwin [5] and Orowan [6] translated Griffith's crack propagation criterion into the form:

$$\sigma_f^2 \pi C = 2 E G_c \quad ( 2.3 )$$

where  $G_c$  = critical crack extension force/crack length

$\sigma_f$  = failure stress  
 $C$  = crack length  
 $E$  = Young's Modulus

By noting that the right hand side of Eqn 2.3 is a material quantity, it is apparent that the left hand side must also be a material quantity, and one then arrives back at the conventional definition of the critical SIF in mode I as

$$K_{IC} = \sigma_f \sqrt{\pi c} \quad ( 2.4 )$$

Further, it can be shown that the energy and the stress requirements for fracture are simply related:

$$G = \frac{K^2}{E'} \quad \text{where} \quad E' = \begin{array}{l} E \quad \text{plane stress} \\ E \\ = \frac{E}{1-\nu^2} \quad \text{plane strain} \end{array} \quad ( 2.5 )$$

Finally, it must be kept in mind that the Griffith criterion is only a necessary but not a sufficient condition

for crack growth. As an energy criterion, it does not take into consideration the path dependency of crack growth. Also, as a thermodynamic approach, the Griffith criterion also does not account for the irreversibility that is inherent in any crack initiation and growth phenomenon.

### 2.1.3 Plastic Zone Correction

The formulations and solutions of problems as outlined in the previous two sections are applicable only in the realm of LEFM. However, true brittle failure occurs only for certain materials such as glass, ceramics and diamond. Therefore, the fracture toughness predicted for most engineering materials using LEFM analysis are conservative.

To extend the accuracy of LEFM analysis to real materials, the earliest attempts had been the use of plastic zone size correction factors to account for material yielding before failure. The general solution methodology was to first estimate the plastic zone size ahead of a real crack created as a result of the loading situation. This plastic zone would then be used to calculate an effective crack length,  $a_{eff}$ , that is greater than the original crack length,  $a_0$ . Field variable calculations would be performed using this adjusted crack length, and the solutions applied to distances moderately far away from the crack tip. Two such approaches would be given here.

### Irwin's Correction

Assuming plane stress and no material strain hardening (the lack of material strain hardening effectively overestimates the actual plastic zone size), Irwin further assumed the plastic zone would begin where the stress in the material exceeds the yield stress (Fig. 2.3). Irwin was able to show that the plastic zone radius takes on the form:

$$r_y = \frac{1}{2\pi} \left[ \frac{K}{\sigma_y} \right]^2 \quad \text{for plane stress} \quad (2.6a)$$

$$r_y = \frac{1}{6\pi} \left[ \frac{K}{\sigma_y} \right]^2 \quad \text{for plane strain} \quad (2.6b)$$

### Dugdale's Solution

Assuming also plane stress and no material hardening, Dugdale [7] approached the problem from an equivalent SIF point of view.

He let the plastic zone be loaded by a continuous distribution of yield stress load points for a crack of original dimensions  $2a$  (Fig.2.4). Applying Westergaard's solution he was able to show that

$$K_{IC} = \frac{2\sigma_y}{\sqrt{\pi}} \sqrt{c} \cos^{-1} \left[ \frac{a}{c} \right] \quad (2.7)$$

He then equated this SIF with that obtainable from an originally elastic crack of length  $2c$ . This then yields:

$$\frac{a}{c} = \cos \left[ \frac{\pi \sigma}{2\sigma_y} \right] \quad (2.8)$$

and as  $\sigma/\sigma_y$  becomes small,  $a/c \rightarrow 1 - \left[ \frac{\pi^2 \sigma^2}{8\sigma_y^2} \right]$

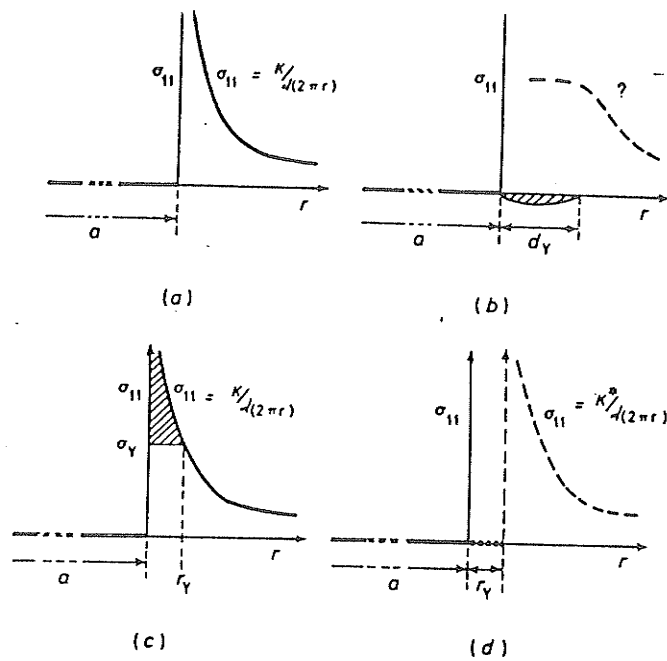


Figure 2.3 Graphical representation of the Irwin plastic zone correction. (after Ref. 10)  
 (a) Elastic stress distribution,  
 (b) Formation of plastic zone,  
 (c) First estimation of plastic zone size,  
 (d) "Notional" elastic crack.

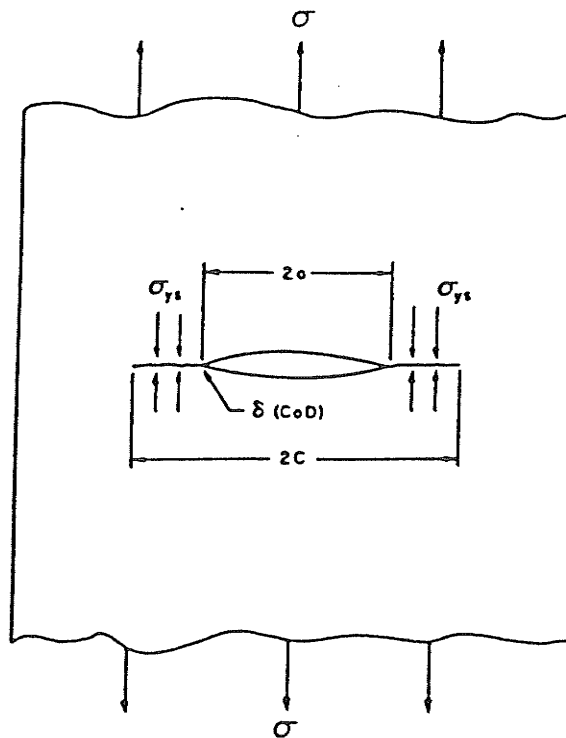


Figure 2.4 Graphical representation of the Dugdale plastic zone correction. (after Ref. 50)

and by letting  $2r = c - a$  ,  $r_y = \frac{\pi K^2}{16 \sigma_y^2}$  ( 2.9 )

## 2.2 Elastic Plastic Fracture Mechanics

In LEFM, by assuming negligible yielding or a plastic zone size correction, one uses a stress/force approach to arrive at a fracture toughness parameter, K. In Elastic Plastic Fracture Mechanics (EPFM), one recognizes that in most real-life situations where failure is ductile in nature, some strain energy released from the fracture process goes into plastic zone formation (crack blunting) and not crack propagation. Therefore, the general stress and strain fields cannot be accurately modelled by LEFM.

The purposes of EPFM are therefore two folds:

- 1) a better understanding of the process of ductile fracture
- 2) to circumvent the problem of LEFM (large specimens are needed to qualify for LEFM test procedures for ductile materials) by correlating EPFM test results (using small specimens) with the conventional LEFM fracture parameter, K.

In the field of EPFM, there are currently three approaches that seek to account for crack blunting.

### 2.2.1 Crack Opening Displacement and Stretch Zone Width

In 1960, both Cottrell [8] and Wells[9] independently proposed that the amount of crack opening prior to crack extension, for a given material tested under a given set of conditions, as a parameter to characterize the crack tip region. According to Dugdale's solution for plane stress

based on Westergaard's stress function, the CTOD (Crack Tip Opening Displacement) at failure is given by:

$$CTOD_C = \frac{8 \sigma_y}{\pi E} a \ln \left[ \sec \left( \frac{\pi \sigma_f}{2 \sigma_y} \right) \right] \quad (2.10)$$

which from either a geometric argument [9] or assuming  $\sigma_f \ll \sigma_y$  [10] yields

$$CTOD_C = \frac{\sigma_f^2 \pi a}{\sigma_y E} = \frac{K^2}{\sigma_y E} \quad (2.11)$$

Wells was able to show further that by letting

$$CTOD_C = \frac{4K}{E} \sqrt{\frac{2r}{\pi}} \quad (2.12)$$

and using Irwin's plastic zone correction factors (Eqns 2.6)

$$CTOD_C = \frac{K^2}{m \sigma_y E'} \quad \begin{array}{l} m = 0.785 \text{ for plain stress} \\ m = 1.36 \text{ for plain strain} \end{array} \quad (2.13)$$

Dawes[11], by assuming linear elastic material behavior (Eqn 2.17), extended Eqn 2.13 to

$$CTOD = \frac{J}{m \sigma_y} \quad (2.14)$$

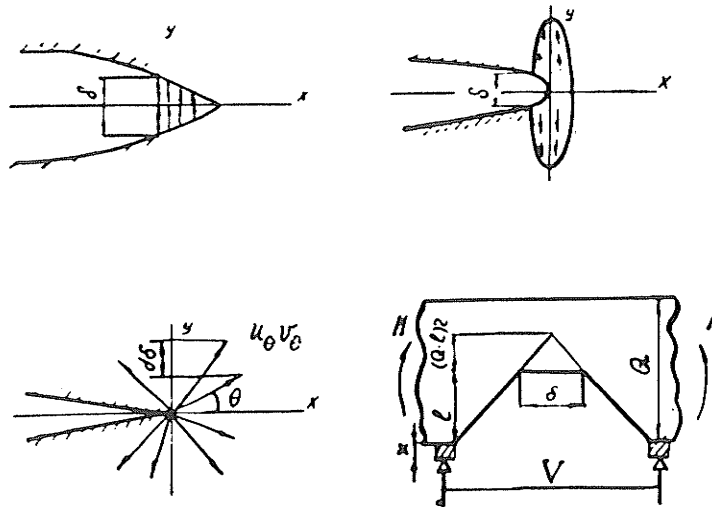
where  $m$  is estimated to range from  $\pi/4$  to greater than 2 (Figs. 2.5) [12].

It is reasoned that even if an exact numerical relationship between CTOD and fracture toughness is not known, proof of the uniqueness of CTOD as a material parameter would still allow for a meaningful qualitative comparison of results from small laboratory specimens to real life loading situations.

A scheme for CTOD determination	CTOD calculation by means of the model	Relationship of CTOD with $K_I$	Reference	Description of the model
Fig. 11 <sup>a</sup>	$\delta = 2v(0,0)$	$\delta = \frac{K_I^2}{E\sigma_y}$	[16-18]	A plastic zone ahead of the crack tip is replaced by a slit with the cohesive forces applied to the crack faces. The model agrees satisfactorily with the conditions of plane-stress state.
Fig. 11 <sup>b</sup>	$\delta = 2u(0,0)$	$\delta = 0.58 \frac{1-\nu^2}{E\sigma_y} K_I^2$	[19]	The model is similar to the preceding one, but agrees rather with plane-strain conditions.
Fig. 11 <sup>c</sup>	$\delta = \int_{-\pi}^{\pi} v(r, \theta) \cdot \cos \theta d\theta$	a) $\delta = 0.671 \frac{K_I^2}{E\sigma_y}$ b) $\delta = 0.717 \frac{K_I^2}{E\sigma_y}$ c) $\delta = 0.425 \frac{K_I^2}{E\sigma_y}$	[20]	For perfectly plastic material the slip-line theory (a) and the asymptotic solution of the elastic-plastic problem (b) predict strain singularity at the crack tip of the order $r^{-1/2}$ ; relationship (c) is obtained by the finite elements method.
Fig. 11 <sup>d</sup>	$\delta = \frac{V}{1 + \frac{l+z}{r(Q-1)}}$	$r$ -depends on approaching a definite value when tends to infinity		The crack faces rotate round the point (the rotation center) located at the distance of $r(Q-1)$ from the crack tip. The model is similar to the hypothesis of plane sections.

Note:  $u, v$  are displacement along the  $x, y$  axes, respectively;  
 $V$  is displacement measured by a displacement gage (Fig. 11<sup>d</sup>);  
 $z$  is the distance from the gage to the crack tip.

( a )



( b )

Figure 2.5 Mathematical models of crack tip opening displacement (CTOD). (after Ref. 12)  
(a) Summary of results,  
(b) Graphical models of crack tip used in 2.5a.

The main difficulty in using CTOD, however, has been the practical measurement of the onset of crack initiation,  $CTOD_i$ . Various formulae were introduced to correlate the values from a specimen face mounted crack opening displacement gage (COD) to CTOD [10,13].

Although problems exist in the exact determination of CTOD at crack initiation, the underlying principle of crack blunting and subsequent material constraint to crack growth is valid enough. Therefore, it would seem reasonable to examine a material process which concentrates more closely on crack initiation for fracture characterization.

Spitzig [14] was the first researcher to notice the correlation between CTOD and a "stretch zone" - a relatively featureless, slightly rippled region, observed between the fatigue-cracked and the overloaded fracture region (brittle or stable crack growth) of fracture specimens (Fig. 2.6).

The change in contour associated with the stretch zone (SZ) facilitates the determination of its boundary under stereoscopic viewing of scanning electron micrographs. Spitzig had found a typical SZ variation of 25% to 50% across the fracture surface.

For the two known cases where the SZ width( $w$ ) and height( $h$ ) were independently measured, the stretch zone slope angle  $\theta$  was found to be  $\sim 37^\circ$  (Fig. 2.6) [12,14]. Yet conventionally,  $\theta$  is assumed to be  $45^\circ$  [15]. Obviously,  $\theta$  is at least a function of the flow properties of the material, the orientation of local slip planes and the

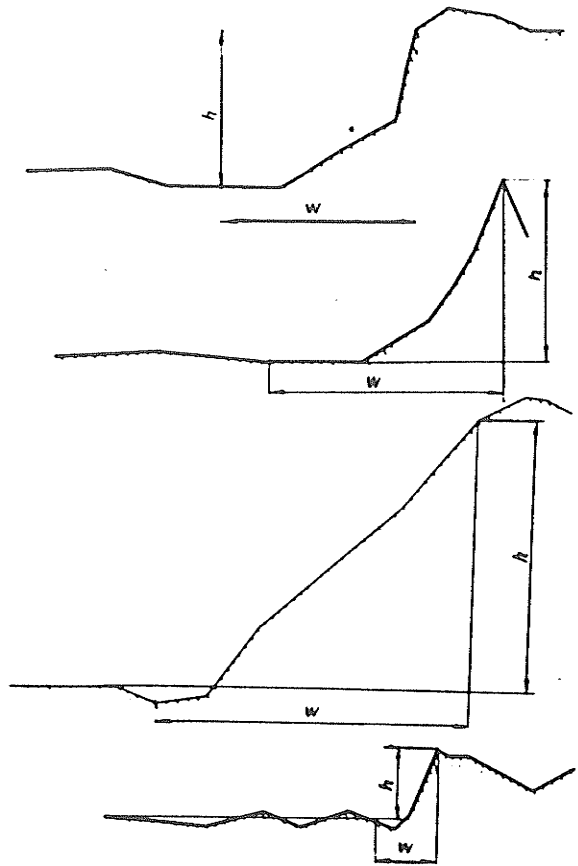


Figure 2.6 Definition of stretch zone based on actual width of stretched fracture area. (after Ref. 12)

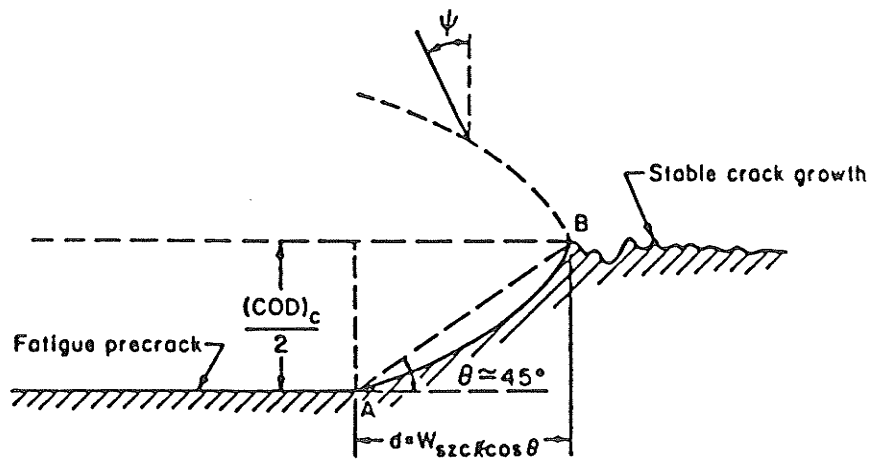


Figure 2.7 Illustration of the stretch zone width based on a diagonal definition. (after Ref. 15)

stress state (plane stress/strain), with the relative importance of any one of these factors uncertain.

Also, the stretch zone width is known alternately as the actual width of the SZ (Fig. 2.6) [14], or the diagonal of the SZ measured at 45° to the plane of fatigue crack propagation (Fig. 2.7) [15]. Currently, the JSME (Japanese Society of Mechanical Engineers) uses the actual width of stretch zone to determine  $J_{IC}$  [16].

Although SZ measurement represents the most direct record of the fracture process, SZ determination requires a high capital investment in a scanning electron microscope (SEM). In addition, a SEM requires meticulous specimen preparation after the fracture process before micrographs of the fracture surface could be taken. Therefore, this method of fracture toughness characterization does not lend itself to automated data analysis and is also time consuming.

### 2.2.2 J-integral

In contrast to SZ measurement, J-integral determination represents the state-of-the-art automated fracture toughness testing procedure. Since its introduction less than twenty years ago, the J-integral has firmly established itself as an elastic-plastic fracture toughness parameter.

#### 2.2.2.1 J-integral Theory

The J-integral, as proposed by Rice[17], is a path independent two dimensional energy line integral that

evaluates as a fracture parameter for linear and non-linear elastic materials subject to proportional loading and deformation plasticity constraints. With reference to Fig. 2.8,

$$J = \oint_{\Gamma} \left( W dy - T_i \frac{\partial u_i}{\partial x} ds \right) \quad (2.15)$$

where  $W$  is the strain energy density,  $T_i$  is the surface traction vector ( $\sigma_{ij}n_j$ ),  $U_i$  is the displacement vector,  $ds$  is a differential element of an arc length along  $\Gamma$  and  $n_j$  are the direction cosines of a unit vector  $\bar{n}$ . Proportional loading implies  $d\varepsilon_{ij} = c \varepsilon_{ij}$ , such that the loading process introduces no inhomogeneity into the material. Deformation plasticity implies  $\sigma_{ij} = f(\varepsilon_{ij})$ , or that no unloading or history dependent deformation is allowed. With the deformation plasticity assumption,  $W = \int \sigma_{ij} d\varepsilon_{ij}$ . The crack tip region is treated as a stress/strain singularity.

With its path independence,  $J$  computed on a contour remote from the crack tip is seen to directly control the near tip stress/strain distribution and magnitudes before the onset of fracture.

Knott[10] has shown that  $J$  can be seen as the net energy reduction (change in potential energy) for the case bounded by a sharp crack ( $J = \int W dy$ ) and that of a strictly blunted crack ( $J = \int T_i \frac{\partial u_i}{\partial x} ds da$ ). Similarly, Paris [18] has shown  $J da$  to be the energy change in crack extension (Fig. 2.9) with

$$J da = \oint_{\Gamma} W dy da - \oint_{\Gamma} T_i \frac{\partial u_i}{\partial x} ds da \quad (2.16)$$

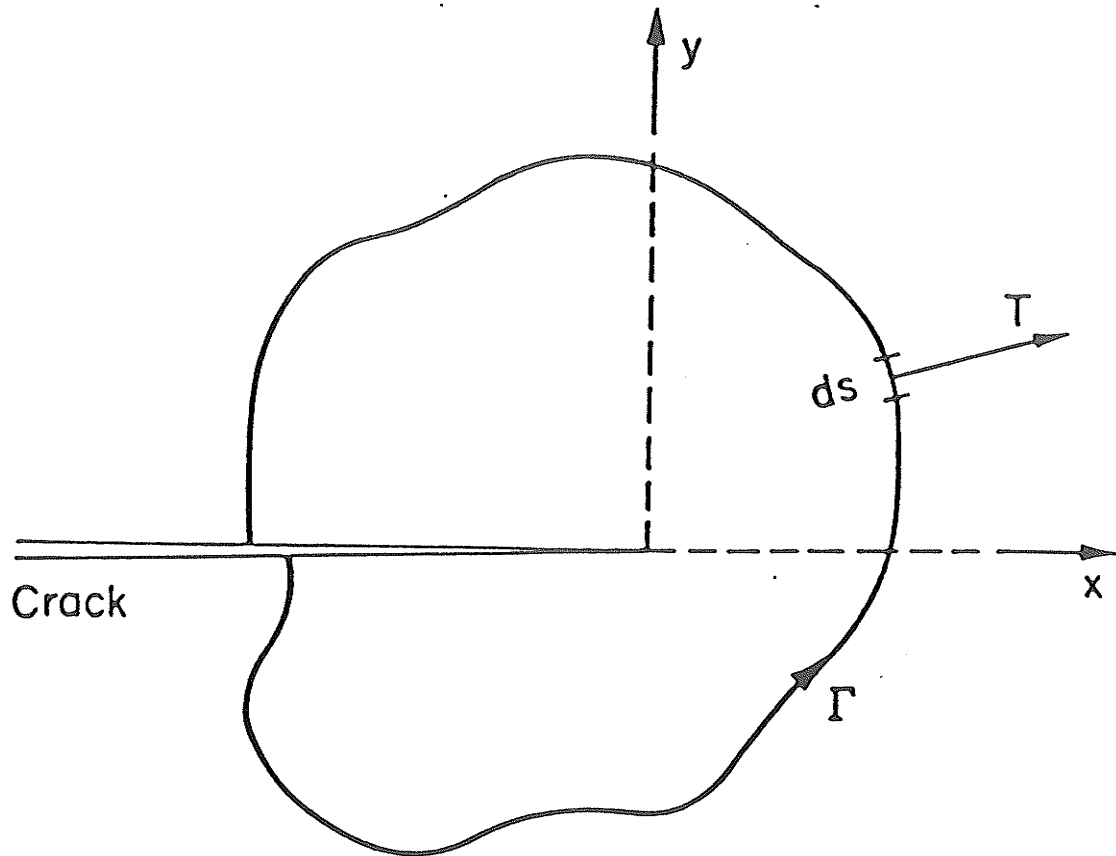


Figure 2.8 Graphical Definition of the J-integral. (after Ref. 50)

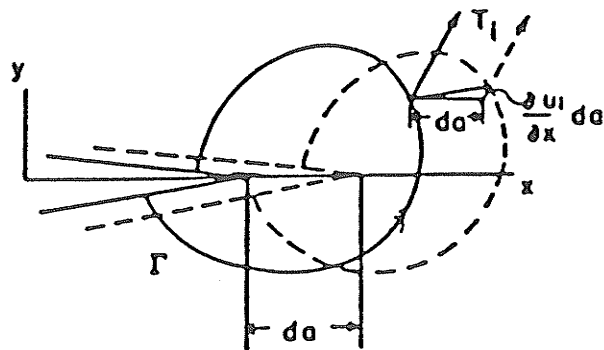


Figure 2.9 J around contour  $\Gamma$  at a crack tip. (after Ref. 18)

$\int W dy da$  = the strain energy gained (and lost) by moving to the new contour (for non linear elasticity) and

$\int T_i \frac{\partial u_i}{\partial x} ds da$  = work done by traction on the contour in moving

Rice [17] has further shown that for the linear elastic case

$$J = G = \frac{K^2}{E'} \quad ( 2.17 )$$

and that for nonlinear elastic cases,  $J=G$  due to  $J$ 's potential energy change definition.

Rice and Rosengran [19] and Hutchinson [20] both independently showed that  $J$ , analogous to  $K$  (Fig. 2.2), controls the stress/strain fields for a power law hardening material in the vicinity of the crack tip (the HRR solution). McClintock [21] further showed this relationship in an explicit form:

$$\sigma_{ij}(r,\theta) = \sigma_y \left( \frac{J}{I_n \sigma_y} \right)^{\frac{n}{n+1}} \frac{1}{r^{n/n+1}} \bar{\sigma}_{ij}(\theta) \quad ( 2.18a )$$

$$\epsilon_{ij}(r,\theta) = \left( \frac{J}{I_n \sigma_y} \right)^{\frac{1}{n+1}} \frac{1}{r^{1/r+1}} \bar{\epsilon}_{ij}(\theta) \quad ( 2.19b )$$

where  $I_n$  is a function of the work hardening exponent  $n$ , and the mode of crack opening. For the case of linear elasticity, these two equations transform into the equations listed in Fig. 2.2, and thereby extending an analytical stress/strain solution to a previously uncharted region.

#### 2.2.2.2 J-integral Determination

Providing the stress/strain fields of a body are known, the J-integral can simply be evaluated using the line integral definition (Eqn 2.15). This is the typical J-integral evaluation method for finite element analysis. The major considerations are the proper modelling of material behavior through the use of constitutive equations and accurate modelling of the crack tip region, the crack blunting process and crack advance.

Experimentally, the evaluation of J has its first basis in J's definition as the potential energy decrease rate/unit crack length,  $J = -dU/da$ . Begley and Landes [22] performed the first experimental evaluation of J in 1972 via this definition. Their methodology suffered in that a number of specimens of different a/w ratios were needed to identify  $J_{IC}$ . However, the most serious disadvantage of this method is the fact that crack initiation was not identified in any of these tests. Crack initiation was taken to be coincident with maximum load,  $P_{max}$ , which for any real engineering material that contains blunting of the crack tip, this would yield an optimistic  $J_{IC}$ .

Subsequently, J-integral estimation formulae were developed to estimate J for different specimen shapes. The most important one is the estimation formula for all specimen shapes, subjected to a bending moment, where the only significant specimen dimension is the remaining ligament width. Rice [23] showed that for this case J can be evaluated exactly through

$$J = \frac{2 U}{b} \quad ( 2.19 )$$

where U = the area of the load displacement curve per unit thickness  
 b = remaining ligament length

Applied to a Compact Tension Specimen, Eqn 2.19 takes on the form [24]:

$$J = \frac{1 + \alpha}{1 + \alpha^2} \frac{2 U}{b} \quad ( 2.20 )$$

where  $\alpha$  = geometric factor for compact tension specimen

Currently, a standard for  $J_{IC}$  testing has been issued by ASTM (American Society for Testing and Materials) under E813-85. The J-integral Resistance curve method is illustrated in Fig. 2.10.

For all real deformation cases, J's interpretation as the change in potential energy lends itself as a characterizing energy parameter that encompasses the overall energy requirement of the fracture process. It is this interpretation that is utilized as the theoretical basis for interpreting the load/load-line displacement curves generated in this work.

### 2.2.3 Strain Energy Density Factor

In general, ductile crack initiation and propagation involves the creation of many microcracks along the path of the main crack (cracks), and therefore dilational and distortional energy must be considered. The conventional approach of using Von Mises's yield criterion (plastic deformation (deviatoric stresses) leading to failure) is

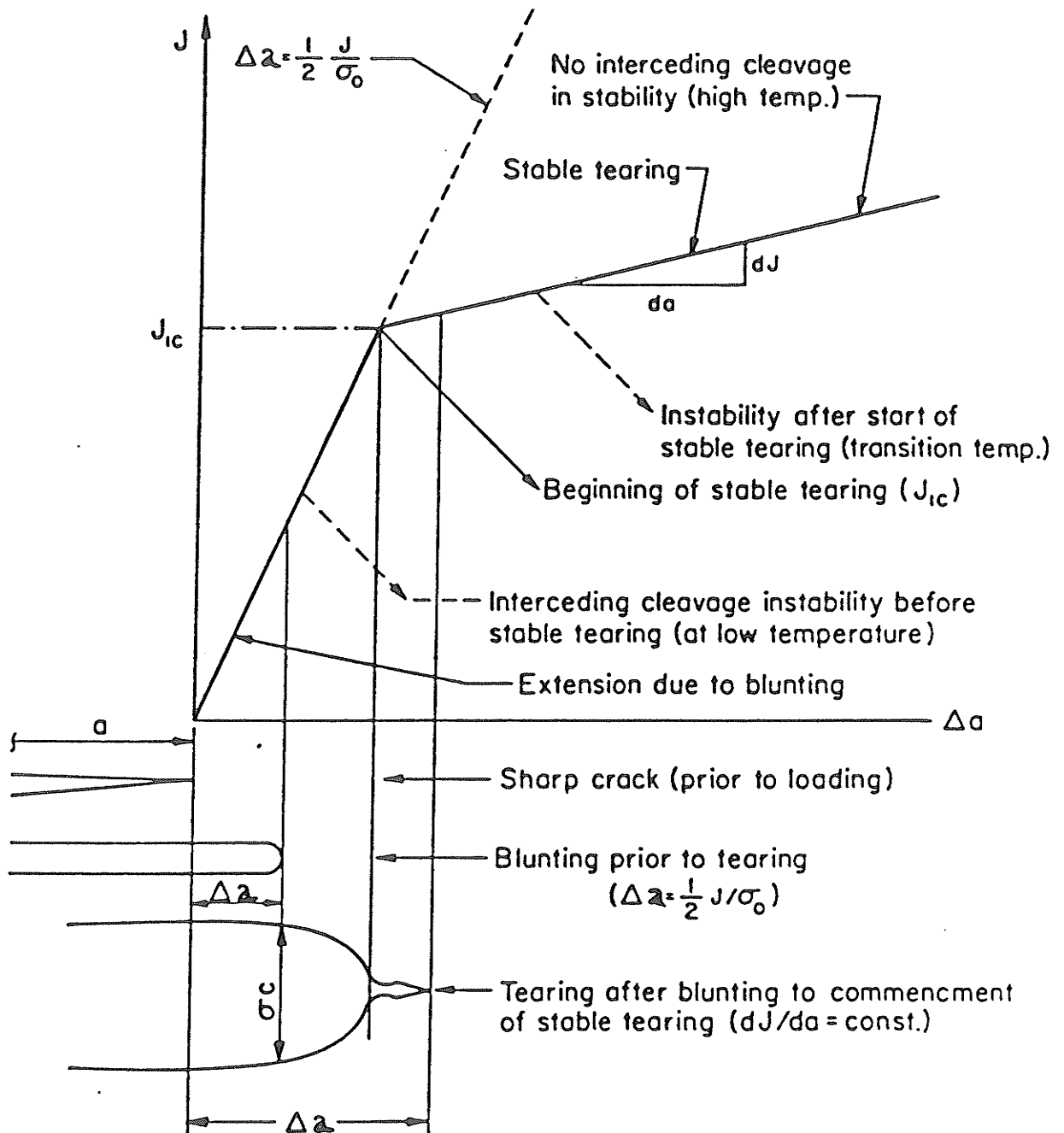


Figure 2.10 Illustration and diagrammatic details for J-integral R-curve technique. (after Ref. 50)

incomplete as it does not account for the dilational energy or the creation of microcracks. Therefore, it seems reasonable to use the total strain energy function  $W = \int \sigma_{ij} d \epsilon_{ij}$  to characterize fracture.

As noted in section 2.1, in the elastic region,  $\sigma_{ij} = \frac{K_i}{\sqrt{2 \pi r}} f_{ij}(\theta)$  and that in the elastic plastic region

(section 2.2),  $\sigma_{ij} = \frac{J_i}{r^\lambda} g_{ij}(\theta)$  where  $\lambda \neq 1/2$ . It is

apparent that a stress discontinuity occurs over the elastic-plastic interface, and therefore any fracture parameter based on a stress criterion has unknown errors. However, the strain energy density for both K and J controlled regions exhibit a  $1/r$  singularity [19,20], and therefore strain energy density promises to be an analytical basis for examining both the elastic and elastic-plastic regions. Sih[25] therefore proposed a strain energy density function,  $dW/dV$  such that

$$\frac{dW}{dV} = \frac{S}{r}, \quad S = \text{strain energy density factor}$$

$S$  is a finite quantity defined by the area under the curve at a distance  $r$  (Fig. 2.11), and  $dW/dV$  is the area under the true stress and true strain curve.

The fracture process is assumed to be governed by a material achieving a critical strain energy density function as a crack propagates to global failure, or

$$\left[ \frac{dW}{dV} \right]_C^* = \frac{S_1}{r_1} = \frac{S_2}{r_2} = \dots = \frac{S_j}{r_j} = \dots = \frac{S_c^*}{r_c^*} \text{ or } \frac{S_0^*}{r_0^*} = \text{const}$$

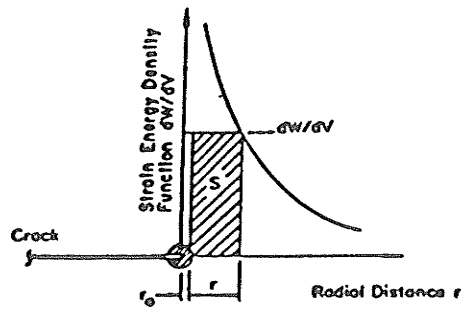


Figure 2.11 Graphical definition of the strain energy density function. (after Ref. 25)

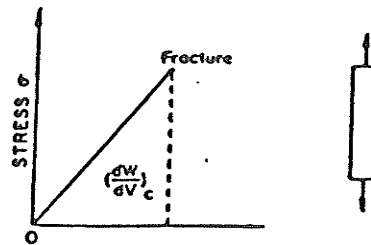


Figure 2.12 Crack growth in elastic portion of elastic-plastic stress field. (after Ref. 25)

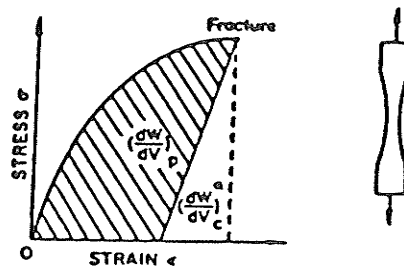


Figure 2.13 Crack growth with yielding along the path. (after Ref. 25)

$r_c$  is the critical ligament that triggers failure and  $(dW/dV)_c$  is determined experimentally from an uniaxial tensile test. For brittle materials (Fig. 2.12),

$$\left[ \frac{dW}{dV} \right]_C^* = \left[ \frac{dW}{dV} \right]_C \quad ( 2.22 )$$

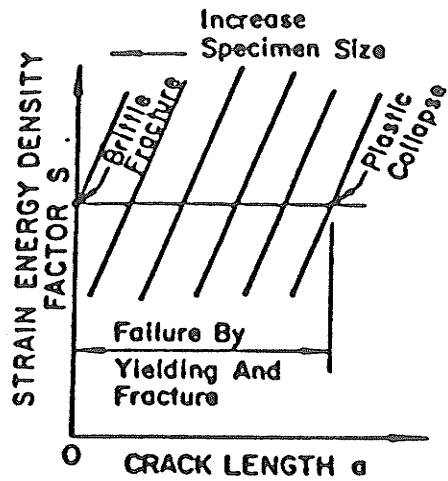
and for elastic plastic cases (Fig. 2.13):

$$\left[ \frac{dW}{dV} \right]_C^* = \left[ \frac{dW}{dV} \right]_C - \left[ \frac{dW}{dV} \right]_P \quad ( 2.23 )$$

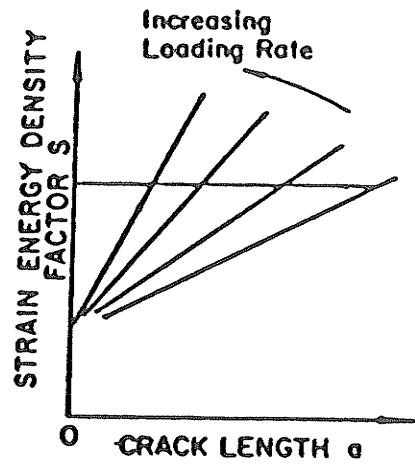
This concept of using a critical strain energy density factor to characterize fracture toughness has been verified, by application to a number of ductile fracture problems, for the assumption of  $dS/da = \text{constant}$  (Figs. 2.14). However, this method of elastic plastic fracture characterization still awaits widespread acceptance.

### 2.3 Specimen Geometry and Fracture Toughness

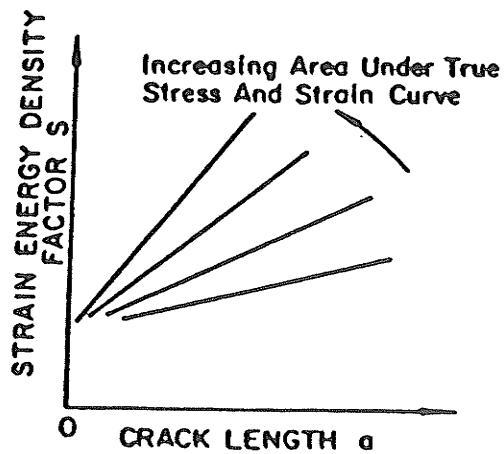
One of the most important goals of experimental fracture mechanics is the "negative" goal to define the limits of test and specimen configurations to arrive at a consistent fracture parameter. In this sense, any measured differences in fracture toughness values (K, J, G) are indications of dependence on testing variables rather than actual material toughness variation. Specifically, specimen geometry variables that should be investigated are the overall specimen configuration, the specimen thickness B, and the remaining specimen ligament b, or equivalently the a/w ratio. An ideal fracture test should be independent of all these variables.



(a)



(b)



(c)

Figure 2.14 Schematic of resistance curves for changes in specimen size, loading rate and material toughness based on strain energy density factor. (after Ref. 25)  
 (a) Change in specimen size,  
 (b) Change in loading rate,  
 (c) Change in material toughness.

### 2.3.1 Overall Specimen Shape

Earlier works on experimental evaluation of the J-integral by Begley and Landes [22] indicated that bend bars and center crack panels yield approximately the same  $J_{IC}$  values. However, the validity of this assessment is uncertain due to their use of maximum load,  $P_{max}$ , as the point of crack initiation. More recently, works by Penelon, Bassim and Dorlot [26] showed that the J-integral from precracked Charpy size specimens are much lower than those from three point bend specimens.

At present, ASTM stipulates the three point bend (TPB) and the compact tension specimen (CTS) as standard specimens for J-integral and K evaluation. Intuitively, it could be seen that results from these two specimens should be different. Standard quasi-static fracture toughness tests rely on servo-hydraulic test frames to generate both the load and stroke signals. The influence of the overall test frame compliance (test jig and uncracked specimen) is higher in the TPB due to its cantilever configuration, and therefore higher J values can be expected for TPB vs CTS tests. At present, the author is not aware of any direct comparison of TPB to CTS results.

### 2.3.2 Specimen Thickness

With reference to Fig. 2.15, region A is known as the plane stress fracture region where thin sheets fail in slant fracture profiles. Fracture toughness has its highest value in region A due to the higher plastic zone allowed by the

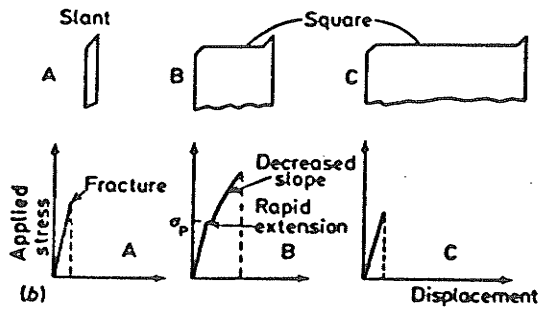
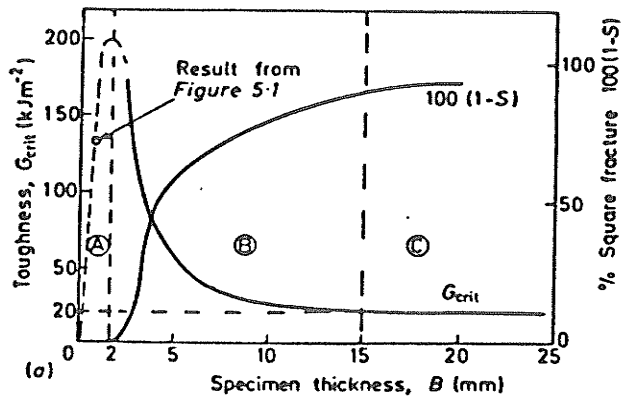


Figure 2.15 Relationship between fracture toughness and specimen thickness. (after Ref. 10)  
 (a) Variation of fracture toughness with thickness for 7075 Alloy (Al-Zn-Mg)-T6.  
 (b) Fracture profiles and stress-displacement curves typical of regions A, B and C.

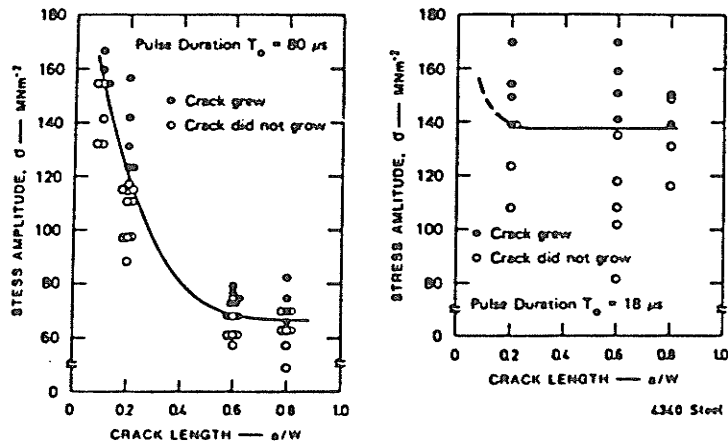


Figure 2.16  $K_{ID}$  vs  $a/w$ . (after Ref. 30)

lack of stress constraints (cf. Eqn. 2.6a). For region C, square fracture in thick sections as a result of crack tip triaxiality and a constrained plastic zone occurs. The stress intensification in region C can be as high as  $3\sigma_y$ . The size of the plastic zone is usually assumed to be of the form in Eqn. 2.6b.

In recognition of the need to clearly identify plane stress/strain fracture mode, associations such as the ASTM (American Society for Testing and Materials) stipulates specimen width constraints in the form of  $B \geq \alpha \left[ \frac{K_{IC}}{\sigma_y} \right]^2$  for standard plane strain fracture toughness testing [27].

### 2.3.3 Crack Length or a/w Ratio

Recent works by Gudas, Joyce and Davis [28] showed that although the absence of side-grooving tends to raise the apparent  $J_{IC}$  values due to the lack of crack extension constraint and shear lip formation,  $J_{IC}$  is on the whole not a function of the a/w ratio. However, an inverse parabolic variation of G, the strain energy release rate, with a/w was found by Adams and Munro [29]. Similarly, Kalthoff et al [30] have shown that  $K_{ID}$  is a function of a/w for dynamic fracture (Fig. 2.16). This was explained in terms of the effective crack length as "sensed" by a short duration pulse. The relation  $K = \sigma \sqrt{\pi a}$  implies a decrease in fracture stress as the crack length, a, increases to maintain a constant  $K_{IC}$ . However, in stress wave loading, as the crack length increases the envelope of the loading

pulse becomes of similar magnitude to the crack length and a limiting fracture stress is reached. This limiting fracture stress translates into a rise in the critical fracture toughness value.

Furthermore, Dawes [10] reported that the critical crack opening displacement,  $COD_C$ , is also a function of  $a/w$  and specimen thickness,  $B$ . In particular, for  $a/w \leq 0.5$ ,

$$\begin{aligned} \text{where } a/B = 0.5, \quad COD &= COD_C \\ a \ll B \quad \quad \quad COD &= 10 COD_C \quad (\text{low } a/w) \\ a \gg B \quad \quad \quad COD &= 2 COD_C \quad (\text{high } a/w) \end{aligned}$$

Dawes' own work have shown that for any temperature,  $COD_C$  decreased as  $a/w$  increased, for  $0.2 \leq a/w \leq 0.5$ , and a similar trend was observed for  $J$ . Similar results were reported by de Castro et al [13]. They investigated the relationship between  $COD$  and  $a/w$  as a function of temperature (Fig. 2.17). As a first approximation, one could view low temperature as similar to high strain rate in its effects on fracture toughness.

From Knott [10], it was shown that agreement of  $K$  and  $J$  values using different specimen geometries depend critically on the relative size of the plastic zone and crack length during test (Fig. 2.18). Although the principle that underlies any crack length criterion (alternatively the  $a/w$  ratio) should depend on the deviation of the real stress distribution from that of a single term approximation (Eqn 2.1), the standard criterion for  $K$  and  $J$  testing is still not based on a percent deviation of stress

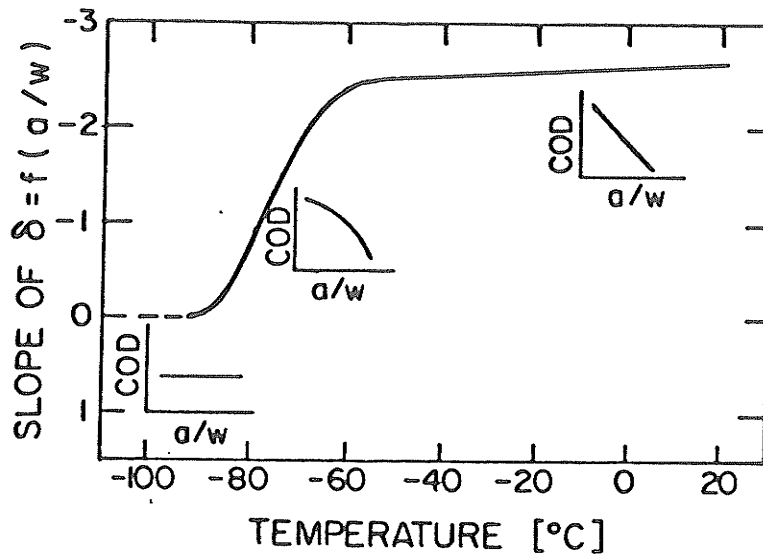


Figure 2.17 Dependence of COD- $a/w$  relationship on temperature. (after Ref. 13)

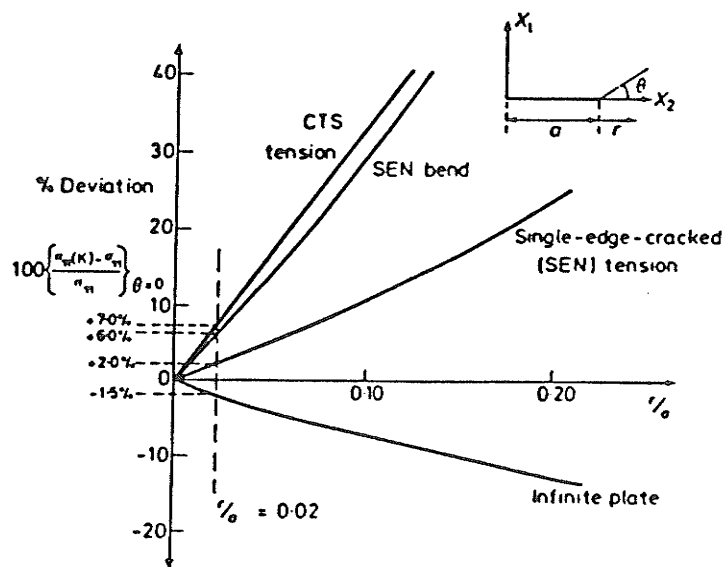


Figure 2.18 Relationship between specimen dependence of fracture toughness and relative size of plastic zone and crack length. The ordinate represents the percentage variation of crack tip stress as calculated from a single-valued stress intensity factor,  $\sigma_{11}(K)$ , and that calculated from the full series,  $\sigma_{11}$ . (after Ref. 10)

but on an arbitrary ratio of the plastic zone and crack length.

#### 2.4 Stress Wave Analysis

In ordinary engineering structures where the applied forces or the reactions are either time invariant or occur over a long period of time, a macroscopic or quasi-static analysis is adequate in explaining and predicting all actions and reactions using classical theories. However, wave analysis must be used for the class of problems where the finite time required for a body to achieve equilibrium is of similar order of magnitude to the loading and reaction times involved. A microscopic analysis of the material in the sense of analyzing the disequilibrium itself as a function of time is needed. Although the basic action-reaction classical laws are not violated, the time dependent nature of the disequilibrium yields results that are very different from those obtained quasi-statically.

#### DEFINITIONS

An elastic wave or pulse is generated and transmitted through a body when different parts of the body are not in equilibrium. As a continuum, a finite time is required for any disturbance in a part of the body to be felt throughout the body. The rate at which a body will respond to this disequilibrium is known as the characteristic speed of wave propagation, or the wave speed, which is a material property. In general, the wave speeds are different in

different directions within the body as a function of the lattice structure.

Fundamental to wave analysis is to make the distinction between the wave speed and the particle speed in a body. The particle speed is the rate at which individual molecules are caused to deviate from their equilibrium position, and is obviously a function of the applied forcing situation.

Waves that travel through the mass of a body are called body waves, whereas those that travel over its surfaces are surface waves. The waves themselves can be either longitudinal or torsional waves. As longitudinal waves they may be compressive waves or tensile waves. In considering a stationary bar, and neglecting Poisson's effect, a longitudinal compressive wave causes the individual particles of the bar to displace or move in the same direction as that which the wave travels; and in the case of a longitudinal tensile wave the particles move in the opposite direction to that which the wave travels. In the case of a torsional wave the individual particles move or oscillate entirely in a plane which is transverse or at right angle to the direction of the wave. The details of wave propagation and the stresses produced are covered in reference [31]. For later reference, the stress produced in a material as a result of stress wave propagation is:

$$\sigma_0 = v \sqrt{E \rho_0} \quad ( 2.24 )$$

where  $v$  = particle velocity  
 $E$  = Young's Modulus  
 $\rho_0$  = material density

## REFLECTION AND SUPERPOSITION OF WAVES

In considering a rectangular pulse in a bar, it is understood that a configuration such as that of Fig. 2.19 exists in the bar itself. The pulse is seen as a localized event that moves within its own envelope. Briefly,

- 1) a compressive(tensile) wave would be reflected at the free end into a tensile(compressive) wave where the overlapped portion would have doubled the original particle speed and be stress free;
- 2) a compressive(tensile) wave at a fixed end would be reflected as a compressive(tensile) wave with the overlapped region doubly stressed and stationary.

### 2.5 Theoretical Dynamic Crack Considerations

Traditionally, dynamic LEFM also assumes that the body in question is governed by some form of the SIF,  $K_{IC}$ . In its extension to elastic-plastic analysis, elastic-viscoplastic models may be used. However, by and large, all analytical/experimental models merely assume numerous material simplifying assumptions, such as material homogeneity and an assumed dynamic yield stress value, to somehow compensate for the average strain rate effect.

Early works in the area of dynamic material response includes those by Achenbach [32] on elastic waves in brittle solid and Clifton [33] on plastic waves. A detail treatise on crack propagation in an elastic solid under various loading rates was presented by Freund [34-36].

More recently, small scale yielding in elastic/rate-dependent solids was investigated by Freund and Hutchinson [37]. By imposing a critical near tip energy release rate

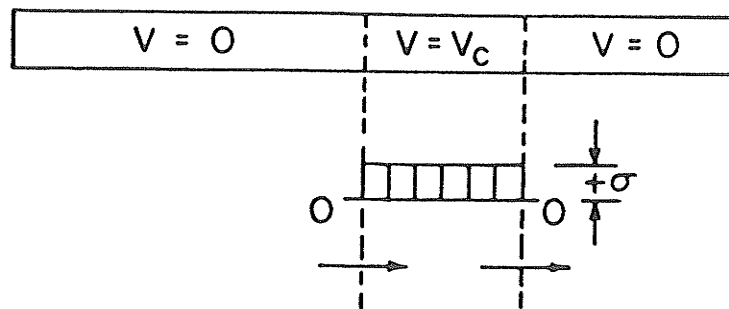


Figure 2.19 Definition of rectangular pulse in bar.  
(after Ref. 31)

as a fracture criterion, they were able to formulate a propagation equation for growing cracks.

In addition, Freund and Douglas [38] have studied the case of steady-state anti-plane crack growth in an elastic ideally-plastic material. Finite element modelling indicated that fracture toughness is very dependent on crack speed due to the significant influence of inertial effects.

With the increased popularity of the J-integral by Rice, there is much interest in the use of dynamic line integrals to characterize dynamic crack initiation.

Extension of the traditional Griffith type energy balance to crack growth in materials exhibiting non-linear deformation characteristics has been tried but resulted in physically unacceptable results [39,40]. There is of course no defect in the idea that energy must balance in the fracture process. Rather, the inconsistency arises due to the fact that macroscopic, continuum models of crack growth does not take into account the energy relations in the fracture process zone, however small that zone may be.

With reference to Fig. 2.20, Rice [41] has shown that the energy flow to the crack tip should be properly modelled as

$$\dot{G}a = \int_{\Gamma} \underline{n} \cdot \underline{\sigma} \cdot \dot{\underline{u}} \, ds - \frac{d}{dt} \int_A W \, dA + \dot{a} \int_{\Gamma} W \, n_x \, dS \quad ( 2.25 )$$

where  $J = \int_{\Gamma} (W \, n_x - \underline{n} \cdot \underline{\sigma} \cdot \partial \underline{u} / \partial x) \, dS$

Rice further showed that  $G = J_{\Gamma}$  and are both material constants if and only if crack growth takes place under conditions of steady state with respect to the moving crack

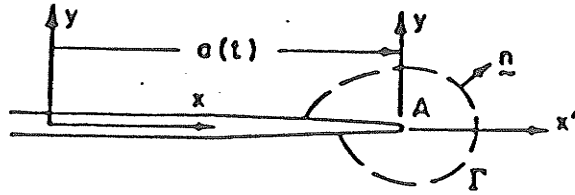


Figure 2.20 Notation for discussing energy flux to a mathematically sharp, structureless crack tip; the  $x'$ ,  $y$  axes, region  $A$ , and contour move through the material with the tip. (after Ref. 39)

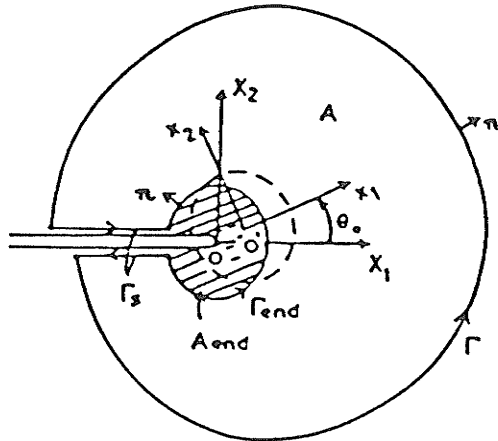


Figure 2.21 Diagrammatic details of line integral by Kishimoto.  $A_{end}$ : fracture process region,  $\Gamma_{end}$ : boundary of  $A_{end}$ ,  $\Gamma$ : arbitrary curve surrounding  $A$  and  $\Gamma_s$ : curves along crack surfaces,  $\theta_0$ : direction of infinitesimal crack extension. (after Ref. 42)

tip, ie,

$$u \neq u(t) \quad \text{and} \quad w \neq w(t)$$

This then casts doubts on the use of the line integral definition of the J-integral as a dynamic crack initiation parameter, since this static integral does not take into account the velocity of the crack tip nor the time rate of change of the strain energy density.

On the other hand, Kishimoto et al [42] proposed a path independent integral,  $\hat{J}$ , that they believe accounts for the fracture process zone, effects of plastic deformation, body forces, thermal strain and inertia for a material of an arbitrary stress-strain relation. Derived on an overall energy balance consideration of the form  $\sigma_{ij,j} + F_i = \ddot{u}_i$ , which recognizes the existence of a net resultant force, they showed that (Fig. 2.21):

$$\hat{J}_k = \int_{\Gamma \rightarrow r_k} \left\{ W_{e k} - T_i \frac{\partial u_i}{\partial X_k} \right\} d\Gamma + \iint_A \left\{ \sigma_{ij} \frac{\partial \epsilon_{ij}^e}{\partial X_k} + (\rho \ddot{u}_i - F_i) \frac{\partial u_i}{\partial X_k} \right\} dA \quad (2.26)$$

with the fracture criterion being  $\hat{J} = \hat{J}_c$  where

$$\hat{J} = \hat{J}_1 \cos \theta_0 + \hat{J}_2 \sin \theta_0$$

$\hat{J}$  represents the rate of energy change in the fracture process zone and is undefined explicitly as continuum mechanics does not operate in the fracture process zone. They view  $\hat{J}$  physically as the crack driving force. By assuming elastic material behavior, and also that body forces, inertia of materials and crack surface traction are absent,

$$\hat{J} = \hat{J}_1 = \int_{\Gamma} \left( W_{e n1} - T_i \frac{\partial u_i}{\partial x_1} \right) d\Gamma \quad (2.27)$$

which is the same as the J-integral by Rice.

## 2.6 Loading Rates and Fracture Toughness

Contrary to specimen geometry dependence of fracture toughness, fracture toughness variation as a function of loading rate is probably the most sought after "positive" relation in current research, as loading rate is one of the two main factors that control cleavage vs ductile fracture (transition temperature is the other factor). Loading rates from quasi-static to dynamic are experimentally and numerically generated to observe fracture toughness variations.

As the fracture mode changes from ductile to cleavage fracture, the energy required to fracture any specimen must necessarily decrease. Therefore, the usefulness of any fracture parameter to characterize strain rate effects depends on the parameter's ability to reflect this fracture energy decrease with change in fracture mode. Within the last ten to twenty years, researchers are beginning to rely heavily on extension of the quasi-static K and J fracture parameters to quantitatively characterize dynamic fracture.

The usual convention for classifying rate effects on fracture toughness is  $\dot{K} = K_{IC}/t_c$ , assuming LEFM conditions apply. The critical time,  $t_c$ , is the time from the time of loading to the critical crack event as defined by the experimenter. It is assumed that  $K = 1 \text{ MPa}\sqrt{\text{ms}^{-1}}$  constitutes the static value [27]. Following the static case:

- 1) conventional fracture mechanics specimens in servo-hydraulic machines

$$\dot{K} \text{ up to } 10^3 \text{MPa}\sqrt{\text{ms}}^{-1}$$

- 2) bending impact specimens using pendulum or drop weight

$$\dot{K} = 10^3 \text{ to } 10^5 \text{MPa}\sqrt{\text{ms}}^{-1}$$

- 3) stress wave loading

$$\dot{K} = 10^4 \text{ to } 10^9 \text{MPa}\sqrt{\text{ms}}^{-1}$$

The dependence of  $K$  on loading rate is different for cleavage and ductile fracture [43]. In the cleavage case  $K$  generally decreases as  $\dot{K}$  increases. However, the trend as depicted by Fig. 2.22 was observed by Klepaczo [44], Eftis and Krafft [45] and Radon and Turner [46]. It is traditionally believed that as the rate of crack loading is increased, the deformation may become adiabatic with respect to the plastic zone, and the subsequent gross relaxation at the crack tip would drive up the  $K$  value. However, a countering view holds that the rising portion of the curve in Fig. 2.22 may actually be measuring crack propagation effects rather than crack initiation energy requirements [43].

On the other hand, work by Costin et al [47] indicates that this general loading rate effect may sometimes be overshadowed by microstructural considerations such as void coalescence. In their work using circular bar specimens, they have found that for SAE 4340 steel no strain rate effect on either  $K_{IC}$  or  $J_{IC}$  was observed. Alternately, SAE 1020 cold-rolled steel was found to exhibit a sharp decrease of both  $J_{IC}$  and  $K_{IC}$  with strain rate.

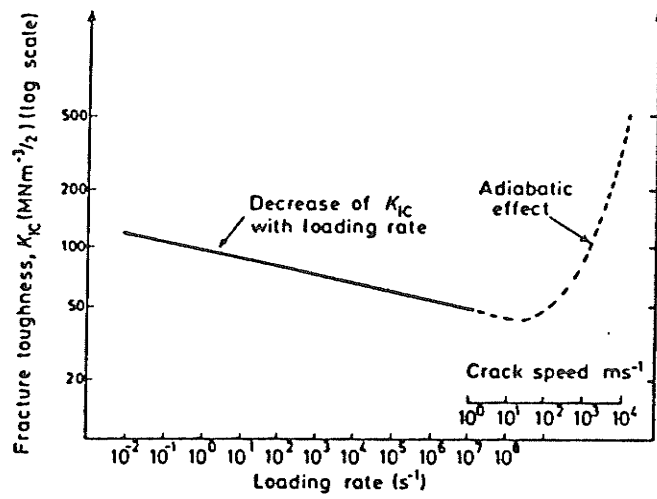


Figure 2.22  $K$  vs  $\dot{K}$  for the case of ductile fracture.  
(after Ref. 46)

Joyce [48] determined a dynamic J value,  $J_{KD}$ , for A533B steel at 150°C and  $\dot{K} \sim 4 \times 10^3 \text{ MPa}\sqrt{\text{ms}}^{-1}$ . The general conclusion was that the slope of the  $J_{KD}$  curve was fairly unaffected by rate effects but that the level was shifted upward about 50% compared to the standard J-Resistance curve. In another investigation on a medium strength alloy steel Joyce [49] found no significant rate effects.

Bayoumi [50], on the other hand, found significant decrease in J values from 68.5 to 27.8  $\text{KJ/m}^2$  as  $t_c$  goes from  $2.66 \times 10^8 \mu\text{s}$  to  $26 \mu\text{s}$  (equivalent  $\dot{K}$  from 0.5 to  $3.1 \times 10^6 \text{ MPa}\sqrt{\text{ms}}^{-1}$ ). In his work, Bayoumi performed dynamic tension tests using a compression Split Hopkinson Bar and Wedge Loaded Compact Tension specimens.

More recently, there is a renewed interest in investigating shear band formation and the role of shear bands in controlling the fracture toughness-loading rate relationship [51-53]. Although a complete understanding of shear band formation and its effects is still lacking, it would appear that high loading rates sometimes result in localized shear bands that tend to lower the fracture toughness of metals.

## 2.7 Historical Development of Dynamic Fracture Toughness Parameters

Experimentally, numerous difficulties still persist after a few decades of intense experimental research into the area of dynamic fracture characterization. Although progress has been made in generating short loading pulses,

there is still great difficulty in accurately measuring the load as sensed by a specimen and the subsequent specimen strain. There is at present no agreed upon specimen geometry, interpretation of experimental results, determination of crack initiation or definition of effective gage length in dynamic fracture analysis. Details of past and current research works are presented in this section. It is precisely this problem that has led to the present work - an attempt to standardize dynamic fracture toughness evaluation through the use of a specimen that possesses an engineering wise realistic stress state.

#### 2.7.1 Qualitative Dynamic Fracture Toughness Parameters

Earliest attempts at dynamic fracture characterization involved qualitative comparison of the conditions that caused brittle/ductile transition in metal fracture mode. These early attempts involved notched bar tests using either Charpy or Izod specimens [54]. These tests provided a high degree of plane strain, and fracture toughness was measured in terms of absorption of impact energy provided by pendulum strikers. These tests suffered in that the relative energy absorption could not be used directly for design calculations. Also, the small specimens used in these tests did not always provide a realistic model of the actual service conditions.

The transition to thicker specimens was pioneered by Pellini [55] and the Naval Research Laboratory. Tests such as the Drop Weight Test and the Dynamic Tear Test used

large, guided falling weights to provide the impact energy. Absorbed impact energy values were then used to qualitatively compare the fracture toughness of metals.

Although qualitative tests only provide dynamic fracture toughness information in terms of "degree of ductility", they have the advantage of simplicity in their construction and data interpretation.

### 2.7.2 Quantitative Dynamic Fracture Toughness Parameters

Although qualitative parameters are economical and simple to obtain, they are inadequate in applications where low safety factors must be maintained. Also, the impact energy levels obtainable from these tests are insufficient to cause stress wave loading of their specimens. Therefore, in modern engineering applications where stress wave loading and low safety factors are present, there is a clear need for quantitative dynamic fracture toughness parameters for metal characterization. The most promising candidates to date are variations of the original Hopkinson Pressure Bar.

#### HOPKINSON PRESSURE BAR

In November 1913, Bertram Hopkinson [56] released a paper describing a simple technique whereby "it is possible to measure both the duration of (a) blow and the maximum pressure developed by it". The primary contribution of the Hopkinson Pressure Bar (HPB) to fracture mechanics is the construction of an essentially compressive/tensile wave

without significant energy loss. The one-dimensional wave thus created makes the resultant analysis relatively easy to handle.

### KOLSKY BAR

Kolsky [57] was the first person to apply Hopkinson's pressure bar concept to dynamic fracture analysis based on a design by R.M. Davies [58]. In his work, Kolsky used explosives to accelerate a striker to impact his disc specimens. The stress-strain signals were measured using condenser microphones. In his paper he gave an excellent description of the compression stress wave phenomenon, and outlined some of the major concerns that are still faced by present day researchers. He was able to measure strain signals of the order of 20  $\mu$ s, and paved the way for future compression Hopkinson Bar tests.

### Compression Hopkinson Bar

Numerous researchers have improved and modified upon the works of Hopkinson and Kolsky since then. Improvements have been made in the area of producing the dynamic compressive loading stress and methods in recording the transient signals accurately. For example, Clifton et al [59] have pioneered work in plate impact, where high shear stresses are produced to simulate material flow properties at high loading rates. Gorham [60], on the other hand, uses high speed photography to measure the fracture behavior of a very small specimen.

### TORSION HOPKINSON BAR

Due to the dispersive nature of the longitudinal Compression Hopkinson Bar, researchers have also turned to the torsion Hopkinson Bar to investigate dynamic material properties. The differential equation governing torsional stress wave is such that no dispersion is present and the solution is exact for the given bar assumptions [31]. Typical of this type of set up is the torsion bar developed by the late Dr. Campbell [61]. The dynamic torque is supplied by a stored torque through a motor and pulley system. Duffy et al [59,62,63] have since used this technique to study strain rate effects and shear band formation.

### TENSION HOPKINSON PRESSURE BAR

Notwithstanding the advances made in dynamic compression and torsion testing, researchers realize that a tensile dynamic tester is of greater practical value since most engineering structures fail dynamically in tension. Efforts in this area include the use of cruciformed mesh specimens by Albertini & Montagnani to achieve biaxial tension [64]; dynamic tensile testing of small, round tension specimens by Nicholas [78] and modifications to the Nicholas design by Ross et al [79]; and the use of circumferentially notched round bar specimens by Duffy et al [47] to study the dynamic SIF  $K_{ID}$ .

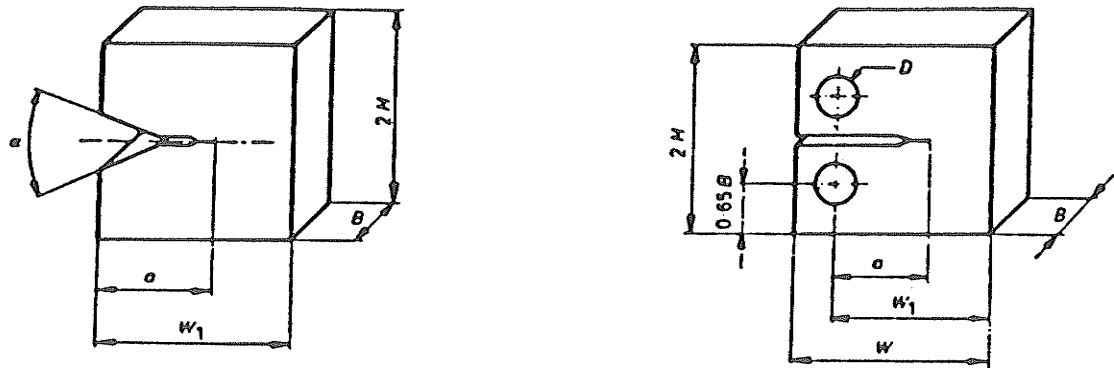
As can be seen, there is ample interest in understanding dynamic material properties and dynamic

fracture toughness. However, aside from Duffy et al [46], few investigators have attempted to combine both tensile loading and stress triaxiality. In Duffy's case, the use of precracked, long round bar specimens was both time consuming and expensive. Also, Duffy's system concentrates on high loading rates, and does not lend itself to a systematic, spectrum investigation of fracture toughness from quasi-static to stress wave speeds. Paris et al [65] were able to perform a limited spectrum investigation of dynamic K values using CTS and a high speed servo-hydraulic test frame, but the critical time in these tests was only in the neighborhood of 40 ms. Klepaczko [44] was the first investigator that attempted to construct a wide spectrum loading fracture toughness system.

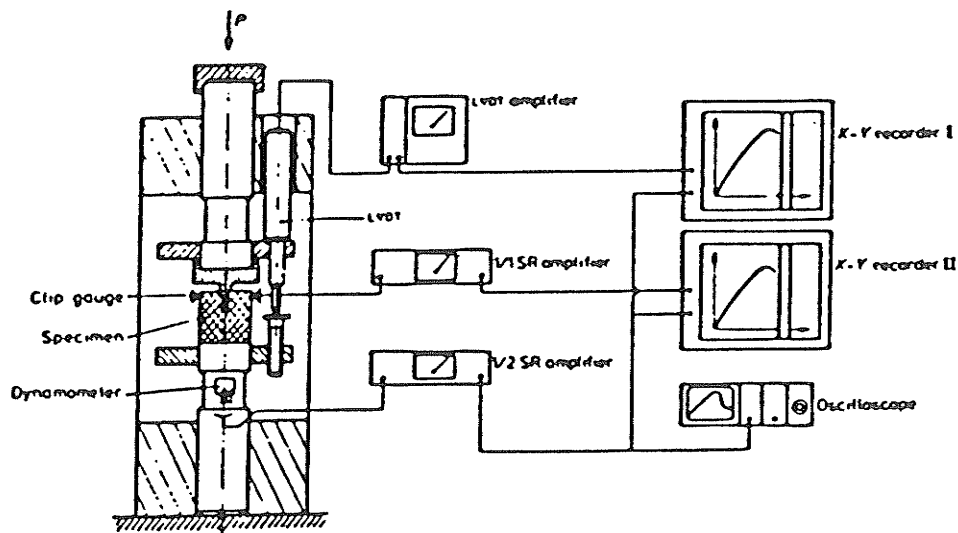
#### Wedge Loaded Compact Tension System

This wedge loaded specimen configuration, devised by Klepaczko[44], was used to investigate the loading rate effect on  $K_{IC}$ . This test system uses a compress gas gun for acceleration of its striker, strain gages for stress-strain measurement and a modified ASTM compact tension specimen for its specimen(Figs. 2.23). This system turns the traditional Compression Hopkinson Bar into a tensile one through wedge loading of the WLCT specimens. The advantage of this set up is that it offers a wide loading spectrum for fracture testing ( $1 < \dot{K}_I < 10^6 \text{ MPa}\sqrt{\text{ms}}^{-1}$ ), while using the same loading mode and incorporating stress triaxiality.

Corran et al [67,68] modified the Klepaczo WLCT system

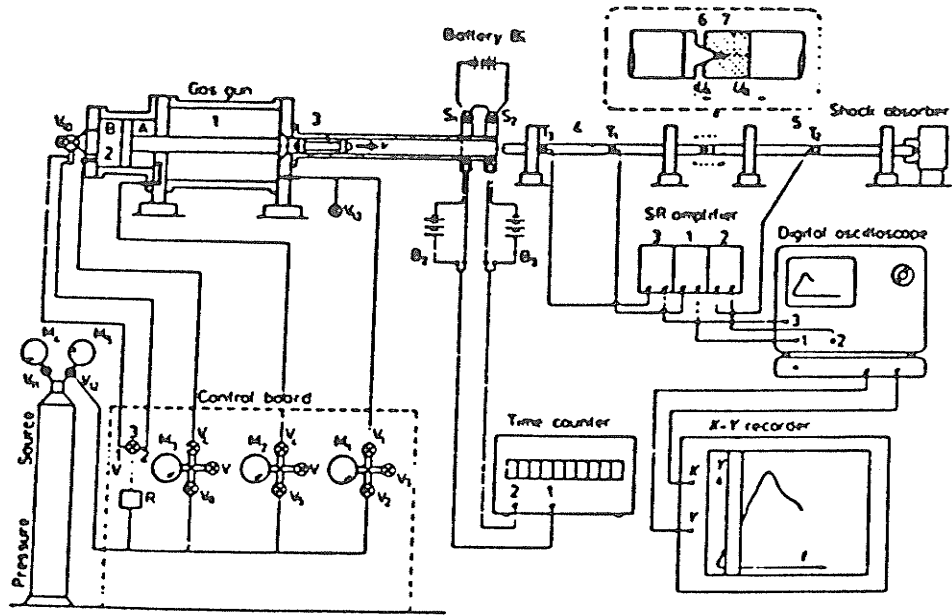


( a )



( b )

Figure 2.23 Wedge loaded compact tension setup.  
 (after Ref. 44)  
 (a) Geometry of a wedge-loaded specimen,  
 (b) Device for quasi-static slow and fast loading. The force  $P$  acting on the wedge is applied by a testing machine.



( c )

Figure 2.23 (c) Split Hopkinson pressure bar applied to fracture dynamics. 1,2A,2B: chambers in gas gun; 3: striker bar; 4: incident bar; 5: transmitter bar; 6: wedge; 7: specimen; T1,T2,T3: strain gage stations; V1-V13: valves; M1-M5: manometers; B1-B3: batteries; D1,D2: photodiodes; S1,S2: light sources.

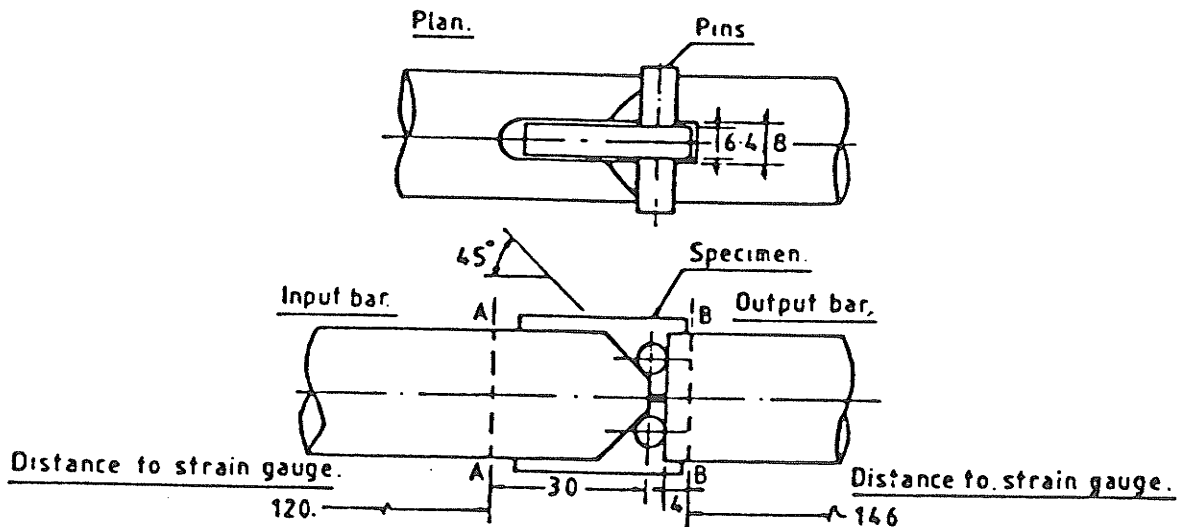


Figure 2.24 Modified wedge loaded compact tension setup. (after Ref. 67)

by replacing the WLCT specimen with a standard CTS, and loads the specimen through its pin holes via an input wedge (Fig. 2.24). Corran's modifications to the WLCT system was meant to minimize the frictional effects of Klepaczo's WLCT system.

Bayoumi et al[80-82], as a result of previous work on coal fracture by Bassim et al[66], have extended the Klepaczo WLCT concept to test for the dynamic J-integral parameter,  $J_{ID}$ . This work by Bayoumi et al represents the only attempt at the experimental determination of the dynamic J-integral. As this present work was in part motivated by Bayoumi's investigation, it would be helpful to briefly discuss the WLCT test methodology as used by Bayoumi to appreciate its advantages and possible shortcomings.

#### J-Integral Determination Using WLCT

The analysis procedure used in the WLCT system by Bayoumi et al[80-82] is essentially similar to the conventional compression Hopkinson Bar theory used by Kolsky[55], and is based on these fundamental assumptions:

- 1) one dimensional wave analysis is applicable;
- 2) strain signals obtained on the instrumented bars are representative of the strain field across the specimen;
- 3) all strain signals are time shifted to the same origin, assuming that equilibrium is established in the specimen during the fracture process.

The uniqueness of this WLCT system lies in the manner that the tensile force is generated and the determination of the point of crack initiation.

This WLCT system utilizes a compressive stress wave for tensile loading of its specimens through a loading wedge that has a wedge angle slightly larger than the notch angle of the WLCT specimen (Fig. 2.25). As the loading wedge is pushed forward by the compressive stress wave, the loading wedge's sides simultaneously separates both halves of the WLCT specimen and hence loads the crack tip of the specimen in tension. Strain gages mounted on the incident and transmitted bars record the load-time signals.

To detect the point of crack initiation, a strain gage is mounted just ahead of the fatigue crack tip on the specimen. The point of crack initiation is taken to be coincident with a drop in the strain gage signal. This signal drop signifies strain relaxation ahead of the crack tip and is associated with crack propagation (Fig. 2.26).

The dynamic J-integral is taken to be proportional to the load/load-line displacement curve up to the point of crack initiation. Correlation with stretch zone measurement results indicates the J-integral using a WLCT specimen is best represented by the equation:

$$J = \frac{\alpha U}{B b} \quad (\text{cf. Eqn. 2.19})$$

where  $\alpha$  = 1, specimen geometry factor  
 $U$  = area under load/load-line displacement curve up to  $t_c$   
 $B$  = specimen thickness  
 $b$  = remaining specimen ligament

The effectiveness of the above WLCT system to characterize the loading rate effects of the J-integral has

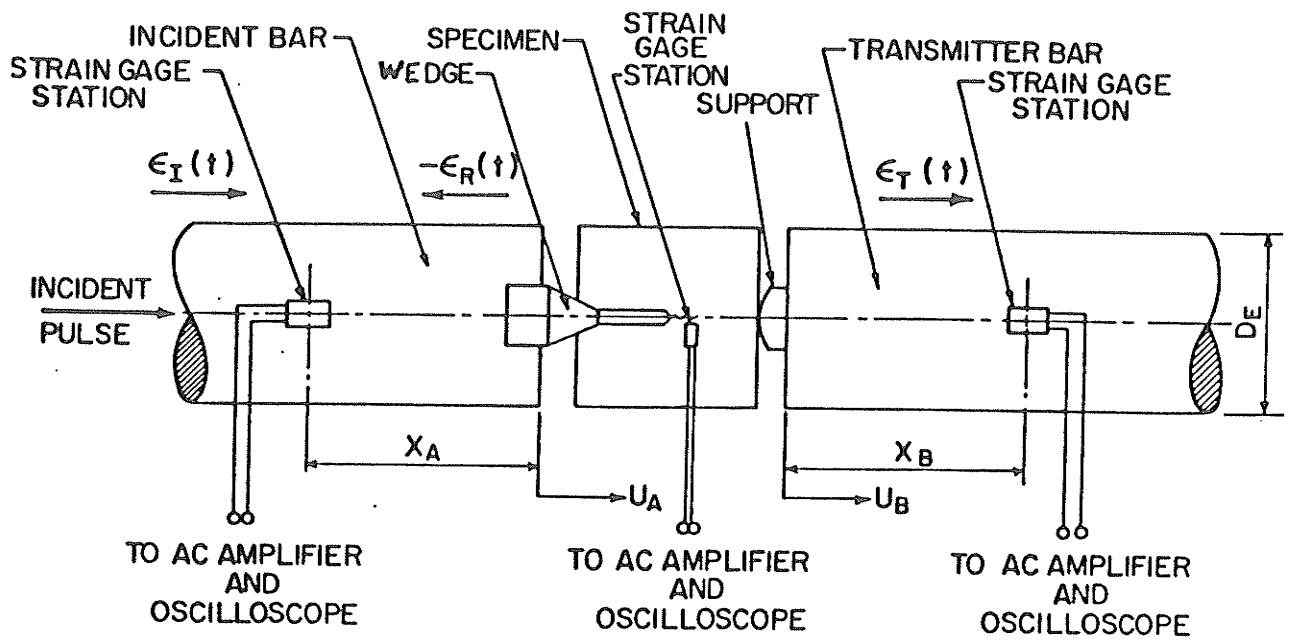


Figure 2.25 Instrumentation on Split Hopkinson Bar for dynamic fracture test using WLCT. (after Ref. 50)

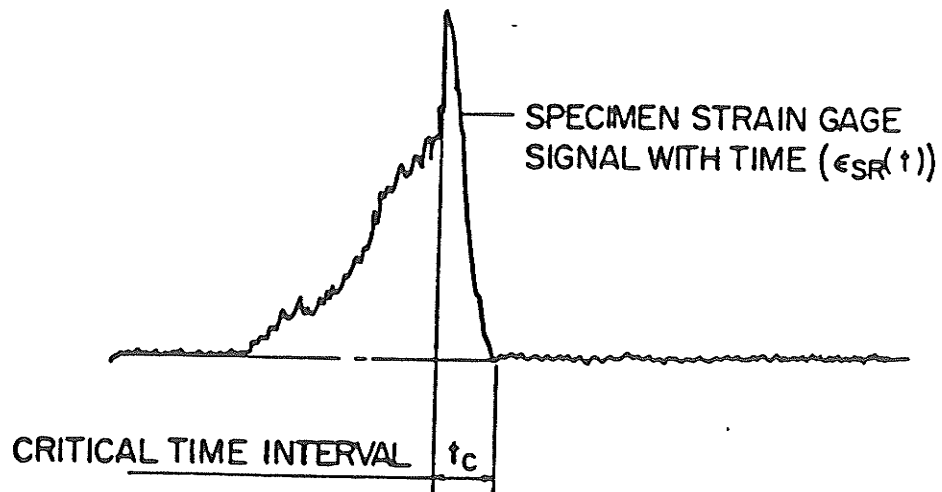


Figure 2.26 Crack initiation detection on WLCT using strain gage. (after Ref. 50)

been demonstrated[50]. Nonetheless, there are several design considerations that warrant closer scrutiny.

Firstly, the experimentally derived geometric factor of  $\alpha = 1$  lacks theoretical confirmation, and is in contrast with the accepted factor of  $\alpha \approx 2.2$  associated with the standard CTS.

Secondly, crack initiation is determined using a specimen surface-mounted strain gage. Variability in gage placement and crack advance across the specimen thickness section for each specimen introduces experimental uncertainties.

Thirdly, the dynamic loading using the loading wedge necessarily introduces compressive loading stresses. In addition, the amount of friction between the loading wedge and the specimen notch also needs to be more accurately accounted for and eliminated.

Finally, it has been learned that, within experimental errors, misalignment of the loading wedge with respect to the specimen introduces significant scatter to the experimental results.

As can be seen, while Klepaczko's, Bayoumi et al's and Corran et al's systems represent the current expertise in tensile dynamic fracture testing, the wedge loading of specimens introduces compressive and frictional forces. As such, these systems are not strictly tensile test systems. In addition, the high degree of experimental error associated with a slight misalignment of the striker with

respect to the WLCT specimen warrants the search for an improved dynamic tensile fracture toughness testing system.

In view of these developments, a fracture toughness testing system that loads standard CTS in an essentially tensile manner, at speeds ranging from quasi-static to stress wave loading is proposed. This overcomes the major shortcomings associated with the WLCT system in terms of compressive loading, frictional effects and uncertainties concerning the choice of specimen geometry factor  $\alpha$ . This present system characterizes fracture toughness via an energy parameter that lends itself to design considerations. This fracture toughness testing system thus represents a forward step in dynamic fracture toughness characterization.

## 2.8 Conclusions

In summary, it can be seen that dynamic fracture toughness investigation is a logical extension of LEFM and EPFM analysis. A dynamic fracture toughness parameter must have clearly defined specimen geometry dependence, and must also be capable of reflecting the decrease in fracture energy associated with a ductile to brittle fracture mode transition. Due to the complexity of stress wave analysis, theoretical analysis of dynamic crack problems are subject to numerous material simplifying assumptions. The state-of-the-art in experimental fracture toughness test systems capable of quasi-static to dynamic tensile loading involve the use of wedge strikers. The compressive and frictional loads associated with the wedge striker and the need for

accurate alignment of the entire test system mean improvements are still needed in the generation of a purely tensile dynamic loading situation.

CHAPTER THREE  
EXPERIMENTAL PROCEDURES

### 3.1 Material

An AISI 1045 steel bar 12.7 mm thick and 76.2 mm wide was used. The chemical composition of this steel is given in table 3.1 and the tensile properties in table 3.2. After cutting the bar into 63.5 mm pieces in length, the short pieces were annealed at 800°C for 1/2 hour to obtain good ductility in the metal before testing.

### 3.2 Specimen

Specimens used in all tests were standard CTS of dimension 63 mm x 60 mm x 12.7 mm (Fig. 3.1). A notch was machined in the longitudinal-transverse (L-T) orientation. The specimens were fatigue precracked, at room temperature, according to ASTM specifications E399 to crack lengths of  $a/w = 0.5, 0.6, 0.7$ . For the last 50% of the fatigue precrack,  $K_{max}$  was kept below  $25 \text{ MPa}\sqrt{\text{m}}$ . The final crack lengths were measured on both sides of each specimen to ensure adherence to the tolerances set forth in the ASTM code.

### 3.3 Reference Fracture Toughness Testing ( $J_{IC}$ )

A Standard ASTM J resistance curve test [69] was performed at quasi-static speed on a specimen of  $a/w = 0.6$  using a servo-hydraulic Instron testing machine (Model 1320) to establish a baseline quasi-static fracture toughness  $J_{IC}$ . For purposes of computation, the load-line displacement was measured via the stroke feedback signal, while the load was measured via the load feedback signal. These two signals

Table 3.1

Chemical Composition of AISI 1045 Steel

C	Mn	P(min)	S(max)	Fe
0.43 - 0.5	0.6 - 0.9	0.04	0.08	balance

(after Bayoumi)<sup>50</sup>

Table 3.2

Mechanical Properties of Annealed AISI 1045 Steel  
at Room Temperature  
(Quasi-Static Tensile Test)

<u>Property</u>	<u>Value</u>
Yield stress $\sigma_y$	300 MPa
Ultimate stress $\sigma_u$	600 MPa
Flow stress $\sigma_f = (\sigma_y + \sigma_u) / 2$	450 MPa
Young's Modulus E	$2.07 \times 10^5 \text{ MPa}^1$
Percent Elongation	40
Percent reduction in area	65

(after Bayoumi)<sup>50</sup>

<1> assumed (30,000 ksi)

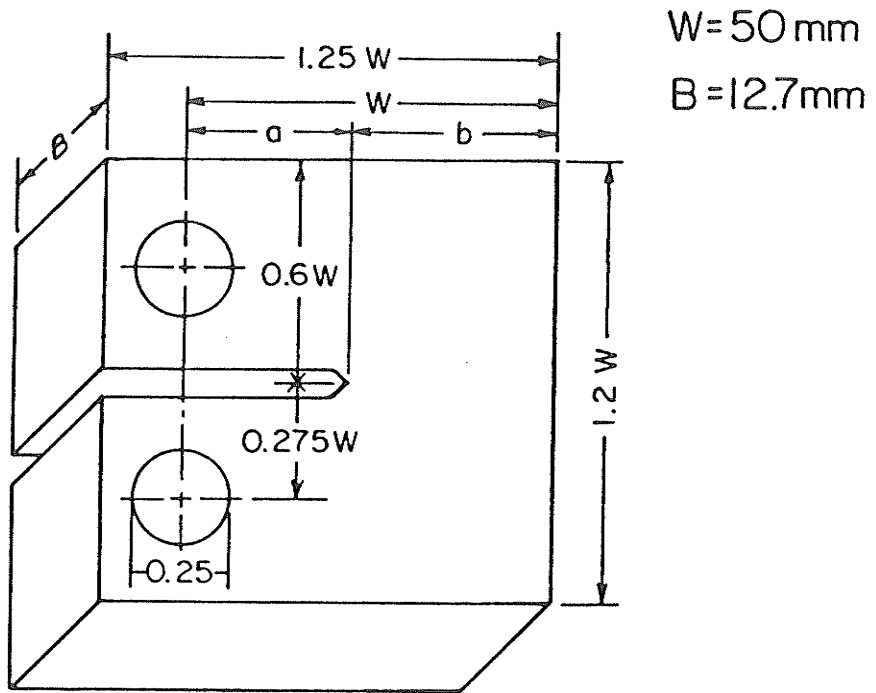


Figure 3.1 Compact tension specimen geometry and dimensions.

were recorded on graph paper using an X-Y plotter with the stroke signal as the X-axis. The graphical data were subsequently manually digitized for computerized analysis.

$J_{IC}$  was determined using the single specimen unloading compliance method, where a series of approximately 10% load unloadings were performed to monitor crack extension during test. The J value at the first unloading was evaluated using Eqn 2.20, and subsequent J values corrected for crack growth were calculated as per E813 recommendations.

A plot of J-integral values vs  $a$  was constructed to obtain the crack advance line. The critical J-integral value,  $J_{IC}$ , was obtained at the intersection of the experimentally constructed crack advance line and the theoretical blunting line originally proposed by Landes and Begley [70]:

$$J = 2 \sigma_f \Delta a \quad ( 3.1 )$$

where  $\sigma_f = ( \sigma_y + \sigma_u ) / 2$

$\sigma_f$  = flow stress

$\sigma_y$  = yield stress

$\sigma_u$  = ultimate stress

Equation 3.1 was developed using Wells' model (Eqn 2.14), with  $m = 1$ , and flow stress was used to account for the plastic behavior associated with crack blunting.

### 3.4 Quasi-Static to Dynamic Fracture Toughness Testing ( $J_Q$ )

Based on the J-integral estimation formula as proposed by Rice and modified by Merkle & Corten and Landes & Clarke (Eqn. 2.20), the J-integral can be regarded as a quasi-

static characterizing fracture energy parameter for all real engineering materials where limited plasticity occurs. As such, it is clear that  $J_{IC}$  could be determined from a single load/load-line displacement record without unloading, provided the point of crack initiation can be accurately identified.

In the case of nonquasi-static loading, Rice[41] has pointed out that the quasi-static J-integral would represent a similar characterizing fracture energy parameter, provided that neither the crack tip displacement nor the strain energy density is a function of time (cf. section 2.5). In stress wave loading where the process of crack tip blunting is of similar duration to the loading event, neither crack tip displacement nor the strain energy density can be considered to be time invariant. However, Rice[41] did not point out the relative importance of this time invariancy consideration in terms of percentage error to the characterizing fracture energy obtained.

Past efforts at dynamic fracture toughness testing using the WLCT systems did not take these factors into considerations, and their analysis was further complicated by their use of a non-standard CTS where a quasi-static J-integral estimation formula is lacking. The combination of these considerations may in part account for their use of a geometric factor  $\alpha = 1$ .

The author designed test system extends past efforts in dynamic fracture toughness testing through the use of a

standardized CTS and the generation of an essentially tensile loading situation. The use of a standardized CTS allows the use of an established J-integral estimation formula, and the presence of tensile loading enables the application of this estimation formula to test results. This original test system is able to determine a characterizing fracture energy parameter, tentatively termed  $J_Q$ , for quasi-static to stress wave loading, and therefore, represents a new step in dynamic fracture toughness characterization of metals. This fracture parameter,  $J_Q$ , is strictly not the J-integral at nonquasi-static loading rates, but approaches  $J_{IC}$  at quasi-static loading.

The fundamentals of the author proposed quasi-static to dynamic fracture toughness testing system is as follows:

- 1) provide tensile loading of CTS without unloading at the desired loading rate;
- 2) construct the corresponding load/load-line displacement curve;
- 3) determine the point of crack initiation using the output of the Crack Opening Displacement-time curve;
- 4) determine the area under the load/load-line displacement curve up to the point of crack initiation
- 5) apply Eqn. 2.20 to calculate the corresponding critical fracture energy  $J_Q$ .

By providing the proper load transducers and crack initiation detection system, the data recording was performed automatically and data analysis was carried out by a computer.

The major contribution of this system to fracture

analysis is that it provides dynamic tensile loading of a standard CTS and a new method of fracture toughness characterization. By using a CTS, the experimentally obtained fracture energy parameter  $J_Q$  lends itself to quantitative design considerations similar to the quasi-static  $J_{IC}$ .

The testing program can be summarized as follow:

- 1) With the Instron test frame used in fatigue pre-crack of the specimens,  $J_Q$  would be determined at quasi-static, slow speed and high speed loading. In the remainder of this report, these tests would be identified as Instron quasi-static test, Instron slow speed tests and Instron high speed tests. Collectively, they are known as the Instron speeds tests.
- 2) With the stress wave loading apparatus, tests would be performed at two striker velocities. In the remainder of this report, these tests would be identified as Dynamic speed tests, Stress wave speed tests or Impact loading tests as used in the context of the report.
- 3) At all speeds, a combination of three a/w ratios (a/w = 0.5, 0.6, 0.7) would be used to investigate the a/w dependence of  $J_Q$ .

#### 3.4.1 Instron Speeds Tests

Photographs of the quasi-static to high speed experimental set-up are shown in Figs. 3.2. Compact tension specimens of three a/w ratios (0.5, 0.6, 0.7) were tested under simple tensile loading at three different test speeds using standard CTS test grips and conditions. The load signal was provided by the Instron's load feedback signal. The load-line displacement and the point of crack initiation were obtained using a high frequency MTS Crack Opening Displacement (COD) gage. This COD gage has a maximum

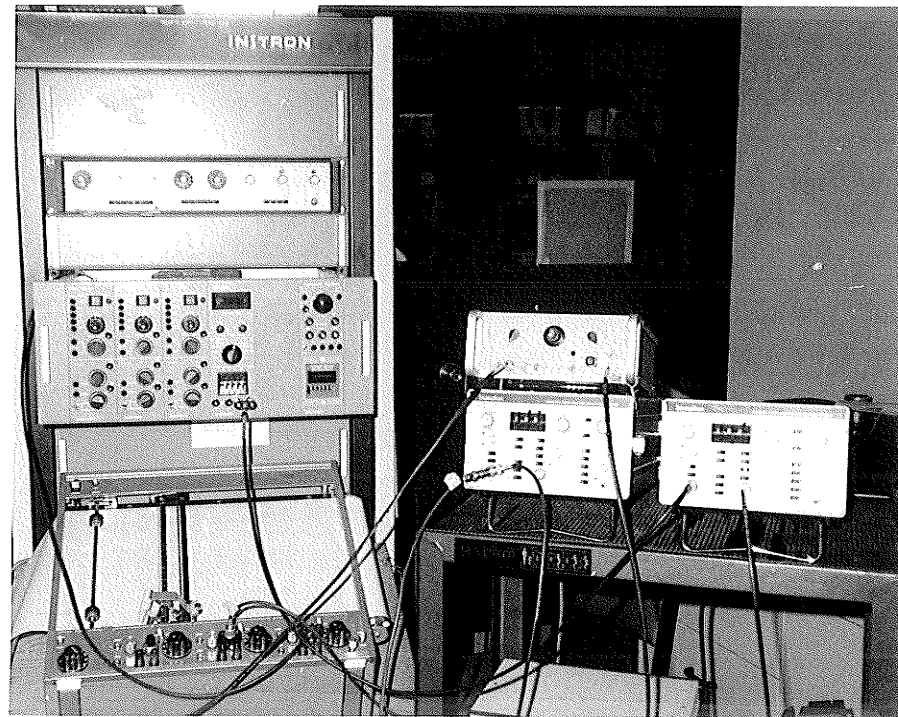
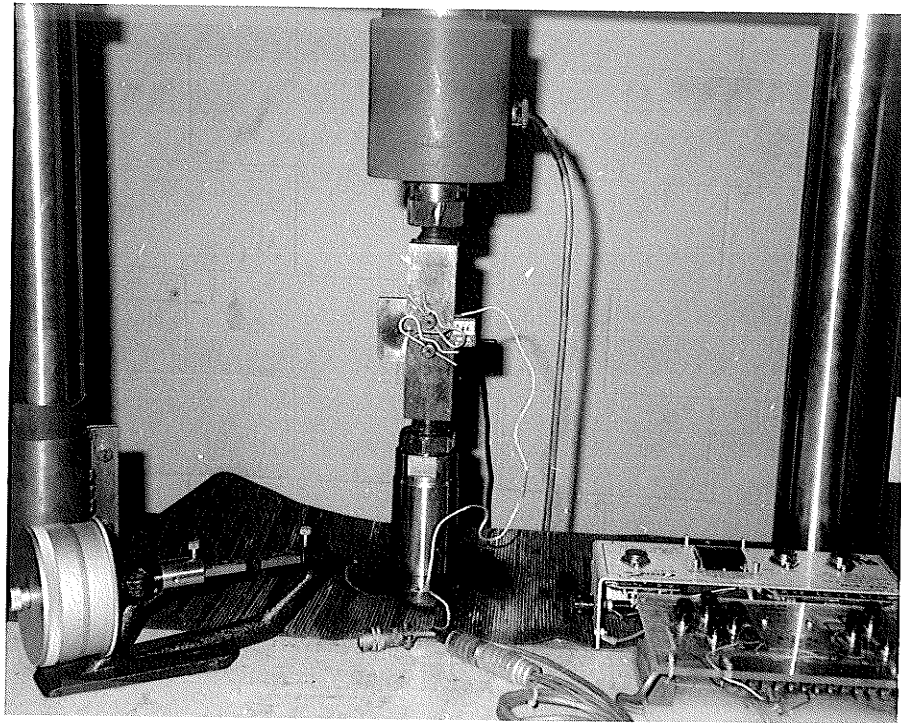


Figure 3.2 (a) Close up of Instron speeds CTS grips and crack opening displacement detection instrumentation.  
(b) Close up of Instron test frame controller and signal recording systems.

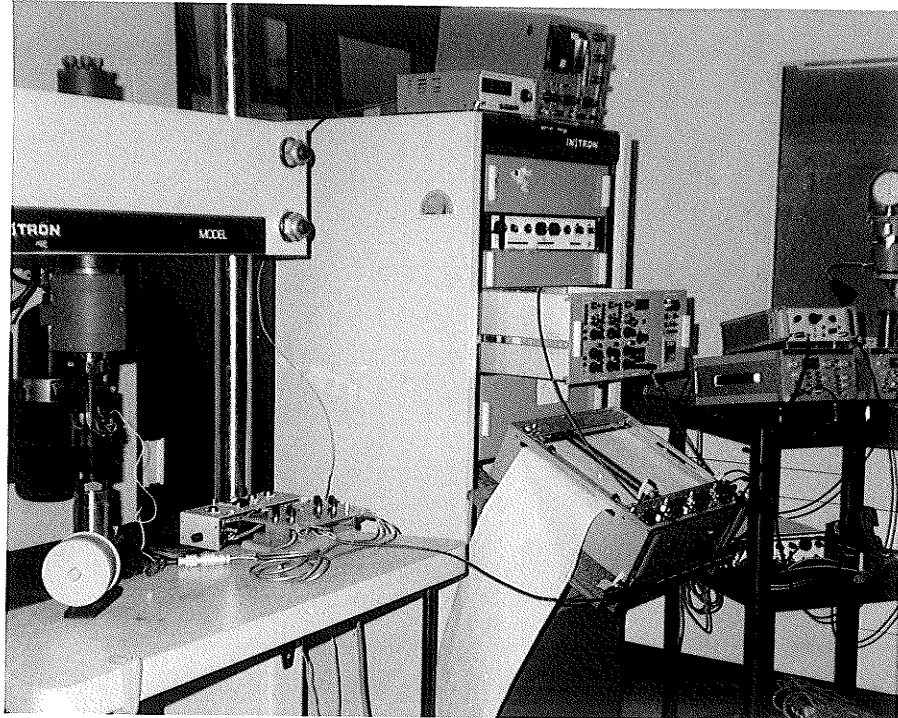


Figure 3.2c Overview of Instron Speeds test setup.

frequency response of 50 kHz and a maximum working range of 2 mm. The Instron high speed tests were subsequently repeated using a MTS COD gage which has a 0-300 Hz frequency response range and a maximum working range of 2.5 mm. The Instron high speed tests were repeated to further confirm the results obtained.

Load-line displacement,  $\delta_{11}$ , was obtained from the COD signal by applying the correction factor,  $\delta_{11}/\delta_0$ , given by Saxena et al [71], where  $\delta_0$  stands for the displacement at specimen face where the COD gage was mounted (Fig. 3.3).

Crack initiation is considered to be coincident with a sudden rise in the slope of the COD-t signal (Fig. 3.4). As a crack blunts, it is reasonable to expect the slope of the COD-t curve to decrease due to the crack's resistance to opening up under load. Once crack initiation begins, the slope can be expected to increase tremendously.

The load and COD signals were off-loaded directly to two Biomation transient recorders. These signals were then plotted onto an X-Y plotter and manually digitized for computerized analysis. The tentative fracture toughness parameter,  $J_Q$ , was then taken to be the area under the load/load-line displacement curve up to critical time  $t_c$ .

When using two transient recorders simultaneously, there was the unique problem of ensuring the trigger levels of each recorder were approximately the same. Since the trigger levels were extremely sensitive and were set by analog and not digital dials, minor differences in trigger

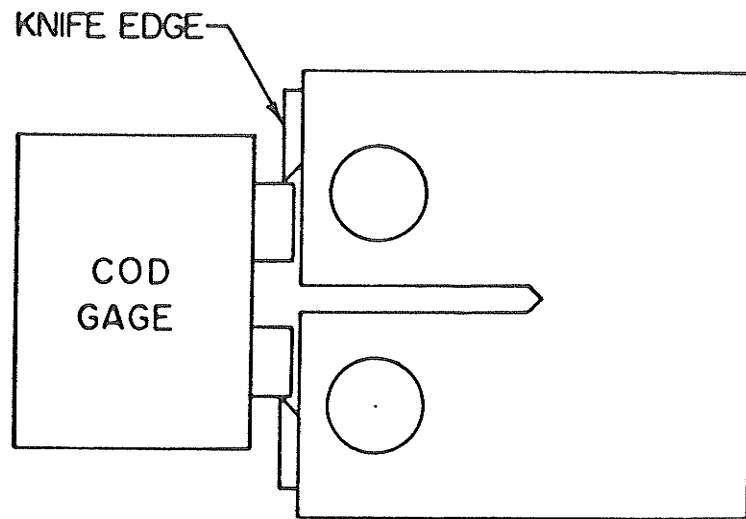


Figure 3.3 COD gage mounted on CTS.

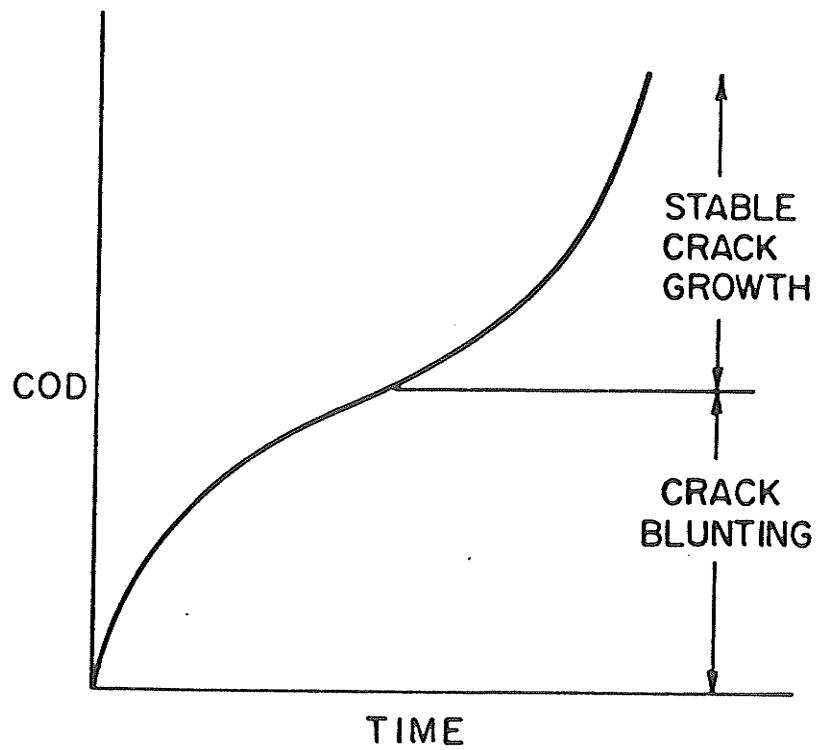


Figure 3.4 Ideal COD gage response to crack blunting.

levels would have meant that one of the signals would always be delayed or lost. To circumvent this problem, the trigger levels were first set manually. A function generator was then used to detect differences in trigger levels. Approximate adjustments were then made to the individual trigger levels to ensure that both trigger levels responded to the same input signal level. For these Instron tests, the trigger level difference was found to be negligible from inspection of the test records.

The Instron loading rates were  $V_0 = 0.33$  mm/min (quasi-static),  $V_1 = 1.2$  mm/sec (slow speed) and  $V_2 = 20$  mm/sec (high speed), with  $V_2$  corresponded to the highest speed achievable on the servo-hydraulic machine. All three Instron test speeds were generated with the ramp function of a digital function generator. Taking the center line distance between the loading pin holes on a CTS as the nominal gage length (27.5 mm), the nominal strain rates,  $\dot{\epsilon}$ , are  $\dot{\epsilon}_0 = 1.5 \times 10^{-4} \text{s}^{-1}$ ,  $\dot{\epsilon}_1 = 4.4 \times 10^{-2} \text{s}^{-1}$  and  $\dot{\epsilon}_2 = 7.3 \times 10^{-1} \text{s}^{-1}$ . The actual strain rates ahead of the crack tip would of course be considerably higher. By using identical test setup, the Instron tests were able to detect fracture toughness variations due only to changes in loading rates.

#### 3.4.2 Impact Loading by Modified Split Hopkinson Bar

The fundamental aspects of tensile stress wave loading system are shown in Fig. 3.5. The box diagram for the experimental setup is shown in Fig. 3.6. Photographs of the experimental setup are shown in Figs. 3.7. The dynamic



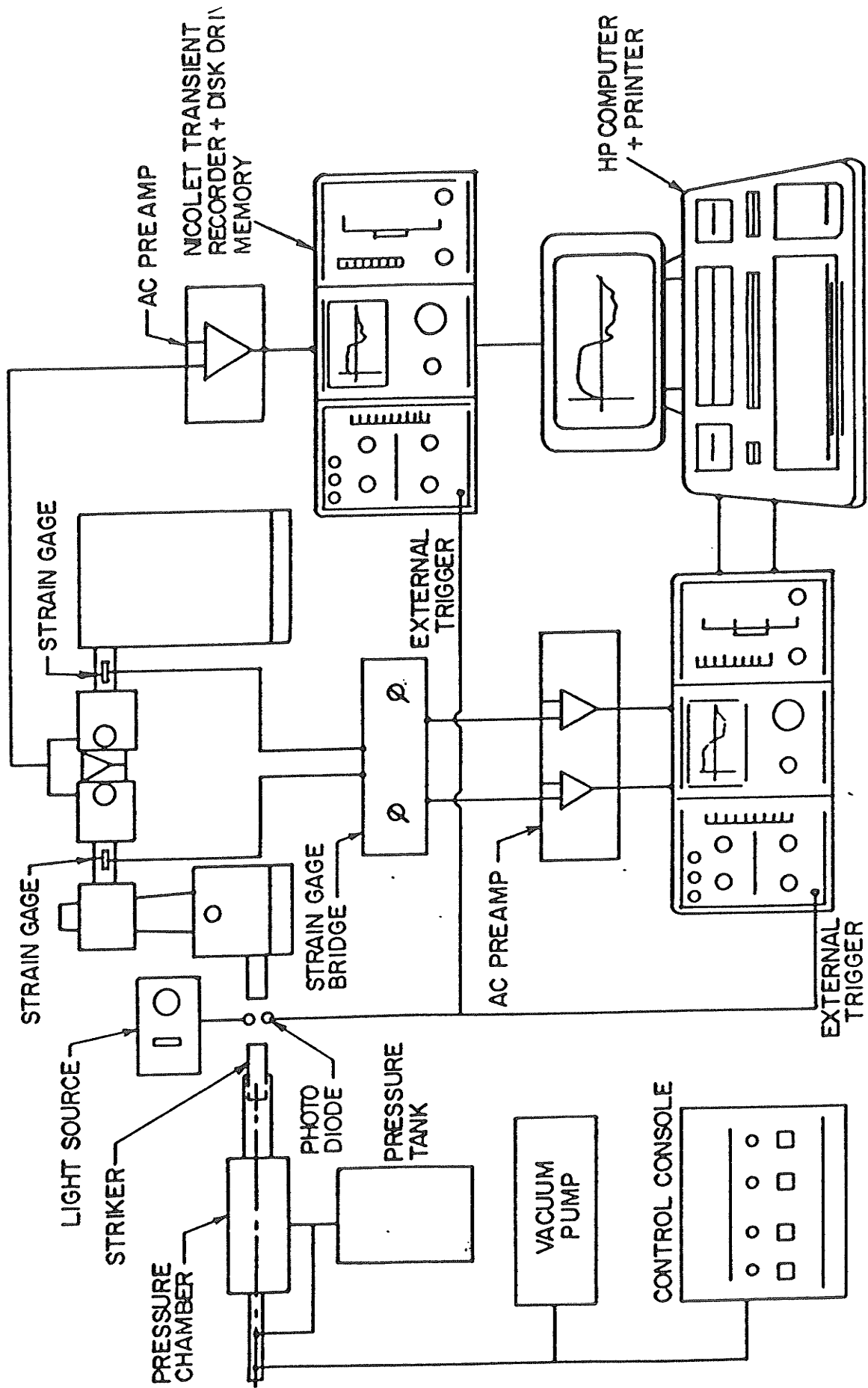
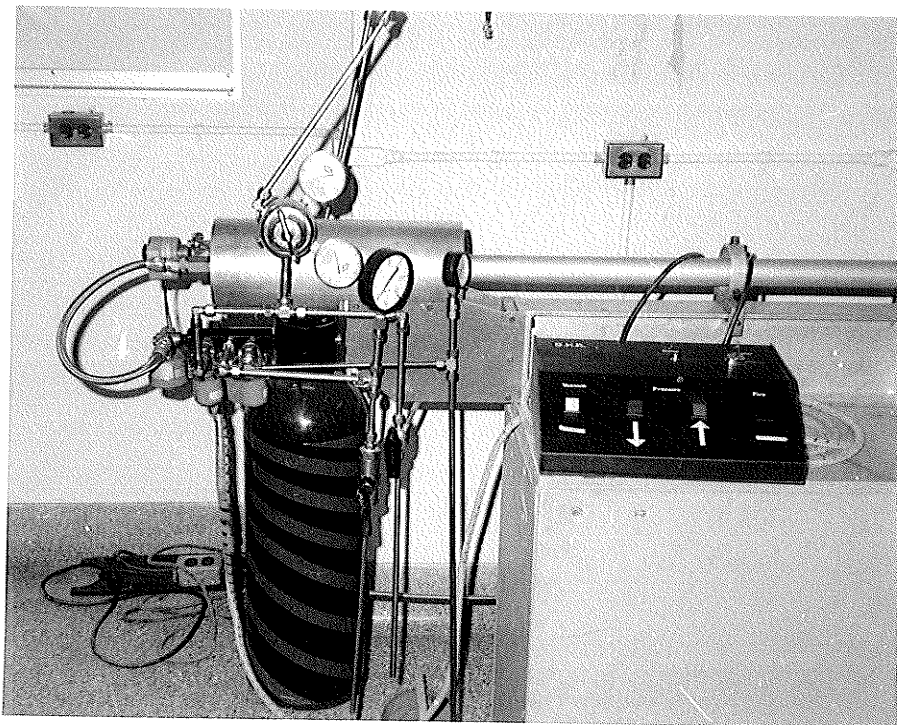


Figure 3.6 Experimental set-up drawing of dynamic tensile test.

( a )



( b )

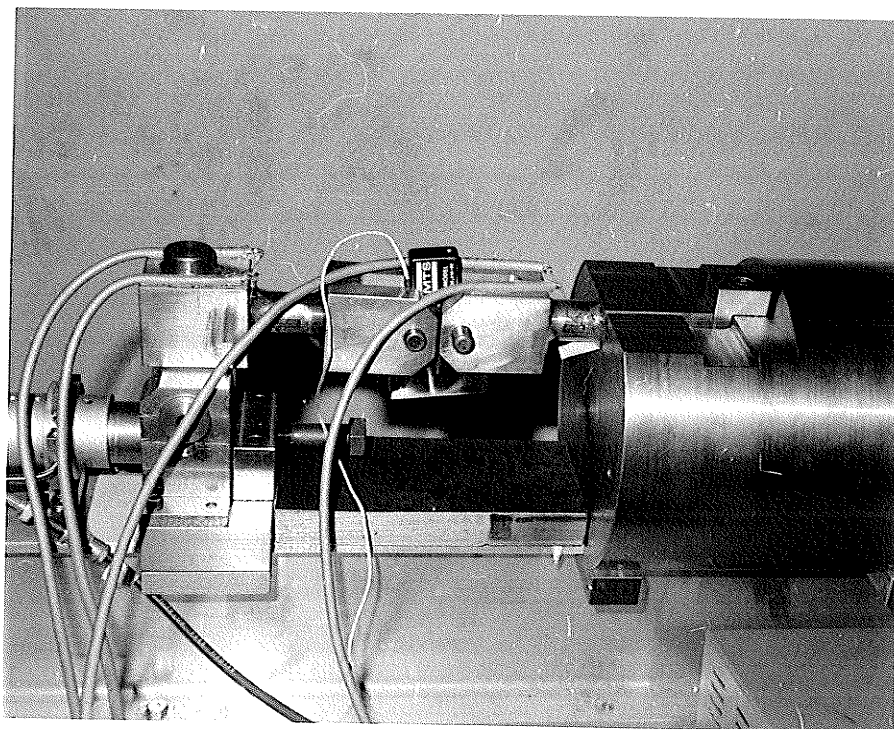
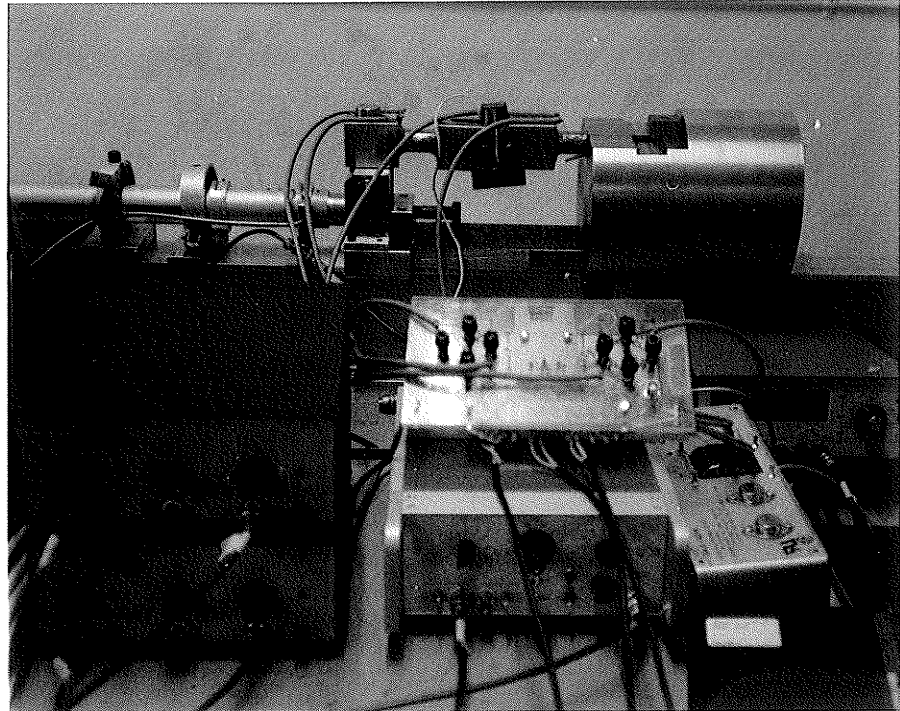


Figure 3.7 (a) Compress gas gun, launching chamber and gas gun instrumentations.  
(b) Close up of dynamic tensile test system.

( c )



( d )

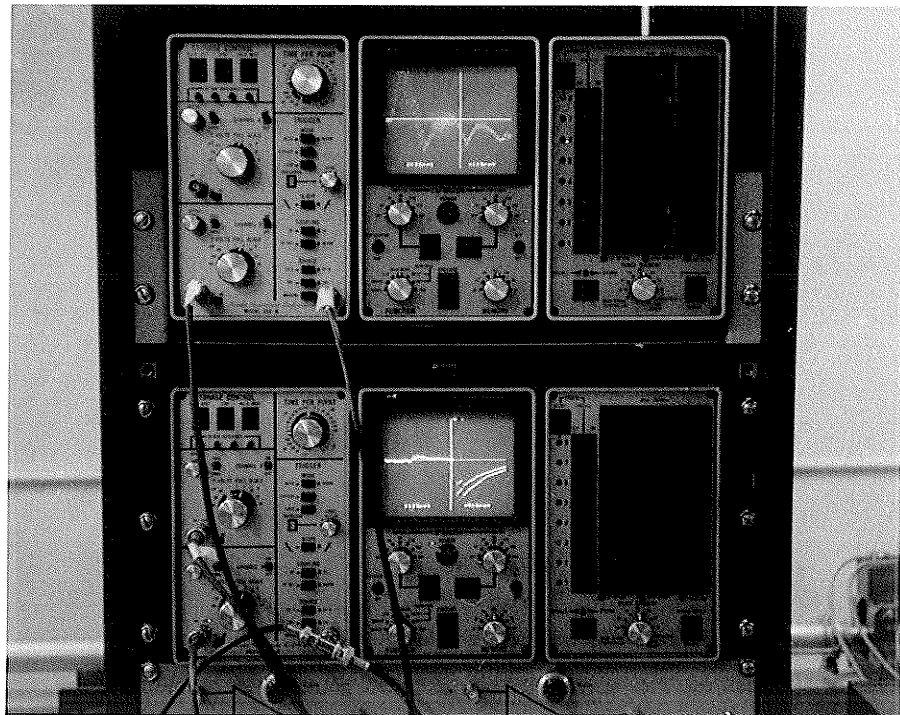


Figure 3.7 (c) Amplifiers and strain gage bridges for dynamic tensile test system.  
(d) Nicolet digital recorders and dynamic tensile loading outputs.

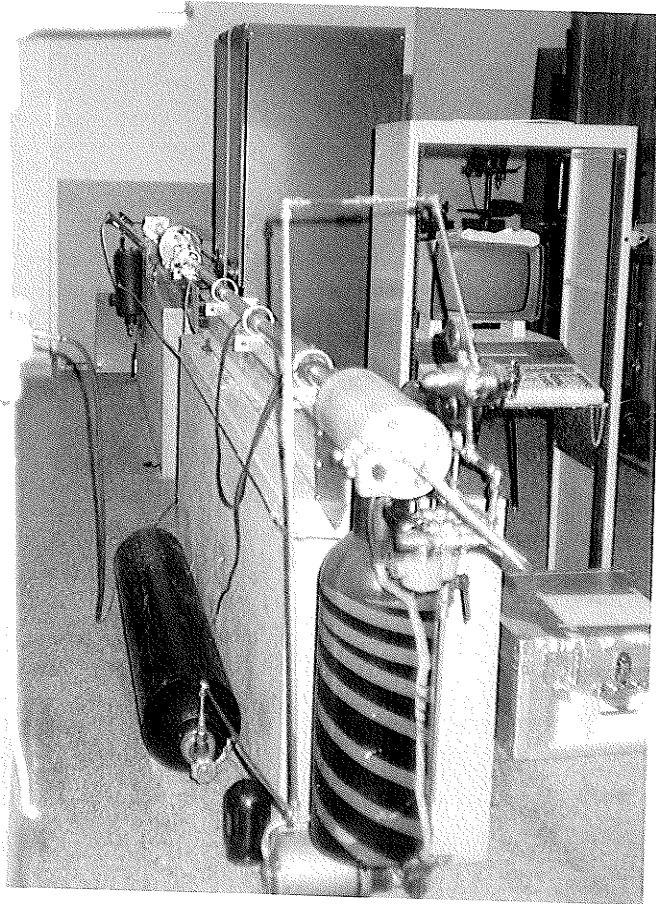


Figure 3.7e Overview of dynamic tensile test system and HP 9845B microcomputer.

testing system consists essentially of a gas gun, a striker, the swing arm assembly, a heavy energy absorption anchor block, modified and instrumented CTS grips (for load detection) that fit into the swing arm and the anchor block, and measuring and recording instruments.

Compact tension specimens of the same geometry as those used in the Instron speed tests were placed between the loading grips. The swing arm assembly converts the kinetic energy of the incoming striker into a tensile loading pulse that propagates through the specimen and cracks the specimen in the process.

#### 3.4.2.1 Rationale for Design

As explained in Chapter One, the objective of this thesis was to devise a tensile fracture toughness testing procedure using CTS, with loading rates ranging from quasi-static to stress wave loading. It was therefore imperative that the conditions of Instron loading should be maintained as closely as possible to ensure compatibility of these dynamic loading rate results with those obtained from the slower Instron speed tests.

A compression Split Hopkinson Bar was already in place at the University of Manitoba as a result of previous research work. The task faced by the author was to convert this compression test setup to fit the objectives of this present work, with as few changes as possible due to economics and time constraints, while not compromising the

integrity of the objectives and the validity of test results thereby obtained.

It became apparent that any proposed system must have at least the following components:

- 1) conventional CTS grips as used on servo-hydraulic test frames;
- 2) absorber block to dissipate leftover energy;
- 3) low inertia to all moving parts;
- 4) load and displacement transducers to record the dynamic load/load-line displacement curve;
- 5) crack initiation detection system.

It was then decided that the simplest approach was to leave the gas gun and its associated parts, as they were, as the source of dynamic stress wave, and to use a swing arm assembly to convert the compressive force from the incoming striker into a tensile loading pulse that directly loads one of the grips, while the anchor grip is safely anchored in the energy absorber block. To minimize the inertia of the swing arm assembly, the loading grip need to be as small/short as possible. Load signals would be recorded by strain gages mounted on the grips themselves. The high frequency COD gage used in the Instron tests would again provide both the load-line displacement signal and the time to crack initiation.

### 3.5.2 Theory of Operation

In the present setup, the swing arm converts the kinetic energy of the incoming striker into a translation of the swing arm's grip end. The velocity of the grip end,

depending on the striker velocity, is able to set up a tensile loading wave prior to its actual spatial translation. The tensile wave then propagates down the grip, fractures the specimen and travels onto the absorber block.

The swing arm rotates freely on a hardened steel dowel pin and has no discernable play in its rotation. The loading grip is taper fitted to the swing arm and constrained by a C ring at the top. No vertical lifting forces on the loading grip are expected, and the C ring is merely there for safety reasons.

The anchor grip is precision slotted into the anchor block, and the tapered wedge at the end ensures that the grip maintains maximum contact with the slot while keeping the grip down at the same time. The tapered wedge is further secured into the block with a machine screw. The swing arm taper and the slot on the anchor block are finely machined to ensure that the grips meet the load-line requirements of E813. Two strain gages each are mounted longitudinally on the grips at the center line to record the dynamic load. The proximity of the gages to the specimen means incident and reflected signals are very likely to overlap.

Recalling that a longitudinal wave is set up as a result of the rapid displacement of one section of a material with respect to the rest of the material; therefore, it is the sudden acceleration of the swing arm

grip end that sets up the longitudinal stress wave, and not the overall translation of the loading grip. The gross movement of the loading grip would introduce deformation that lags well behind the initial stress loading.

In addition to this primary longitudinal tensile stress wave, numerous other secondary pulses are generated. The initial impact of the striker on the swing arm sets up a complex series of bending waves and vibration within the vertical swing arm and its immediate supports, before any physical translation can take place at the swing arm grip end. Also, the area discontinuities of the grips introduce additional wave reflection and dissipation effects into the system. Any air gaps would tend to reflect back the incident wave and further impedes the transmission of the loading wave. Consequently, it is very difficult to theoretically predict the overall contribution of these secondary effects to the loading history of the system.

The CTS is loaded as a result of the swing arm rotating through a small arc, while an essentially longitudinal stress wave passes through the system. The swing arm rotation in the dynamic tests was limited to  $5^\circ$  to minimize bending loads on the grips while allowing for crack initiation at the crack tip. The swing arm rotation introduces limited bending moment on the test assembly of magnitude proportional to the striker velocity and the strength of the CTS. However, since this bending effect is associated with the overall translation of the test assembly, it does not contribute to the initial stress

loading of the specimen.

Depending on the force of impact by the striker, the swing arm assembly would tend to move toward the anchor block, even though the swing arm supports are secured to the test bed with four machine screws. Therefore, steel spacers were placed between the swing arm assembly and the anchor block, with small gaps filled by forcing metal shims into the gaps. The spacers were further clamped onto the test bed with C clamps. As such, no compressive load could be transmitted to the specimen, except for those due to tensile wave reflection and the elastic bending of the test assembly.

Load-line displacement and crack initiation were again measured by the high frequency COD gage mounted on the specimen in the same manner as the Instron tests. The COD and strain gage signals were automatically recorded by two Nicolet transient recorders and subsequently off-loaded onto a Hewlett Packard 9845B micro-computer for analysis. Amplifiers used to condition the COD and strain signals were checked for accuracy and calibrated up to 50 kHz by being subjected to a square wave generated by a function generator. As such, distortion for signals up to 50 kHz was expected to be minimal. The high frequency COD gage was checked quasi-statically through its working range to verify its linearity.

The major problem in setting up these impact experiments was the presence of unexpectedly high levels of

background noise in the room where the tests were conducted. Originally, the recording of all signals was to be triggered by the incident wave form. However, the high noise levels made this form of internal triggering impossible by consistently false triggering the recording system. Finally, an optical diode was used as an external trigger source. The diode was placed just ahead of the base of the swing arm perpendicular to the path of the striker. A pencil light source shone across the striker's path was used to set up a reference voltage with the photo diode. As the striker cuts across the path of the light, a voltage drop was created and this signal was used as the triggering signal. By placing the diode close to the base, an accurate trigger source was produced by the passage of the striker.

### 3.4.3 Theory of Analysis

Conventional Compression Split Hopkinson Bar analysis is based on these fundamental assumptions [72]:

- 1) one dimensional wave analysis is applicable.
- 2) strain signals obtained on the instrumented bars are representative of the strain field across the specimen
- 3) all strain signals are time shifted to the same origin, assuming that equilibrium is established in the specimen during the fracture process

At first glance, it would seem that conventional SHB analysis cannot be used here due to violation of conditions 1 & 2 as a result of area discontinuities and the secondary wave effects. However, since for these impact tests one is interested in the overall energy dissipation associated with

the fracture process only (ie. the load-line loading history), the modified analysis for this particular test set-up is actually simpler.

A CTS specimen is in essential compression or tension due to the load being transmitted through the pin holes of the grips and the specimen, and no significant bending or torsional effects are transmitted (the pins are free to rotate with no discernable play in their rotation). Therefore, only longitudinal stresses are transmitted by the grips. The longitudinally placed strain gages are able to pick up the overall longitudinal strain wave loading in the grips, and one dimensional wave analysis can thus be applied as a first approximation to obtain the overall loading history on the specimen. In the evaluation of  $J_Q$ , one is interested in the loading history of the specimen at the start of stress wave loading, and not the complete loading history of the entire assembly.

#### Load-line displacement calculation

In conventional SHB analysis [72], the load-line displacement is calculated using the following equation:

$$\delta(t) = C_0 \int_0^t [ \epsilon_I(t) - \epsilon_R(t) - \epsilon_T(t) ] dt$$

$$\text{where } C_0 = \sqrt{E / \rho_0}$$

In applying this equation, separation of the incident and reflected wave signals on the loading grip is needed. However, since in this present dynamic test setup load-line displacement was directly measured across the specimen gage

face, there was no need to achieve separation of these wave forms. Nonetheless, the COD values would have to be adjusted to yield actual load-line displacement.

### Dynamic Load Calculation

Analysis of the loading wave forms is similar to that introduced by Kolsky and discussed in [73,74]. Specifically, with reference to Fig. 3.5:

$$P_A(t) = E A [ \epsilon_I(t) + \epsilon_R(t) ] \quad ( 3.2a )$$

$$P_B(t) = E A \epsilon_T(t) \quad ( 3.2b )$$

$$P(t) = 1/2 [ P_A(t) + P_B(t) ] \quad (3.2c)$$

where  $E$  = Young's Modulus  
 $A$  = area of grip section where the strain gages are mounted  
 $\epsilon_{I,R,T}$  = incident/reflected/transmitted stress waves' strain signals  
 $P_{A,B}$  = dynamic loads on sides A and B of specimen  
 $P(t)$  = average load as sensed by specimen

Although equilibrium in the specimen is assumed, the equilibrium equations

$$\epsilon_I + \epsilon_R = \epsilon_T \quad (3.3a)$$

$$\text{and } P(t) = E A \epsilon_T(t) \quad (3.3b)$$

are not used and the average load is calculated using Eqn 3.2c to maximize accuracy of the results. Similar to the Instron tests, the critical time to fracture,  $t_c$ , is related to a sudden increase in the slope of the COD-t signal.

As mentioned previously, the proximity of the strain gages on the loading and anchor grips to the specimen means an overlap of the incident and reflected signals is

expected. Noting that the incident wave is a positive signal and the reflected wave a negative signal, inability to separate these two signals in time would result in an overestimation of  $P_A(t)$  and therefore also the average load  $P(t)$ . The degree of this overestimation is lessened as the reflected wave approaches the incident wave. With the present dynamic setup and strain gage positions (Figs. 3.5, 3.8),

$$t_A < t_B < t_C$$

Therefore, the overestimation of  $P(t)$  approaches zero as  $t_B$  approaches  $t_A$ .

No prior test calibration was done on the grips since neither a dynamic load cell nor appropriate fixtures were available on the Instron for this purpose. As a matter of fact, no mechanical calibration system capable of stress wave loading is commercially available, and this of course was one of the reasons behind this work.

To circumvent the lack of prior load calibration, certain assumptions were made with respect to analysis methodology. Keeping in mind the wave nature of all signals, noise interference and dynamic material properties must be considered. Electrical noise in the signals obtained would be eliminated through the use of a multi-order polynomial that best represents the trend of the signals. As for dynamic material properties, only the yield and flow stresses would be loading rate adjusted.

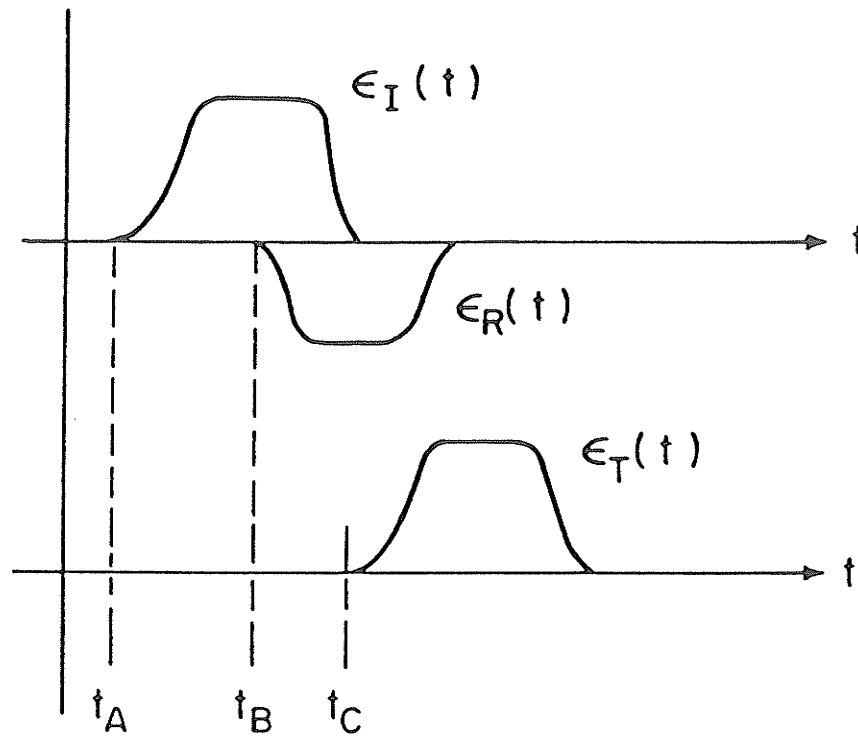


Figure 3.8 Dynamic load overestimation due to proximity of strain gages to CTS.

## Dynamic Mechanical Properties

Assuming a general relationship between flow stress and strain rate, at constant temperature and strain, of the following form [75]:

$$\sigma = C (\dot{\epsilon})^\beta \Big|_{\epsilon, T} \quad (3.4)$$

$$\text{where } \beta = \frac{\log (\sigma_2 / \sigma_1)}{\log (\dot{\epsilon}_2 / \dot{\epsilon}_1)} \quad (3.5)$$

$$\text{therefore } C = \frac{\sigma_1}{(\dot{\epsilon}_1)^\beta} \quad (3.6)$$

$$\text{and } \sigma_2 = \sigma_1 \left( \frac{\dot{\epsilon}_2}{\dot{\epsilon}_1} \right)^\beta \quad (3.7)$$

with  $C$  = constant of proportionality  
 $\beta$  = strain rate sensitivity factor  
 $\sigma_1, \dot{\epsilon}_1$  = reference static stress and strain rate  
 $\sigma_2, \dot{\epsilon}_2$  = corresponding dynamic stress and strain rate

With reference to section 3.4, let the static material properties assume the following values:

$$\dot{\epsilon}_1 = 10^{-3} \text{s}^{-1}, \quad \sigma_y = 300 \text{ MPa}, \quad \sigma_f = 450 \text{ MPa} \text{ and } m=0.018$$

then the corresponding dynamic values are:

$$\dot{\epsilon}_2 = 10^3 \text{s}^{-1}, \quad \sigma_y = 400 \text{ MPa}, \quad \sigma_f = 600 \text{ MPa}$$

The choice of  $\dot{\epsilon}_2$  is based on the static flow stress of the steel and a nominal gage length of 27.5 mm, and will be shown to be a reasonable, though conservative, first choice in Chapter Four.

The grips and the swing arm assembly were made of high strength steels with a fully annealed yield strength of 480 MPa. Assuming similar strain rate strengthening relations apply to this steel, the dynamic yield stress of the test

system is approximately 600 MPa or a yield load across the grip sections of 300 kN. Load values exceeding 300 kN are assumed to signify yielding of the test grips.

#### Maximum Load Calculation

The actual test strain signals were converted into load values assuming linear material response ( $\sigma = E \epsilon$ ) of the test grips. A modified linear elastic, perfectly plastic material model (based on material flow stress) was used to account for material strain hardening in the specimen as a result of plastic loading of the specimen.

When considering the fracture of a CTS, the fracture load is a combination of tensile and bending loads. In the absence of dynamic load calibration of the grips, it is helpful to estimate the maximum dynamic fracture load sustainable by the CTS. Maximum dynamic fracture load calculations provide both a check of the analysis used thus far and an approximate upper bound to experimental results.

Plastic limit analysis by Saxena et al [71] indicated a lower bound plastic load,  $P_p$ :

$$P_p = \sigma_y B c (2 \alpha )$$

where  $B$  = specimen thickness  
 $c$  = half length of remaining specimen ligament  
 $\alpha$  = geometric factor for CTS

For the case of CTS with  $a/w = 0.6$ ,  $\alpha = 0.123$ .

It must be borne in mind that the above analysis by Saxena does not take into account either the increase in general yield stress due to stress triaxiality, nor the potential notch strengthening/weakening effects as a

function of the failure mode (ductile/brittle) and strain rate [75]. Orowan [76] had shown that the longitudinal yield stress in the presence of a notch could be 2.5 times that of the unnotched case. This factor of 2.5 is known as the plastic constraint factor.

In view of these considerations, the maximum allowable dynamic fracture load for these tests is assumed not to exceed the dynamic flow load,  $P_{f1}$ , such that

$$P_{f1} = \sigma_{df1} B 2c = 150 \text{ kN}$$

where  $\sigma_{df1}$  = dynamic flow stress

In summary, the use of strain gages and a COD gage for load and load-line displacement measurements enable automatic data recording and computerized data analysis of these fracture tests at the desired speed. Determination of the characterizing fracture energy parameter,  $J_Q$ , in this macroscopic manner is therefore both fast and efficient. However, to verify the accuracy of the analysis and assumptions associated with this macroscopic method, a microscopic examination of the fracture surfaces was also carried out as described in the next section.

### 3.6 Stretch Zone Width Measurement

Past work has shown that the J-integral is related to the critical crack opening displacement and, therefore, is also related to the stretch zone width (SZW). Since  $J_Q$  has the same energy interpretation as the J-integral in the quasi-static case, it seems reasonable to extend the J-integral/SZW relationship to the case of  $J_Q$ . Stretch zone

(SZ) measurements would be used to provide reference fracture toughness values in the form of  $J_Q$  obtained based on microstructural features. SZ measurements would therefore serve to assess the success of the macroscopically obtained  $J_Q$  in reflecting the change in fracture toughness (ductile vs brittle) with loading rate.

As explained in section 2.2.1, discrepancies surround the value of the stretch zone slope angle,  $\theta$  (Fig. 2.7). In this work, scanning electron micrographs of the stretch zone at two tilting angles ( $\psi = 37^\circ, 45^\circ$ ) were taken. Arithmetic averages of the SZW as measured on the micrographs at both these angles were calculated. SZW assumes its highest value when  $\psi = \theta$ . With this in mind, a better estimate of  $\theta$  for these tests could be determined. SZWs based on this  $\theta$  were then used to calculate  $J_Q$ .

Calculations show that the SZW is relatively independent of the assumed SZ angle  $\theta$ . Variations up to  $\pm 8^\circ$  would only mean a  $(1/\cos 8^\circ)$  correction to Eqn 3.12b, or approximately  $\pm 1\%$  in SZW differences. The concern with the appropriate angle of  $\theta$  used to calculate  $J_Q$  is due to the CTOD's dependence on  $\theta$  via the sine function (Eqn. 3.11). For example, using  $\theta = 41^\circ$  introduces a  $\pm 8\%$  error in CTOD calculations if  $\theta$  is either  $45^\circ$  or  $37^\circ$ .

In accordance with Phuc Nguyen-Duy's analysis [11], and using the convention of designating the diagonal of the stretch zone as the SZW (Fig. 2.7), one gets:

$$SZW_c = \frac{L}{\cos(\theta - \psi)} \times \frac{1}{G} \quad ( 3.10 )$$

where  $SZW_c$  = critical SZW at crack initiation  
 $L$  = measured length of SZW on micrograph  
 $\theta$  = angle of stretch zone slope  
 $\psi$  = angle of tilt/observation  
 $G$  = magnification factor

With this definition of SZW, it follows that

$$CTOD_c = 2 SZW_c \sin\theta \quad ( 3.11 )$$

By using Eqn. 2.14 to relate  $SZW_c$  with  $J_Q$ , and replacing  $\sigma_y$  with  $\sigma_f$  to account for the elastic plastic nature of the real material,

$$J_Q = 2 m \sigma_f SZW_c \sin\theta \quad ( 3.12 )$$

$$\text{or } J_Q = 2 m \sigma_f \frac{L \sin\theta}{\cos(\theta - \psi)} \times \frac{1}{G} \quad ( 3.13 )$$

The value of  $m$  to be used in Eqn 3.13 would be experimentally determined. SZW measurements and the macroscopic  $J_Q$  values from corresponding tests would be compared to arrive at the value of  $m$  that best represents the data. The value of  $m$  should fall between 1 and 2 as explained in section 2.2.

CHAPTER FOUR  
EXPERIMENTAL RESULTS

#### 4.1 Fracture Toughness ( $J_{IC}$ ) from Compliance Method

The J-resistance curve, obtained using the ASTM standard (E813) for  $J_{IC}$  evaluation as applied to the CTS single specimen unloading method, is plotted in Fig. 4.1. The intersection of the crack advance line and the theoretical blunting line gives the  $J_{IC}$  value as  $62 \text{ kJ/m}^2$ . This compares well with a  $J_{IC}$  of  $65 \text{ kJ/m}^2$  obtained by Bayoumi [48] in his work on this same metal under room temperature using TPB specimen.

The value of  $J_{IC} = 62 \text{ kJ/m}^2$  meets the size requirements of B,  $b \geq 25J_{IC}/\sigma_o$  ( $25 J_{IC}/\sigma_o = 3.4 \text{ mm}$ ). Therefore, this value of  $J_{IC}$  is considered valid as the fracture toughness of this material based on ASTM Specification E813-81.

The J-  $\Delta a$  curve was generated by manually digitizing the load/load-line displacement curve as recorded on an X-Y plotter. An HP 9845B microcomputer was programmed to calculate the corresponding J and  $\Delta a$  (crack extension during test) values based on these digitized data.

#### 4.2 Instron Speeds Fracture Toughness ( $J_Q$ )

The characterizing energy parameter,  $J_Q$ , for quasi-static to high speed Instron speeds tests was calculated using Eqn. 2.20 based on the load/load-line displacement curve of each test at the desired speed. Results for the Instron tests are presented in Table 4.1. The various Instron test speeds are identified by their respective average test speed and nominal strain rate. In Table 4.1, COD\_CRIT refers to the adjusted load-line displacement at

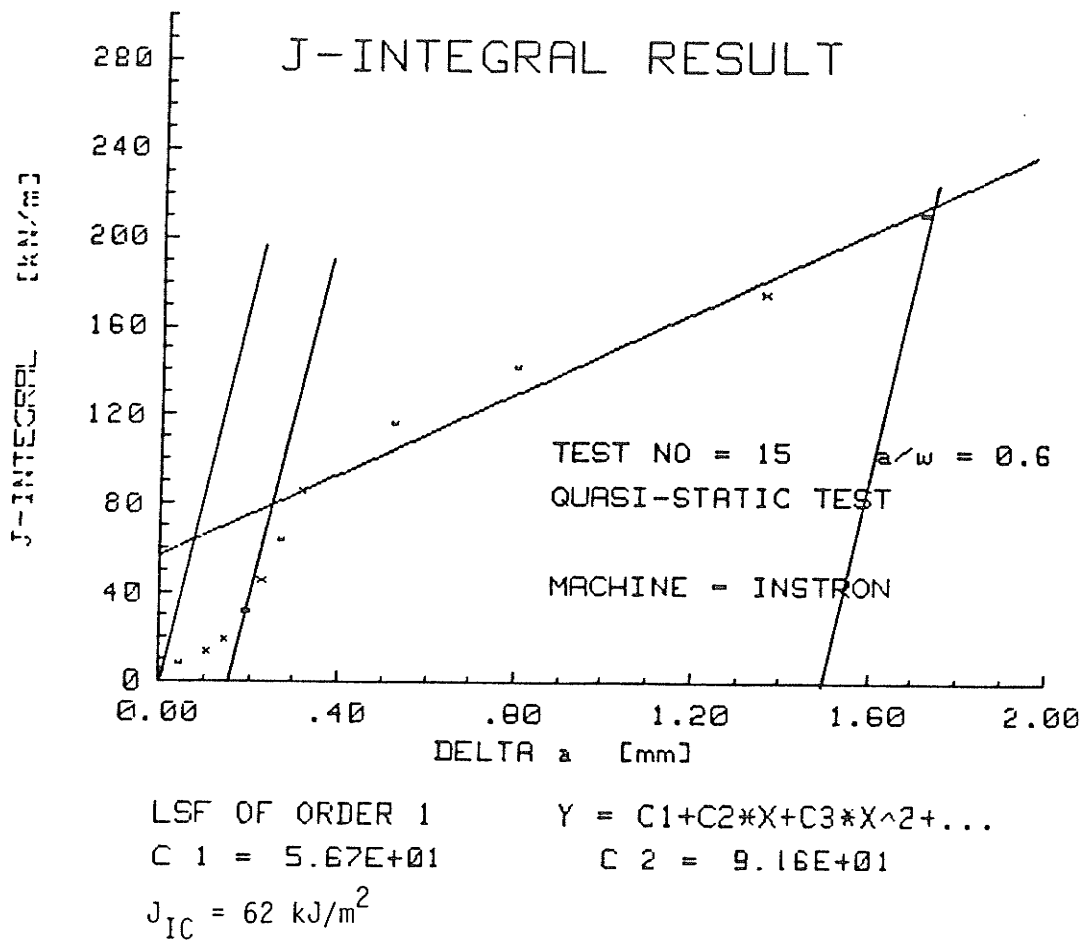


Figure 4.1 Experimental J-Resistance curve.

Table 4.1

## INSTRON TESTS

SPEED	TEST NO.	SPECIMEN NO.	a/w	<sup>4</sup> COD-CRIT [ $\mu\text{m}$ ]	CRITICAL TIME tc [ $\mu\text{s}$ ]	<sup>5</sup> Jq [KJ/m <sup>2</sup> ]	<sup>6</sup> Jq [KJ/m <sup>2</sup> s <sup>-1</sup> ]	<sup>10</sup> K [MPa m]	<sup>6</sup> K [MPa ms <sup>-1</sup> ]	
<sup>1</sup> HIGH SPEED	2	A2	0.5	0.423	1.95x10 <sup>4</sup>	46.7	2.4x10 <sup>3</sup>	103	5.3x10 <sup>3</sup>	
	3	B1	0.6	0.538	1.84x10 <sup>4</sup>	30.4	1.7x10 <sup>3</sup>	83	4.5x10 <sup>3</sup>	
	5	C1	0.7	<sup>7</sup> 0.541	1.87x10 <sup>4</sup>	23.9	1.3x10 <sup>3</sup>	74	4.0x10 <sup>3</sup>	
	6	C2	0.7	0.511	1.55x10 <sup>4</sup>	17.8	1.1x10 <sup>3</sup>	63	4.1x10 <sup>3</sup>	
	16	A9	0.5	<sup>7</sup> 0.541	2.02x10 <sup>4</sup>	42.8	2.1x10 <sup>3</sup>	99	4.9x10 <sup>3</sup>	
	18	B11	0.6	<sup>7</sup> 0.571	1.45x10 <sup>4</sup>	38.3	2.6x10 <sup>3</sup>	93	6.4x10 <sup>3</sup>	
	<sup>2</sup> SLOW SPEED	7	A3	0.5	<sup>8</sup> 0.542	6.92x10 <sup>5</sup>	4.84	-	-	-
		9	B3	0.6	<sup>8</sup> 0.571	5.87x10 <sup>5</sup>	4.77	-	-	-
12		C4	0.7	<sup>8</sup> 0.595	5.02x10 <sup>5</sup>	22	-	-	-	
<sup>3</sup> QUASI- STATIC	14	A6	0.5	<sup>9</sup> 0.757	3.04x10 <sup>8</sup>	66.4	0.2	123	0.4	
<sup>3</sup> E813	15	B10	0.6	-	-	62	-	119	-	

<1>  $v = 20 \text{ mm/sec}$ ,  $\epsilon = 7.3 \times 10^{-1} \text{ s}^{-1}$

<2>  $v = 1.2 \text{ mm/sec}$ ,  $\epsilon = 4.4 \times 10^{-2} \text{ s}^{-1}$

<3>  $v = 0.004 \text{ mm/sec}$ ,  $\epsilon = 1.5 \times 10^{-4} \text{ s}^{-1}$

<4> COD-CRIT - load line crack opening displacement at tc

<5>  $Jq = 2(1+\alpha) U$

$$1+\alpha^2 \frac{Bb}{J}$$

<6>  $J = J/tc$ ;  $K = K/tc$

<7> COD-CRIT - from estimated COD-t inflection point

<8> COD-CRIT - expected value based on general strain rate effect

<9> COD-CRIT - estimated to show probable value of Jq

<10>  $K = \frac{JE}{\sqrt{1-\nu^2}}$ ,  $\nu = 0.3$

the point of slope change on the COD-t curve,  $t_c$ .

All test plots associated with the Instron tests were computer generated. Experimental results as recorded by an X-Y plotter were manually digitized and fed into a computer for further analysis and display.

The anticipated COD-t behavior for critical time determination was observed only in the high speed Instron tests. For purposes of future reference, the interval it takes for crack initiation to take place, 0 to  $t_c$ , will be called the event window.

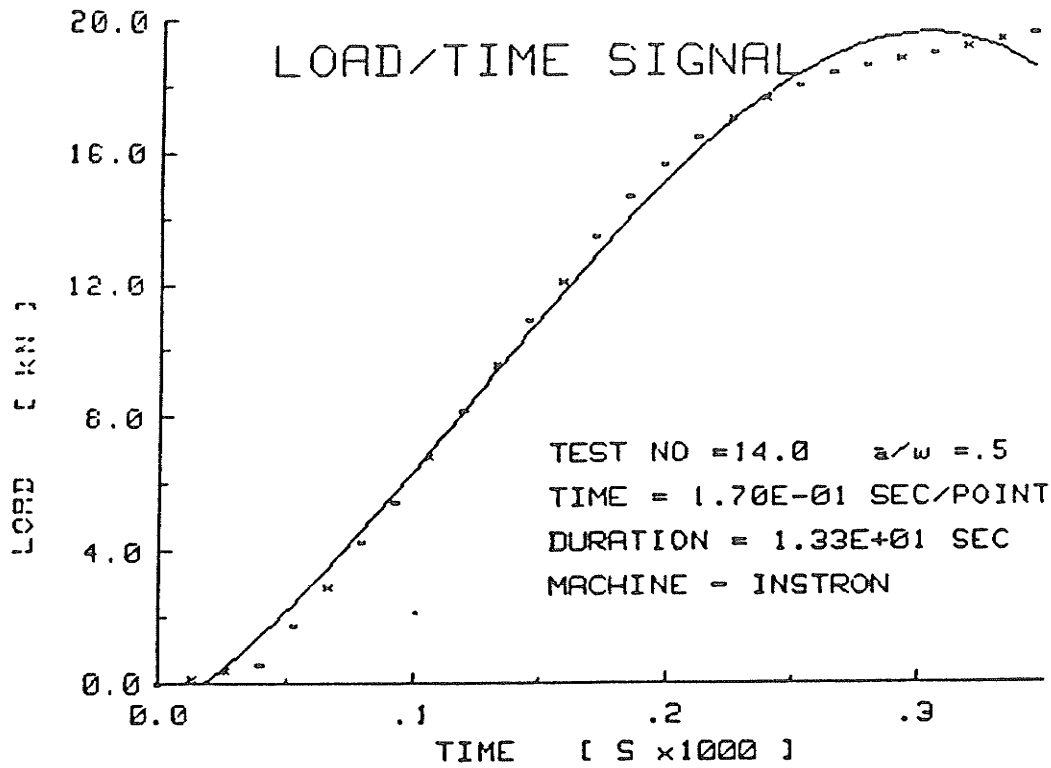
#### 4.2.1 Quasi-Static Instron Tests

Two specimens of  $a/w = 0.5$  were tested at this speed. However, errors in test procedures invalidated test #13. The various plots associated with test #14 are shown in Figs. 4.2.

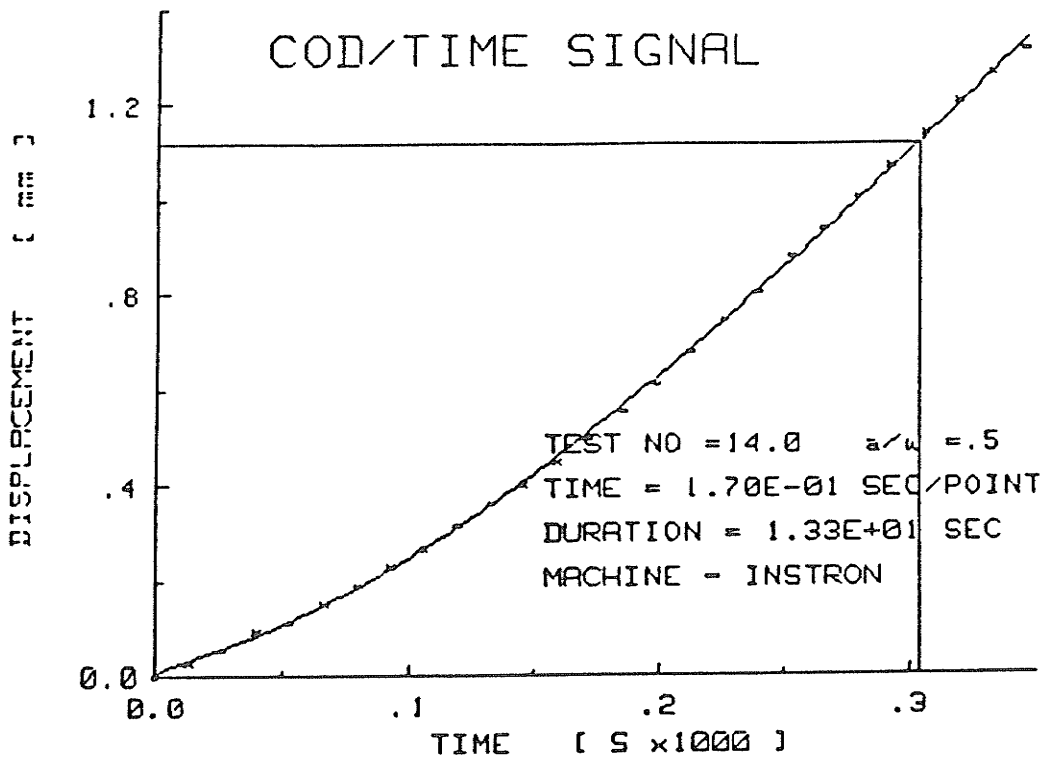
As can be seen, no definite slope change associated with crack initiation is observed in Fig. 4.2a. A  $J_Q$  value evaluated near  $P_{max}$  ( $\delta_{11} \sim 0.8$  mm) yielded a  $J_Q = 66.4$  kJ/m<sup>2</sup>. When compared to the standard compliance  $J_{IC}$  value of 62 kJ/m<sup>2</sup>, it is clear that the actual COD\_CRIT is  $\sim 0.8$  mm, and therefore the event window was indeed recorded by Figs. 4.2.

#### 4.2.2 Slow Speed Instron Tests

Two specimens at each of the 3  $a/w$  ratios were tested at this speed. Test #11 was aborted due to initial compressive loading of the specimen. The various plots



LSF OF ORDER 3     $Y = C1+C2*X+C3*X^2+...$



LSF OF ORDER 3     $Y = C1+C2*X+C3*X^2+...$   
 T\_CRIT( 1 ) = 3.04E+02 SEC

Figure 4.2 a,b Load-t, Cod-t results for test #INST14.

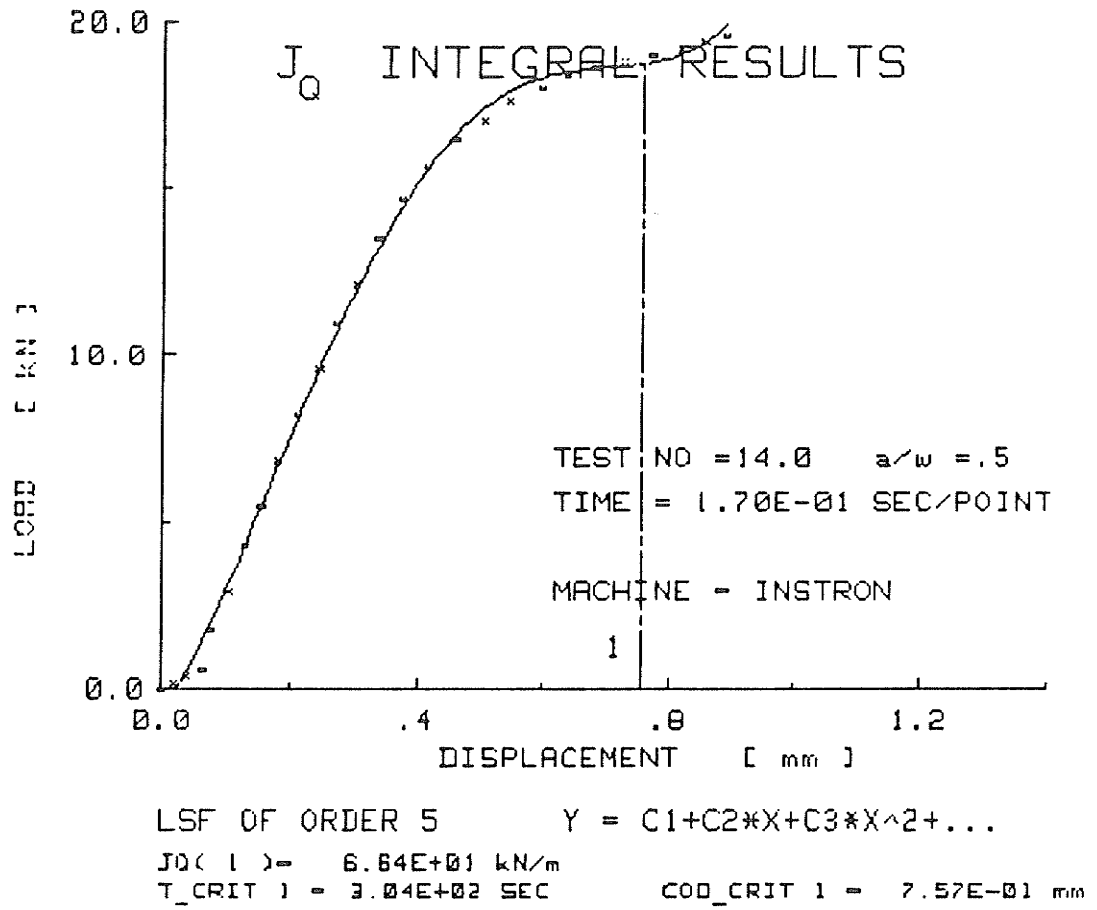


Figure 4.2c  $J_Q$  result for test #INST14.

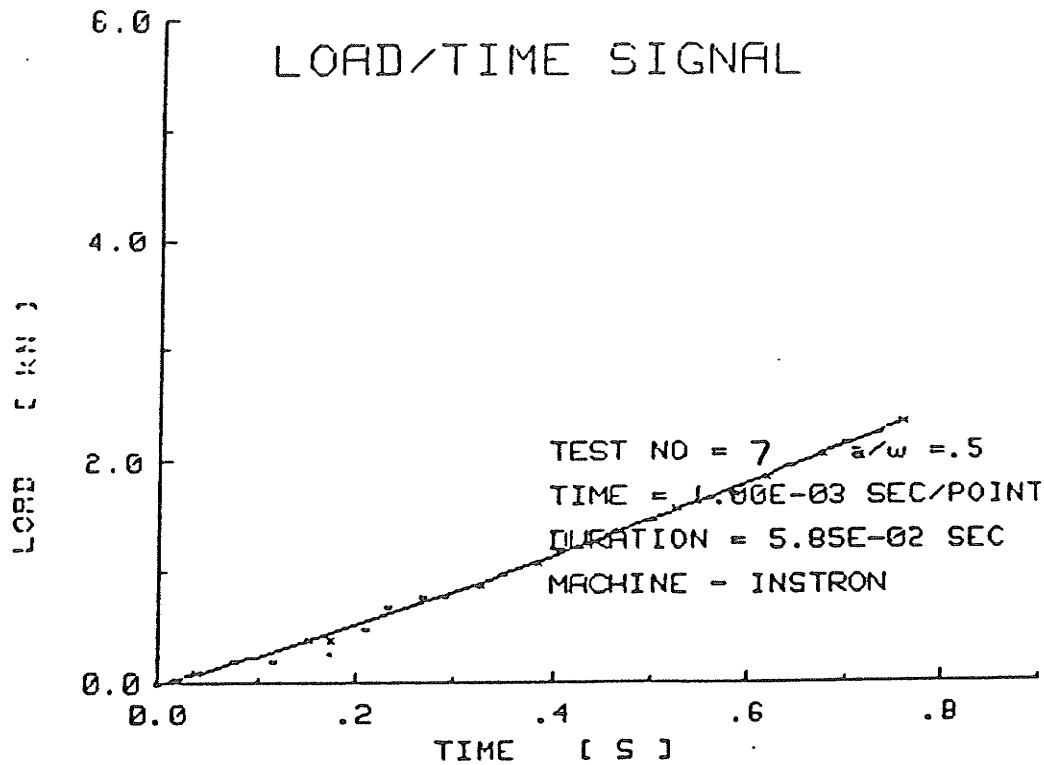
associated with tests #7 and #12 are shown in Figs. 4.3 and Figs. 4.4. The remaining test plots are included in Appendix A.

The experimental COD signals as recorded by the X-Y plotter were superimposed with a 60 Hz background noise, and best fit curves were first applied to the COD signals before digitizing the results. Again, the sudden change in the slope of the COD-t signal was not detected.

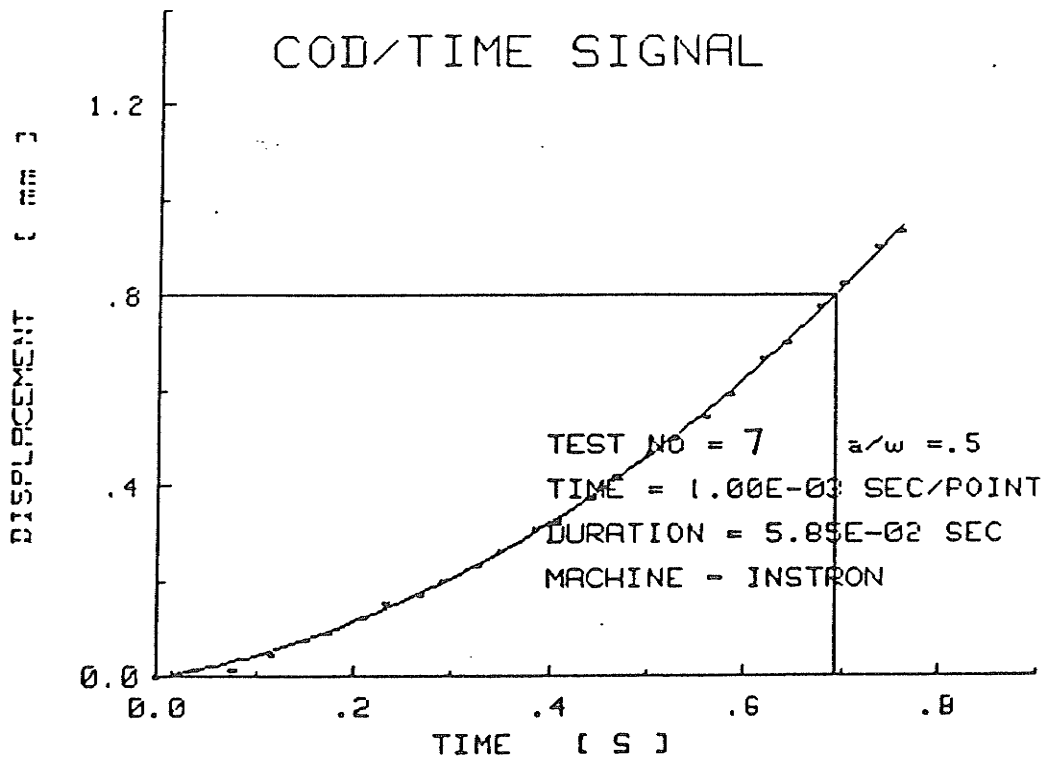
In addition, tests #7 to #10 exhibited uncharacteristically low rise time for the load signal within the event windows (Figs. 4.4a), and this accounted for the unrealistically low values of  $J_Q$ . Representative experimental  $J_Q$  values for tests #7 to #10 are listed in table 4.1. These  $J_Q$  values were determined using COD\_CRIT values that fall between the quasi-static and the high speed test results.

Load signals for tests #7 to #10 are seen to be unrealistic for two reasons. Firstly, the maximum load level should have varied inversely with increasing  $a/w$  ratios. As the  $a/w$  ratio increases, the applied moment to the CTS is higher and less load to cause crack initiation is expected. The fact that the maximum load level for  $a/w = 0.5$  is higher than that for  $a/w = 0.6$  validates this analysis (Fig. 4.5), and results for the high speed tests showed clearly the expected trend (Fig. 4.8).

Secondly, regardless of the exact load variation trend as a function of loading rate, results for the slow speed tests should fall somewhere between the quasi-static result



LSF OF ORDER 3      $Y = C1+C2*X+C3*X^2+...$



LSF OF ORDER 3      $Y = C1+C2*X+C3*X^2+...$

$T\_CRIT( 1 ) = 6.92E-01$  SEC

Figure 4.3 a,b Load-t, Cod-t results for test #INST7.

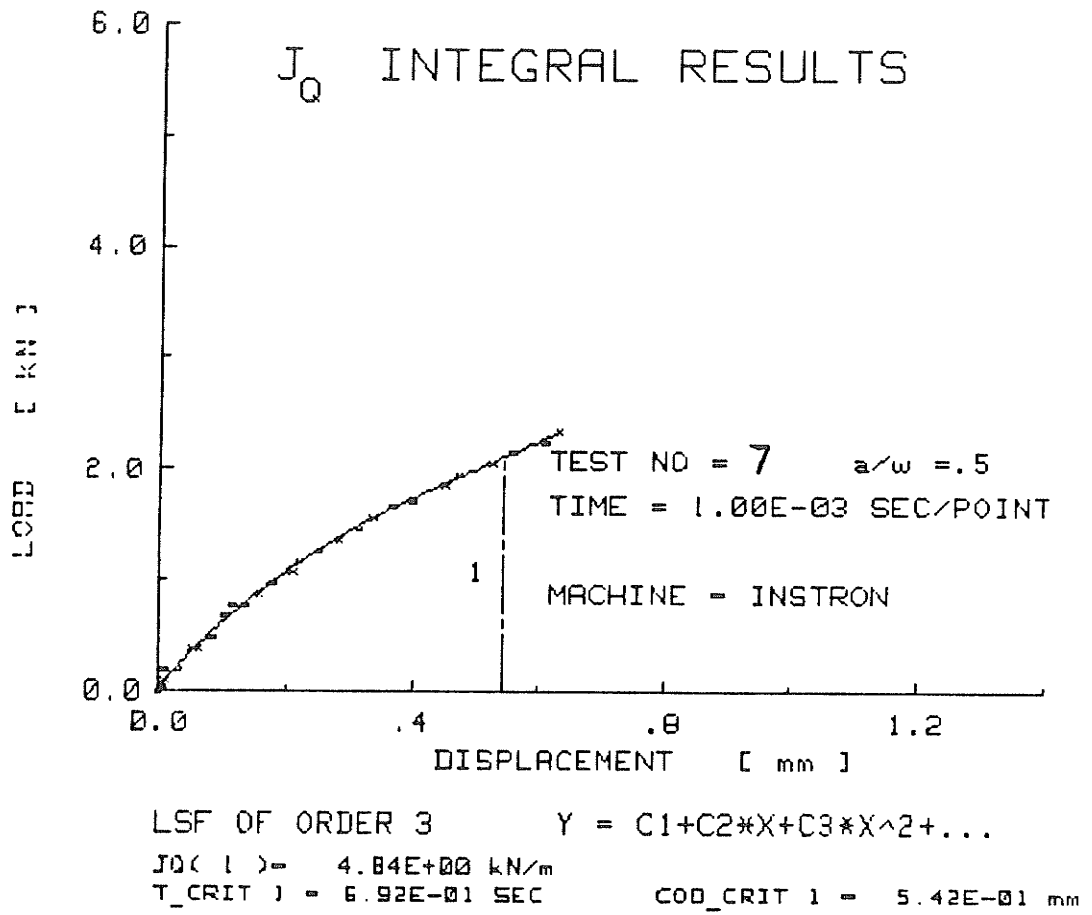
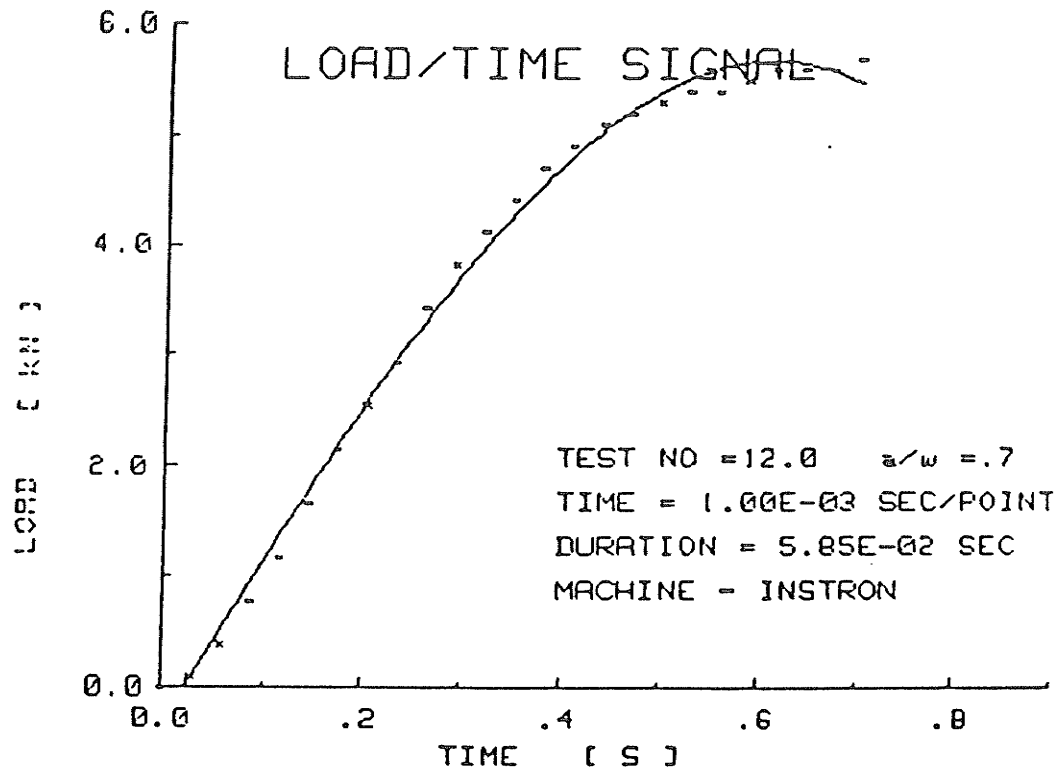
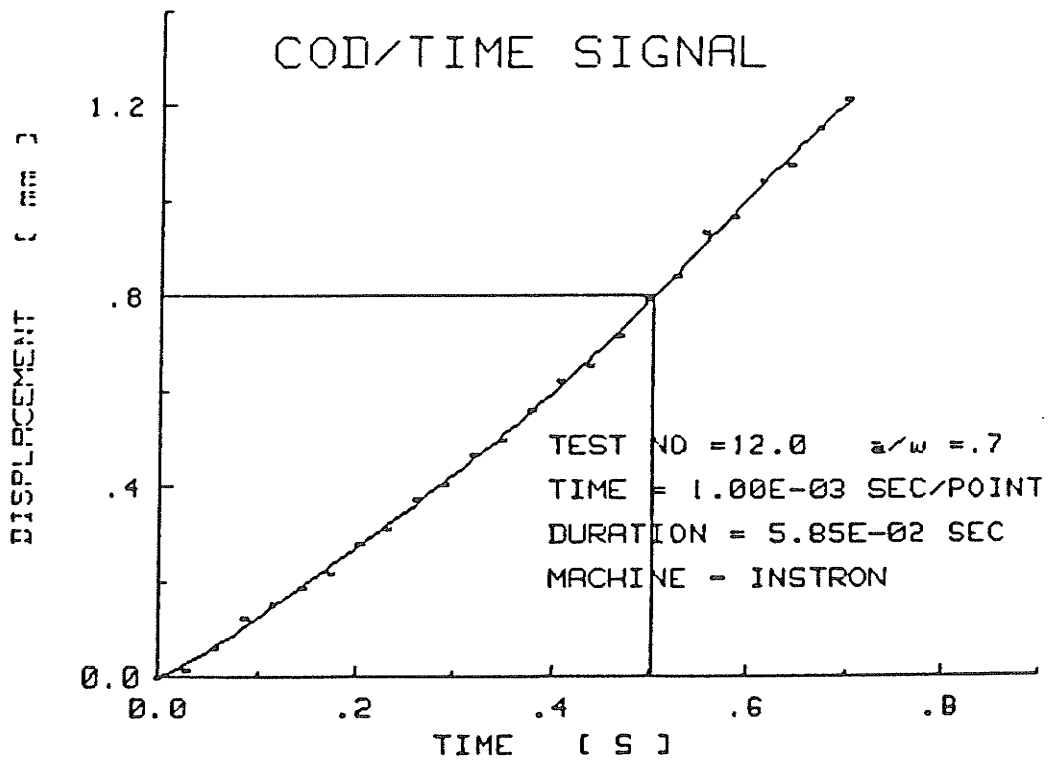


Figure 4.3c  $J_Q$  result for test #INST7.



LSF OF ORDER 3     $Y = C1 + C2 * X + C3 * X^2 + \dots$



LSF OF ORDER 6     $Y = C1 + C2 * X + C3 * X^2 + \dots$

$T\_CRIT( 1 ) = 5.02E-01$  SEC

Figure 4.4 a,b Load-t, Cod-t results for test #INST12.

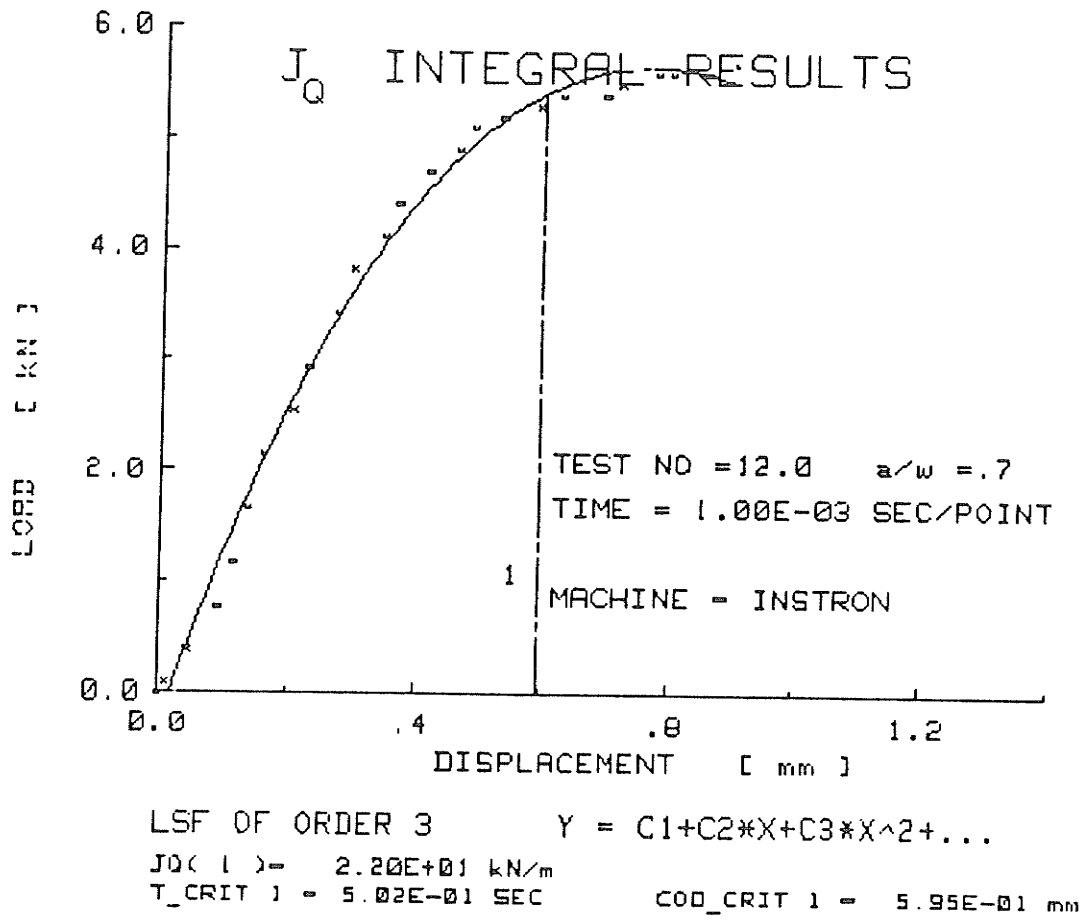


Figure 4.4c  $J_Q$  result for test #INST12.

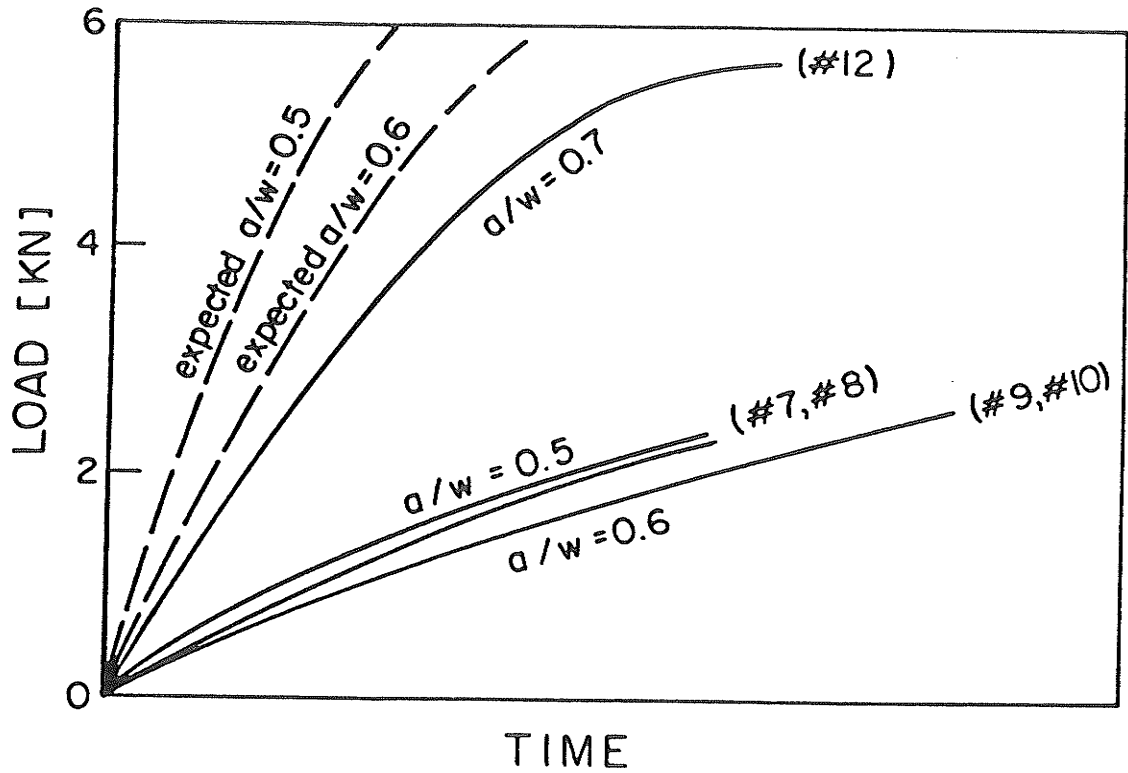


Figure 4.5 Load-t curves as a function of  $a/w$  for slow speed Instron tests.

(test #14, Fig. 4.2) and the high speed tests (Fig. 4.6). This of course was not true for tests #7 to #10. It should be noted that test #12 did exhibit the expected strain rate dependence. The corresponding  $J_Q$  was estimated to be  $22 \text{ kJ/m}^2$ , based on the expected COD\_CRIT value and the estimated COD-t inflection point.

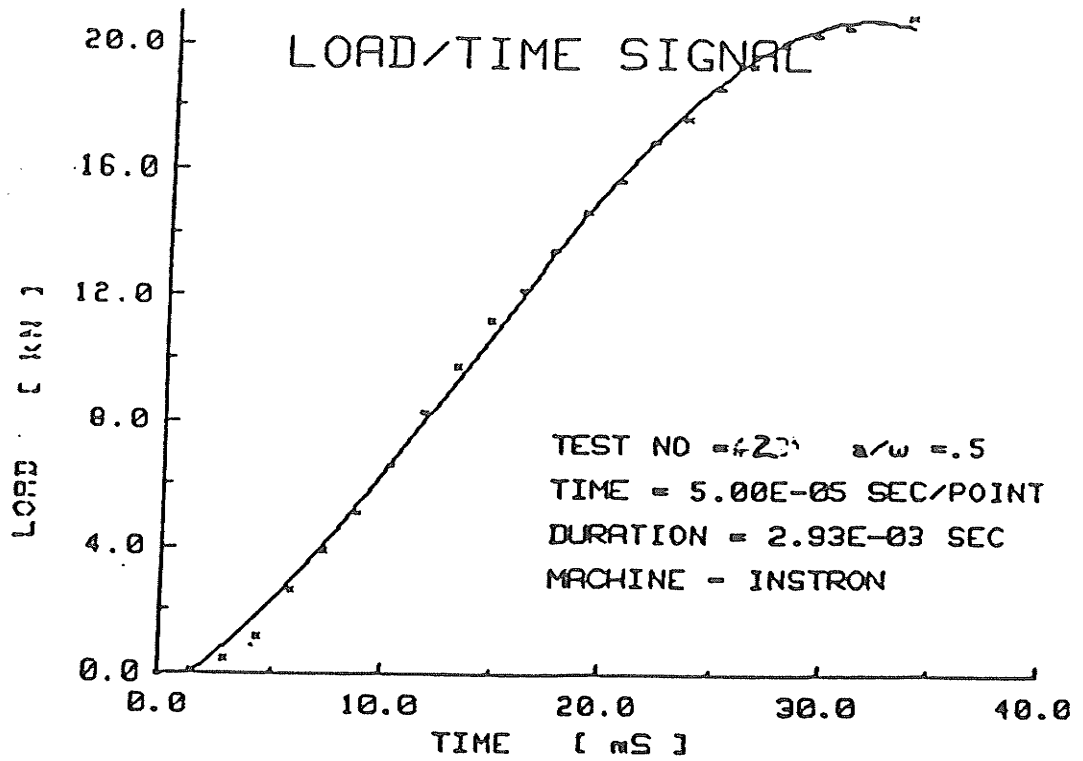
Therefore, it is clear that mechanical failure of either the load recording or generating equipments was responsible for these unrealistic results, and no conclusive  $J_Q$  values could be established. Corresponding  $J_Q$  values for these slow speed Instron tests would have to be established through stretch zone measurements.

#### 4.2.3 High Speed Instron Tests

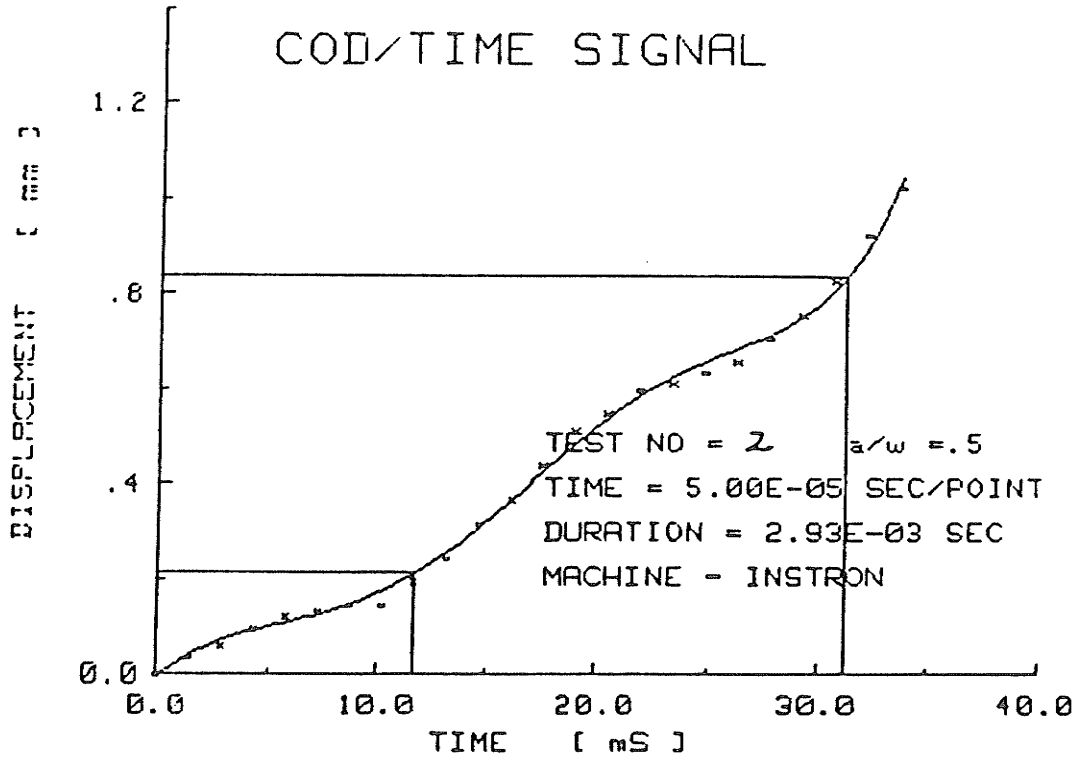
Two specimens at each of the three a/w ratios were tested at this speed. The various plots for tests #2 and #3 are presented in Figs. 4.6 and Figs. 4.7. The remaining plots are listed in Appendix B.

During this series of tests, the slope change associated with crack blunting was very clearly observed in tests #1, #2, #3 and #6. For tests #2, #3 and #6, the COD\_CRIT was determined as the difference between the two critical times identified. The initial portion of the COD-t curve is associated with the proper seating of the COD gage onto the knife edges mounted on the specimen face.

A very definite load-a/w relation is established (Fig. 4.8). The much lower load level of test #1 is similar to

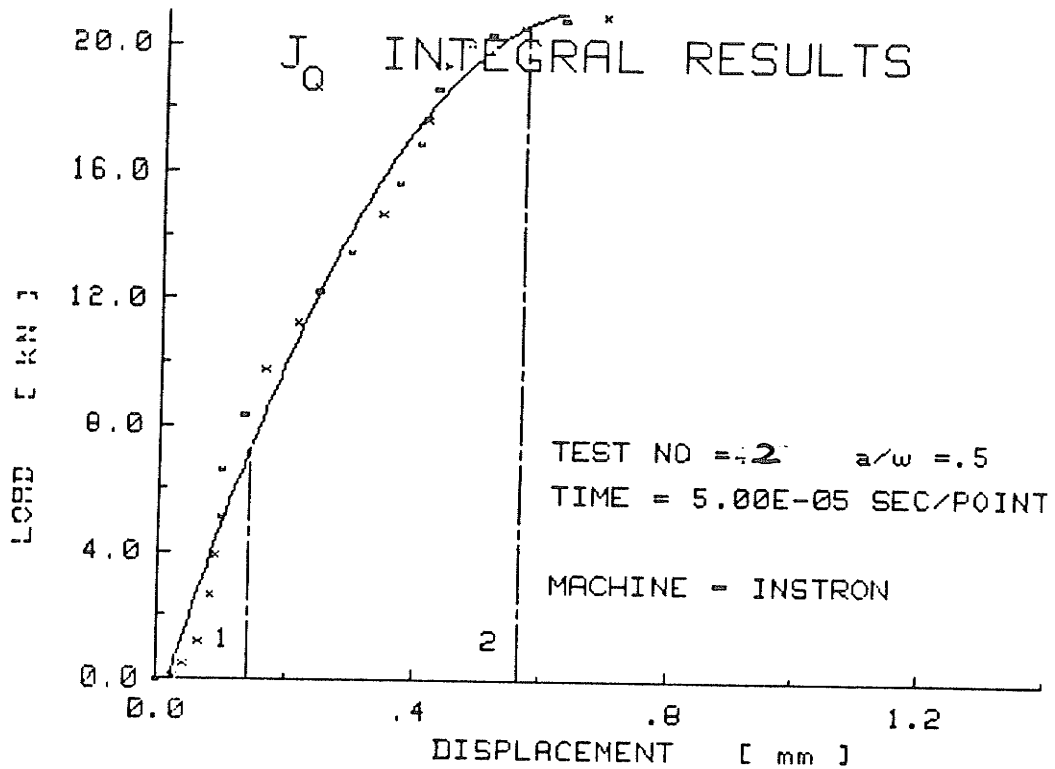


LSF OF ORDER 3  $Y = C1+C2*X+C3*X^2+...$



LSF OF ORDER 8  $Y = C1+C2*X+C3*X^2+...$   
 T\_CRIT( 1 ) = 1.17E-02 SEC  
 T\_CRIT( 2 ) = 3.12E-02 SEC

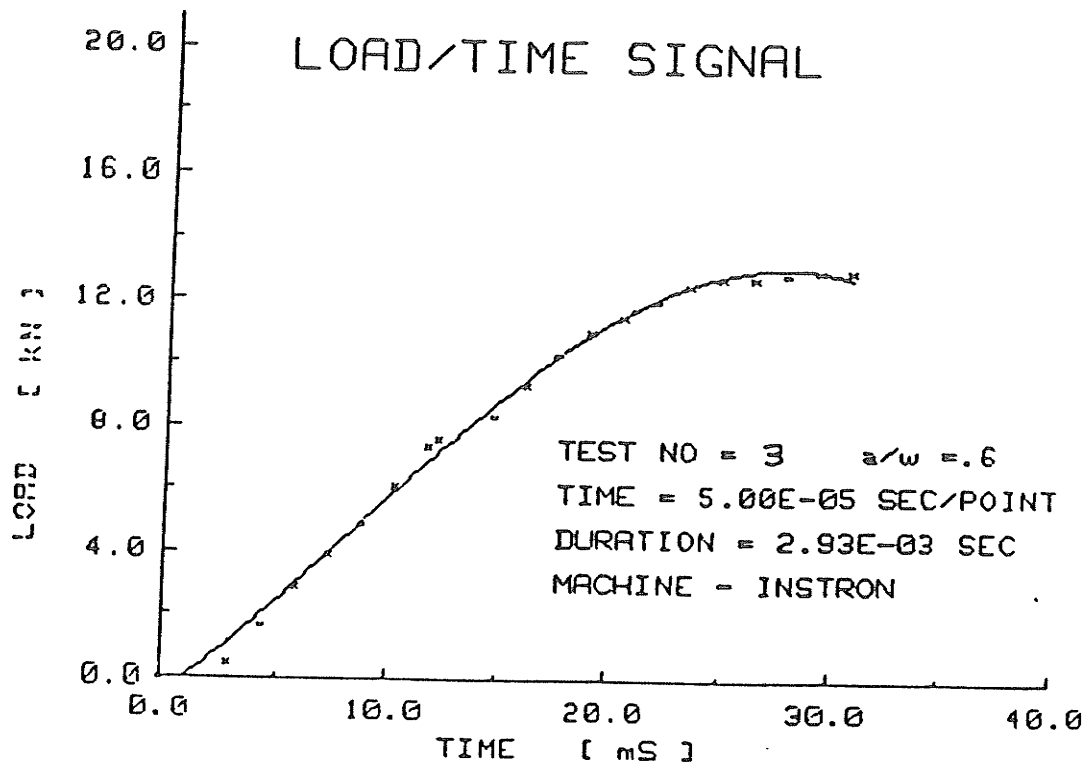
Figure 4.6 a,b Load-t, Cod-t results for test #INST2.



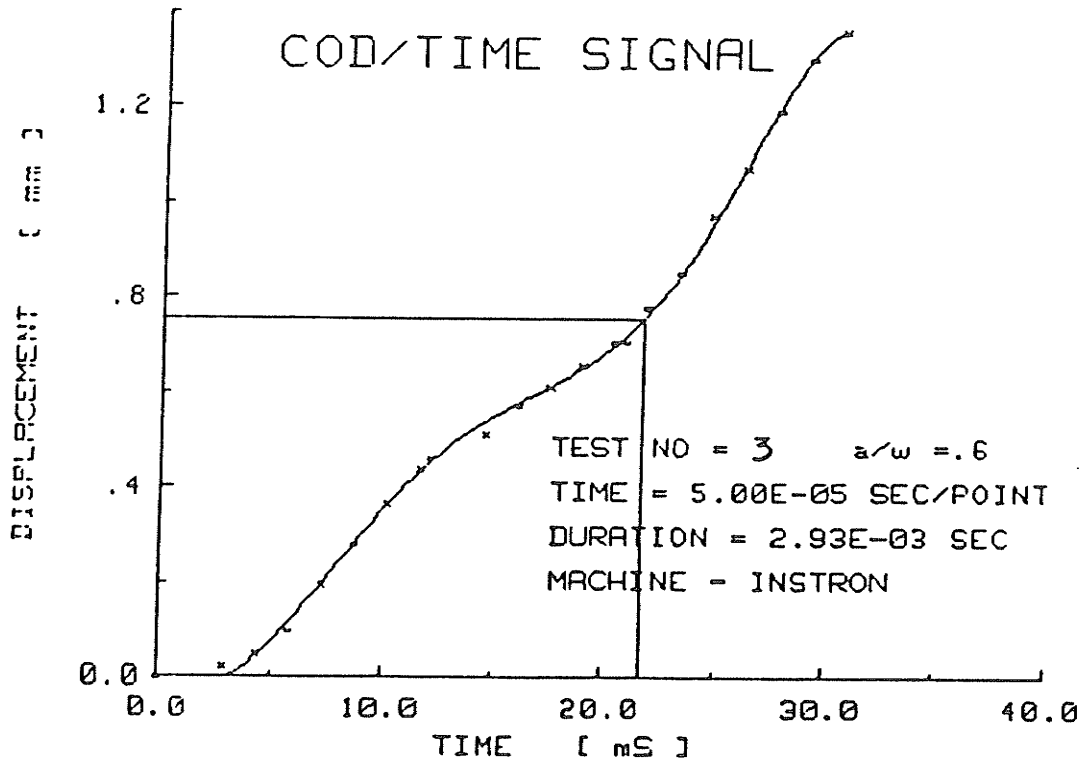
LSF OF ORDER 3     Y = C1+C2\*X+C3\*X^2+...

JQ( 1 )	3.30E+00 kN/m	
T_CRIT 1	1.17E-02 SEC	COD_CRIT 1 = 1.43E-01 mm
JQ( 2 )	5.00E+01 kN/m	
T_CRIT 2	3.12E-02 SEC	COD_CRIT 2 = 5.66E-01 mm

Figure 4.6c J<sub>Q</sub> result for test #INST2.



LSF OF ORDER 3     $Y = C1+C2*X+C3*X^2+...$



LSF OF ORDER 8     $Y = C1+C2*X+C3*X^2+...$

$T\_CRIT( 1 ) = 2.17E-02$  SEC

Figure 4.7 a,b Load-t, Cod-t results for test #INST3.

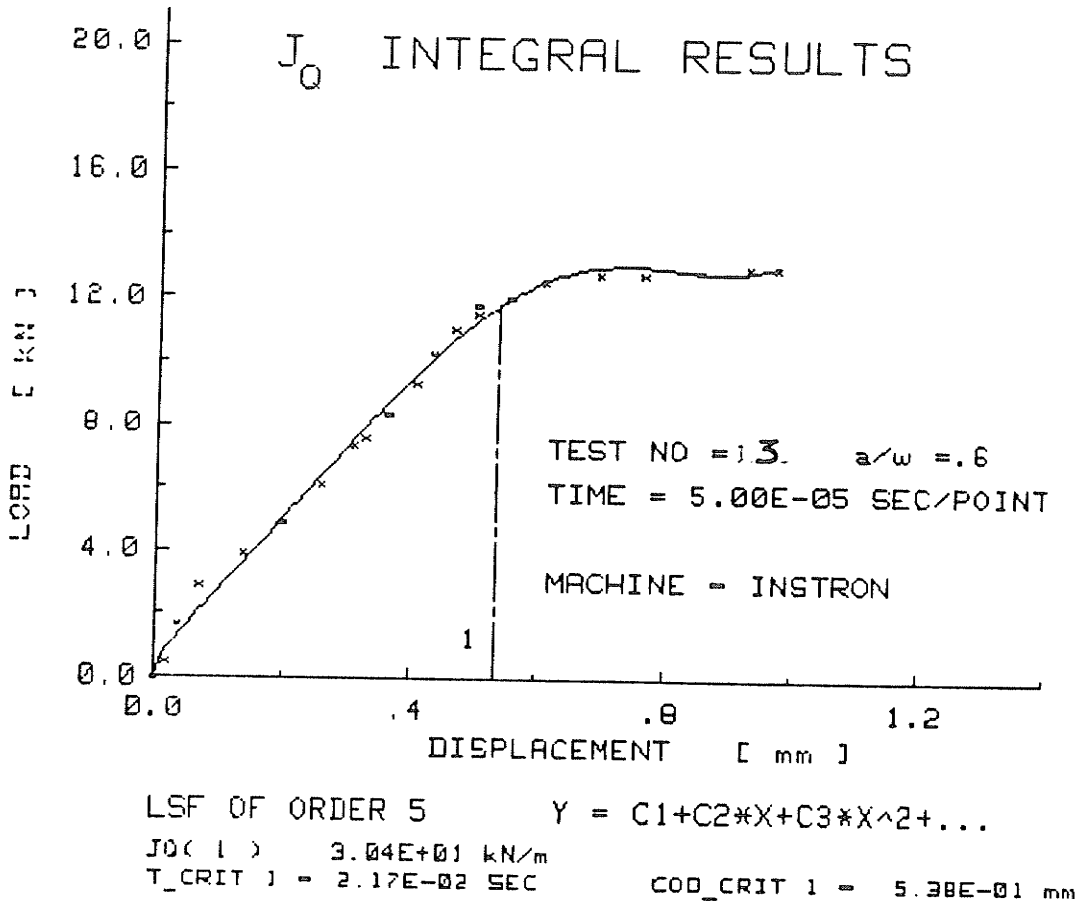


Figure 4.7c  $J_Q$  result for test #INST3.

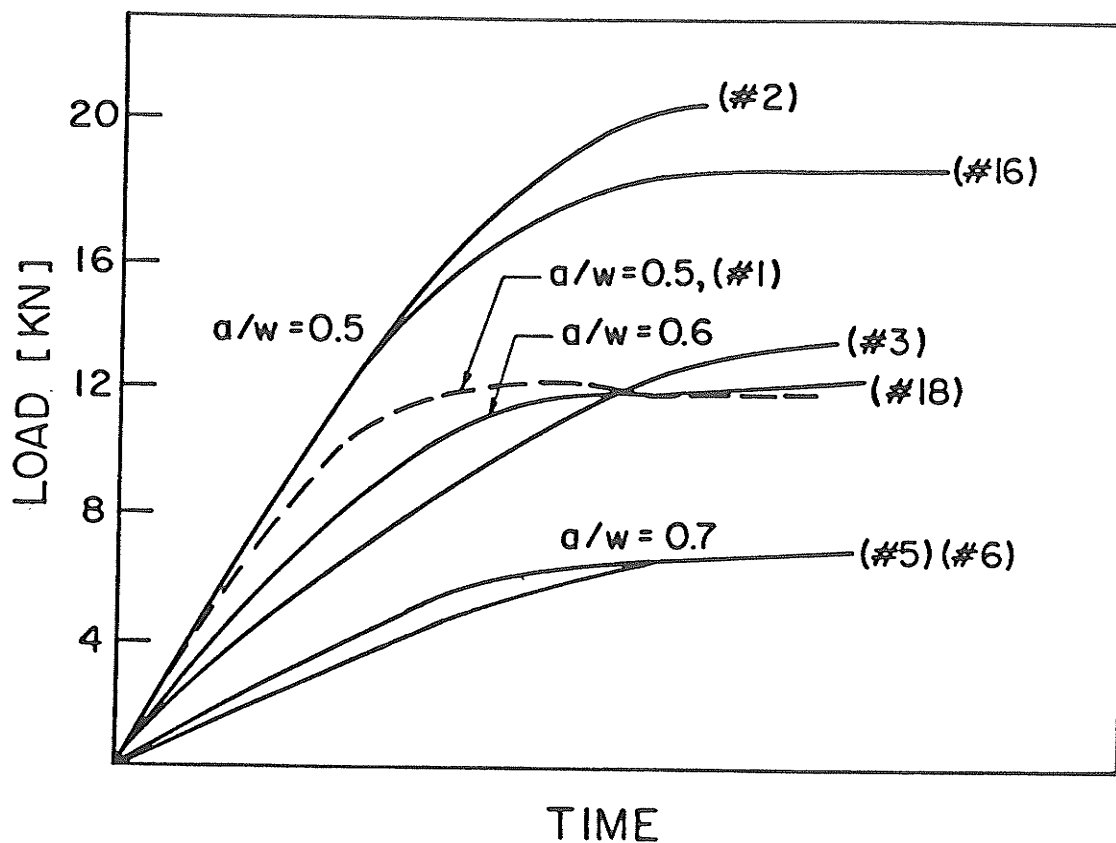


Figure 4.8 Load-t curves as a function of  $a/w$  for high speed Instron tests.

that experienced in the slow speed tests, and is assumed to be caused by similar mechanical problems.

COD signals from tests #16 and #18 were recorded using a low frequency gage with a 2.5 mm gage range. Although these two tests did not provide a clear crack initiation time,  $t_c$ , they did further confirm the load-a/w relationship.  $J_Q$  values were further evaluated at COD signals based on the COD\_CRIT of tests #2 and #3 and the estimated inflection points. These values further support those already obtained.

The  $J_Q$  values obtained in these tests exhibit a clear inverse a/w relationship. Namely,  $J_Q$  takes on the average value of 45, 34 and 21 kJ/m<sup>2</sup> as a/w goes from 0.5, 0.6 to 0.7. In addition, when compared to tests #12, #14, #16 and #18, these  $J_Q$  values indicate a definite decrease in fracture toughness value with strain rate (Fig. 4.9).

#### 4.3 Impact Loading Fracture Toughness ( $J_Q$ )

Seven specimens of two a/w ratios were tested under two striker velocities. The experimental results are listed in table 4.2, while the test wave forms for test #4 are listed in Figs. 4.10. The remaining dynamic test results are listed in Appendix C. Tests #1 and #2 were invalidated due to recording errors. Tests #6 and #7 were unsuccessful because the strain gages mounted on the loading grip had developed hair line fractures.

An extensive computer program was developed to analyze and display the dynamic test results. The horizontal time

Table 4.2

## DYNAMIC TENSILE TESTS

STRIKER VELOCITY	TEST NO.	SPECIMEN NO.	a/w	COD- <sup>1</sup> CRIT [ $\mu\text{m}$ ]	CRITICAL TIME [ $\mu\text{s}$ ]	$J_{\text{q}}$ [ $\text{KJ}/\text{m}^2$ ]	$\dot{J}_{\text{q}}$ [ $\text{KJ}/\text{m}^2\text{s}^{-1}$ ]	K [ $\text{MPa m}$ ]	$\dot{K}$ [ $\text{MPa m s}^{-1}$ ]
p=8 psi	3	B5	0.6	0.65	1	1.5	$1.5 \times 10^6$	19	$1.9 \times 10^7$
v=15 mm/ms	4	B6	0.6	13.6	2	5.1	$2.6 \times 10^6$	34	$1.7 \times 10^7$
p=15 psi	5	B7	0.6	7.2	2	4.7	$2.4 \times 10^6$	33	$1.6 \times 10^7$
v=25 mm/ms									

<1> COD-CRIT - load-line crack opening displacement

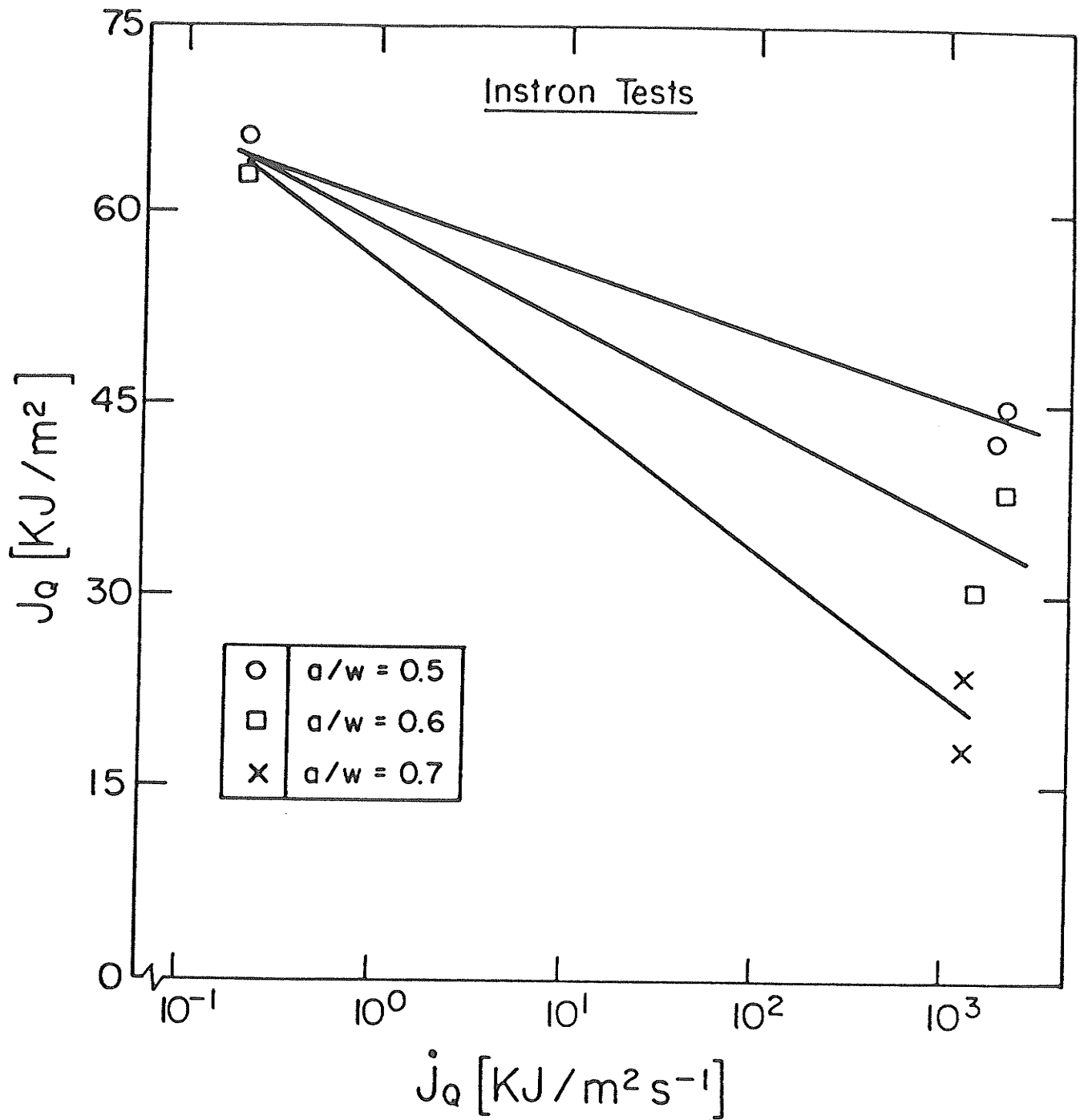


Figure 4.9 Relationship between fracture toughness ( $J_Q$ ) and loading rate ( $\dot{J}_Q$ ) for Instron tests.

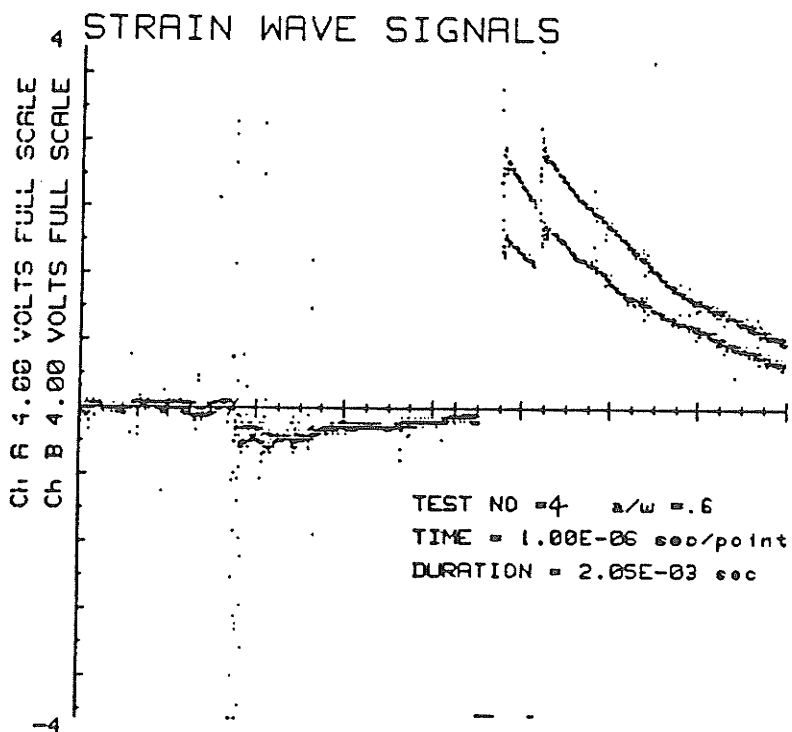
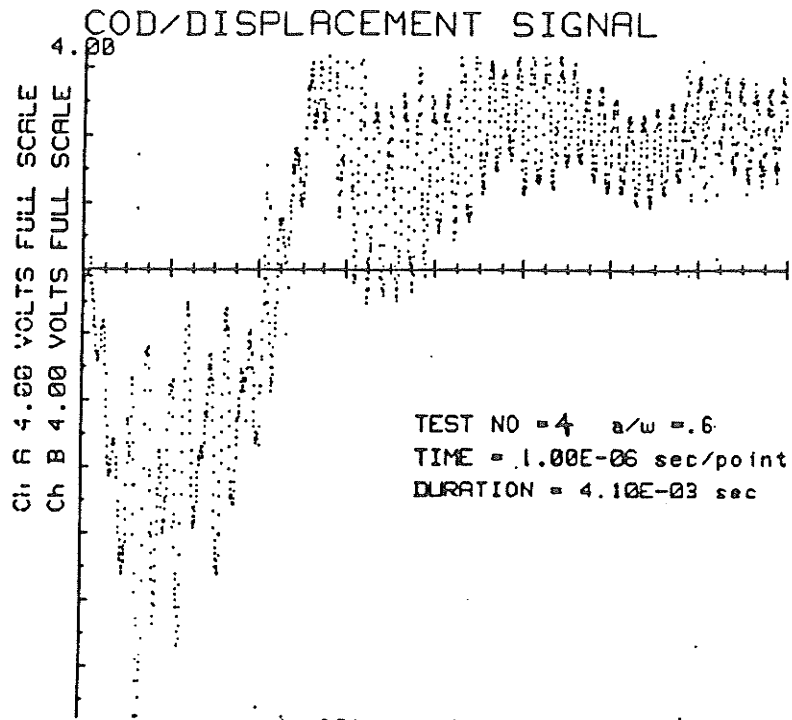


Figure 4.10 a,b Load-t, Cod-t results for test #SHB4.

axis of the actual test records (Figs. 4.10a) was programmed to adjust for the "floating" zero point during these tests. The floating zero point is a direct result of the high noise level in the test room as explained in section 3.4. The vertical axis is in units of volts - the amplified output of the COD and strain signals.

Although the sampling rates for all the signals of each individual test were the same, the COD signal had twice the stored memory as compared to the strain signals. This was done since it was critical that  $t_c$  be determined accurately. Therefore, the time scale of the COD signal was twice that of the strain signals.

Similar to procedures used in section 3.4, the trigger levels for the COD and strain signals were set as precisely as possible. The intersection of all signals with the time axis represents the transition from compressive to tensile loading. The trigger delay difference is seen to be negligible, as the COD and strain signals intersect the time axis at almost exactly the same instance in time.

Although the noise contribution to the COD signals were significant, the general trend of the COD signals are unambiguous. The initial compressive strain signals were the combined result of background noises and the swing arm assembly elastically moving forward due to the force of impact as explained in section 3.4.

The load response of this dynamic tensile fracture system was very different from those obtained in previous

compression SHB tests using WLCT or cylindrical specimens [48]. The smooth loading pulses in WLCT experiments (Fig. 4.11) were not present in these dynamic tests. The differences were due to the presence of plastic waves during loading of the CTS, the lower critical time encountered in these dynamic tests and the overlapping of incident and reflected wave signals.

The fracture process could be better understood by concentrating the analysis over a region close to the initial tensile loading region. The corresponding regions of analysis for test #4 are indicated in Fig. 4.12, where the boxed regions represent the portion of the signals that were digitally expanded for closer scrutiny. Expanded plots for test #4 is listed in Figs. 4.13.

Focussing attention on the load-time plot for the moment, it is seen that "apparent" maximum tensile loads from 400 kN to 800 kN (tests #3 to #5) were registered within  $4\mu\text{s}$  of tensile loading. These are considered "apparent" load values because, as mentioned in section 3.4.3, the maximum dynamic fracture load sustainable by the CTS is assumed to be 150 kN, while the maximum elastic tensile load sustainable by the test assembly is 300 kN. These maximum load values are based on the given strain rates and material modelling assumptions. In view of these high tensile loads, it is safe to assume that the following four factors were responsible for these high load values:

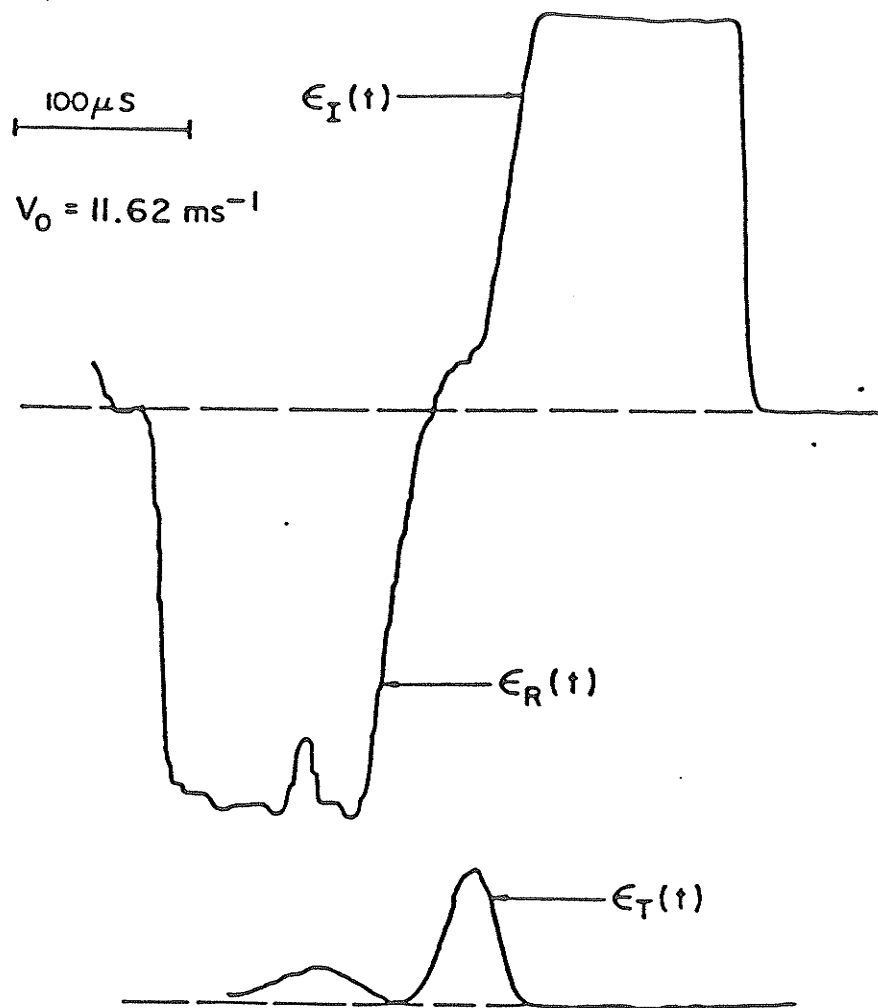


Figure 4.11 Smooth loading pulses from WLCT Split Hopkinson Bar Test. (after Ref. 50)

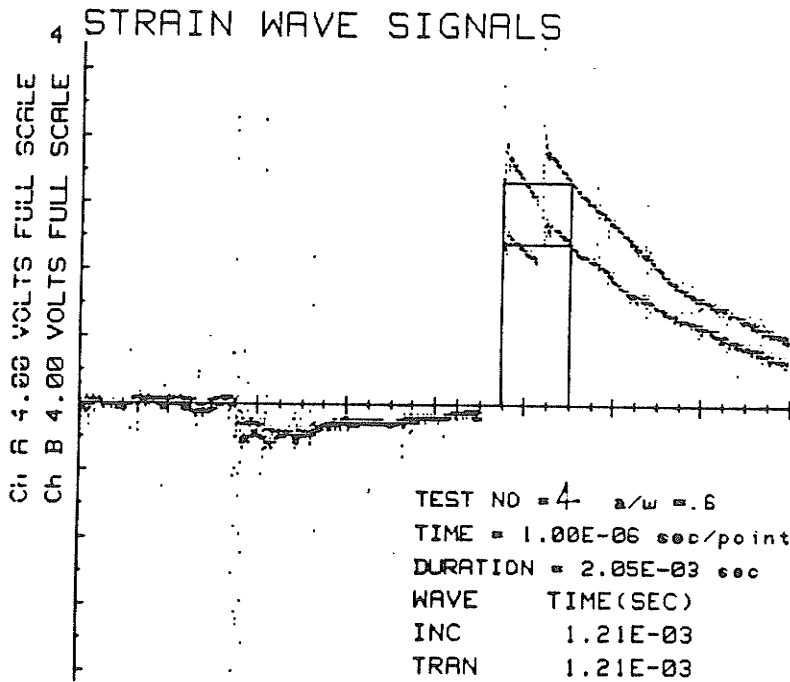
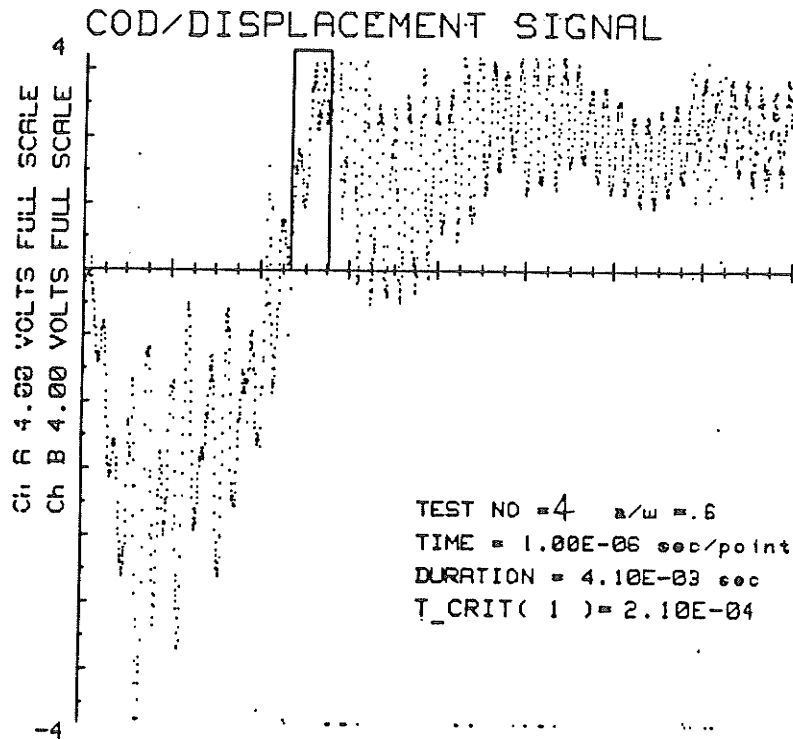
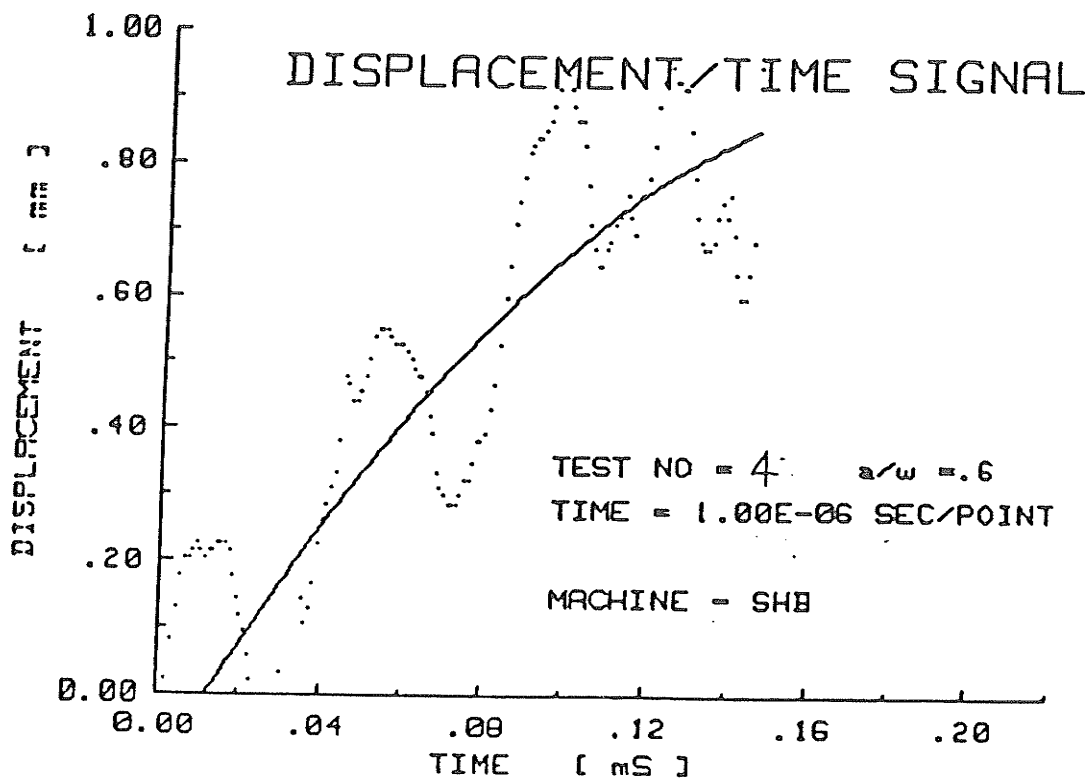


Figure 4.12 a,b Locations of digitally expanded regions for test #SHB4.



LSF OF ORDER 2     $Y = C1+C2*X+C3*X^2+...$

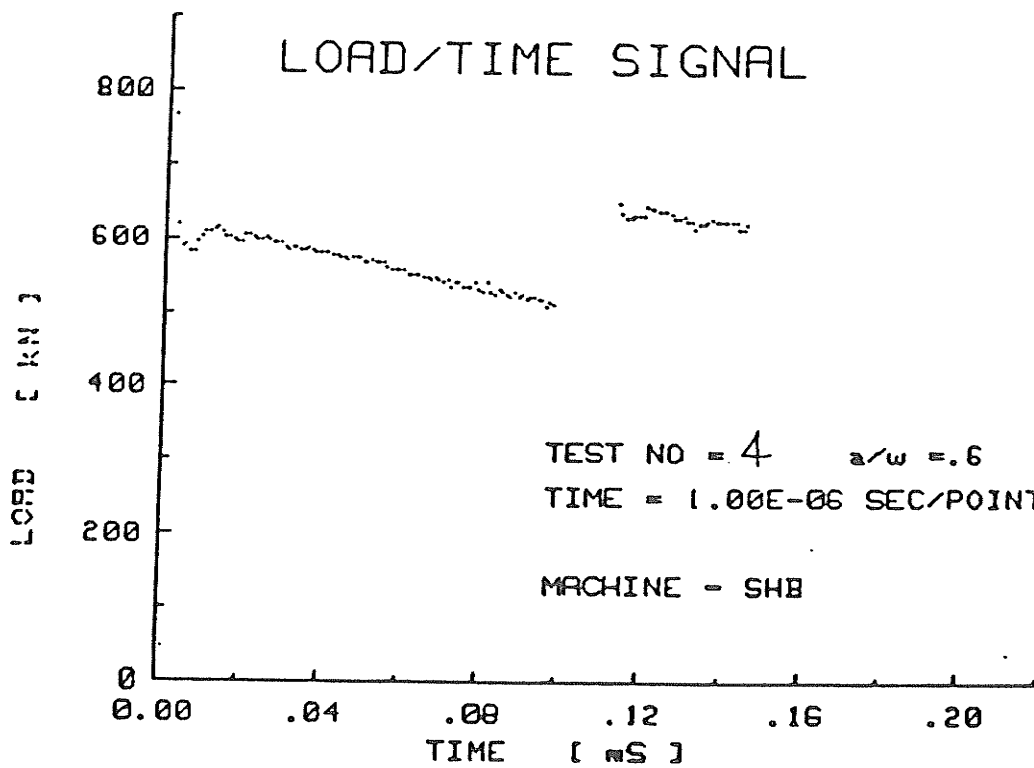


Figure 4.13 a,b Expanded COD-t, load-t results for test #SHB4.

- 1) the actual dynamic strain rate and/or strain hardening coefficient  $\beta$  (Eqn. 3.5) values were underestimated for the specimen material and overestimated for the grip material;
- 2) slight plastic loading of the test grip sections where the strain gages were mounted, and hence nonlinear response of the strain gages;
- 3) due to the geometry discontinuity of the grips, partial stress wave reflection occurred in the grips which resulted in a less severe loading of the specimens than indicated by the strain gages. The similarity in strain signals from both the loading and anchor grips indicates that the stress wave reflection was limited;
- 4) overestimation of the dynamic load due to partial overlap of incident and reflected wave signals.

Nonetheless, it is seen that the previous estimate of maximum dynamic fracture load of 150 kN (or equivalently a maximum dynamic fracture stress of 600 MPa) for the CTS was conservative. However, engineering sense dictates that the actual fracture load should be well under 300 kN (equivalent fracture stress of 1100 MPa).

Keeping in mind that reasonable assumptions were made in deriving the maximum specimen fracture load of 150 kN, it seemed proper that a conservative yet realistic estimate of the actual fracture energy requirement would result by adjusting the load scale of these load-t plots to reflect the dynamic fracture load based on a linear elastic perfectly plastic model of the specimen material. As such, the maximum fracture load was estimated to be 150 kN. Results from scanning electron microscopy in the next section showed that this analysis approach was only slightly conservative in its estimate of the fracture energy parameter  $J_Q$ .

Of equal interest is the response of the COD gage in light of these "instantaneous" plastic stress waves. In Fig. 4.13a, the boxed region is the portion of the COD signal curved fitted with multi-ordered polynomials to best represent the trend of this signal (cf. section 3.5.3). Both COD signals from tests #2 and #5 reached a maximum value at approximately 120  $\mu$ s, well behind the critical time of  $\sim 2$   $\mu$ s as sensed by the strain gages. The critical fracture time was taken to be  $\sim 2$   $\mu$ s since crack initiation must occur before maximum load.

From these two vastly different values of critical time, it would appear that the COD gage was not responding to the plastic loading of the crack tip. However, it will be shown that the COD gage signal in fact corresponded to the average local particle velocity of the crack faces at yielding, and was therefore a direct measure of the strain field during crack initiation at the crack tip. At maximum COD, the COD gage separated from the specimen and trailing oscillation of varying frequencies were recorded. As a first approximation, the displacement history at the crack tip is assumed to follow the trend set by the COD gage. A detailed examination of the COD signal is covered in the next chapter.

Proceeding with the analysis, the strain signals were further expanded digitally to more accurately determine the load-line displacement history at the crack tip at the onset of crack initiation. The expanded load-t plot for test #4

is shown in Fig. 4.14. In view of the background noise associated with the COD-t signals, a second order fit of the COD-t curve of test #4 was used as the representative COD-t curve for these dynamic tests. Again, the COD-t curve was adjusted for load-line displacement.

From the load-t and COD-t plots, the load/load-line displacement records were constructed. As previously mentioned, the apparent maximum load values were adjusted to 150 kN (Fig. 4.15).

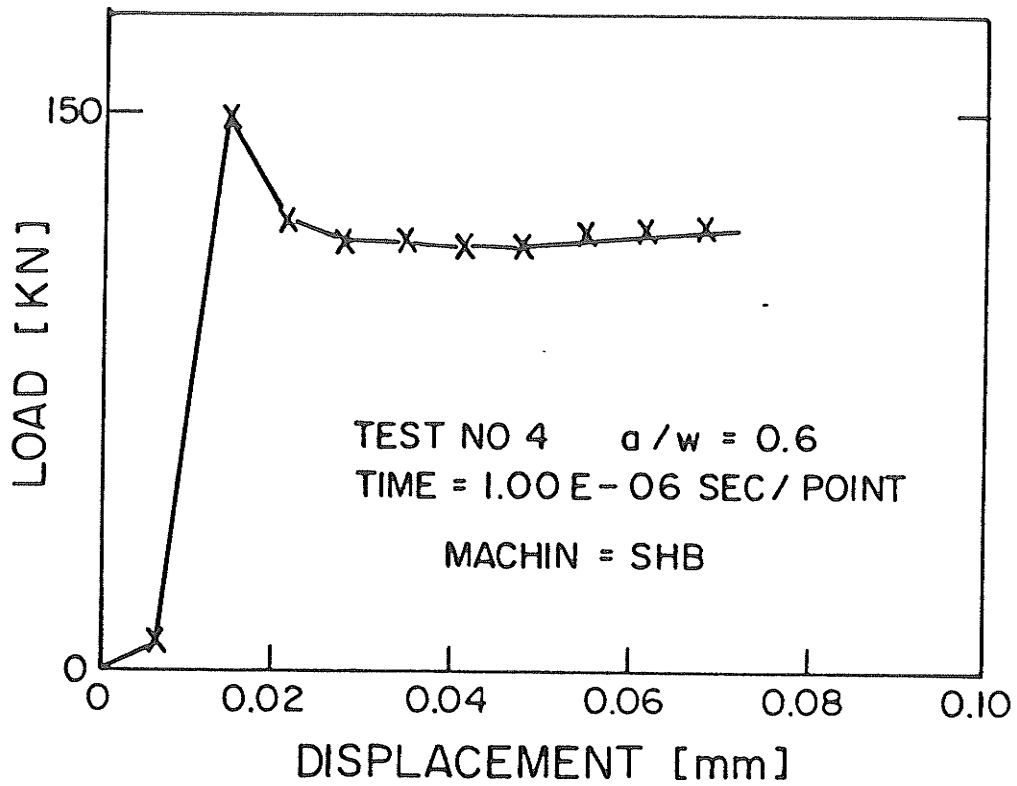
Based on the above analysis the dynamic characterizing fracture energy parameter  $J_Q$  was found to range from 1.5 to 5.1 kJ/m<sup>2</sup> for  $a/w = 0.6$  and 2 striker velocities. Taking  $J_Q$  as a measure of the average rate of fracture energy inputted into the test system, the extremely high  $J_Q$  values reflect the severity of the loading situation.

#### 4.4 Stretch Zone Measurements

Scanning electron microscopy was used to measure stretch zone widths of fracture surfaces of specimens that cover four nominal strain rates and three  $a/w$  ratios. These stretch zone measurements provided a direct record of the fracture energy requirement based on microstructural details. In addition, examination of the stable crack growth regions indicates whether the fracture processes were ductile or brittle in nature.

Tilting angles of  $\psi = 37^\circ$  and  $45^\circ$  were used to examine the fracture surfaces. On the whole, the stretch zone widths at  $\psi = 37^\circ$  were either higher or equal to those at





$J_Q = 5.1 \text{ KN/m}^2$

T CRIT = 2.00E - 06 SEC

COD. CRIT = 1.36E - 02 mm

Figure 4.15 Fracture toughness ( $J_Q$ ) determination for test #SHB4.

45°. Equal values of the SZW at  $\psi = 45^\circ$  and  $37^\circ$  meant the actual stretch zone slope angle  $\theta = 41^\circ$ . Therefore, it was reasonable to assume  $\theta = 41^\circ$ . The arithmetic averages of the SZWs at  $\psi = 37^\circ$  and  $45^\circ$  were themselves averaged, and along with  $\theta = 41^\circ$ , were used in subsequent calculations.

The results of the stretch zone measurements are tabulated in table 4.3 and graphically presented in Fig. 4.16. All stretch zone measurements were conducted using stereoscopic pictures at  $\psi = 37^\circ$  and  $45^\circ$  and at 180X magnification .

For the Instron speeds tests, the failure mode was entirely ductile (Fig. 4.17) and 10-20% error in SZW determination is to be expected.

In the dynamic tests, tests #1 and #2 exhibited ductile failure fracture surface profiles (Fig. 4.18), whereas tests #3 to #5 were clearly brittle in nature (Fig. 4.19). The determination of stretch zone boundaries was more difficult for tests #1 and #2, and a minimum error of 20% is expected. For tests #3 to #5, an approximate upper bound of 11 mm on stretch zone measurement was observed, as it was impossible to determine SZW more precisely. The complete set of micrographs are presented in Appendix D.

To experimentally determine the proper value of  $m$  in Eqn 3.13,  $J_Q$  values from the load/load-line displacement results (table 4.2) were plotted against stretch zone widths from the corresponding tests (Fig. 4.20). Lines of constant  $m$ 's were drawn in as reference lines:

Table 4.3

## SZW

SPEED	TEST NO.	SPECIMEN NO.	a/w	SZ <sup>1</sup> [ $\mu\text{m}$ ]	Jq <sup>2</sup> <sub>m=1</sub> [KJ/m]	Jq <sup>3</sup> <sub>m=2</sub> [KJ/m]	tc [ $\mu\text{s}$ ]	j <sub>q</sub> [KJ/m <sup>2</sup> s <sup>-1</sup> ]
DYNAMIC	1	A7	0.5	19.7	16	-	2	$8.0 \times 10^6$
	2	A8	0.5	28.3	22	-	2	$1.1 \times 10^7$
	3	B5		12.8	10	-	1	$1.0 \times 10^7$
	4	B6	0.6	11.1	9	-	2	$4.5 \times 10^6$
	5	B7		11.1	9	-	3	$3.0 \times 10^6$
HIGH	1	A1	0.5	22.2		26	$1.80 \times 10^4$	$1.4 \times 10^3$
	3	B1	0.6	26.1		31	$1.84 \times 10^4$	$1.7 \times 10^3$
	6	C2	0.7	21.9		26	$1.55 \times 10^4$	$1.7 \times 10^3$
SLOW	7	A3	0.5	42.5		50	$6.92 \times 10^5$	72
		B3	0.6	40.3		48	$5.87 \times 10^5$	81
	12	C4	0.7	42.5		50	$5.02 \times 10^5$	100
QUASI- STATIC	14	A6	0.5	33.3		39	$3.04 \times 10^6$	0.13

<1>  $\theta = 41$

<2> static ofl = 450 MPa

<3> dynamic ofl = 600 MPa

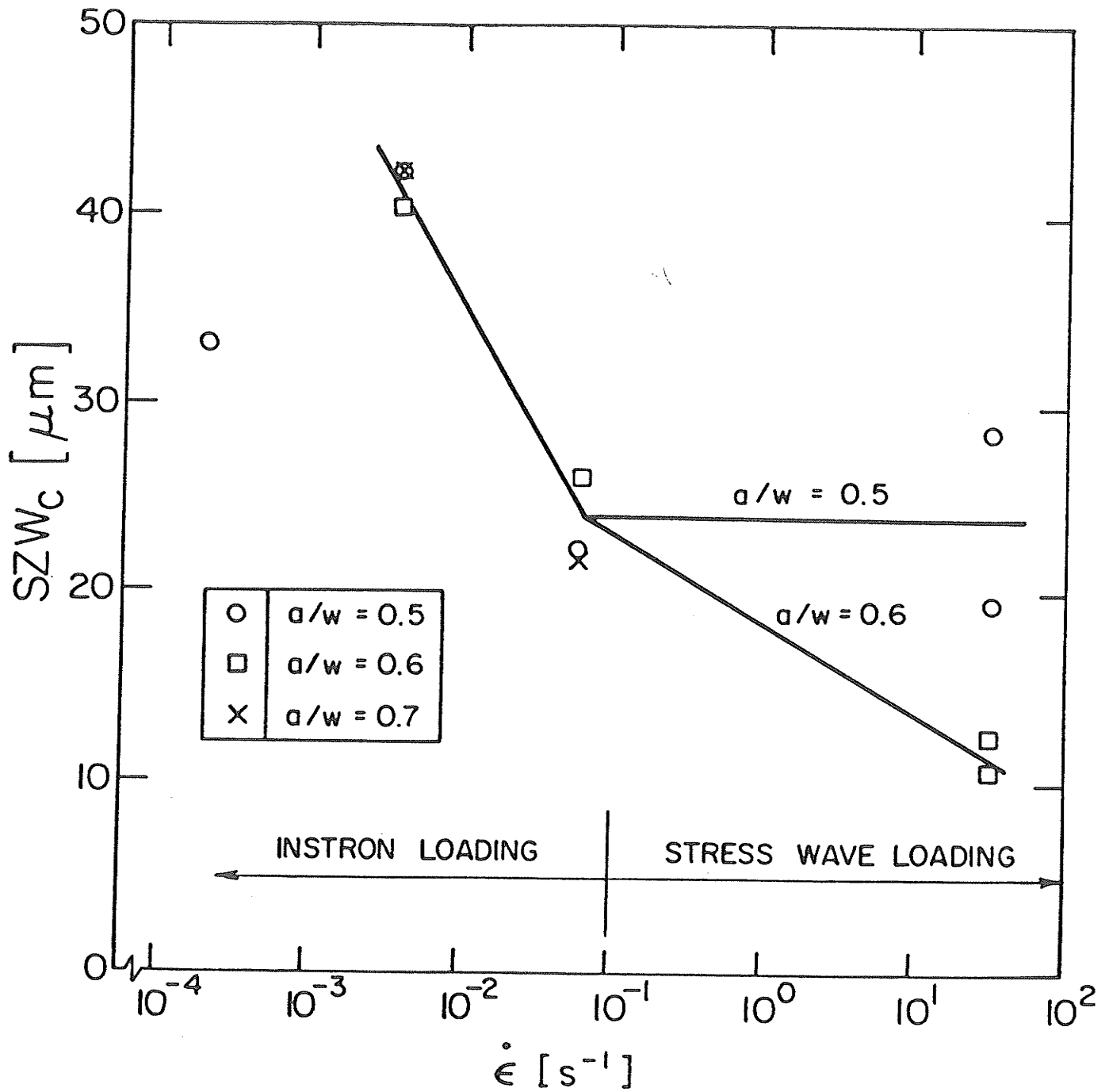
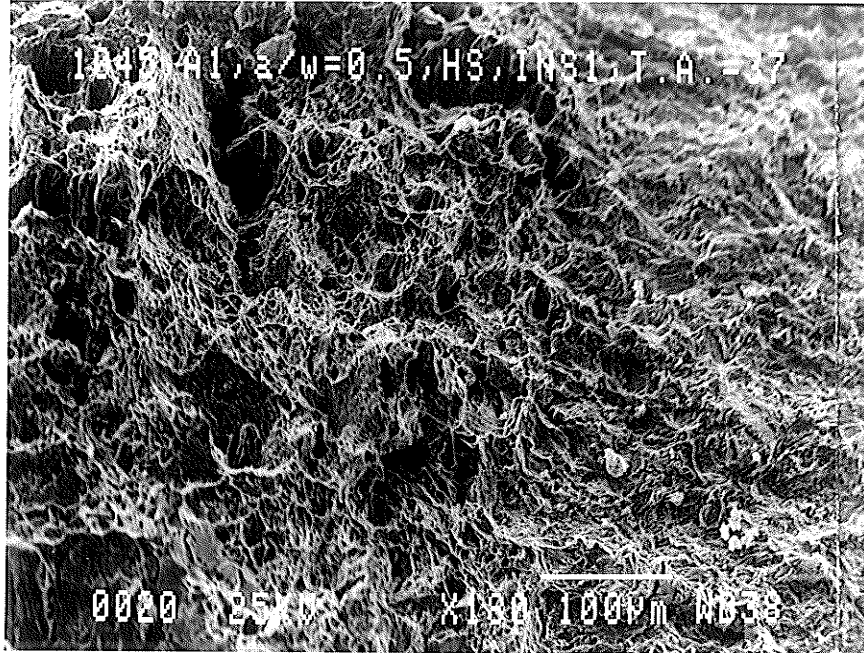


Figure 4.16 Relationship between stretch zone width and nominal strain rate,  $\dot{\epsilon}$ .

a      b      c      d      e



f      g

- a - specimen material AISI 1045 steel
- b - specimen no. (eg. A1)
- c - a/w ratio (eg. 0.5)
- d - test condition
  - INS# - Instron speeds test no. (eg. INS1)
  - HS - high speed
  - SS - slow speed
  - QS - quasi-static
- e - tilt angle  $\psi$
- f - scanning electron microscope magnification
- g - scaling for micrograph

Figure 4.17 Representative stretch zone micrographs ( a ) for Instron speeds tests illustrating ductile fracture mode (from #INS1).

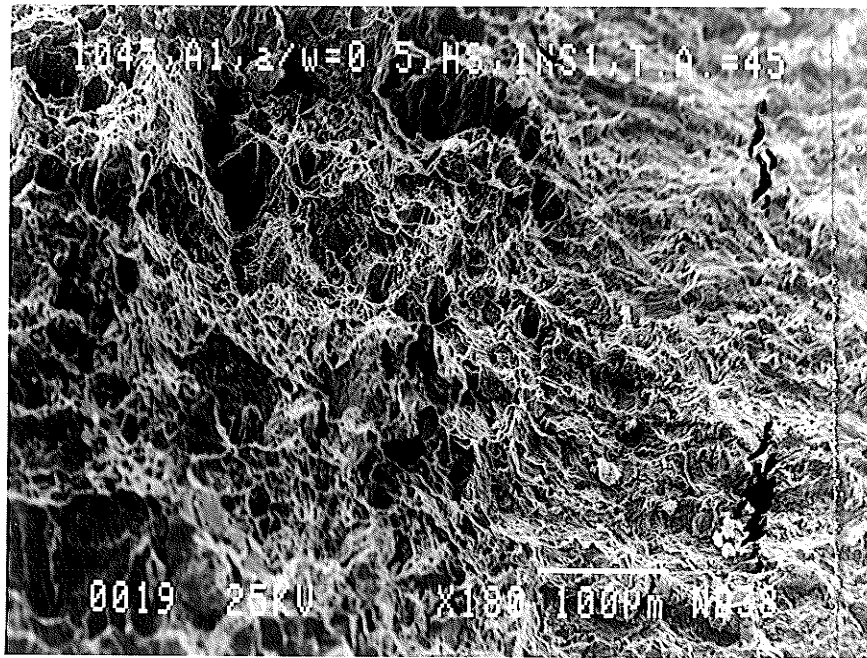


Figure4.17b Stretchzone micrograph for Instron test #INS1.

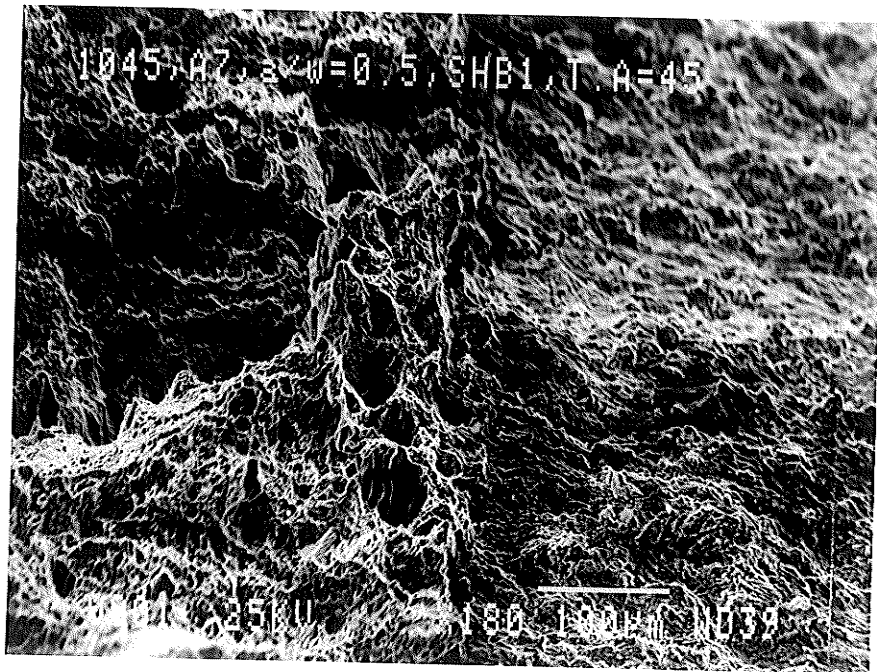
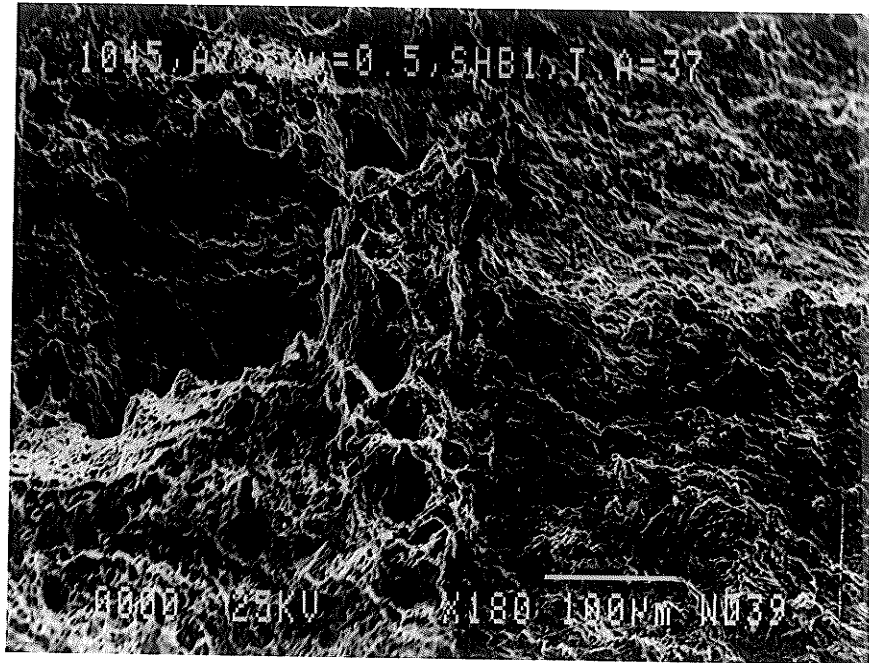


Figure 4.18 Stretch zone micrographs for dynamic test (a)-(b) #SHB1 illustrating ductile fracture mode.



Figure 4.19 Stretch zone micrographs for dynamic test (a)-(b) #SHB4 illustrating brittle fracture mode.

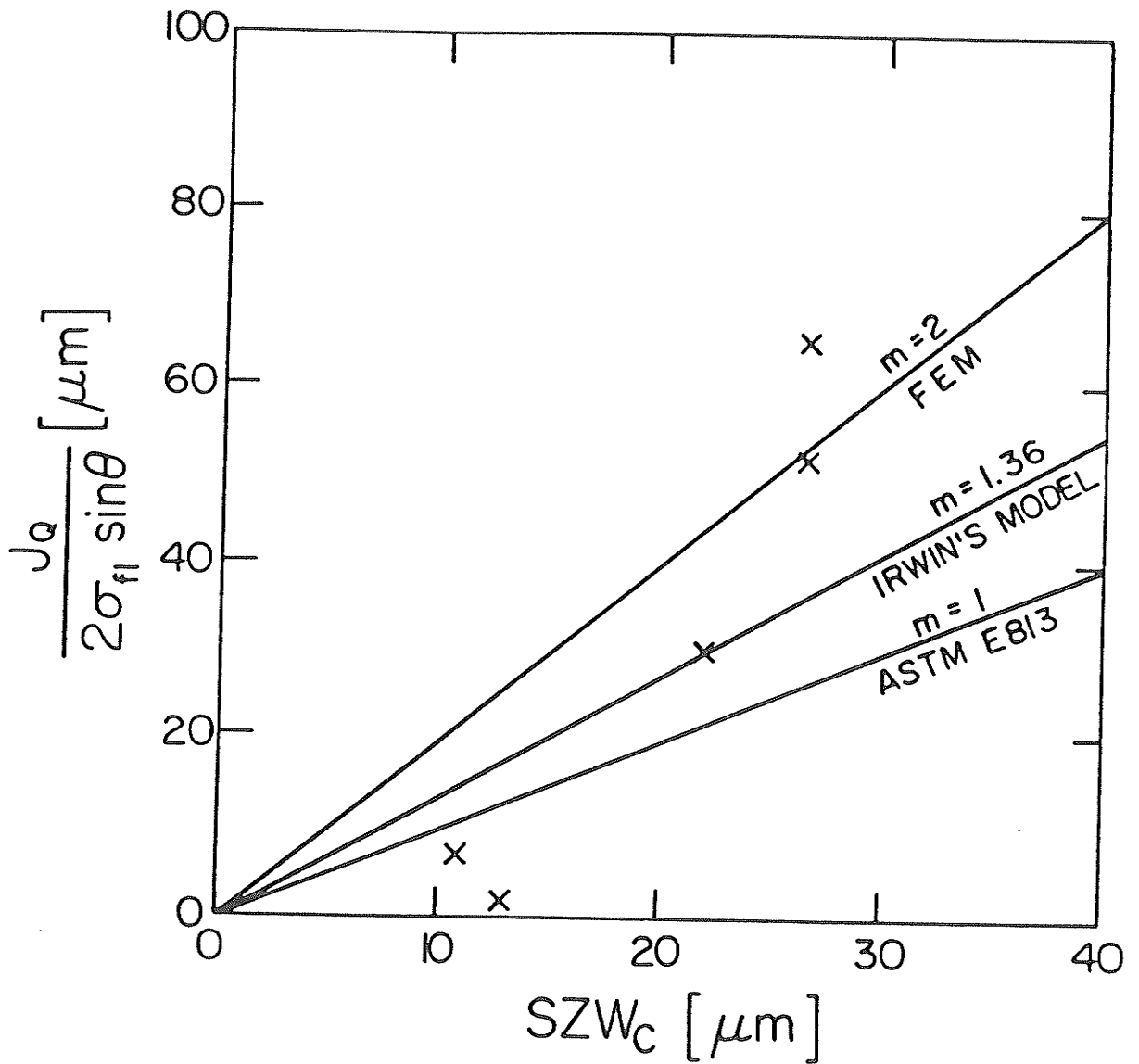


Figure 4.20 Relationship between the load/load-line displacement method and the stretch zone method of determining fracture toughness ( $J_Q$ ).

- 1)  $m=2$  is the generally accepted value of  $m$  found in the literatures based on finite element results (Fig. 2.6)
- 2)  $m=1.36$  is based on Irwin's plastic zone correction factor
- 3)  $m=1$  is used in ASTM E813 to determine the crack blunting line

The Instron data appear to exhibit quite a scatter in  $m$  value dependence, with the best fit  $m$  value being approximately 2. On the other hand, the dynamic  $J_Q$  values are seen to be best represented by the lower bound value of  $m = 1$ .

It would appear, therefore, that increasing the loading rate from Instron speeds to stress wave loading resulted in a transition of the fracture mode as characterized by two values of  $m$  in Eqn. 3.13:  $m=1$  for the dynamic case and  $m=2$  for the slower cases. By using the proper  $m$  value and the respective static and dynamic flow stresses, the  $SZW_C$  values were replotted in the form of the characterizing fracture energy parameter,  $J_Q$  (Fig. 4.21). In Fig. 4.21,  $J_Q$  is seen to clearly decrease with increasing strain rate and  $a/w$  ratio. For purposes of comparison, these microscopic (SZW)  $J_Q$  values were replotted using  $\dot{J}_Q$  values to represent the loading condition (Fig. 4.22). These  $\dot{J}_Q$  values were calculated using the corresponding  $t_c$  for each test from Table 4.1 and Table 4.2.

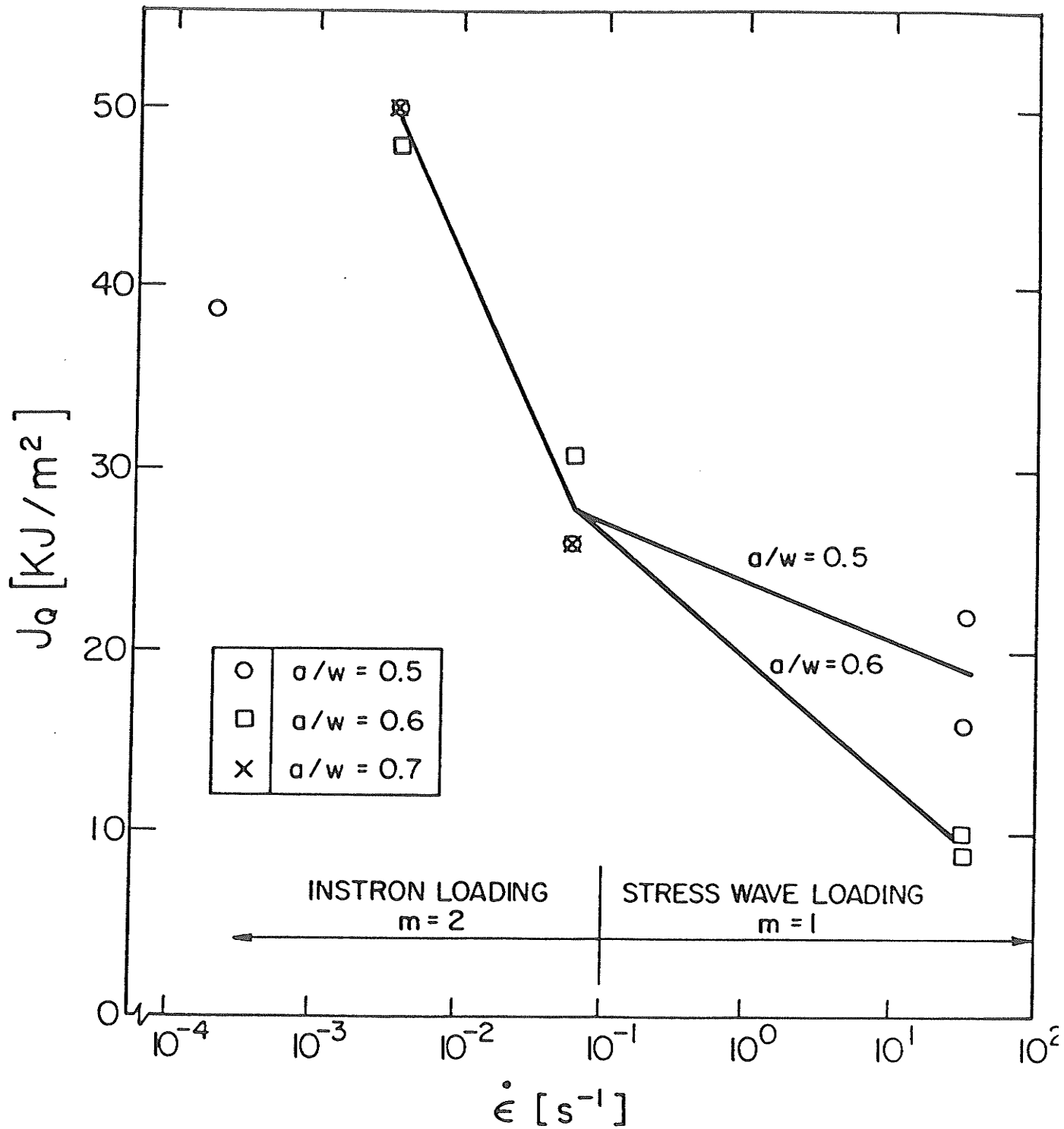


Figure 4.21 Relationship between fracture toughness ( $J_Q$ ) and nominal strain rate based on stretch zone measurements.

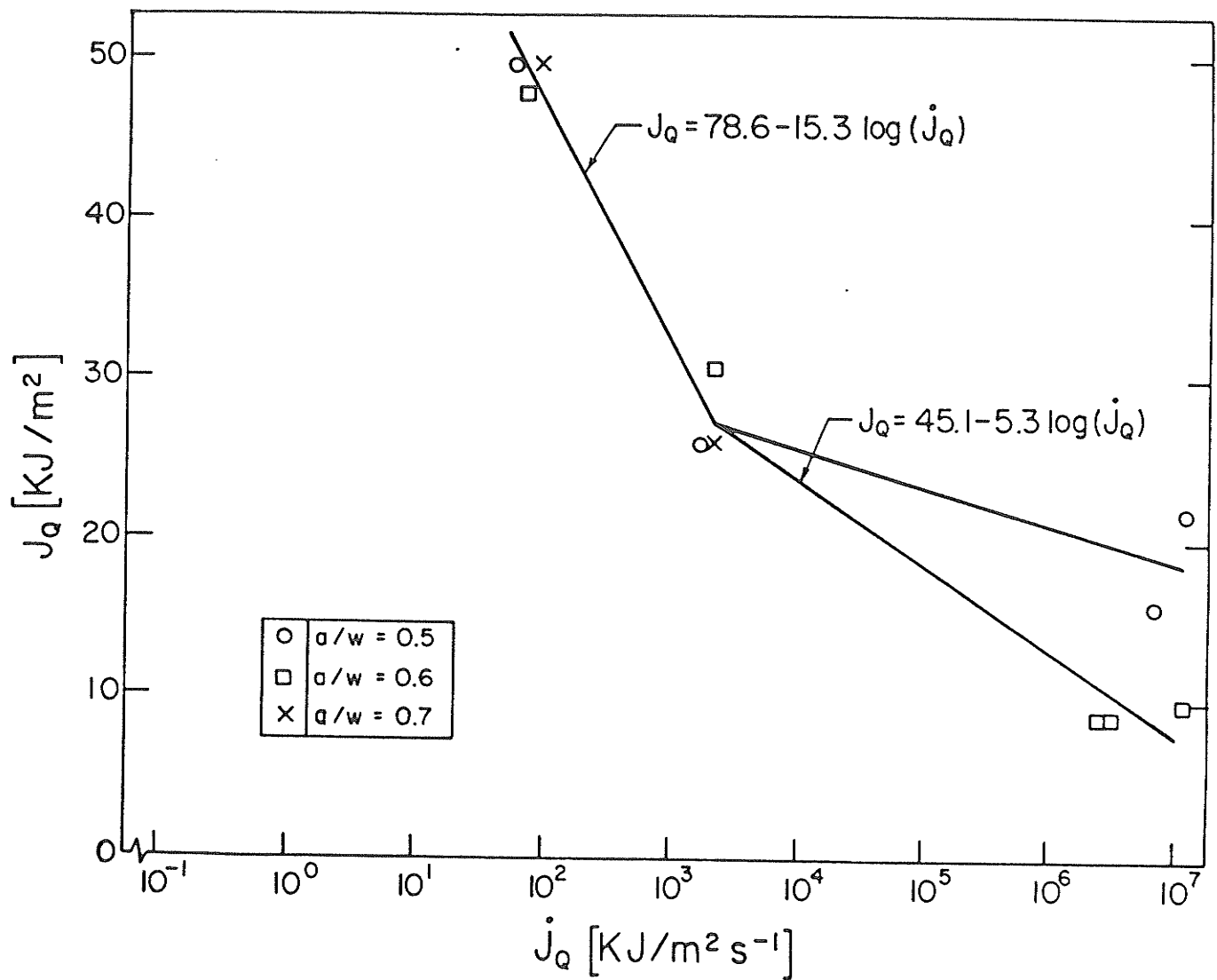


Figure 4.22 Relationship between fracture toughness ( $J_Q$ ) and loading rate ( $\dot{J}_Q$ ) based on stretch zone measurements.

CHAPTER FIVE  
DISCUSSION OF RESULTS

The objective of this thesis work was to set up an experimental fracture toughness testing procedure that utilizes tensile loading and stress triaxiality to characterize quasi-static to stress wave induced fracture. In examining the fracture toughness results obtained using both the macroscopic (load/load-line displacement curve) and the microscopic (stretch zone measurement) methods, it is seen that the objective of this thesis work has been successfully met.

The success of this test system to characterize fracture toughness through the energy parameter  $J_Q$  will be discussed in its application to the testing of AISI 1045 steel. This will be followed by a general discussion on the test methodology used in this work. This chapter will be concluded with a discussion on the relevance and application of  $J_Q$  to fracture mechanics.

### 5.1 Macroscopic $J_Q$ Results

One of the goals of this thesis work was to establish a characterizing fracture energy parameter that reflects the loading rate dependence of material fracture toughness. In addition, this parameter should permit its evaluation through automated data recording and analysis procedures. Examination of the quasi-static to dynamic test results indicate that this goal has been successfully met.

A clear decrease in the macroscopically obtained  $J_Q$  is associated with increasing loading rate, with the average  $J_Q$  ranging from  $65 \text{ kJ/m}^2$  (quasi-static) to  $4 \text{ kJ/m}^2$  (dynamic)

(Fig. 5.1). In this way,  $J_Q$  confirms that it indeed does characterize the loading rate effect of fracture toughness by exhibiting the well-known qualitative relationship between loading rate and fracture toughness. The loading rate in these tests is defined in terms of  $\dot{J}_Q$ , which represents the average rate of fracture energy input into the system, or alternately a measure of the severity of the loading situation.

The fracture toughness/loading rate relationship for this steel, for the case of  $a/w = 0.6$ , can be approximated by a bilinear function through eight orders of magnitudes of  $\dot{J}_Q$  in the form:

$$J_Q = 61 - 6.3 \log (\dot{J}_Q) \quad \text{for } 10^{-1} < \dot{J}_Q < 10^4$$

$$\text{and } J_Q = 99 - 15 \log (\dot{J}_Q) \quad \text{for } 10^4 < \dot{J}_Q < 10^7$$

with  $J_Q$  in units of  $\text{kJ/m}^2$  and  $\dot{J}_Q$  in units of  $\text{kJ/m}^2\text{s}^{-1}$

For the dynamic tests, the effects of striker velocity on  $J_Q$  is not evident since the critical time to maximum load at both striker velocities are approximately the same.

However, a clear  $a/w$  dependence of  $J_Q$  is observed. With reference to Fig. 5.1,  $J_Q$  is seen to vary from  $45 \text{ kJ/m}^2$  to  $21 \text{ kJ/m}^2$  as  $a/w$  goes from 0.5 to 0.7 for the case of high speed Instron tests. In addition, this  $J_Q$ - $a/w$  dependence is seen to also depend on the loading rate, as  $J_Q$  results from Instron tests performed at the quasi-static speed were relatively specimen geometry independent.

The  $J_Q$ - $a/w$  dependence is due partly to the significant dependence of the applied moment on  $a/w$  as a result of the

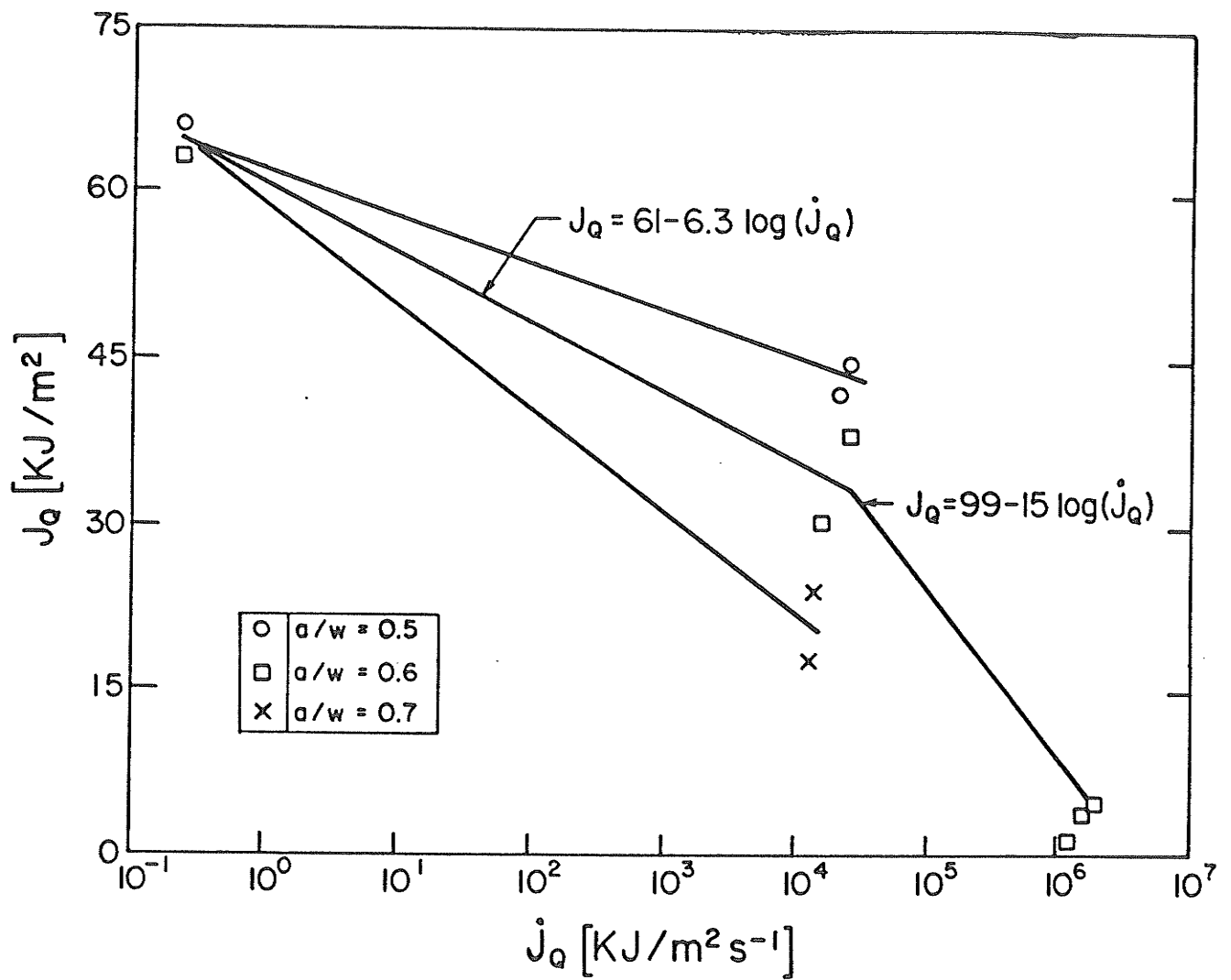


Figure 5.1 Relationship between fracture toughness ( $J_Q$ ) and loading rate based on load/load-line displacement curves.

shifting of the neutral axis on the compact tension specimen. With a smaller  $a/w$ , a significantly higher fracture load would have to be used to compensate for the reduced bending moment available. In the impact tests, this reduction in moment was seen as a major cause for ductile fracture in the  $a/w = 0.5$  case and brittle fracture in the  $a/w = 0.6$  case, as will be covered in the next section.

Although this macroscopic method of fracture toughness determination exhibits a strong  $a/w$  dependence, by focusing its use on standardized specimens (CTS,  $a/w = 0.6$ ), a time saving, economical method of quantifying the loading rate/fracture toughness relationship is possible.

## 5.2 Microscopic $J_Q$ Results

Determination of the fracture parameter  $J_Q$  through stretch zone (SZ) measurement provides a more direct, though time consuming, record of the fracture energy requirement based on microstructural details. As an alternate method of  $J_Q$  evaluation, this microscopic approach serves to evaluate the accuracy of the time saving macroscopic approach.

Results from SZ measurements confirm those obtained via the macroscopic method. In particular, SZ results demonstrate a similar loading rate/fracture toughness relationship (Fig. 4.16).

To convert these stretch zone measurement results to an equivalent fracture energy parameter, two values of  $m$  in Eqn. 3.13 was seen to be needed to characterize the Instron and dynamic speed tests (Fig. 4.20). From the corresponding

micrographs of these test, it is evident that these two values of  $m$  in fact differentiated between ductile and brittle fracture. From section 2.2.1, it is known that  $m$  represents the degree of crack tip plasticity or constraint associated with the crack blunting process. When the fracture mode changes from ductile to brittle, the associated plastic zone ahead of the crack tip diminishes and a corresponding drop in the value of  $m$  is to be expected. In this work on AISI 1045 steel,  $m=2$  is associated with ductile fracture whereas  $m=1$  best represents brittle fracture.

Evaluation of the microscopic  $J_Q$  based on these two values of  $m$  yields Fig. 4.21. Figure 4.21 clearly demonstrates a bilinear dependence of  $J_Q$  on loading rate due to the change in crack tip constraint associated with two values of  $m$ . As mentioned in the previous section, the loading situation can best be seen through the loading rate parameter  $\dot{J}_Q$  (Fig. 4.22). For the case of  $a/w = 0.6$ , the fracture toughness/loading rate relationship is in the form:

$$J_Q = 78.6 - 15.3 \log (\dot{J}_Q) \quad \text{for } 10^{-1} < \dot{J}_Q < 10^3$$

$$\text{and } J_Q = 45.1 - 5.3 \log (\dot{J}_Q) \quad \text{for } 10^3 < \dot{J}_Q < 10^7$$

with  $J_Q$  in units of  $\text{kJ/m}^2$  and  $\dot{J}_Q$  in units of  $\text{kJ/m}^2\text{s}^{-1}$

The fracture energy parameter  $J_Q$  evaluated using SZ measurement is seen to be less specimen geometry dependent as compared to the macroscopic method. Negligible  $a/w$  dependence is seen for the Instron speed tests while  $J_Q$  is seen to decrease from  $19 \text{ kJ/m}^2$  to  $10 \text{ kJ/m}^2$  as  $a/w$  goes from

0.5 to 0.6 for the dynamic tests. The relatively large SZ associated with  $a/w = 0.5$  and dynamic loading correctly reflects the greater resistance to fracture offered by the larger remaining specimen ligament, and the ductile fracture surface over the stable crack growth region (Fig. 4.18) supports the large SZ measured. On the other hand, the much lower SZ associated with  $a/w = 0.6$  and dynamic loading is a direct consequence of the transition from ductile fracture for the Instron cases to the present brittle fracture mode.

### 5.3 Agreement of Macroscopic/Microscopic $J_Q$ Results

The relative agreement between the macroscopic and microscopic methods of  $J_Q$  determination can be seen in Fig. 5.2. A clear decrease of  $J_Q$  is associated with increasing  $J_Q$  for both methods, while the macroscopic method has a greater  $J_Q$ - $a/w$  dependence. The agreement between these two methods therefore confirms the general validity of the assumptions and models used in their determination of  $J_Q$ .

By focusing attention on  $a/w = 0.6$ , the fracture toughness/loading rate relationship of this steel can be further simplified. A linear function that spans eight orders of magnitudes of  $\dot{J}_Q$  loading can be used to approximate this relationship in the form:

$$J_Q = 62 - 8.2 \log (\dot{J}_Q) \quad \text{for } 10^{-1} < \dot{J}_Q < 10^7$$

with  $J_Q$  in units of  $\text{kJ/m}^2$  and  $\dot{J}_Q$  in units of  $\text{kJ/m}^2\text{s}^{-1}$

From Fig. 5.2, it is seen that the macroscopic  $J_Q$  values for the dynamic loading tests are quite low. These low  $J_Q$  values can be traced in part to the material model

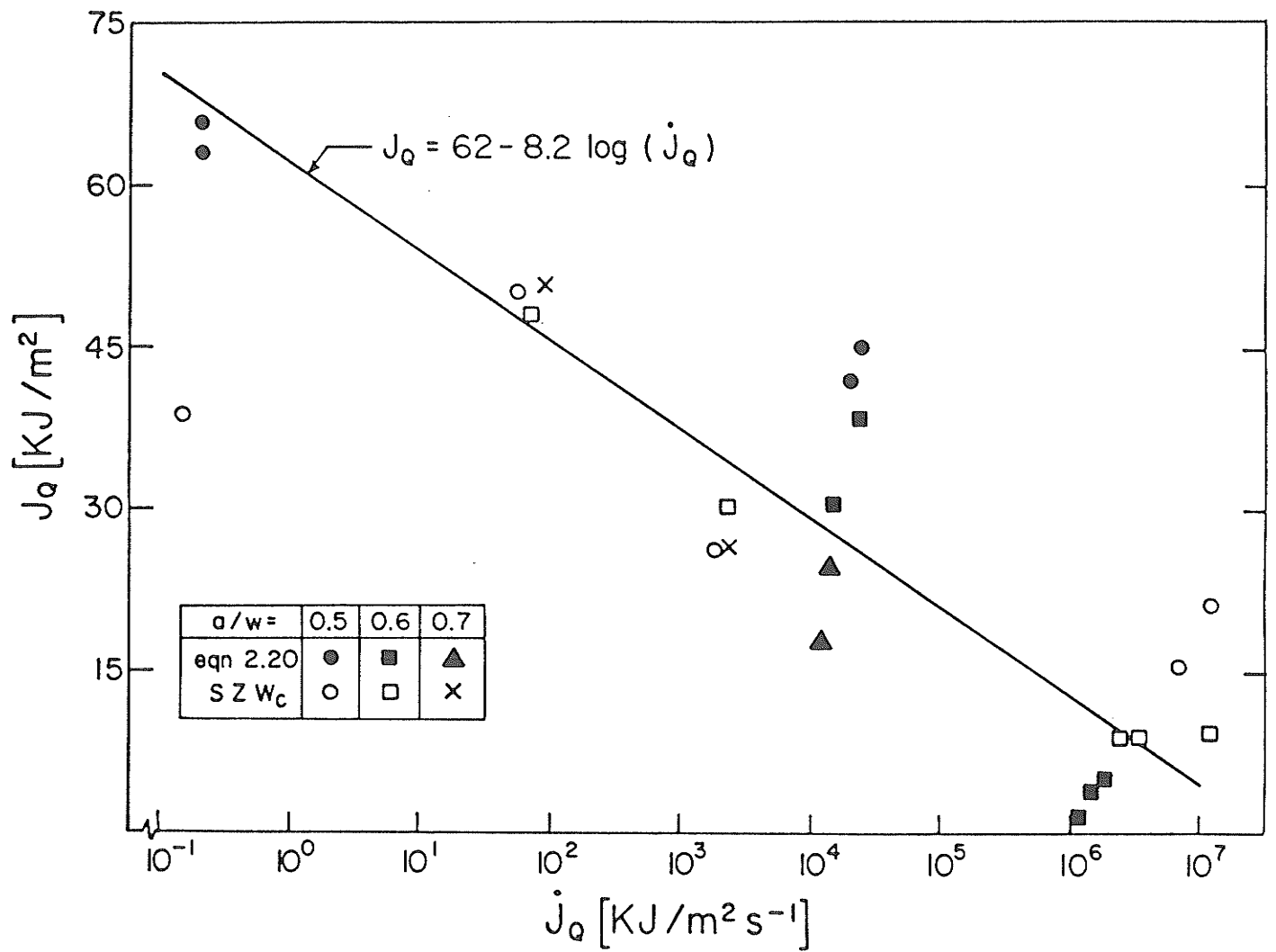


Figure 5.2 Comparison of macroscopic and microscopic methods of fracture toughness ( $J_Q$ ) determination.

used in their determination. In addition, these macroscopic dynamic  $J_Q$  values also depend on the choice of maximum load. These two topics will be covered in the next section under general test methodology.

#### 5.4 General Test Methodology

In this section, a general discussion on test methodology will be given. This discussion will cover the three main areas of 1) crack initiation detection using COD gage; 2) dynamic load/load-line displacement interpretation and 3) stretch zone width measurement. This general discussion will evaluate the data interpretation procedures used and point out some of the possible sources of errors associated with these procedures.

##### 5.4.1 Crack Initiation Detection using COD Gage

The use of a COD gage to detect the onset of crack initiation was seen to be ineffective for the quasi-static and slow speed single pull tests performed on the Instron test frame. The inability to detect crack initiation in these tests could be explained in terms of the available time for crack blunting. In essence, the COD gage measured any sudden change in the crack opening rate. The lack of a sudden COD-t slope change for these two Instron speeds meant the material around the crack tip had time to relax as the crack blunting process progressed.

For the case of Instron high speed loading, the

detection of a slope change implies a lack of strain relaxation around the crack tip, and points to a change in the crack blunting mechanisms at the crack tip as compared to the slower Instron tests. It is expected that this lack of strain relaxation is intensified at dynamic loading rates.

The relatively slow rate of loading during the Instron tests (quasi-static to high speed) means the crack initiation process for the Instron tests was the result of the physical separation of the two halves of the CTS due to the hydraulic actuator's movement, and not a stress wave phenomenon.

On the other hand, the crack initiation process in the dynamic tensile loading case was clearly a wave phenomenon. In this case, the COD gage is postulated to have measured the crack edges' average local particle velocity. This local particle velocity is caused by plastic stress waves in the vicinity of the crack edges (Eqn. 2.24). As COD\_CRIT is a function of the local particle velocity and therefore the stress state, COD\_CRIT directly relates to the critical time to fracture, and differs from the critical time based on maximum load by a constant factor related to specimen geometry considerations.

It is postulated that the COD gage was simply placed too far away from the crack tip to respond to the local straining at the crack tip. By being positioned on the specimen face, the COD gage only responded to the average physical translation of the crack faces due to the

substantial area that the gage was mounted on, and not the fracture process over the crack tip fracture process zone.

Based on a linear elastic perfectly plastic material model, one dimensional tensile waves travelling toward the free surface of the specimen crack tip would, at yielding, result in a local particle velocity of 15 m/s. This velocity, applied over the COD gage working range ( $\sim 1.5$  mm), yields an event time of 100  $\mu$ s. This corresponds well with the average COD\_CRIT time of 120  $\mu$ s, considering the fact that a complex wave reflection pattern existed within the specimen (a combination of the initial compression due to the elastic bending of the swing arm assembly and the nature of the incoming tensile wave). This same yield velocity, when applied near the crack tip, would obviously cause crack initiation in much less time since the region of interest is much smaller.

Analysis based on stretch zone results (table 4.3) indicates a dynamic COD/CTOD ratio of approximately 80X. This translates into a crack tip critical fracture time of 1.5  $\mu$ s, which compares very well with the experimental critical time of 1-2  $\mu$ s based on maximum load (table 4.2). In addition, the notch in the specimen tends to increase the local strain rate ahead of the notch, and thereby further affects the critical time at the crack tip.

The effects of local particle yield velocity on the COD signal is easily distinguishable from the natural background 60 Hz noise. A 60 Hz signal has a period of  $\sim 16$  ms vs the

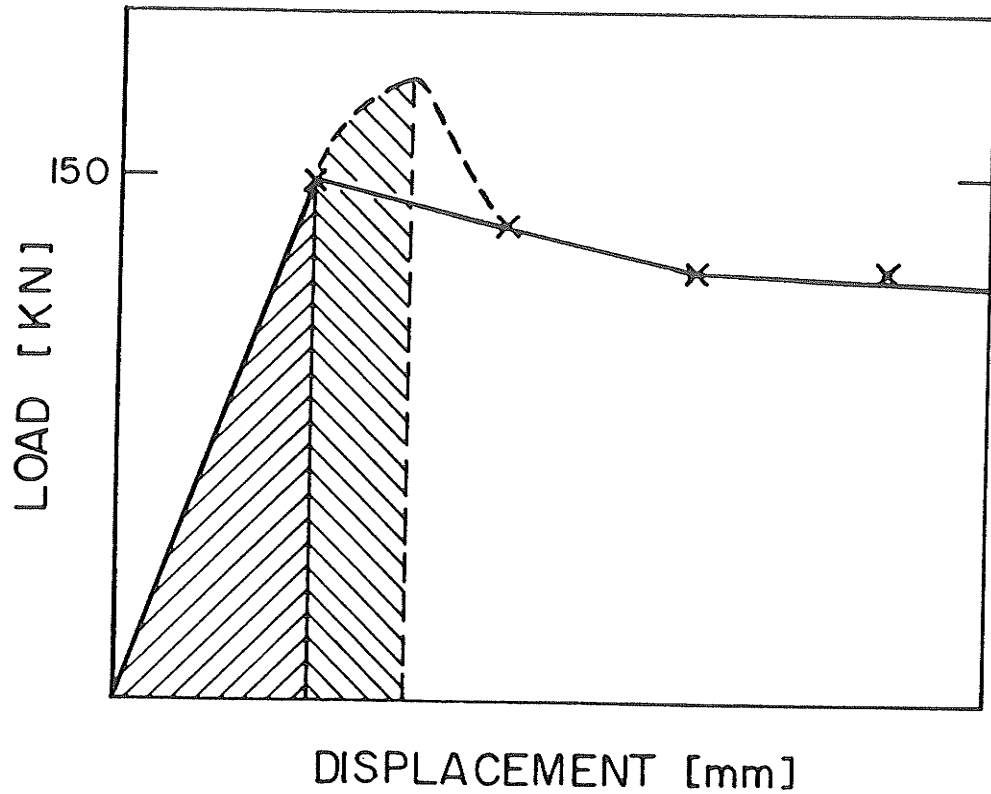
100  $\mu$ s associated with specimen yielding under maximum load. The background noise is seen very clearly in test #1's record (Appendix C).

#### 5.4.2 Dynamic Load/Load-line Displacement Interpretation

##### Material Modelling

In evaluating the dynamic  $J_Q$  values using the macroscopic(load/load-line displacement curve) method a modified linear elastic perfectly plastic model for the specimen material was used to arrive at a maximum dynamic fracture stress. This material model was used since the microscopic method of  $J_Q$  determination (Eqns 2.14, 3.13) is based on this model. Flow stress is used in place of yield stress to account for material strain hardening.

In the application of this model to analyze the dynamic load/load-line displacement curves, a linear interpolation between the origin and the maximum load point was used. With reference to Fig. 5.3, this interpolation procedure is seen to be necessarily conservative. The degree that this interpolation procedure underestimates the actual fracture energy  $J_Q$  depends on the degree of material strain hardening during the fracture process. A finer time resolution on the digital transient recorders used to record the load signals would be needed to more accurately determine the macroscopic  $J_Q$ .



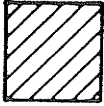
- 
 $J_Q$  based on maximum load of digitized load-displacement curve
- 
Portion of  $J_Q$  underestimated by digitized load-displacement curve

Figure 5.3 Underestimation of  $J_Q$  based on digitized load/load-displacement curve.

### Dynamic Material Properties

In addition to the choice of material model to account for material strain hardening, the dynamic  $J_Q$  values also depended on the value of the maximum dynamic fracture stress.

Equation 3.4 was used to account for the strain rate strengthening of material properties (yield and flow stresses) since it applies to quasi-statically ductile materials in general[75], and had been used in past work on AISI 1045 steel [48]. The choice of  $\beta = 0.018$  represents the only value referenced in the literatures[77]. In establishing the dynamic strain rate, it was necessary to assume a similar definition of gage length (27.5 mm) as that used in the Instron tests, and to use the particle velocity corresponding to the static flow stress (as a first estimate) to determine the dynamic strain rate. The resultant dynamic strain rate was therefore  $4 \times 10^2 \text{ s}^{-1}$ .

With the above analysis, the use of 150 kN as a maximum specimen fracture load was a reasonable assumption based on available data. The relatively good agreement between the macroscopic and microscopic results verifies the general validity of the analysis used.

Nevertheless, a better understanding of the dynamic tensile properties of the test material through additional experimentation is needed to enhance the accuracy of the analysis. The generally lower values of the macroscopic  $J_Q$  points to a need to verify the use of  $\beta = 0.018$  and a dynamic strain rate of  $10^2 \text{ s}^{-1}$ .

The dynamic strain rate was determined assuming the same definition of strain rate applies equally to the slower Instron tests and the stress wave loading tests. At present, there is no agreed upon quasi-static or dynamic strain rate definition for the CTS, and therefore the definition used in this work represents a necessary assumption. However, it seems reasonable to assume that the dynamic strain rate used in this work was a conservative estimate. This assumption is based on the fact that with stress wave loading, material outside the crack tip region was not able to respond to the straining at the crack tip as quickly as the slower speed Instron tests, and therefore the actual strain rate should be higher than assumed.

Of equal importance in influencing the dynamic material properties of the specimen material were the stress intensification effects of the notch. As explained by Dieter [75], the general yield stress of the notched specimen (based on Tresca's yield criterion) was higher than the uniaxial yield stress due to the confining nature of triaxial stresses on the plastic zone, while the basic material yield stress remained unchanged. In addition, depending on the striker velocity or the applied strain rate, the notch's stress intensification effects were greater for the brittle fracture than the ductile fracture case.

### 5.4.3 Stretch Zone Measurement

There is no doubt that stretch zone measurement is a valid fracture characterizing parameter. The fact that it too exhibits the well known qualitative strain rate and a/w effects validates its use. However, it is important to appreciate the potential sources of errors in using SZ measurements for this work.

Stretch zone measurement depends on subjective interpretation or operator dependency. The first basic dependency is the operator's choice of a representative stretch zone for measurement. As stretch zone is known to vary from  $\pm 25-50\%$  in width, the choice of the stretch zone location is therefore a source of error.

Secondly, the choice of SEM magnification determines the extent the details of the fracture surface appear and consequently the choice of the stretch zone.

Thirdly, the conventional approach of using arithmetic averages of stretch zone widths, based on an arbitrary sample size and sample selection, is also a source of error.

Finally, a ductile or brittle fracture mode carries with it different amount of SZ measurement errors. Contrary to the relatively sharp outline of the SZ in the case of brittle fracture, ductile fracture results in a very jagged SZ outline. Stereoscopic pictures are of limited help in this case due to the extreme unevenness of ductile fracture surfaces. Depending on the extent of ductile tearing near the stretch zone, this image enhancement method may be relatively ineffective.

Notwithstanding the above criticisms of the stretch zone measurement method of fracture toughness determination, its use in fracture toughness testing is unquestionably needed. As an investigative tool aimed at the fracture surface, stretch zone measurement represents the most direct record of the fracture process. Any quantitative fracture parameter must therefore be able to reflect the changes in stretch zone appearance as a function of the testing variables.

#### 5.5 Relevance and Application of $J_Q$ to Fracture Mechanics

One of the current issues in the field of dynamic fracture study is whether a one parameter, macroscopic dynamic fracture toughness value exists. To answer this question, it is helpful to briefly review the principles behind current static fracture toughness parameters.

In the case of static loading, the use and validity of both  $K_{IC}$  and  $J_{IC}$  have been firmly established both theoretically and experimentally.  $K_{IC}$  is essentially an ideal, critical stress/crack size limiting parameter that accounts for the breaking of atomic bonds in materials without significant plasticity. In design situations, a geometric factor,  $\alpha$ , is added onto this necessarily conservative value to yield critical design stresses.

The use of  $J_{IC}$  as a fracture parameter is based upon the same philosophy, except that  $J$ 's formulation is based on a minimal energy requirement for fracture. In practice,  $J_{IC}$  is converted into an equivalent  $K_{IC}$  value and used to

approximate the design stresses needed.

One is then inclined to say that a parallel situation of dynamic  $K_s$  and  $J_s$  may exist for the dynamic loading situation. However, stress wave loading introduces more complex theoretical questions which can be considered only for a very limited number of geometries and boundary conditions, and poses numerous additional problems in terms of the experimental evaluation of a dynamic fracture parameter.

Fundamentally, fracture involves the initial breaking of atomic bonds. Therefore, a global energy consideration is valid for crack initiation for cases of quasi-static to stress wave loading. The question is then how one accounts for the different modes of wave loading when stress waves impinge upon a crack front. The mathematical answer to the above question lies in the realm of applied mechanics. Experimentally, it is possible to obtain this global, critical fracture energy parameter without full understanding of the stress wave history involved. This present work has demonstrated that  $J_Q$  is indeed a fracture parameter capable of characterizing quasi-static to dynamic loading.

From a design point of view, the key to any static/dynamic fracture parameter is not to just obtain a unique, characteristic number that is sufficient in differentiating the varying degrees of fracture toughness in materials (like a Charpy number), but a number that can also

be related back to some design stress based on a critical material loading condition (like a  $K_{IC}$ ).

Presently, there is no research work in progress to systematically evaluate the accuracy in converting  $J_{IC}$  into  $K_{IC}$  for design work. Similarly, the use of dynamic  $K_{IC}$  value,  $K_{ID}$ , is without analytic or design verification.

Consequently, the use of the author proposed dynamic fracture parameter,  $J_Q$ , also awaits such design verification. However, since  $J_Q$  is a critical fracture energy parameter similar to the static J-integral, a reasonable first approximation would be to likewise convert  $J_Q$  values to K values for design purposes.

CHAPTER SIX

CONCLUSIONS

The success of the present experimental fracture toughness testing procedure that utilizes tensile loading and stress triaxiality to characterize quasi-static to stress wave induced fracture has been demonstrated.

Specifically, standard ASTM compact tension specimens were loaded in simple tension, at rates ranging from quasi-static to stress wave loadings, using a standard servo-hydraulic test frame and an original stress wave loading arrangement based on a modified compression Split Hopkinson bar. The load during testing was monitored by a load cell for the servo-hydraulic test frame case and by instrumented loading grips in the stress wave loading arrangement. Crack initiation and load-line displacement at all speeds were determined using a specimen face-mounted high frequency crack opening displacement gage.

Fracture toughness based on this testing procedure is expressed in terms of a characterizing fracture energy parameter,  $J_Q$ , derivable from either the load/load-line displacement test record or from a microscopic examination of the fracture surface's stretch zone using scanning electron microscopy. The loading rate during testing is expressed in terms of  $\dot{J}_Q$ , the fracture energy parameter divided by the crack initiation time.

A study of the variation of fracture toughness,  $J_Q$ , of an AISI 1045 steel in the annealed condition, with loading rates ranging from quasi-static to stress wave loading, was undertaken using compact tension specimens of three different a/w ratios (0.5,0.6,0.7). The experimental

results based on stretch zone measurements and load/load-line displacement records both indicate a significance decrease in fracture toughness for this steel at high loading rate. In addition, fracture toughness is seen to decrease with increasing  $a/w$  ratio for these two methods of fracture toughness determination. However, fracture toughness based on stretch zone measurements indicates a lesser dependence on specimen  $a/w$  ratio than the method of load/load-line displacement records.

Notwithstanding the success of this prototype, improvements can be made in crack initiation detection and crack tip displacement calculations. Modifications to the present dynamic test setup are needed to strengthen it against impact loads and to minimize the experimental errors and uncertainties. Efforts should be made to improve the applicability of one-dimensional wave theory.

Further experimentations are needed to improve the modelling accuracy of the dynamic tensile properties used in stress wave analysis. In particular, a more accurate estimate of the dynamic yield strength of the test material is needed.

## REFERENCES

1. Airy, G.B., Brit. Assoc. Advance., Sci. Rept. (1862).
2. Inglis, C.E., Trans. Instn. Nav. Archit., LV, 1, 219(1913).
3. Westergaard, H.M., J. Appl. Mech., 4, 49(June, 1939).
4. Griffith, A.A., Trans. Royal Society of London (1920) A-221.
5. Orowan, E., Trans. Inst. Engrs. Shipbuilders Scotland, 89, 165(1945).
6. Irwin, G.R., 9th Inter. Congr. Appl. Mech., VIII, Paper 101(II), University of Brussels, 245(1957).
7. Douglas, D.S., Journal of Mechanics and Physics of Solids, Vol. 8 (1960) 100-104.
8. Cottrell, A.H., Iron and Steel Institute Spec. Rep., 69, 281(1961).
9. Wells, A.A., Crack Propagation Symposium Proceedings, Cranfield College of Aeronautics 1, 210 (1961).
10. Knott, J.F., Fundamentals of Fracture Mechanics, Wiley, New York (1973).
11. Dawes, M.G., ASTM STP 668 (1979).
12. Krasowsky, A.J., Vainshtok, V.A., Int. J. of Fracture, Vol. 17, No. 6 (December 1981).
13. de Castro, P.M.S.T, Spurrier, J., Hancock, P., ASTM STP 677 (1979).
14. Spitzig, W.A., ASTM STP 453 (1969).
15. Nguyen-Duy, P., Bayard, S., J. Eng. Mater. Technol, 103 (1981).
16. JSME Standard Method of Test for Elastic-Plastic Fracture Toughness  $J_{IC}$ , JSME Standard, s001-1981.
17. Rice, J.R., Trans. ASME, J. Appl. Mechanics, Vol. 35 (1968) 379-386.
18. Paris, P.C., ASTM STP 631 (1977) 3-27.
19. Rice, J.R., Rosengren, G.F., J. Mech. Phys. Solids, (1968) Vol. 1, 1-13.

20. Hutchinson, J.W., J. Mech. Phys. Solids, (1968) Vol. 16, 13-31.
21. McClintock, F.A., Fracture, Liebowitz, H. Ed., Vol. 3, Academic Press, New York, 147 (1971).
22. Landes, J.D., Begley, J.A., ASTM STP 514, (1972), 24-39.
23. Rice, J.R., Paris, P.C., Merkel, J.G., ASTM STP 536, (1973) 231-245.
24. Clark, G.A., Landes, J.D., Journal of Testing and Evaluation, JTEVA, Vol. 7, No. 5, (Sept. 1979), 264-269.
25. Sih, G.C., Modelling Problems in Crack Tip Mechanisms, CFC10, University of Waterloo, August 24-26, 1983, 65-89.
26. Penelon, A., Bassim, M.N., Dorlot, J.M., ASTM STP 677, (1979), 449-462.
27. ASTM Standards E399.
28. Gudas, J.P., Joyce, J.A., Davis, D.A., ASTM STP 677, (1979), 474-485.
29. Adams, N.J.I., Munro, H.G., Engineering Fracture Mechanics, (1974), Vol. 6, 119-132.
30. Kalthoff, J.F., Shockey, D.A., Homma, H., Inst. Phys. Conf. Ser. No. 70, 3rd Conf. Mech. Prop. High Rates of Strain, Oxford 1984, 205-211.
31. Johnson, W., Impact Strength of Materials, Edward Arnold (Publishers) Limited, London (1972).
32. Achenbach, J.D., Mechanics Today, Vol. 1, 1972, Nemat-Nasser, S. Ed., Pergamon Press, (1974).
33. Clifton, R.J., Mechanics Today, Vol. 1, 1972, Nemat-Nasser, S. Ed., Pergamon Press, (1974).
34. Freund, L.B., J. Mech. Phys. Solids, Vol. 20, (1972), 129-140.
35. Freund, L.B., J. Mech. Phys. Solids, Vol. 20, (1972), 141-152.
36. Freund, L.B., J. Mech. Phys. Solids, Vol. 21, (1973), 47-61.

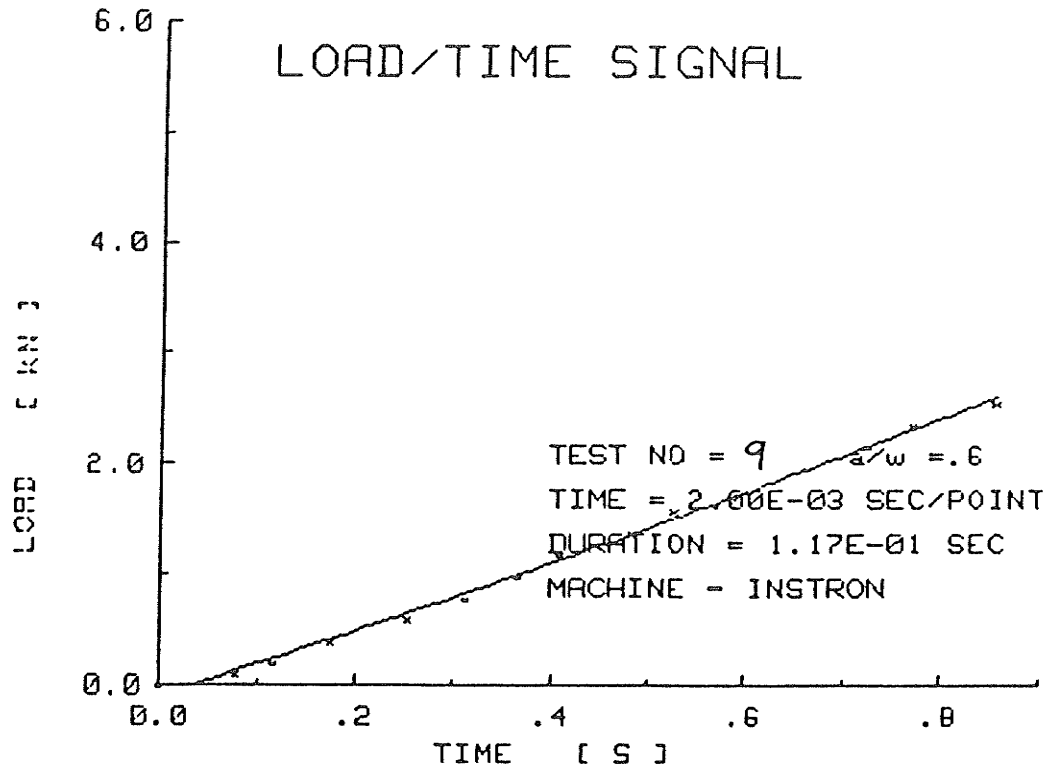
37. Freund, L.B., Hutchinson, J.W., High Strain-Rate Crack Growth in Rate-Dependent Plastic Solids, Division of Applied Sciences, Harvard Univeristy, (June 1984), MECH-53.
38. Freund, L.B., Douglas, A.S., J. Mech. Phys. Solids, Vol. 30, No. 1/2, (1982), 59-74.
39. Rice, J.R., Proc. 1st. Int. Conf. Fracture, T. Yokobori et al. (eds.), Vol 1, Japanese Soc. for Strength and Fracture, Tokyo, (1966), 282-308.
40. Barenblatt, G.I., Entov, V.M., Salganik, R.L., Inelastic Behavior of Solids, M.F. Kanninen et al. (eds.), McGraw-Hill, (1970), 559-584.
41. Rice, J.R., Proc. 8th U.S. National Congres of Applied Mechanics, UCLA (New York: ASME) (1978) 191-216.
42. Kishimoto, K., Aoki, S., Sakata, M., Engineering Fracture Mechanics, Vol. 13, (1980) 841-850.
43. Nilsson, F., Inst. Phys. Conf. Ser. No. 70, 3rd Conf. Mech. Prop. High Rates of Strain, Oxford 1984, 185-204.
44. Klepoczko, J.R., (1982), J. Eng. Matls. and Tech. 104, 29.
45. Eftis, J., Krafft, J.M., J. Basic Eng. (1965), 86, 257.
46. Radon, J.C., Turner, C.E., J. Iron Steel Inst., 204, 842, (1966).
47. Costin, L.S., Duffy, J., Freund, L.B., ASTM STP 627, (1977), 301-318.
48. Joyce, J.A., NUREG/CR-2274 (Washington: USNRC), (1981), 1-37.
49. Joyce, J.A., Proc. CSNI Specialists Workshop on Ductile Fracture Methods Paris (Paris: OECD), (1982), 517-537.
50. Bayoumi, M.R., Ph.D. thesis, University of Manitoba, (1984).
51. Rogers, H.C., Shastry, C.V., Proc. Conf. on Shock Waves and High Strain Rate Phenomena in Metals, Plenum Press, New York, ch. 18, 285-298.
52. Duffy, J., Mechanics of Material Behavior, Dvorak, G.J. et al (eds.), Elsevier Science Publishers B.V., Amsterdam, (1984).
53. Clifton, R.J., Duffy, J., Hartley, K.A., Shawki, J.G., Scripta Metallurgica, Vol. 18, (1984), 443-448.

54. ASTM Standards, pt. 31, (1969), Designation E23-566.
55. Pellni, W.S., Weld. J., Vol. 50, pp. 915-1095, 147s-162s, (1971).
56. Hopkinson, B., Phil. Trans. Roy. Soc. (London), Ser. A, 213, (1914), 437.
57. Kolsky, H., Proc. Phys. Soc. (London), Ser. B., 62, (1949), 676.
58. Davis, R.M., Phil. Trans. A., 240, (1948), 375.
59. Clifton, R.J., Shock Waves in Condensed Matter, Asay, J.R. et al (eds.), ch. 3, (1983), 105-111.
60. Gorham, D.A., Inst. Phys. Conf. Ser. No. 47, (1979).
61. Campbell, J.D. et al, Battelle Collog. on Fundamental Aspects of Structural Alloy Design, Jaffe R.I. et al (eds.), New York: Plenum, (1977), 545-563.
62. Costin, L.S., Duffy, J., J. Eng. Mat. Technol., Vol. 101, (July 1979), 258-264.
63. Hartley, K.A., Duffy, J., Inst. Phys. Conf. Ser. No. 70, 3rd Conf. Mech. Prop. High Rates of Strain, Oxford 1984, 21-30.
64. Albertini, C., Montagnani, M., Inst. Phys. Conf. Ser. 47, (1979).
65. Paris, P.C., Bucci, R.J., Loushin, L.L., ASTM STP 559, (1974), 86-98.
66. Bassim, M.N., Klepaczko, J.R., Hsu, T.R., Engineering Fracture Mechanics (1983).
67. Corran, R.S.J., Benitez, F.G., Ruiz, C., Nojima, T., "Towards the Development of a Dynamic Fracture Initiation Test", private communication.
68. Corran, R.S.J., Benitez, F.G., Harding, J., Ruiz, C., Inst. Phys. Conf. Ser. No. 70, 3rd Conf. Mech. Prop. High Rates of Strain, Oxford 1984, 253-260.
69. ASTM Standards E813-85.
70. Landes, J.D., Begley, J.A., ASTM STP 560 (1974) 170-186.
71. Saxena, A., Hudak, S.J., Int. J. Fracture, Vol. 14, No. 5, (Oct. 1978), 453-467.

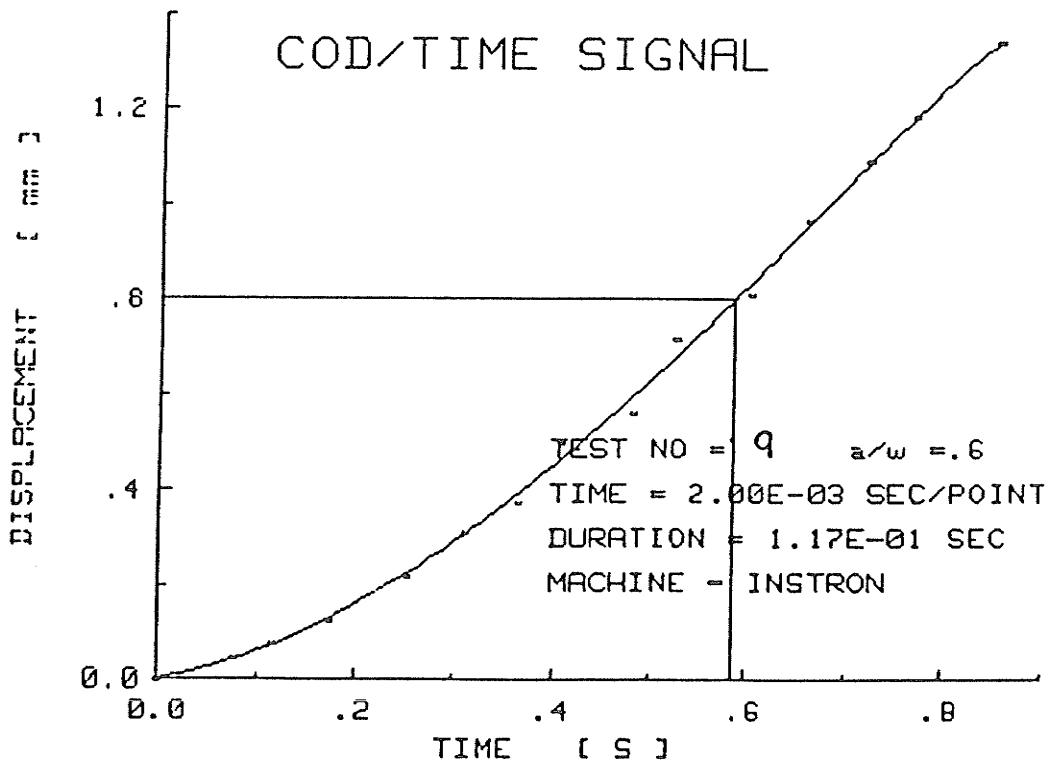
72. Klepaczko, J.R., Inst. Phys. Conf. Ser. No. 70, 3rd Conf. Mech. Prop. High Rates of Strain, Oxford 1984, 245-252.
73. Klepaczko, J., Proc. Inst. Phys. Conf., Serv. No. 47, Bristol (1979) 201-204.
74. Andrzejewski, A., Klepaczko, J., Pluvillage, G., Proc. Inst. Conf. on Analytical and Experimental Fracture Mechanics, Rose, Italy (1980).
75. Dieter, G.E., Mechanical Metallurgy, 2nd ed., McGraw-Hill Book Company, (1976).
76. Orowan, E., Inst. Eng. Shipbuild. Scot., Vol. 89, (1945), 165.
77. Klepaczko, J., Technical Report, No. DMR-79-2325712, Brown University, Providence (April, 1981).
78. Nicholas, T., Experimental Mechanics, 21(5), 177-185, (May, 1981).
79. Ross, C.A., Cook, W.H., Wilson, L.L., Experimental Techniques, (November 1984), 30-33.
80. Bayoumi, M.R., Bassim, M.N., J. Engineering Fracture Mechanics (1983), Vol. 18, No. 3, 679-691.
81. Bayoumi, M.R., Bassim, M.N., Proc. Int. Conf. Matls, ICM4, Stockholm, Sweden (1983), Vol. 2, 803-811.
82. Bayoumi, M.R., Bassim, M.N., J. Testing and Evaluation (1983), Vol. 12, No. 5, 316-322.

APPENDIX A

SLOW SPEED INSTRON TEST RESULTS

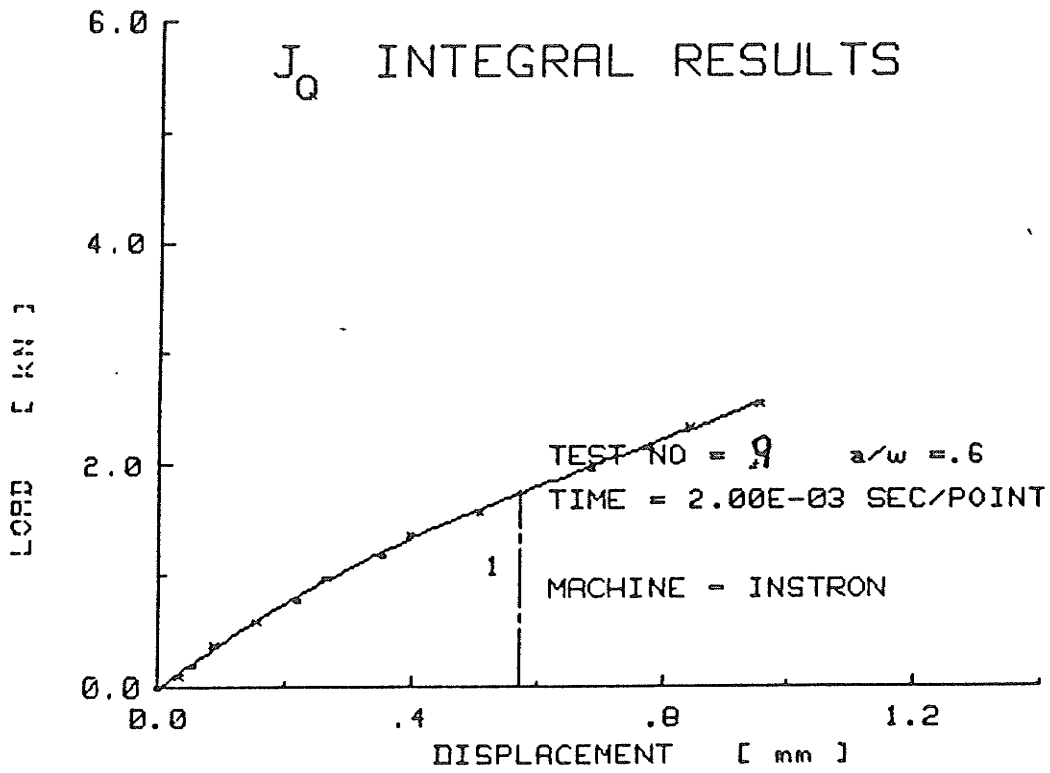


LSF OF ORDER 2       $Y = C1+C2*X+C3*X^2+...$

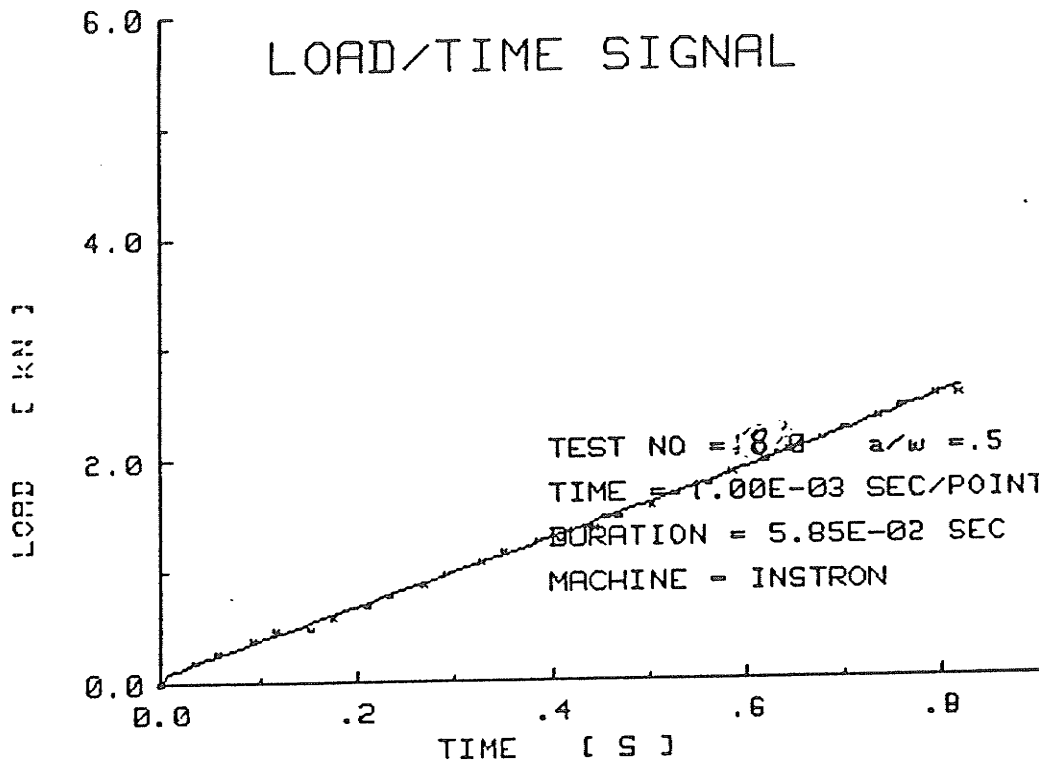


LSF OF ORDER 8       $Y = C1+C2*X+C3*X^2+...$   
 $T\_CRIT( 1 ) = 5.87E-01$  SEC

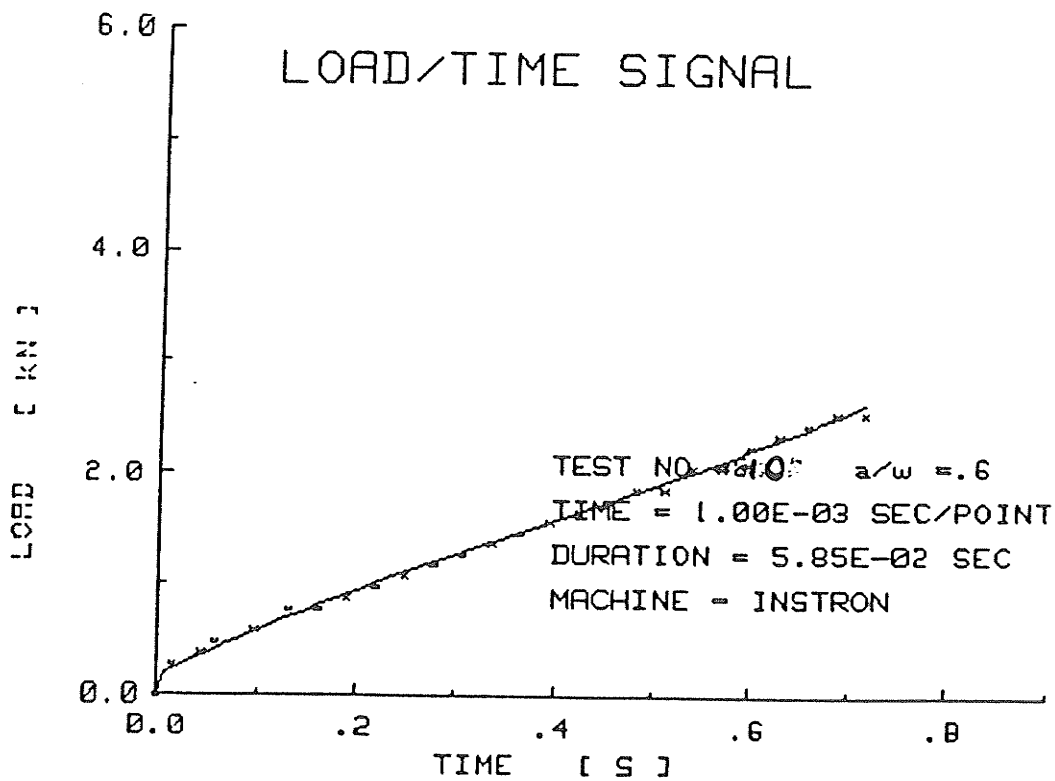
# J<sub>Q</sub> INTEGRAL RESULTS



LSF OF ORDER 3       $Y = C1+C2*X+C3*X^2+...$   
JQ( 1 ) = 4.77E+00 kN/m      COD\_CRIT 1 = 5.71E-01 mm  
T\_CRIT 1 = 5.07E-01 SEC



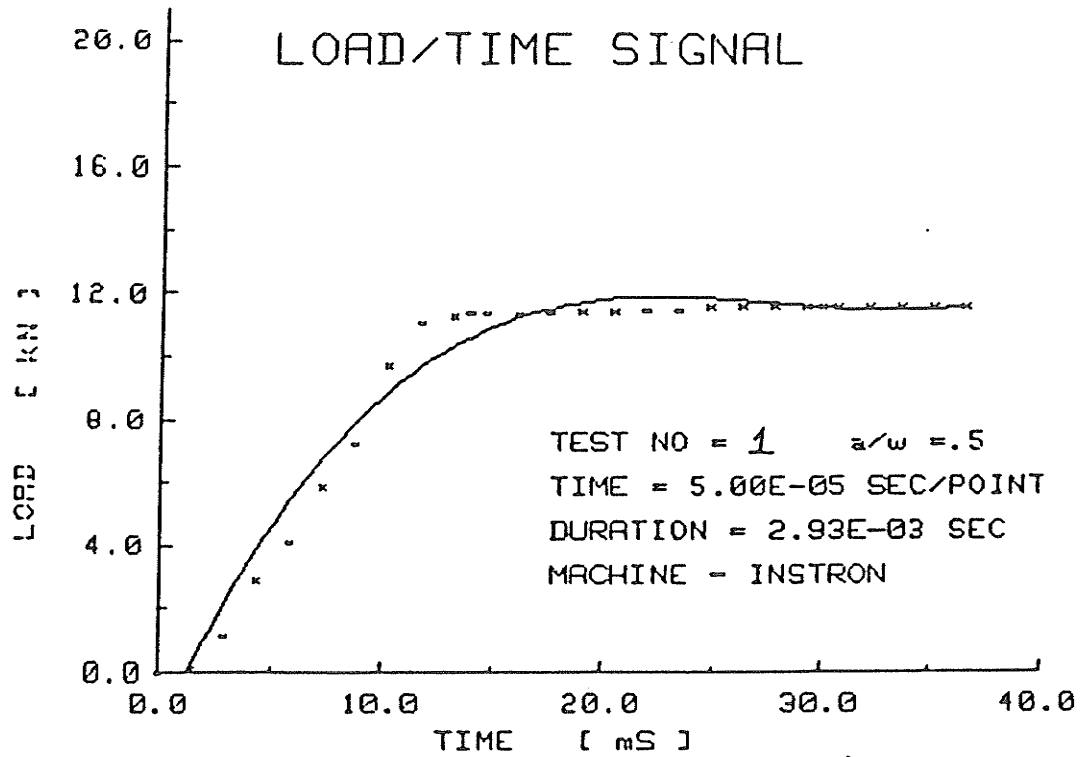
LSF OF ORDER 3       $Y = C1+C2*X+C3*X^2+...$



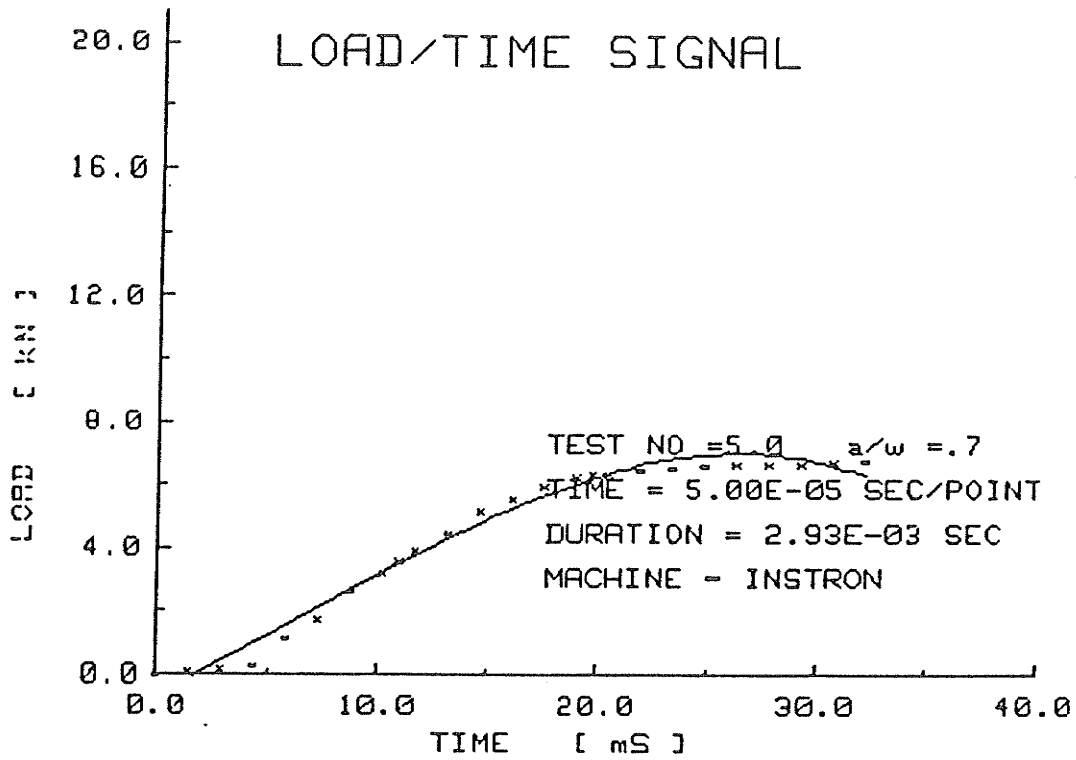
LSF OF ORDER 3       $Y = C1+C2*X+C3*X^2+...$

APPENDIX B

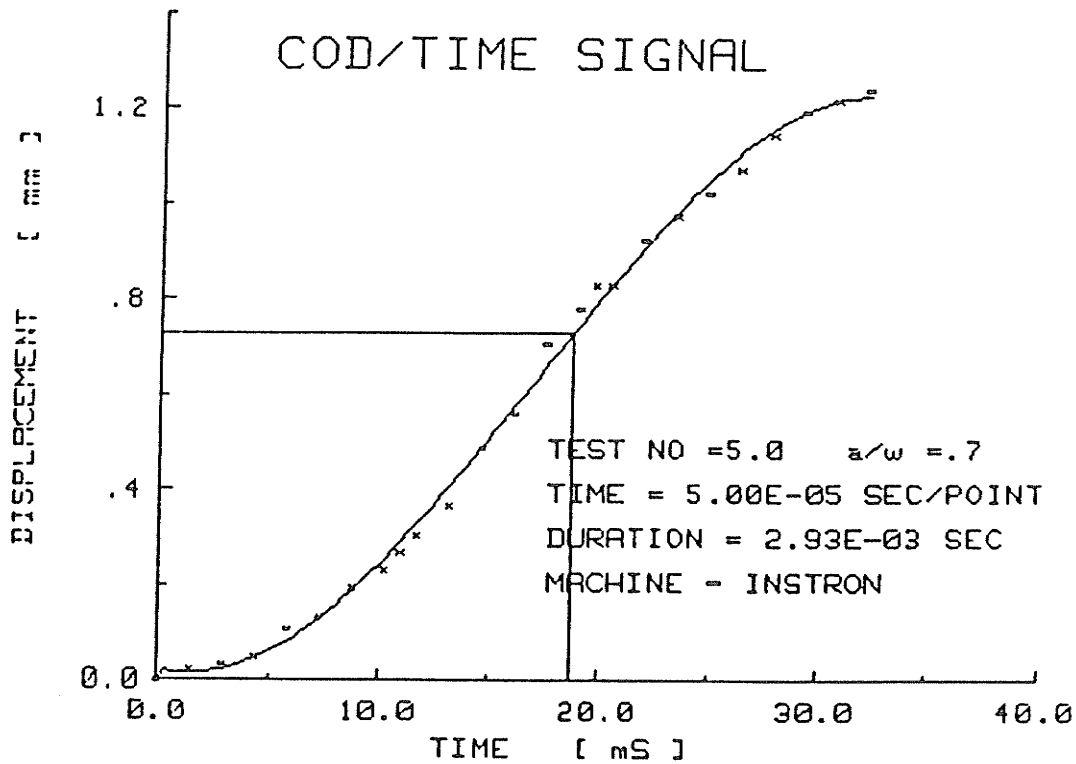
HIGH SPEED INSTRON TEST RESULTS



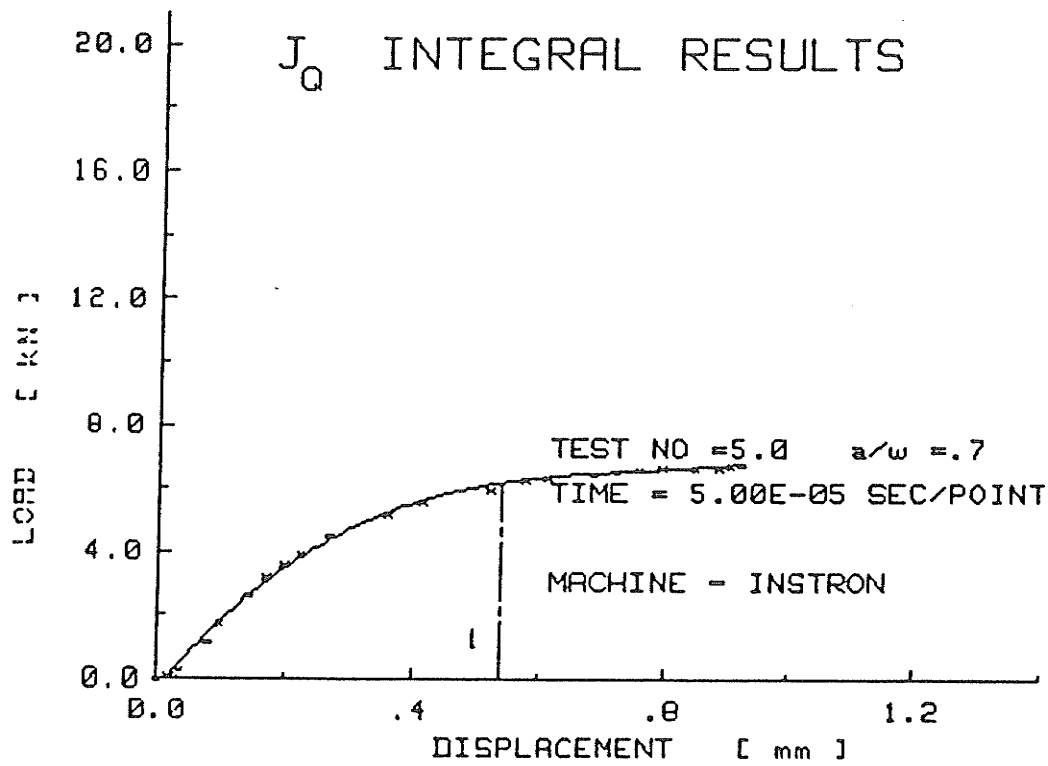
LSF OF ORDER 3      $Y = C1+C2*X+C3*X^2+...$



LSF OF ORDER 3      $Y = C1+C2*X+C3*X^2+...$



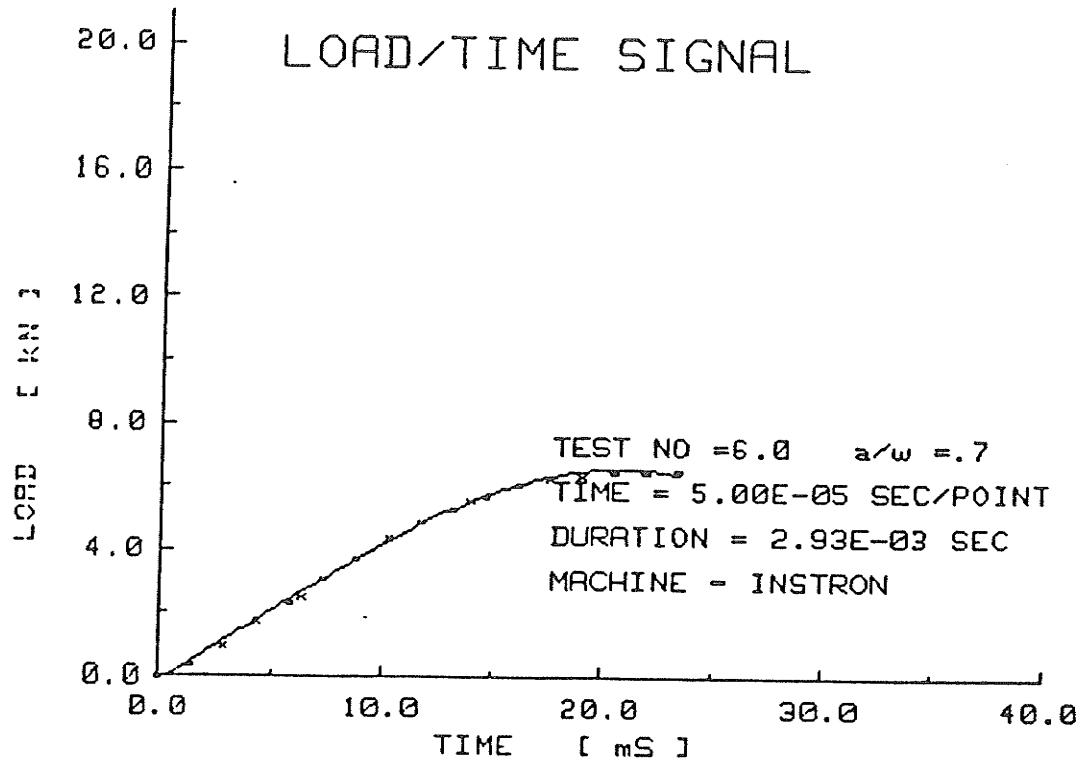
LSF OF ORDER 3      $Y = C1+C2*X+C3*X^2+...$   
 T\_CRIT( 1 ) = 1.87E-02 SEC



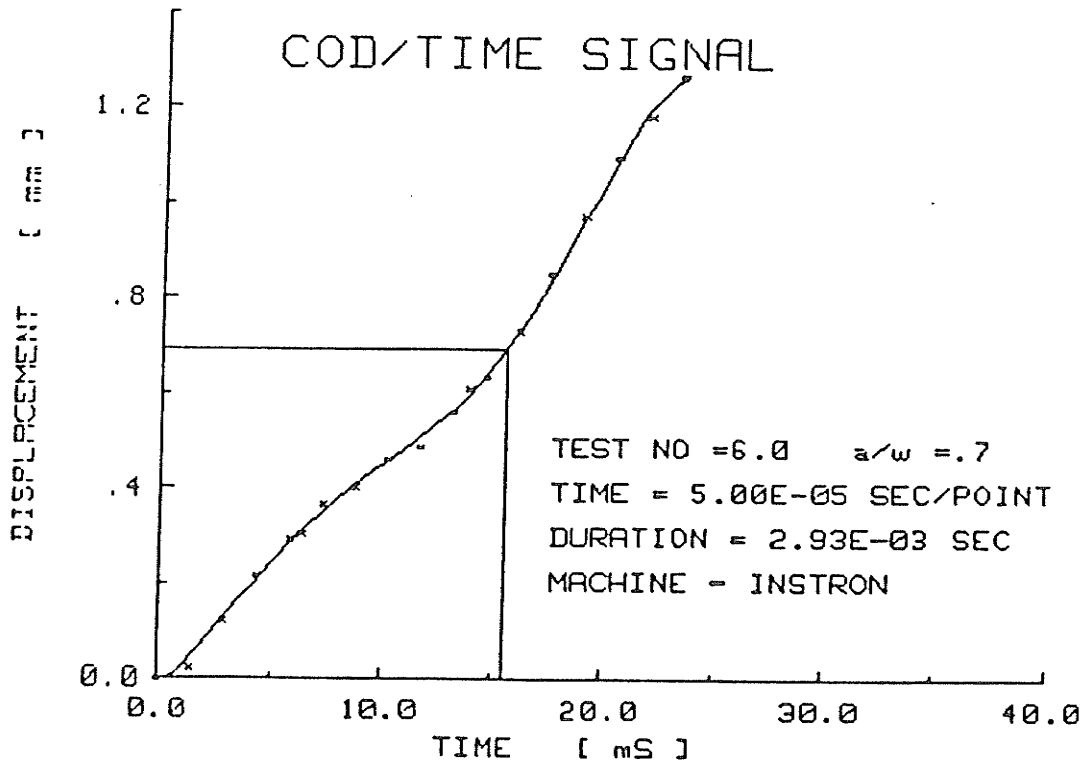
LSF OF ORDER 3      Y = C1+C2\*X+C3\*X^2+...

J0( 1 )      2.39E+01 kN/m

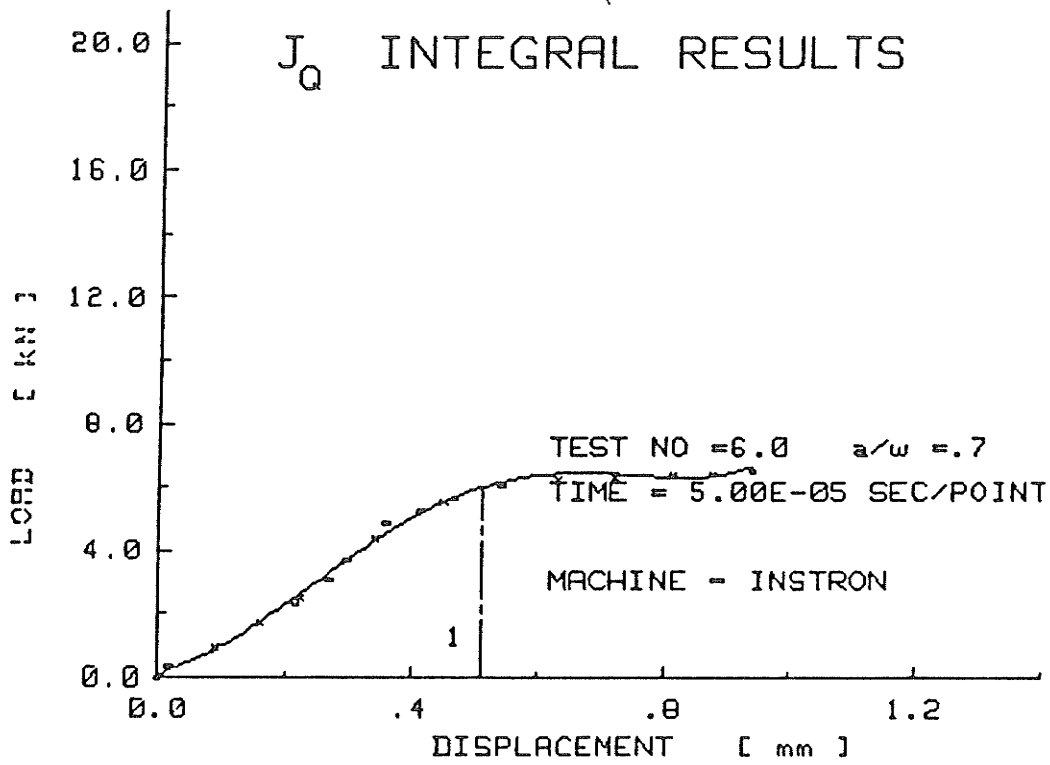
T\_CRIT 1 = 1.87E-02 SEC      COO\_CRIT 1 = 5.41E-01 mm



LSF OF ORDER 3     $Y = C1+C2*X+C3*X^2+...$



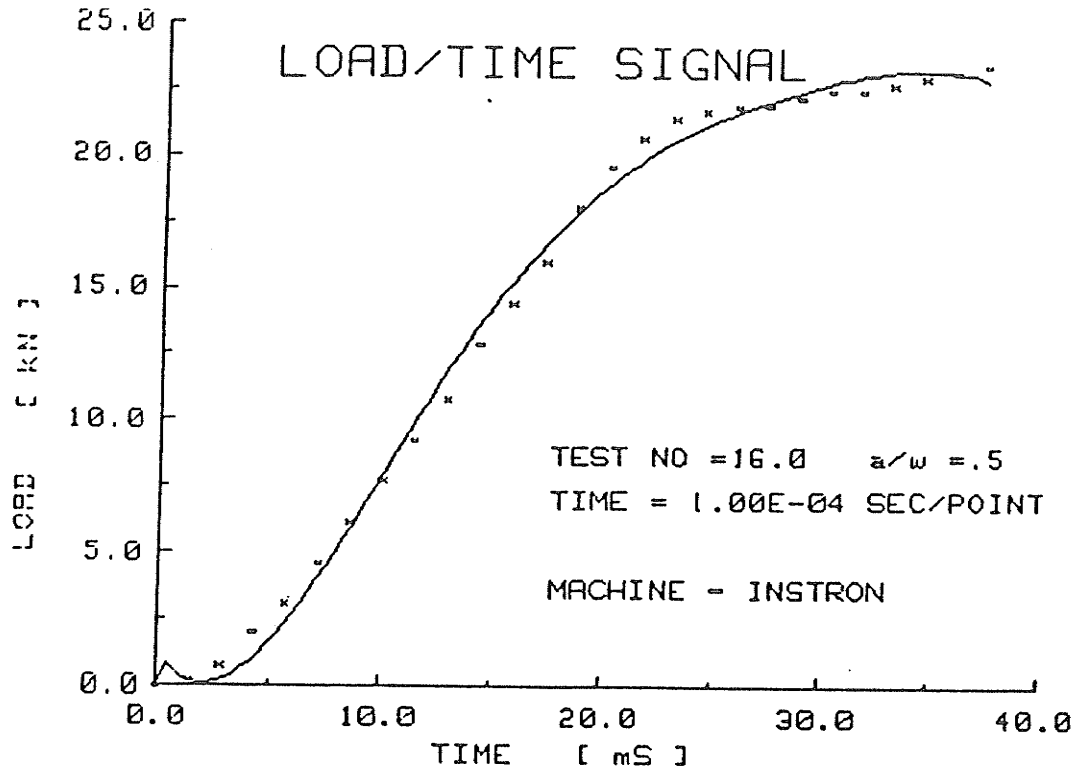
LSF OF ORDER 8     $Y = C1+C2*X+C3*X^2+...$   
 T\_CRIT( 1 ) = 1.55E-02 SEC



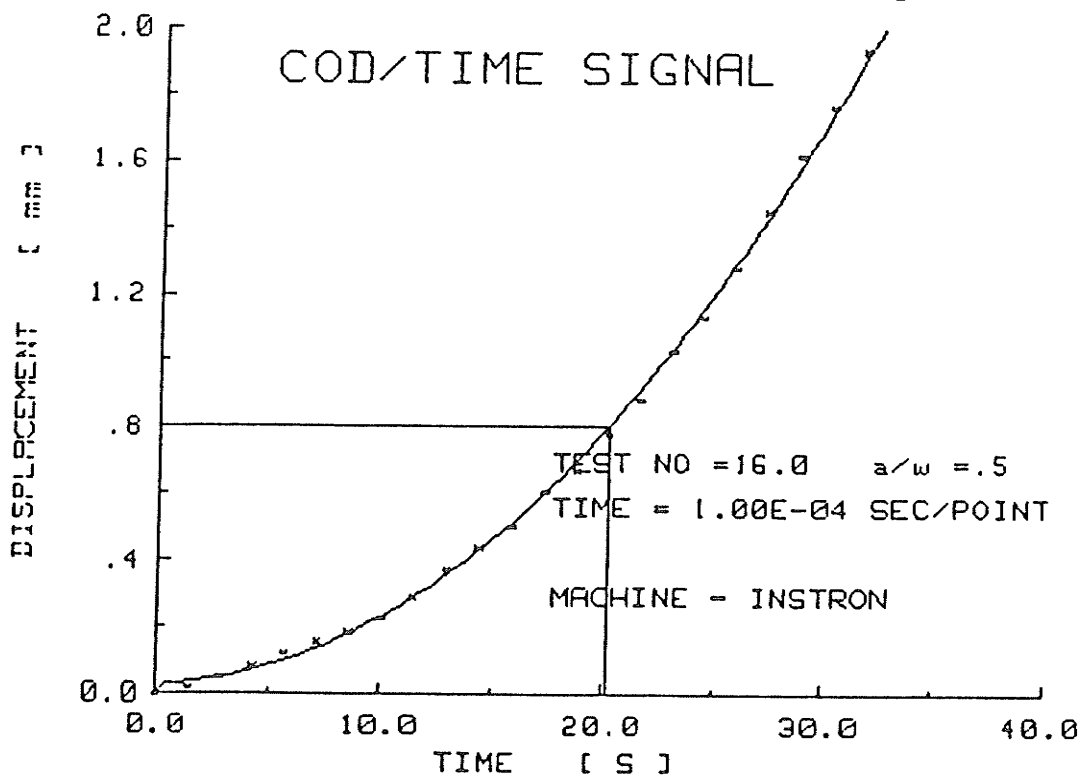
LSF OF ORDER 5      Y = C1+C2\*X+C3\*X^2+...

JQ( 1 )      1.78E+01 kN/m

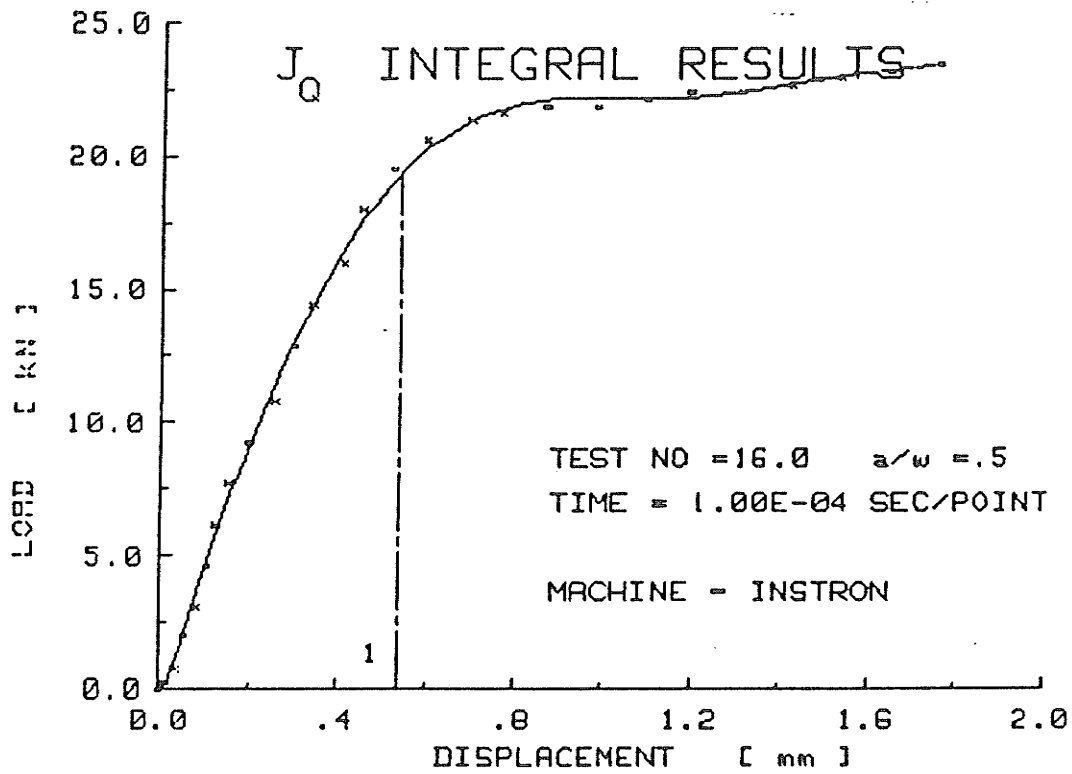
T\_CRIT 1 = 1.55E-02 SEC      COO\_CRIT 1 = 5.11E-01 mm



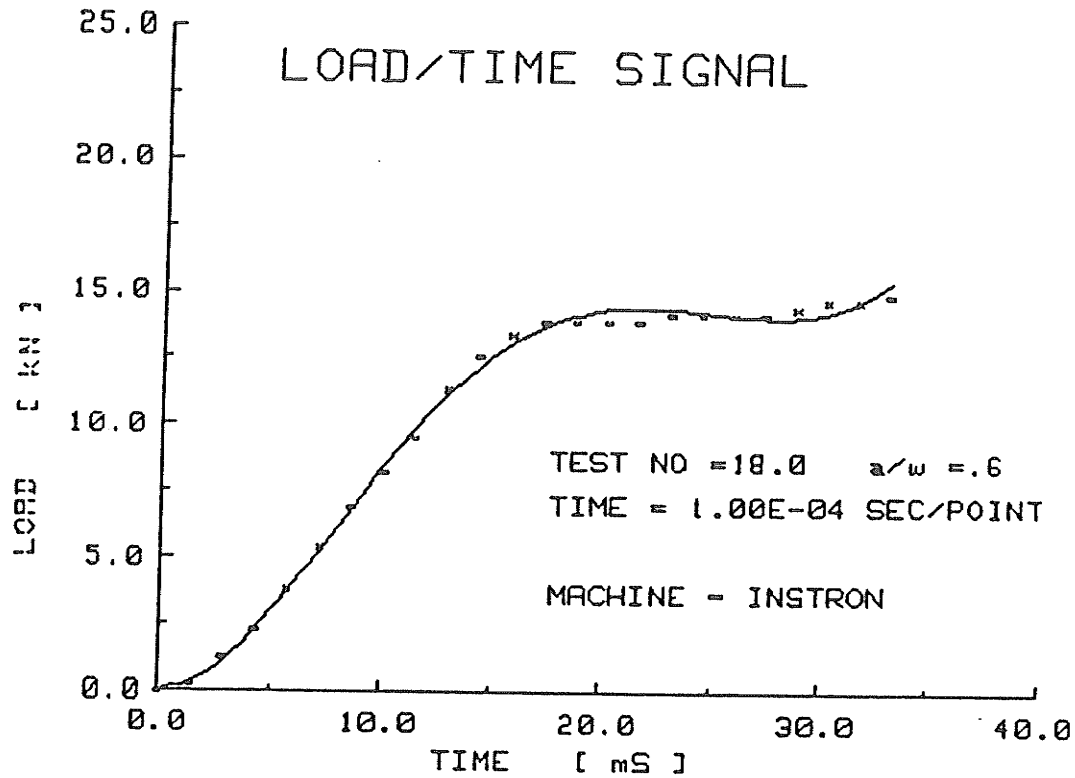
LSF OF ORDER 5     $Y = C1+C2*X+C3*X^2+...$



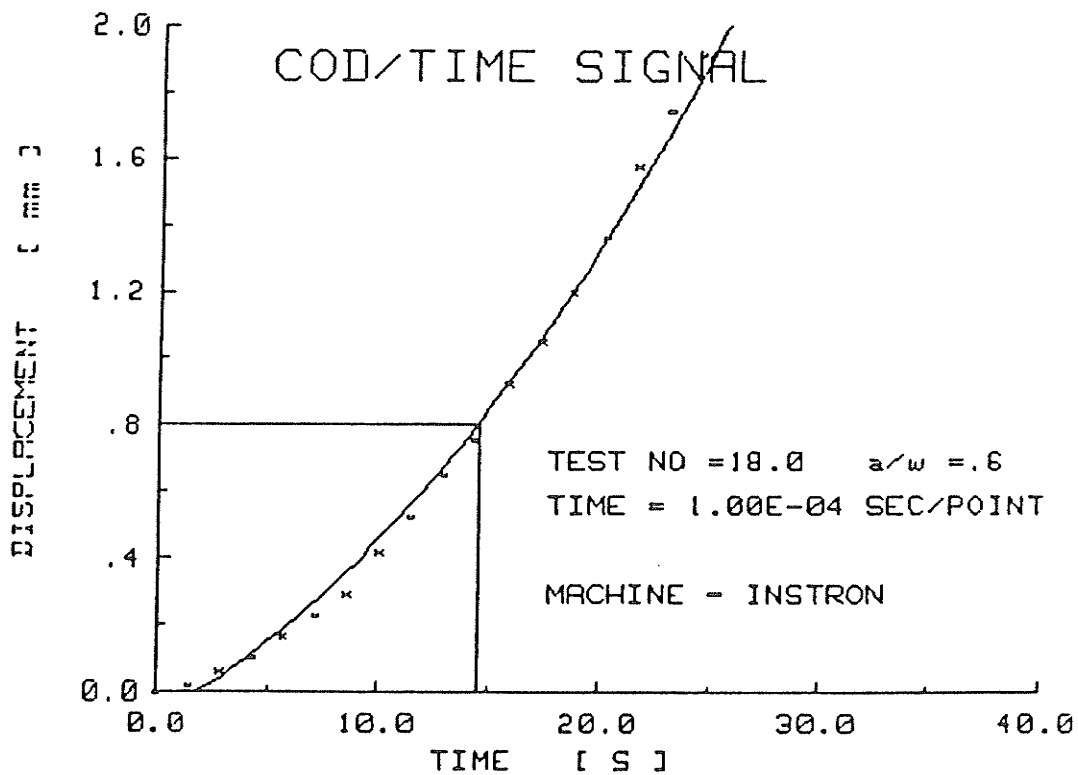
LSF OF ORDER 2     $Y = C1+C2*X+C3*X^2+...$   
 T\_CRIT( 1 ) = 2.02E-02 SEC



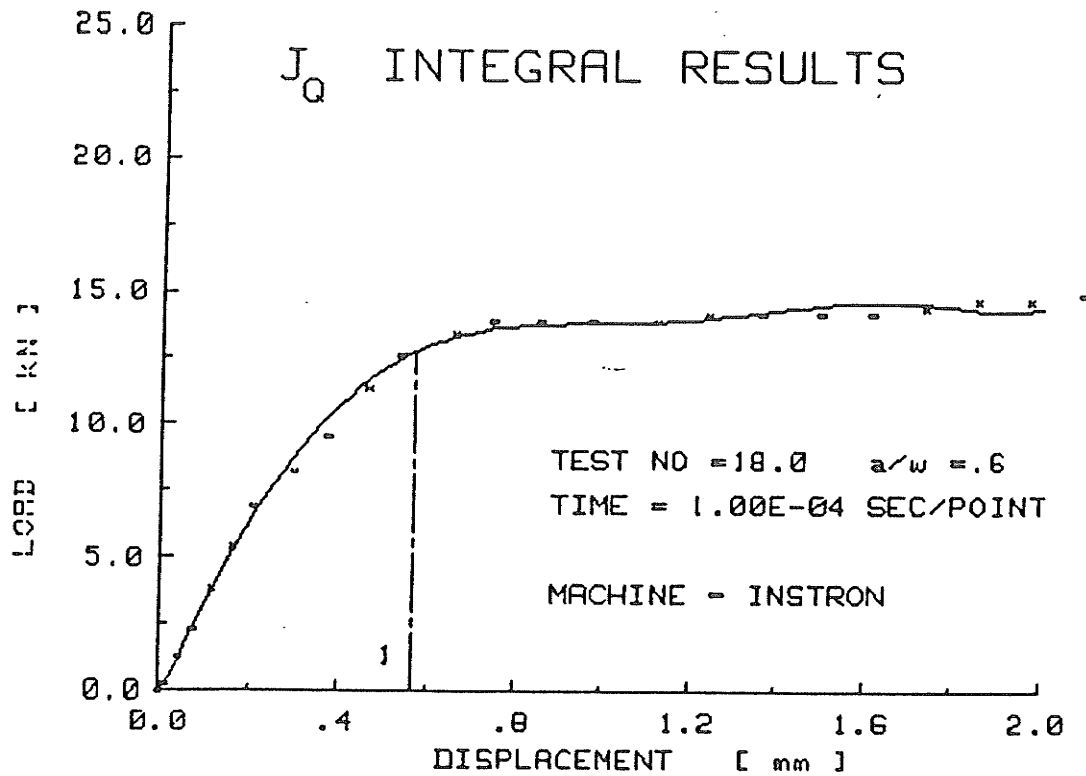
LSF OF ORDER 8       $Y = C1+C2*X+C3*X^2+...$   
 $J0( 1 ) = 4.28E+01$  kN/m  
 $T\_CRIT 1 = 2.02E-02$  SEC       $COO\_CRIT 1 = 5.41E-01$  mm



LSF OF ORDER 5     $Y = C1+C2*X+C3*X^2+...$



LSF OF ORDER 2     $Y = C1+C2*X+C3*X^2+...$   
 T\_CRIT( 1 ) = 1.45E-02 SEC



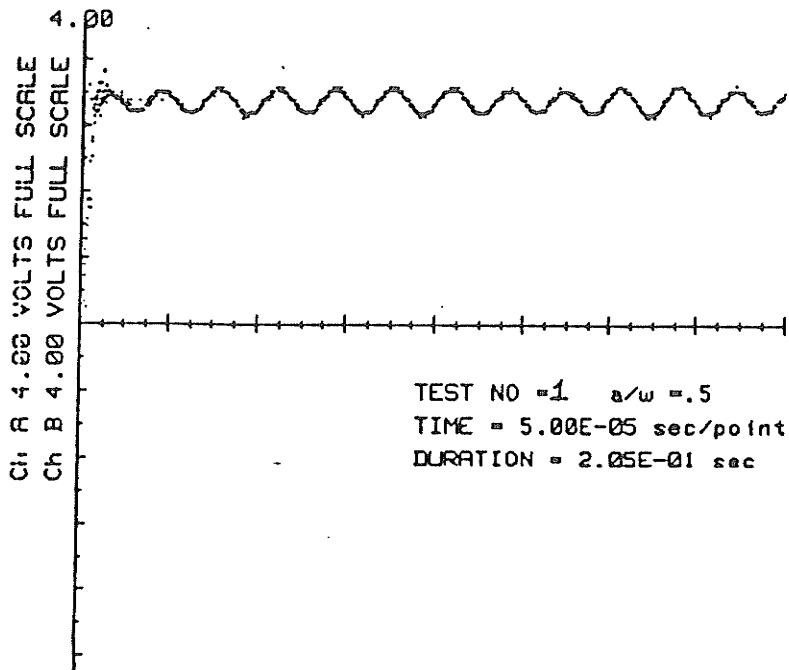
LSF OF ORDER 8      Y = C1+C2\*X+C3\*X^2+...

J<sub>Q</sub>( 1 ) = 3.83E+01 kN/m  
 T<sub>CRIT</sub> 1 = 1.45E-02 SEC      CO<sub>Q</sub> CRIT 1 = 5.71E-01 mm

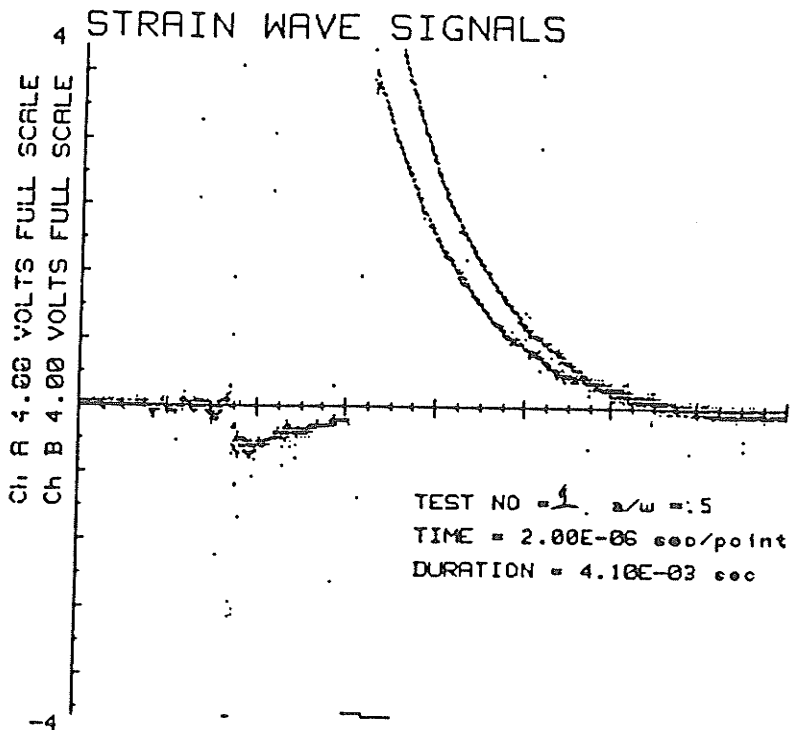
APPENDIX C

STRESS WAVE LOADING RESULTS

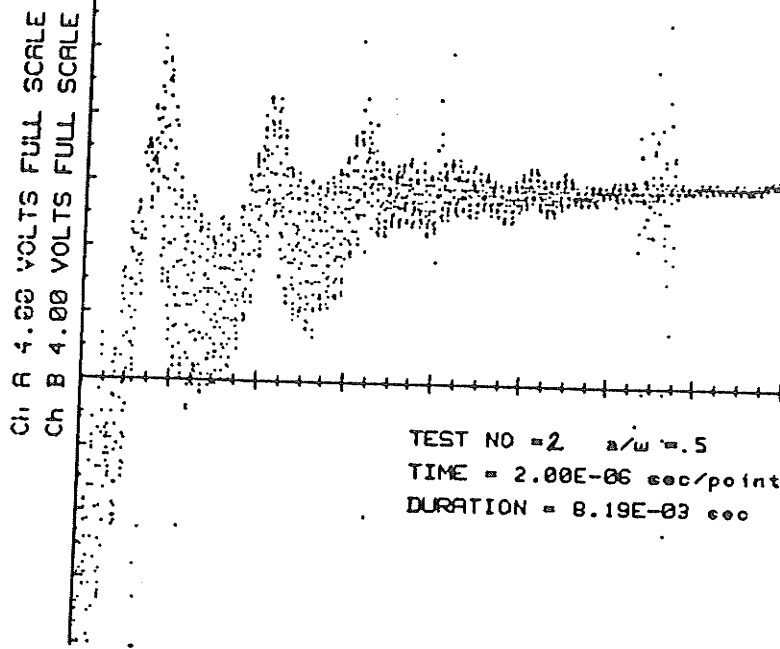
### COD/DISPLACEMENT SIGNAL



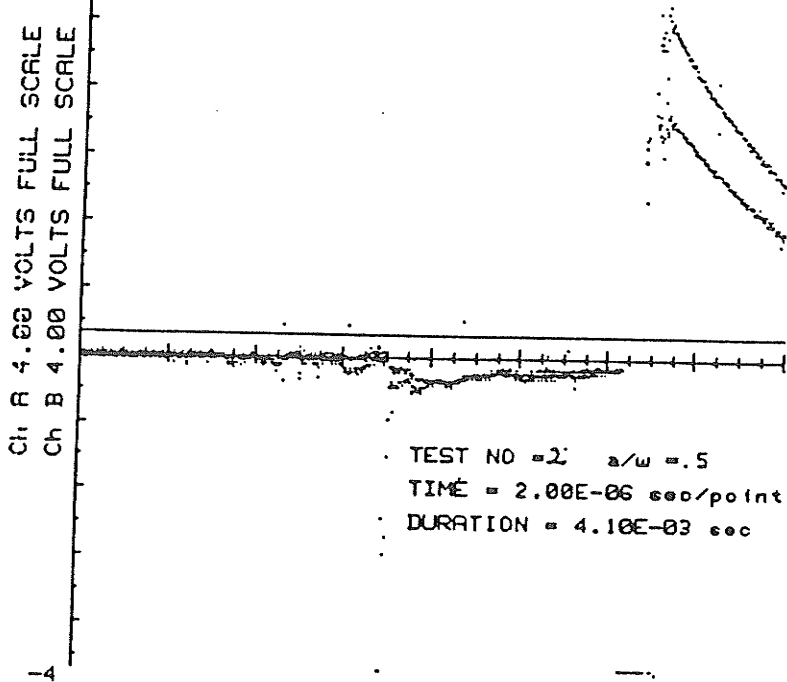
### STRAIN WAVE SIGNALS

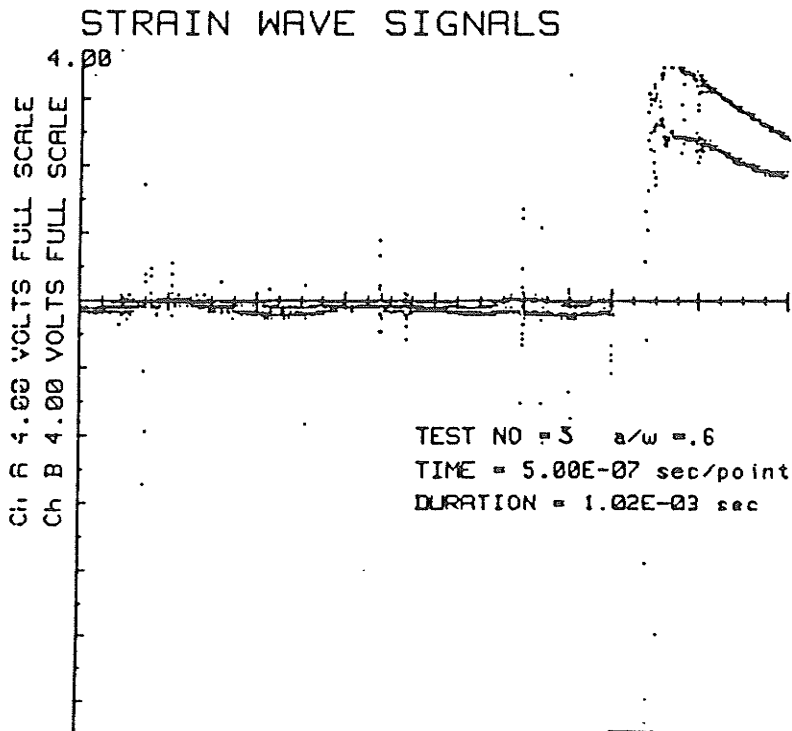
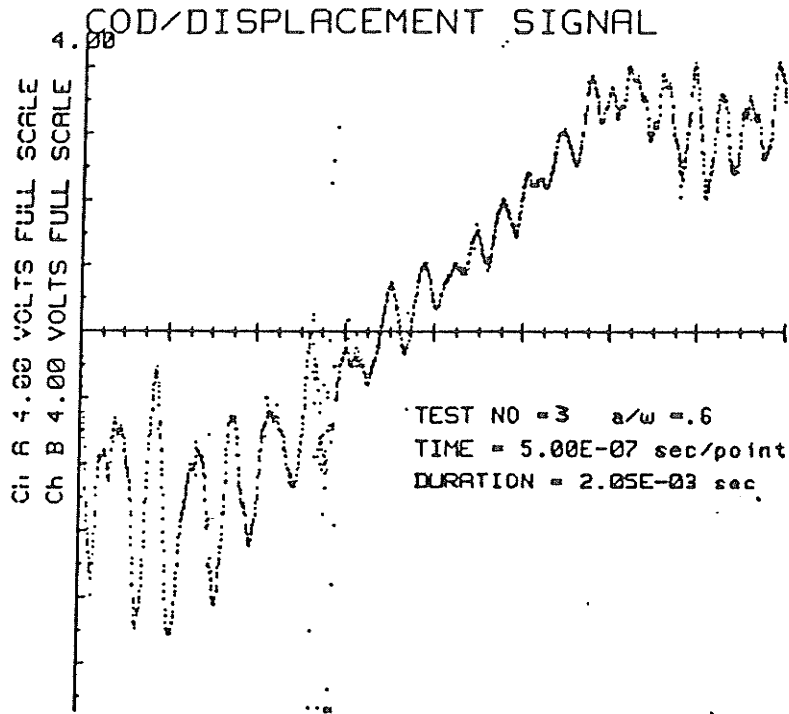


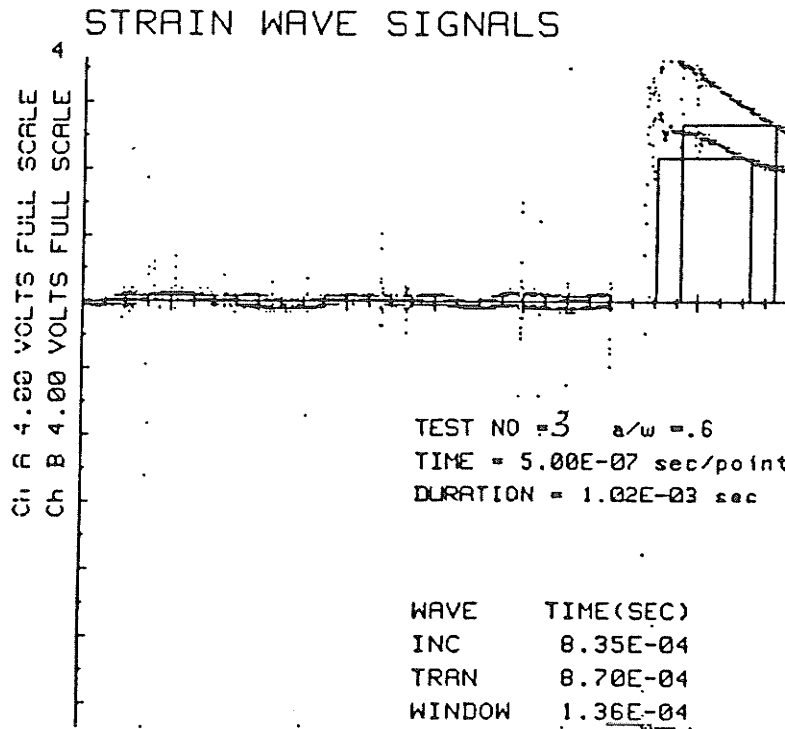
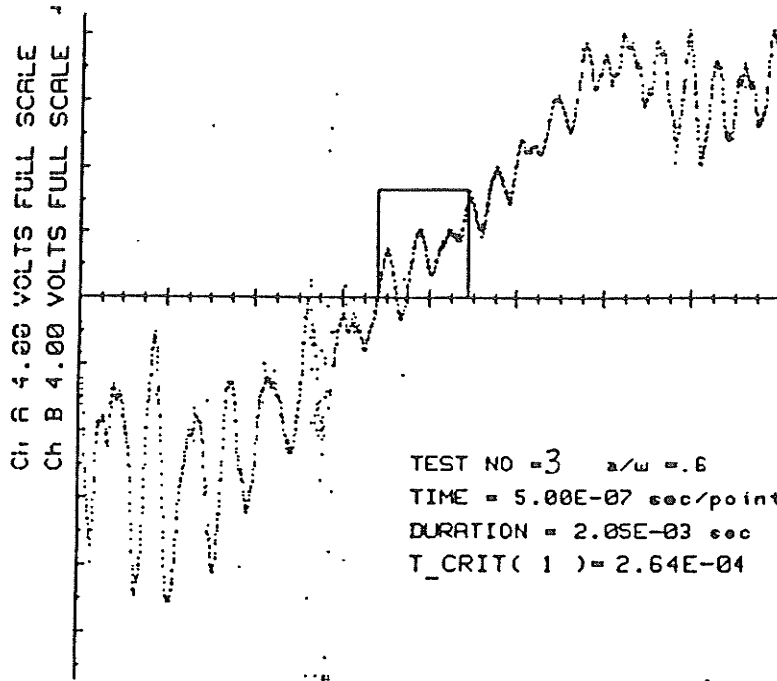
### 4.600/DISPLACEMENT SIGNAL

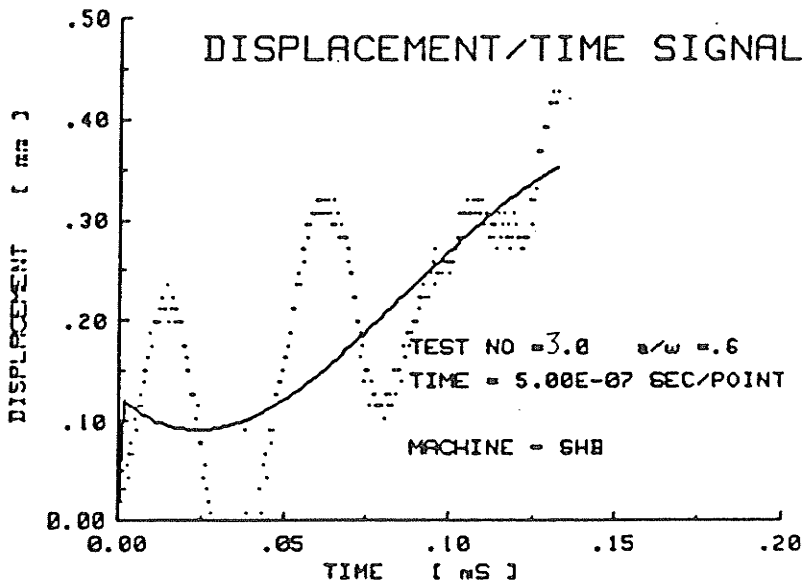
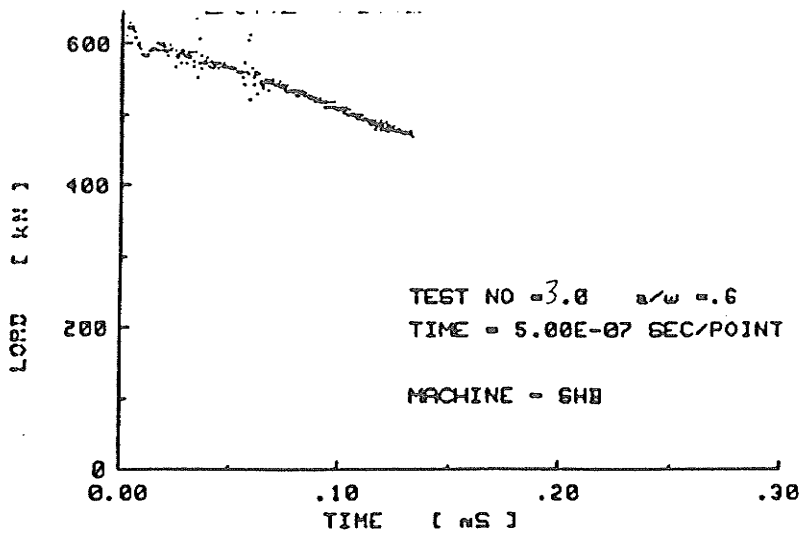


### 4 STRAIN WAVE SIGNALS



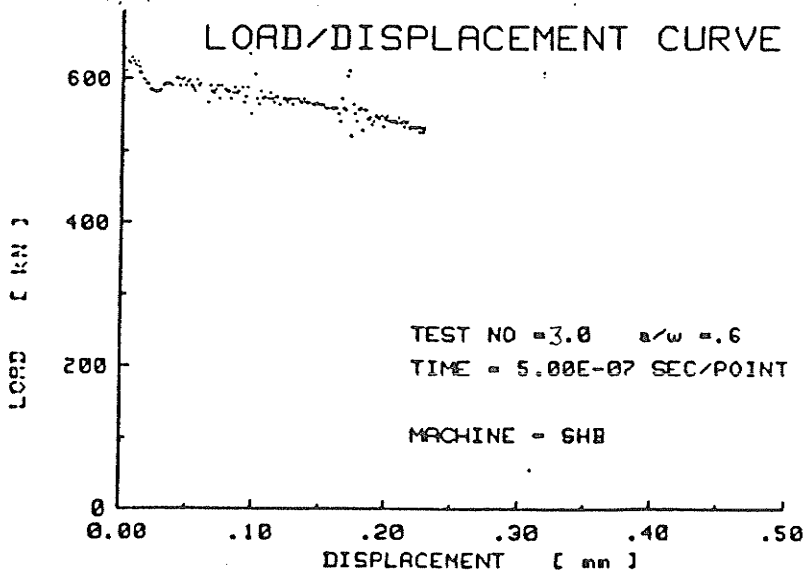


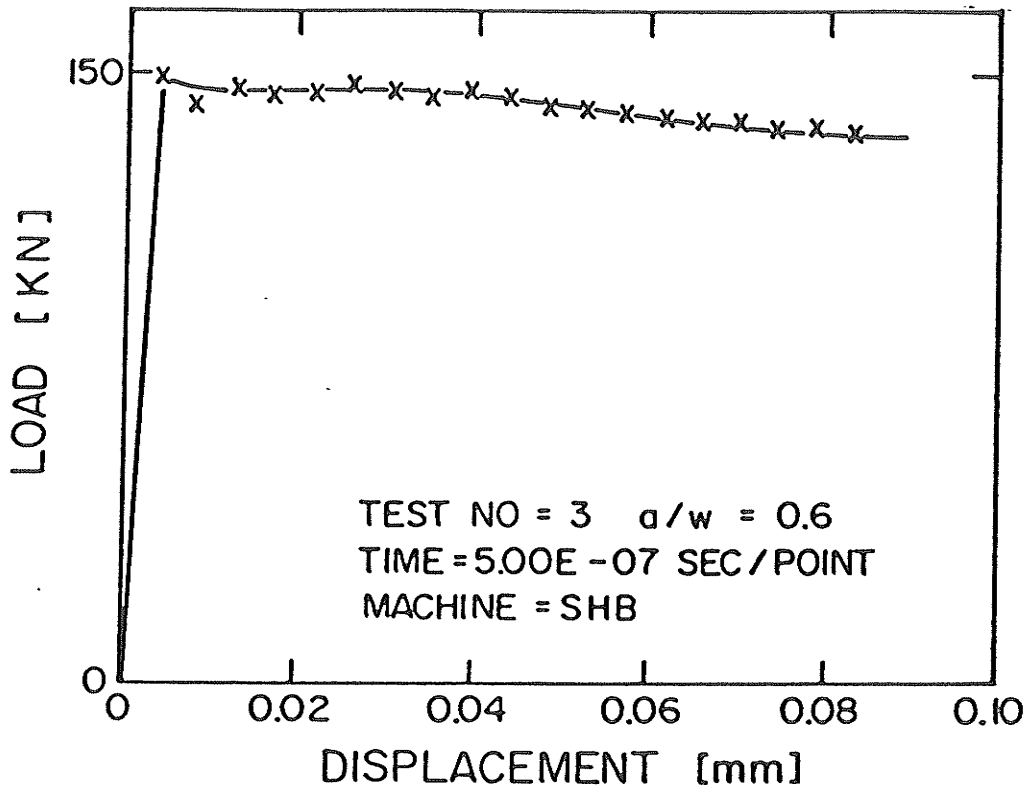




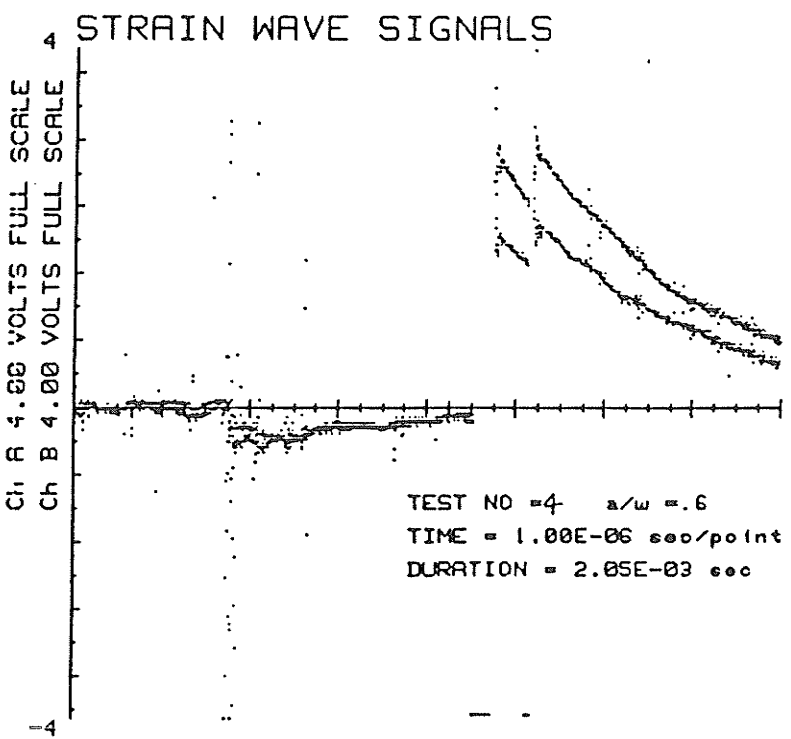
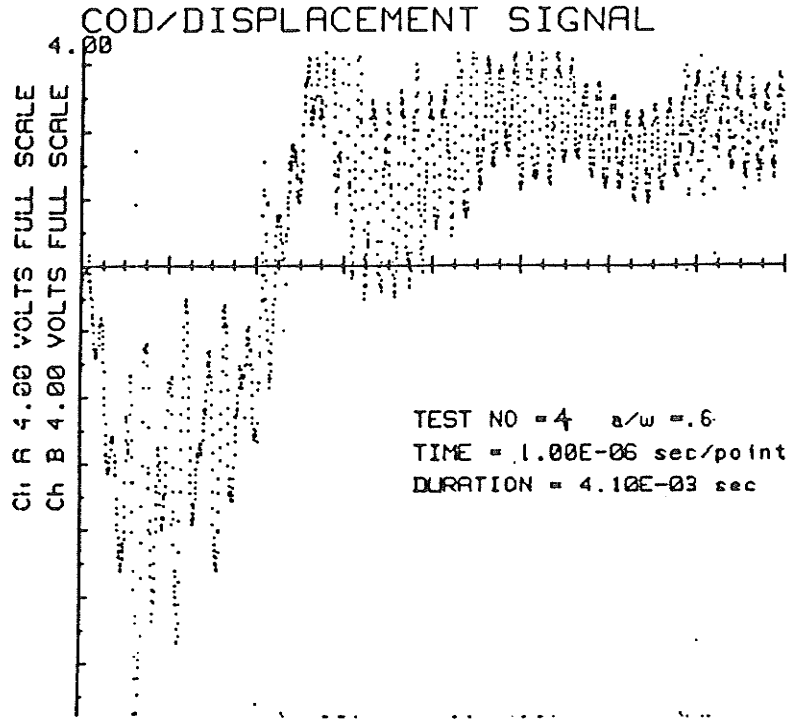
LSF OF ORDER 3      Y = C1+C2\*X+C3\*X^2+...

C 1 = 1.25E-01	C 2 = -2.97E+00
C 3 = 7.14E+01	C 4 = -2.73E+02

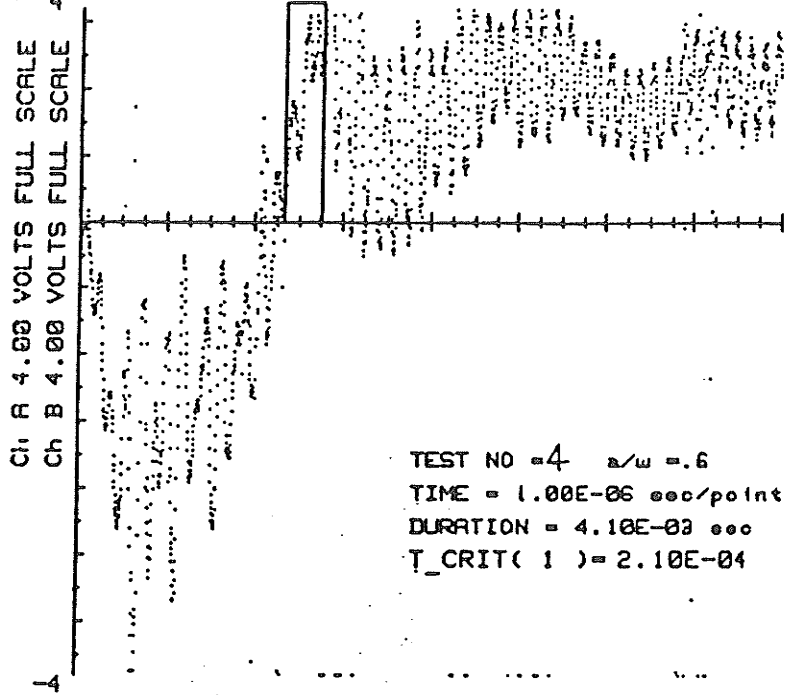




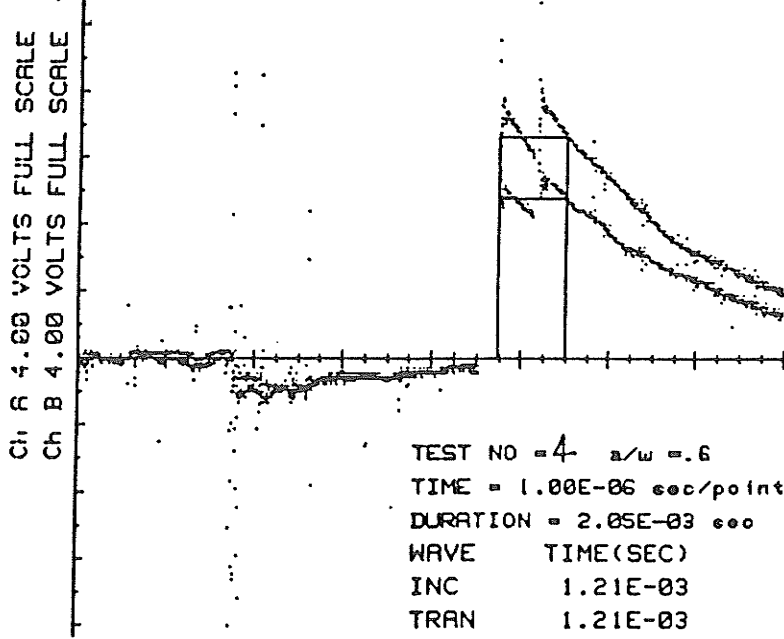
$J_Q = 1.5 \text{ KJ/m}^2$   
 T-CRIT =  $5.00E-07$  SEC  
 COD-CRIT =  $3.36E-03$  mm

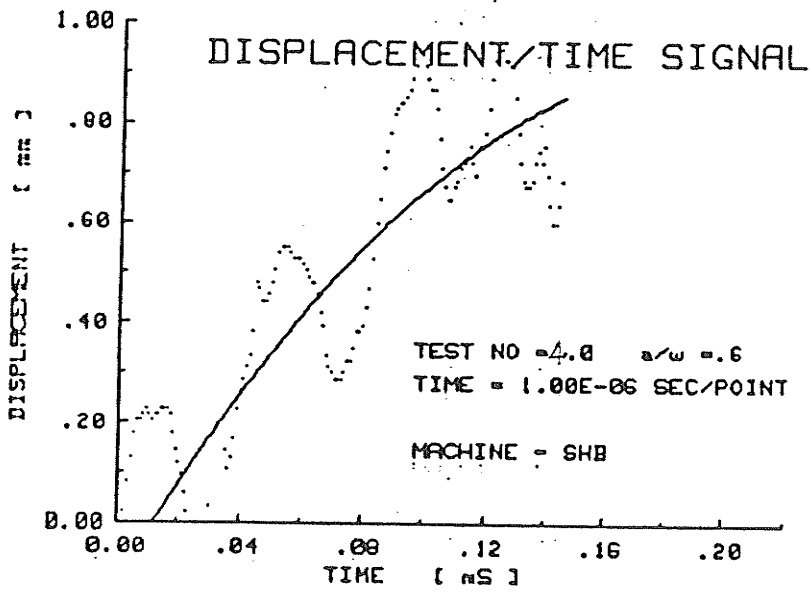
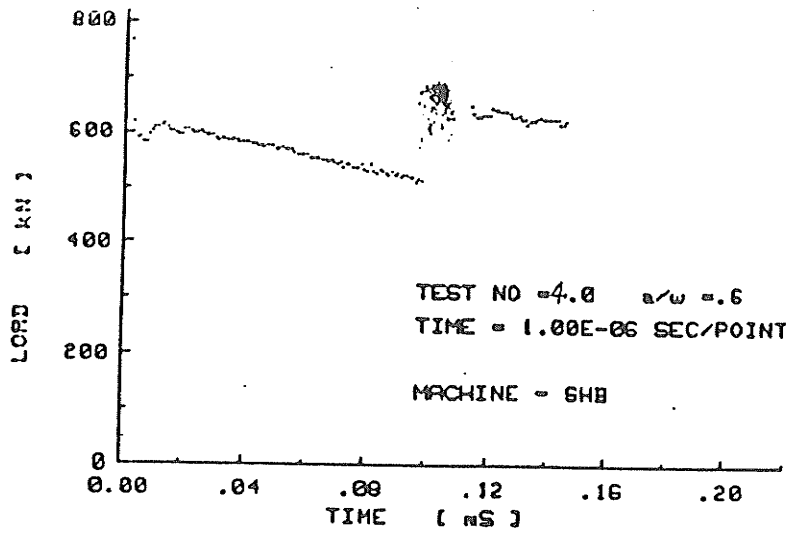


COD/DISPLACEMENT SIGNAL

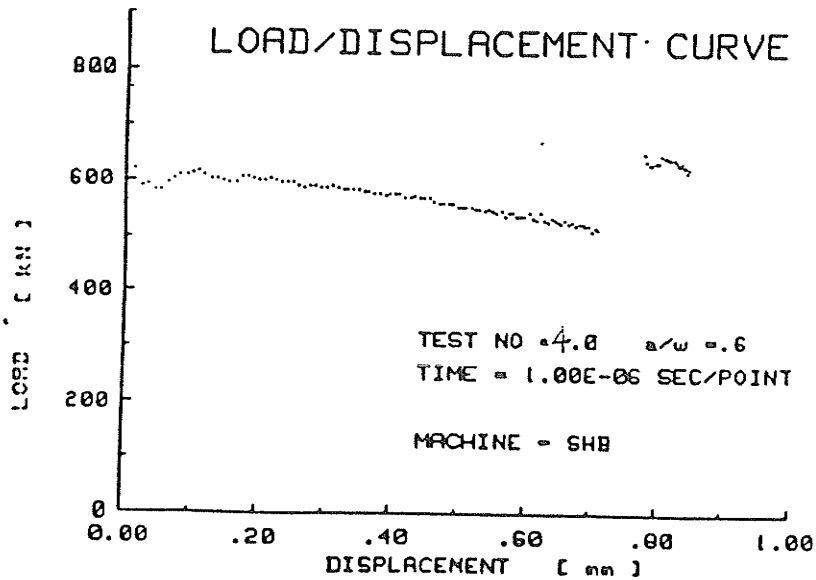


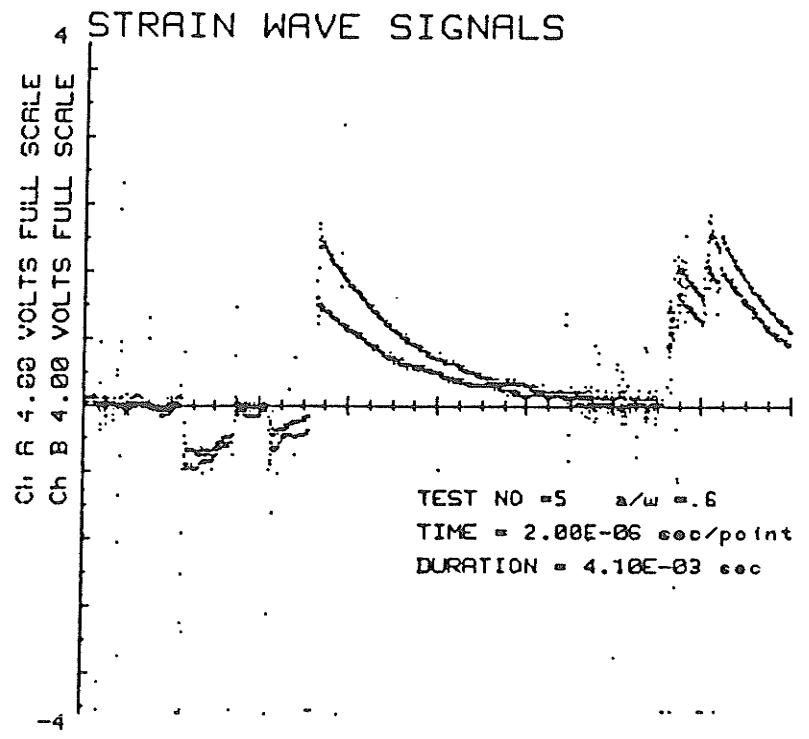
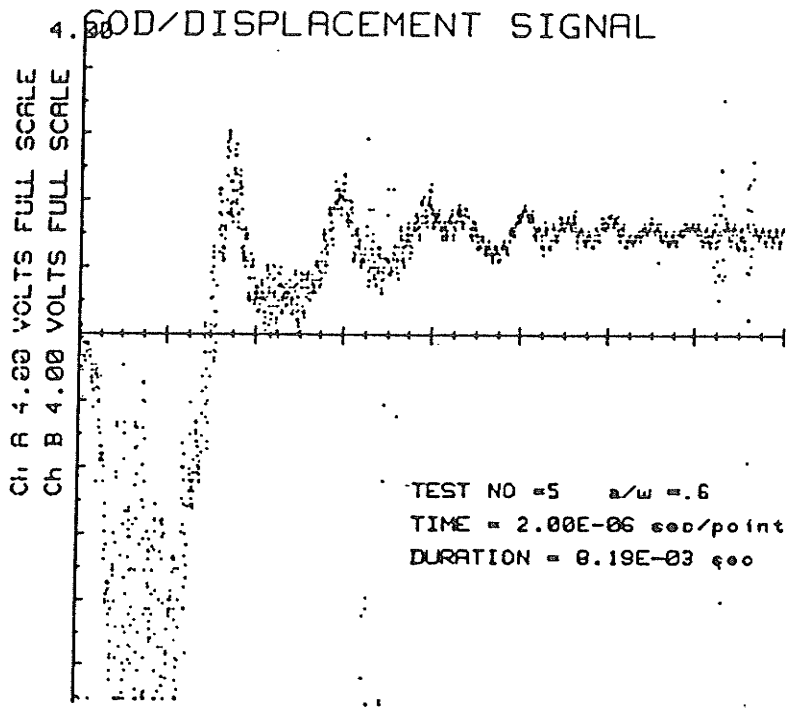
STRAIN WAVE SIGNALS



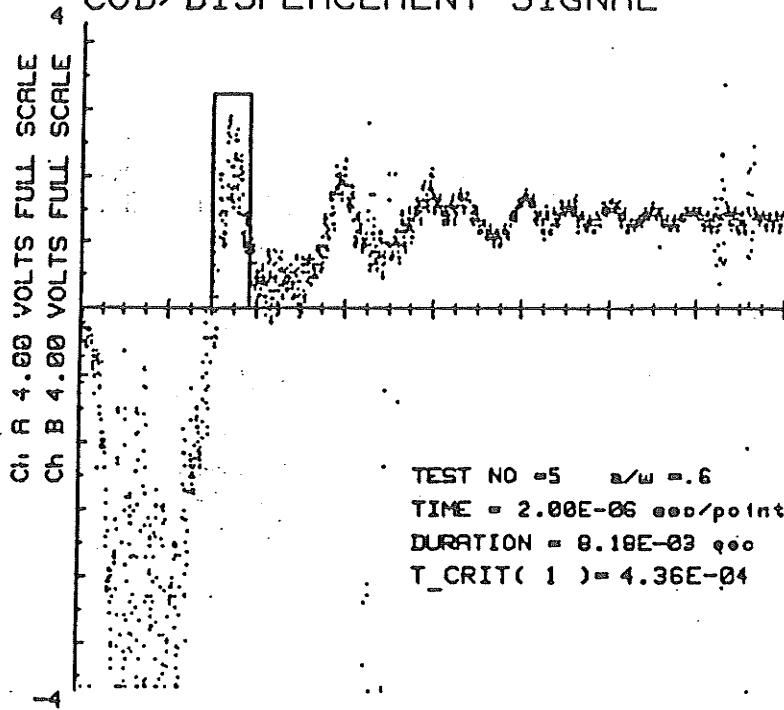


LSF OF ORDER 2       $Y = C1 + C2 * X + C3 * X^2 + \dots$   
 C 1 = -1.22E-01      C 2 = 1.05E+01  
 C 3 = -2.64E+01

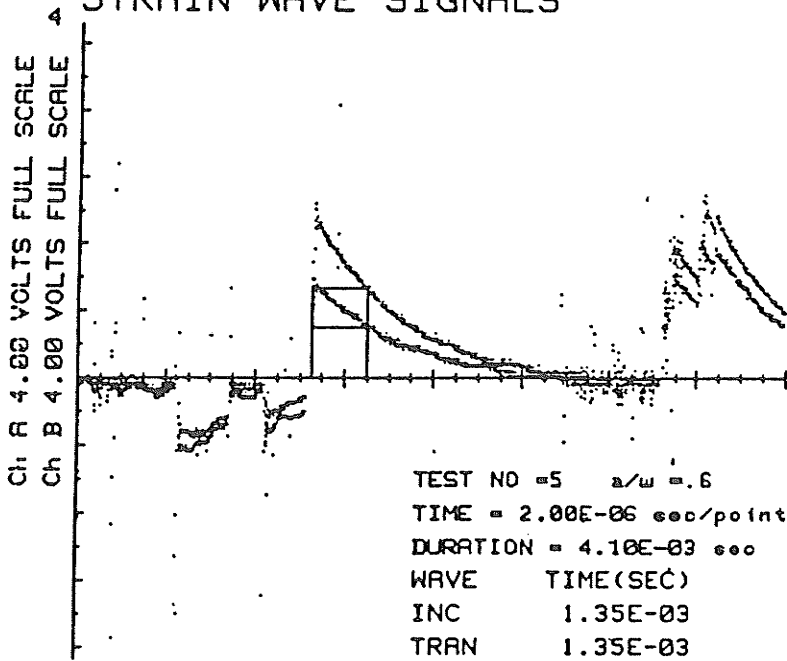


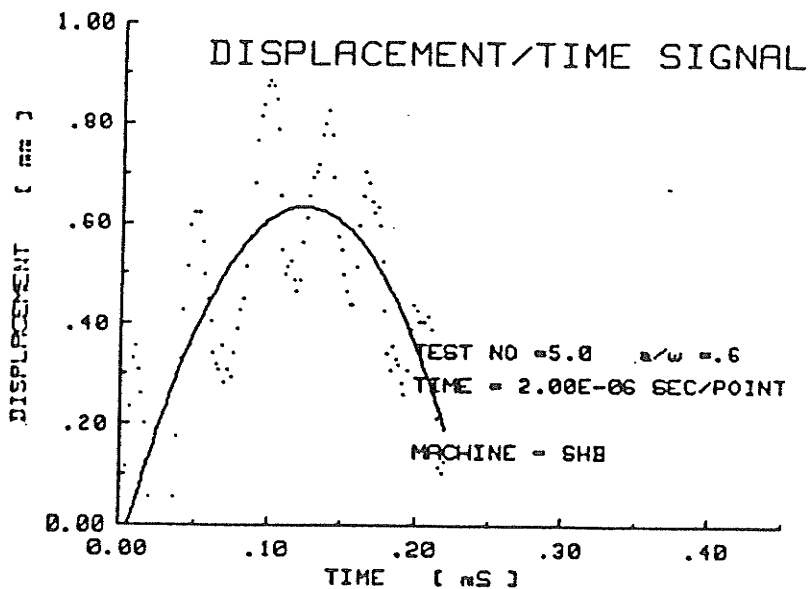
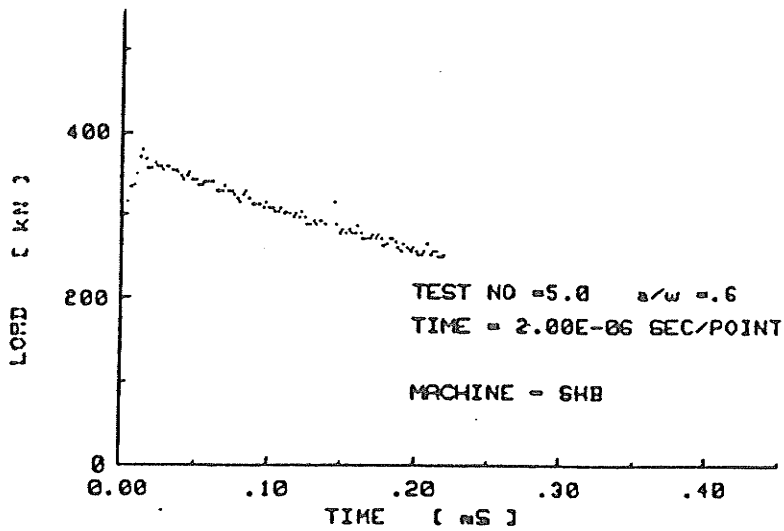


### COD/DISPLACEMENT SIGNAL

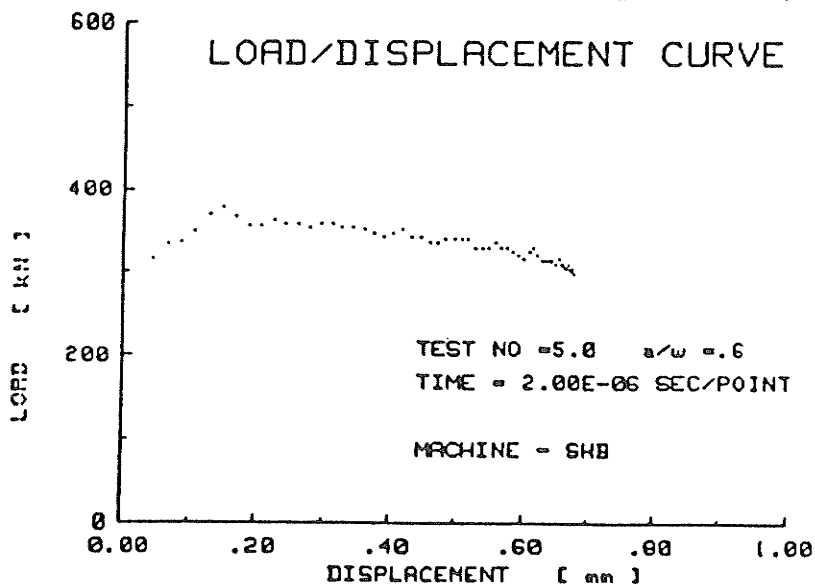


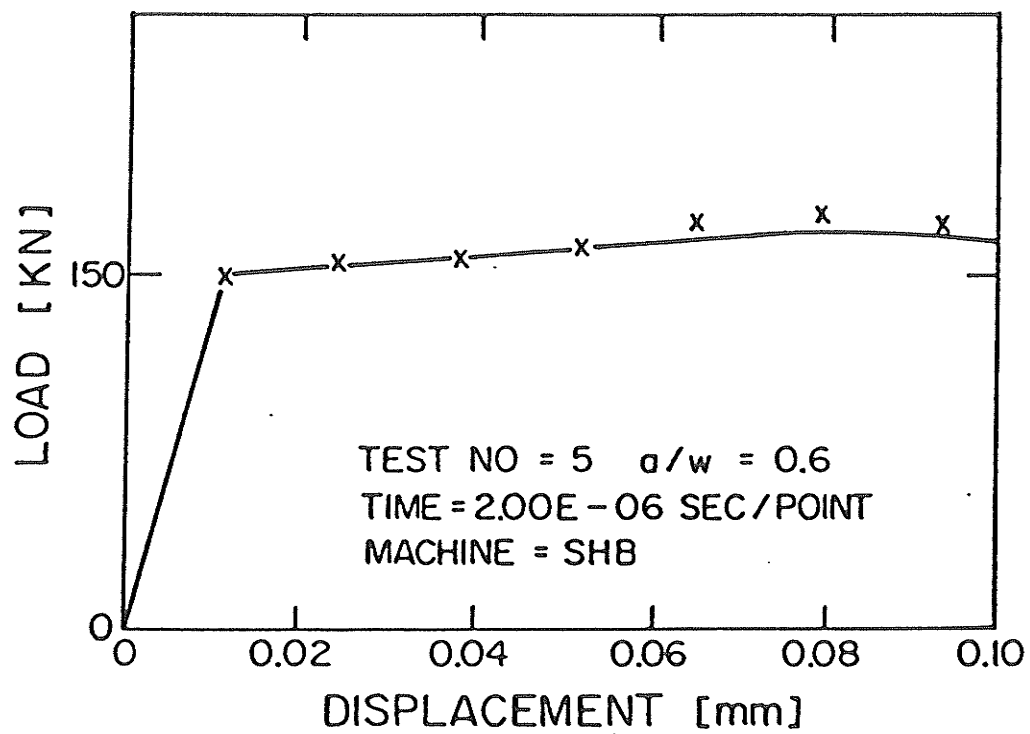
### STRAIN WAVE SIGNALS





LSF OF ORDER 2  $Y = C1 + C2 * X + C3 * X^2 + \dots$   
 C 1 = -6.91E-02 C 2 = 1.14E+01  
 C 3 = -4.66E+01

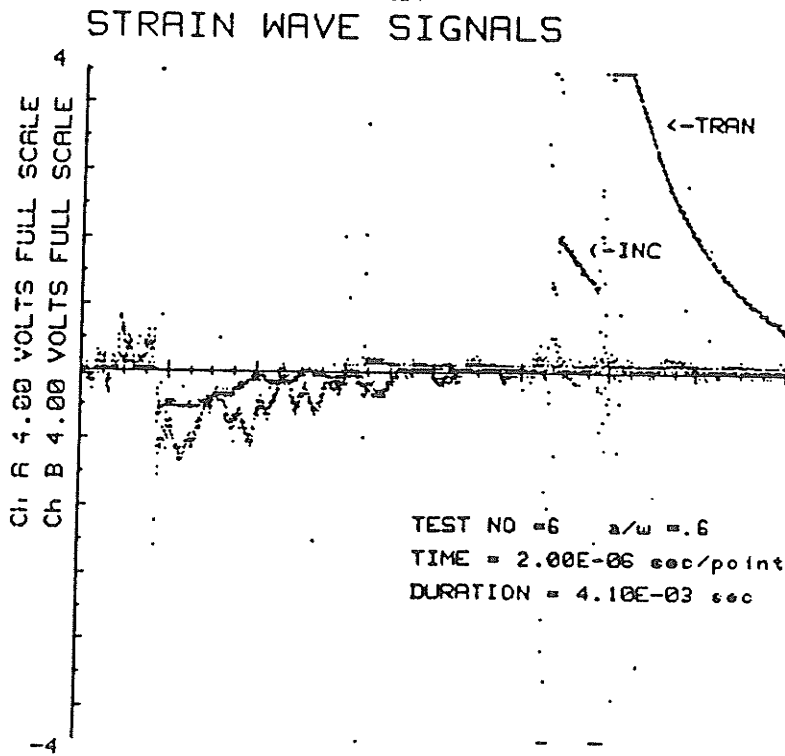
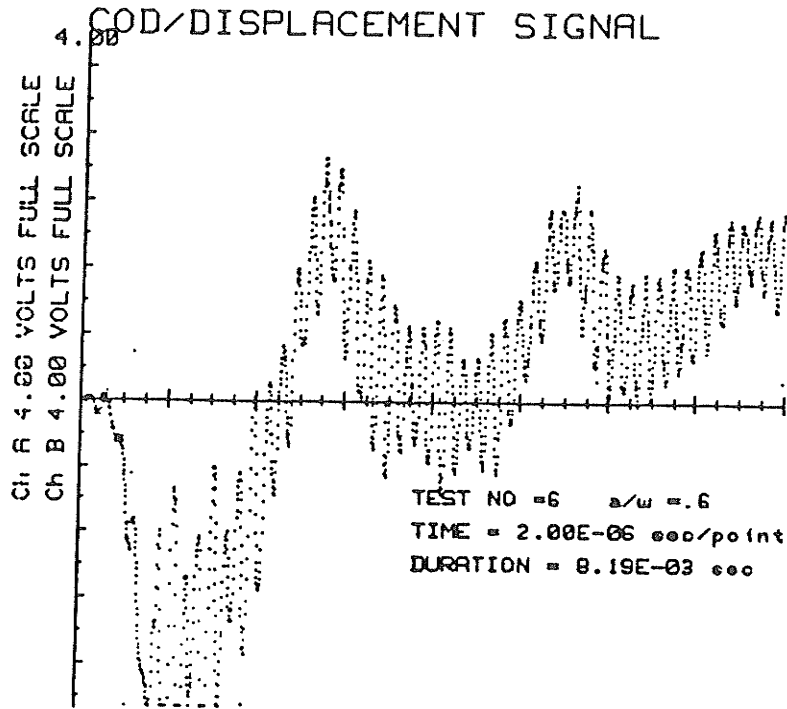




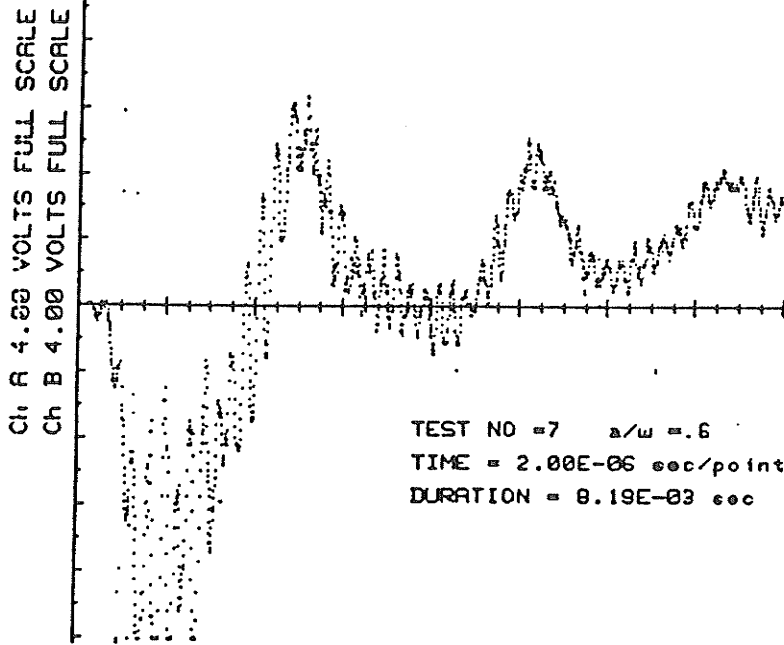
$$J_Q = 4.7 \text{ KJ / m}^2$$

$$T\text{-CRIT} = 2.00E-06 \text{ SEC}$$

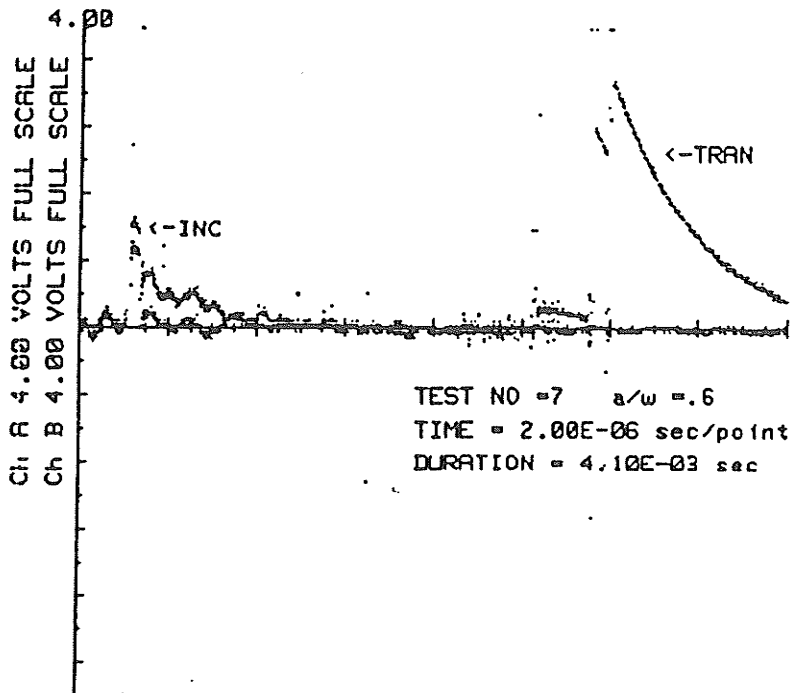
$$\text{COD-CRIT} = 7.15E-03 \text{ mm}$$



### 4.00 COD/DISPLACEMENT SIGNAL

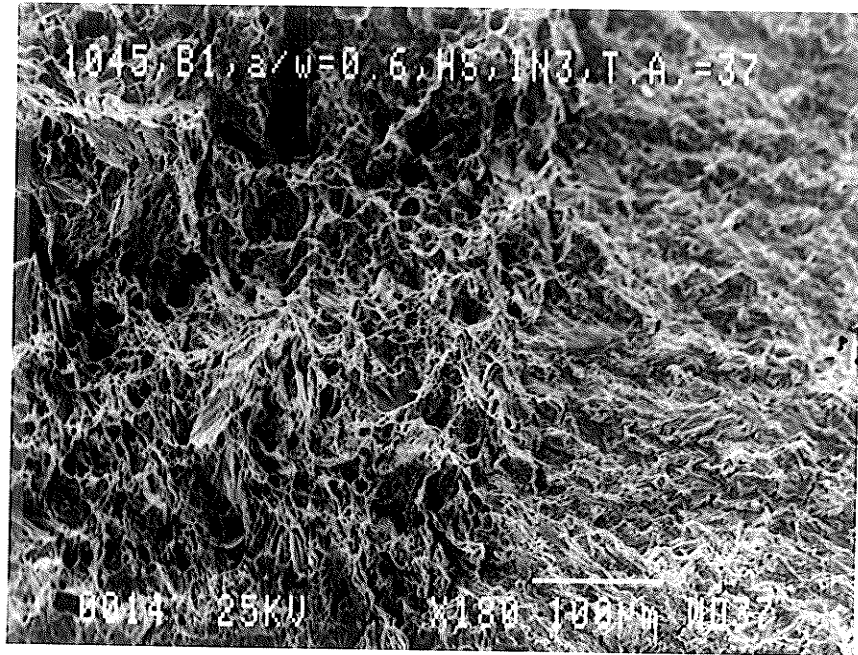


### STRAIN WAVE SIGNALS

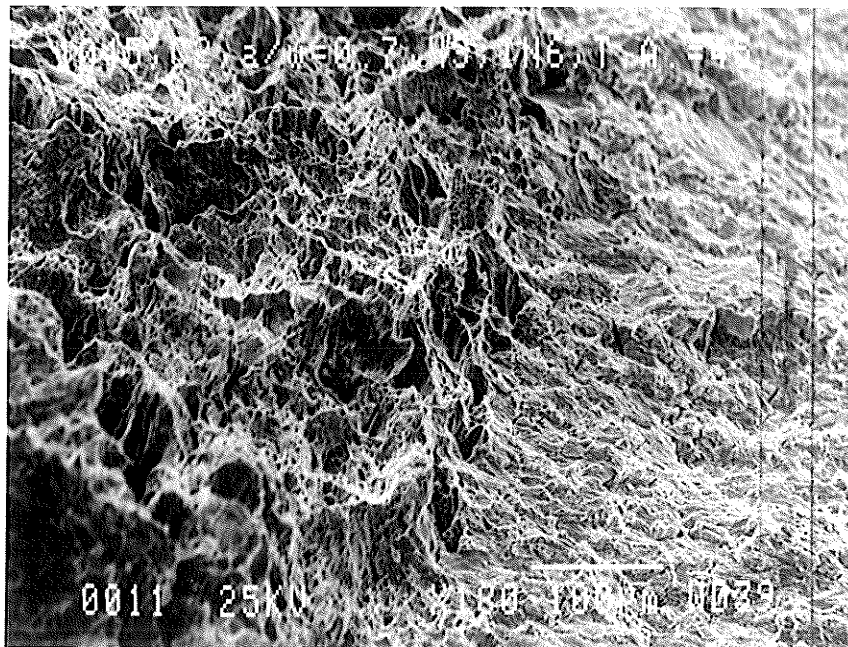
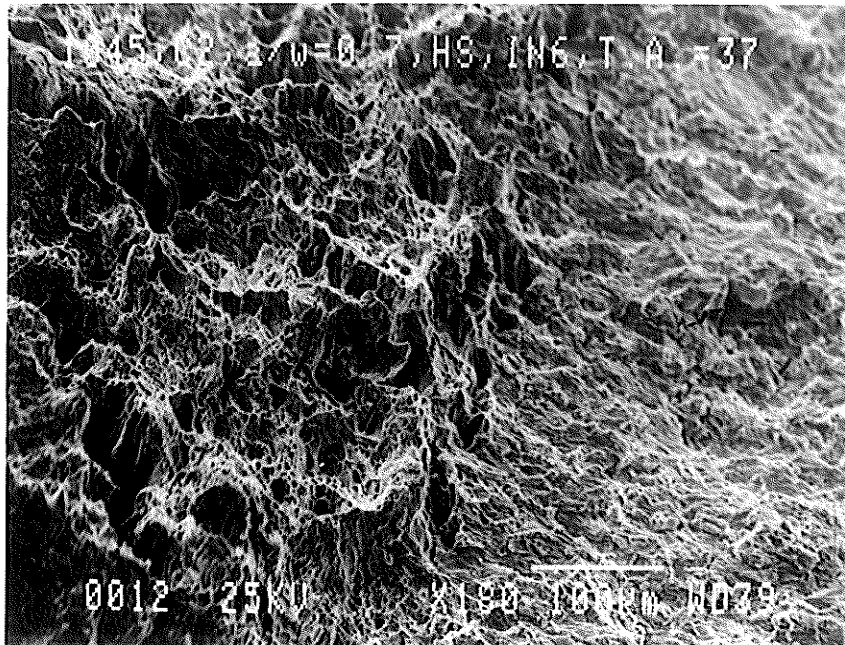


APPENDIX D

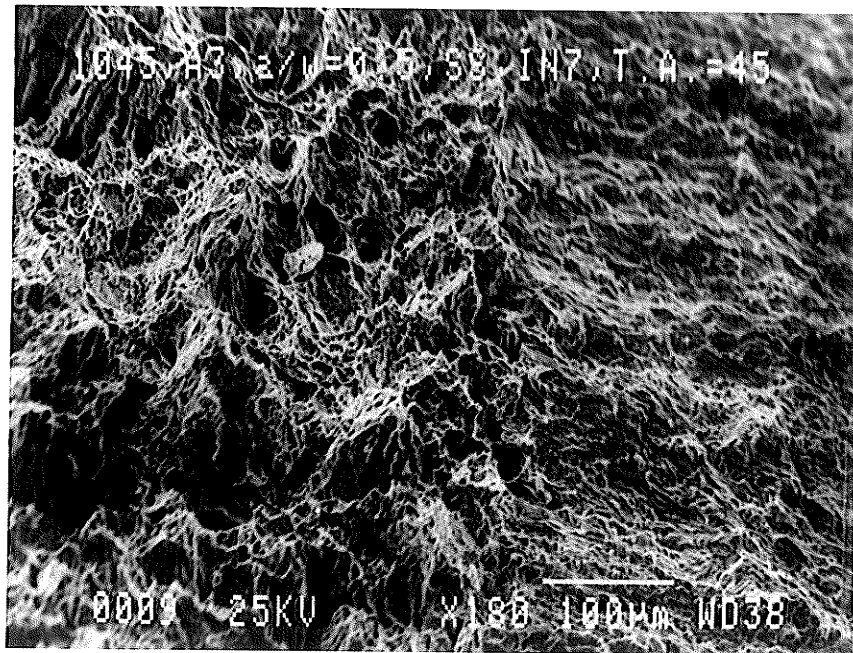
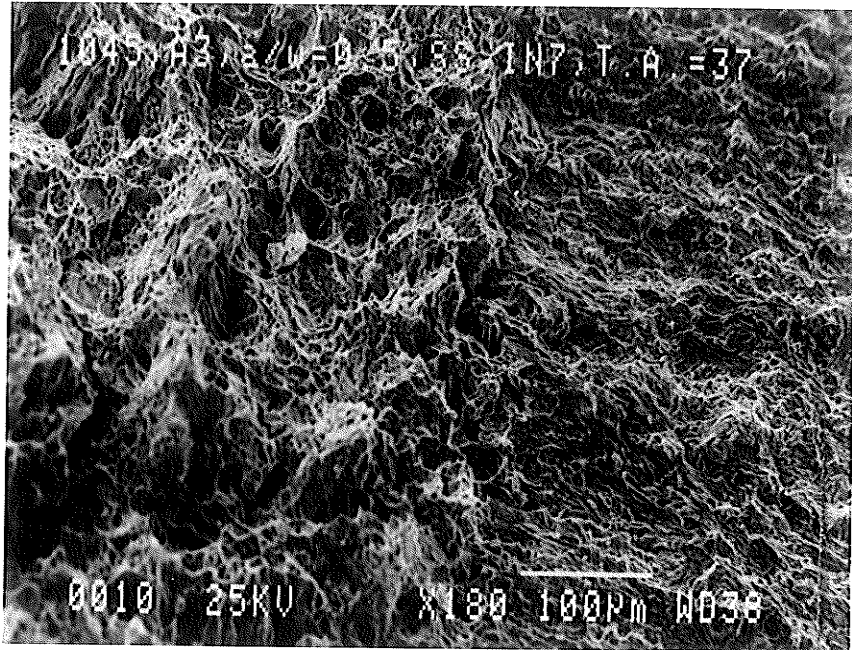
SCANNING ELECTRON MICROGRAPHS FOR ALL TESTS



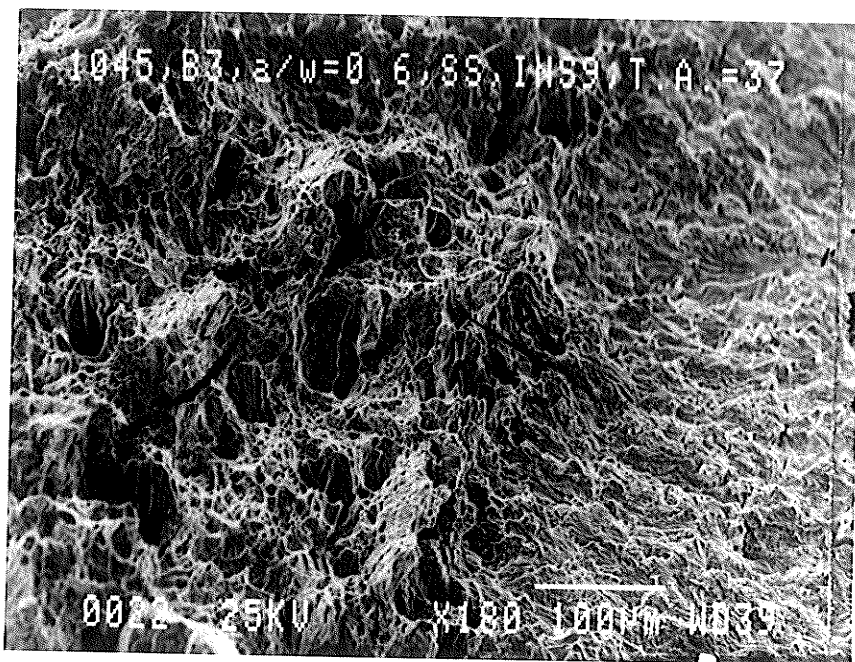
Scanning electron micrographs for test #INST3



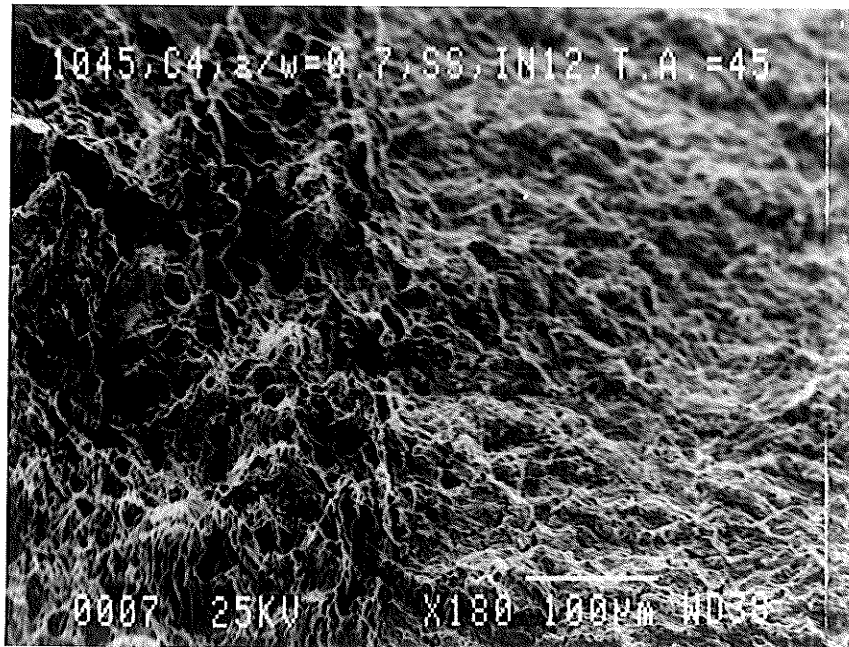
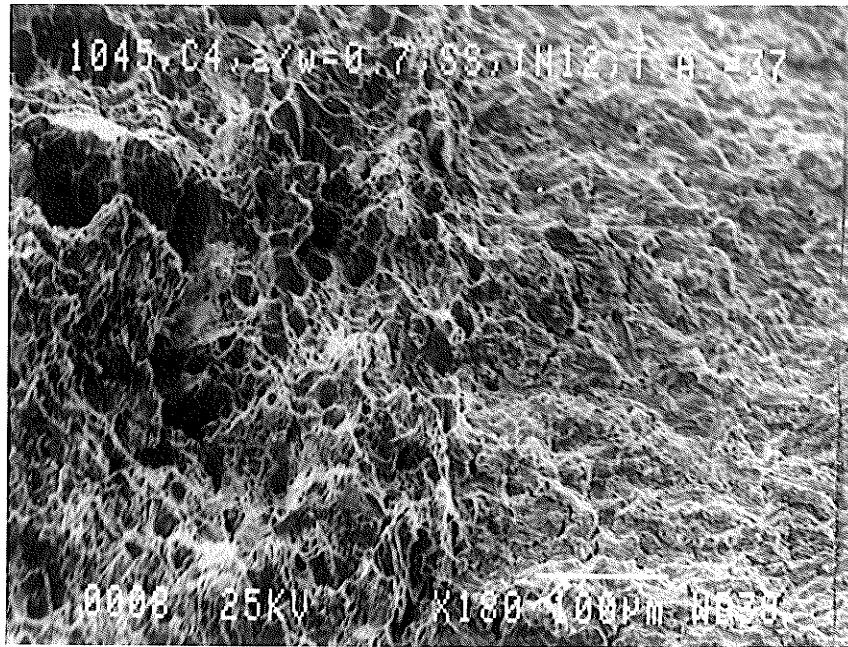
Scanning electron micrographs for test #INST6



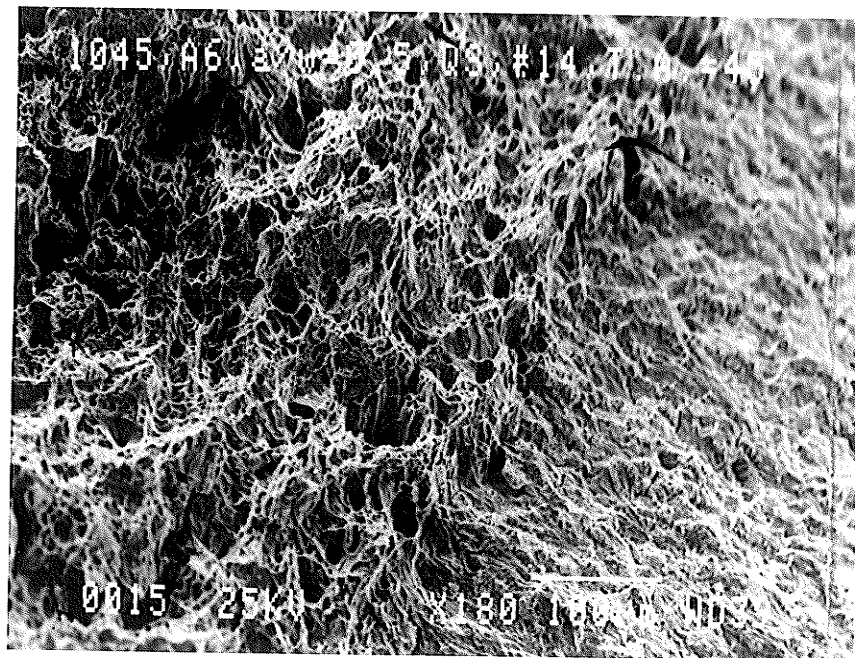
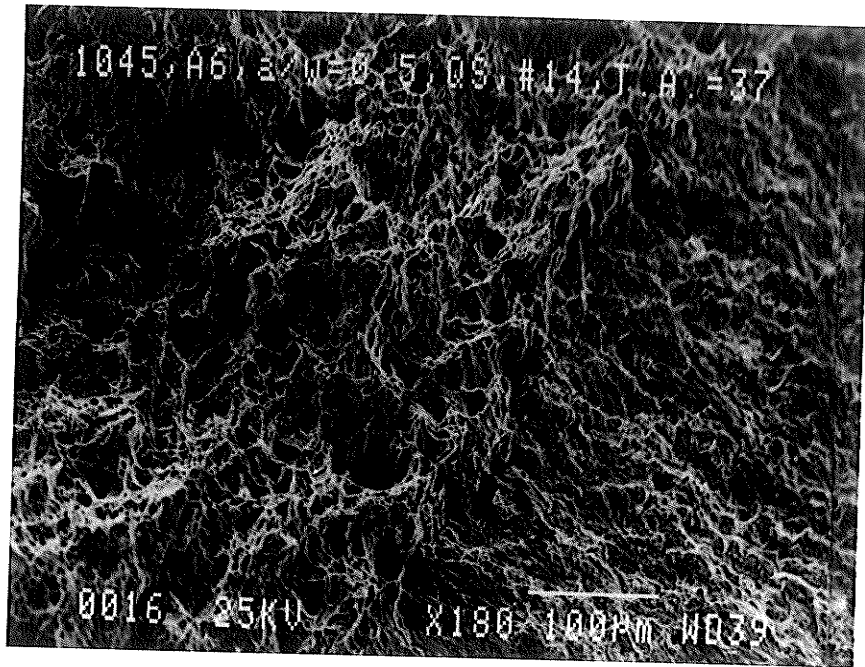
Scanning electron micrographs for test #INST7



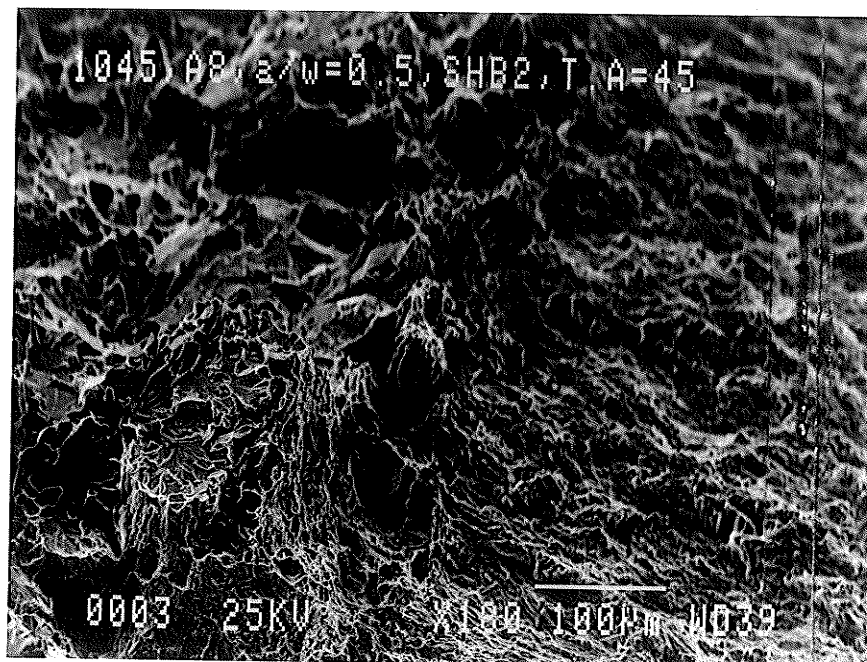
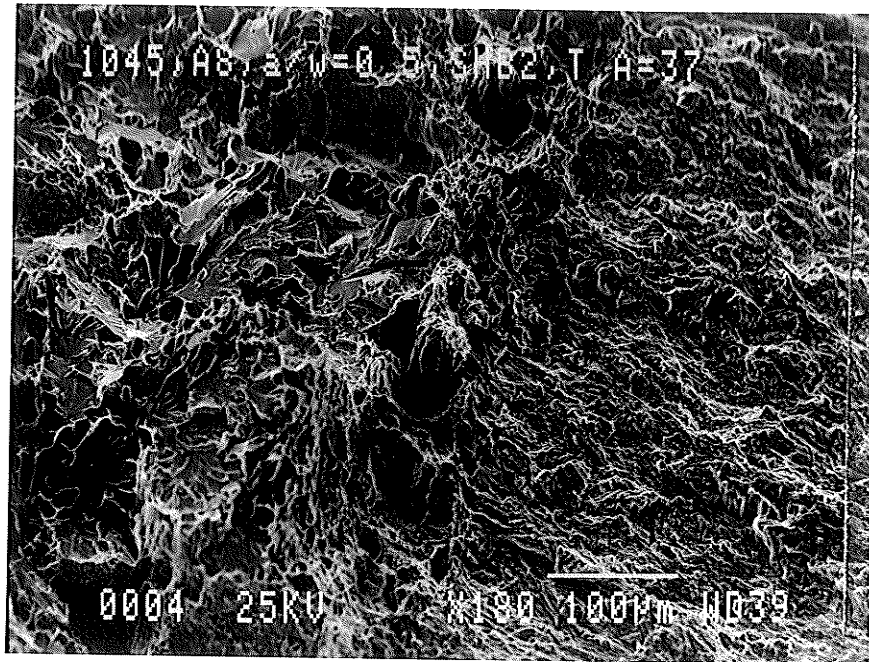
Scanning electron micrographs for test #INST9



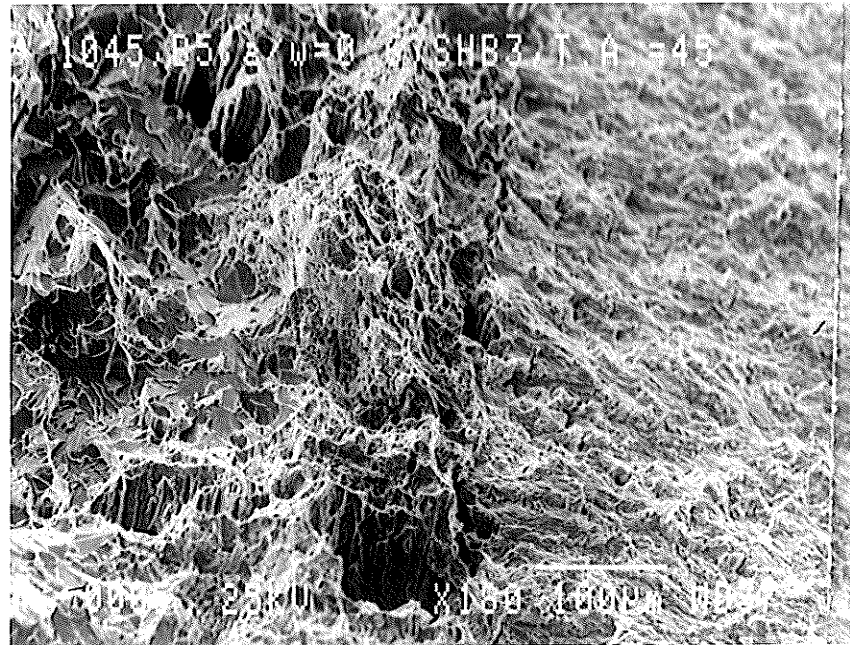
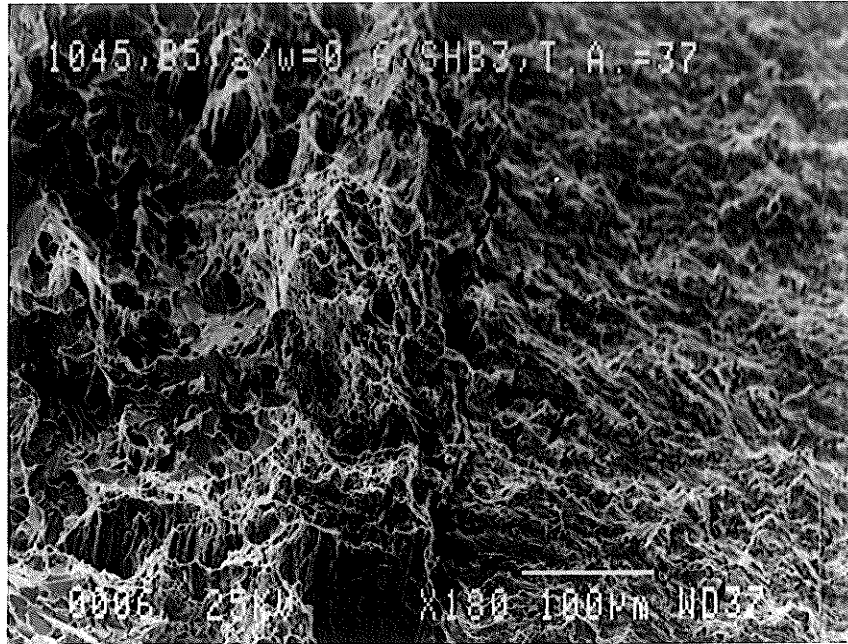
Scanning electron micrographs for test #INST12



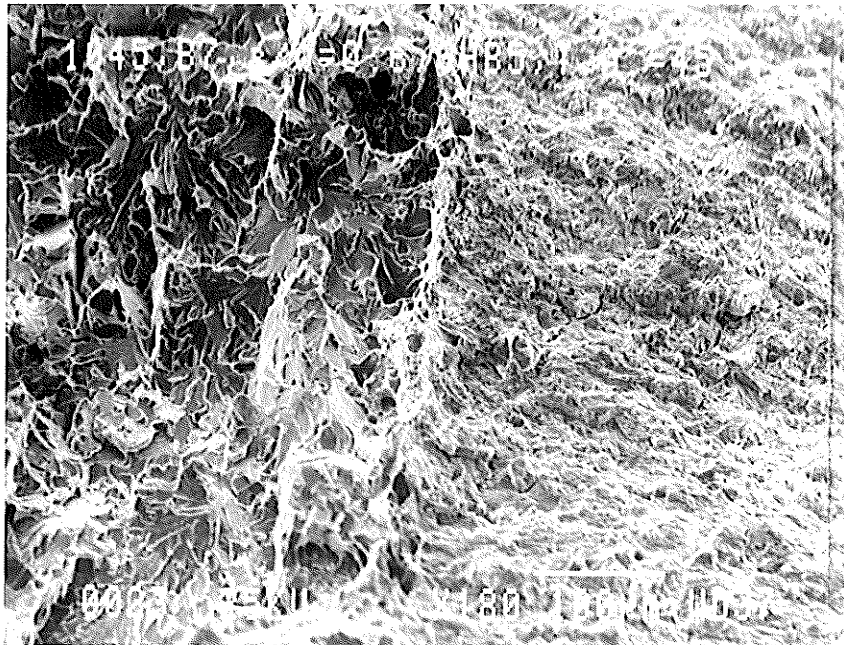
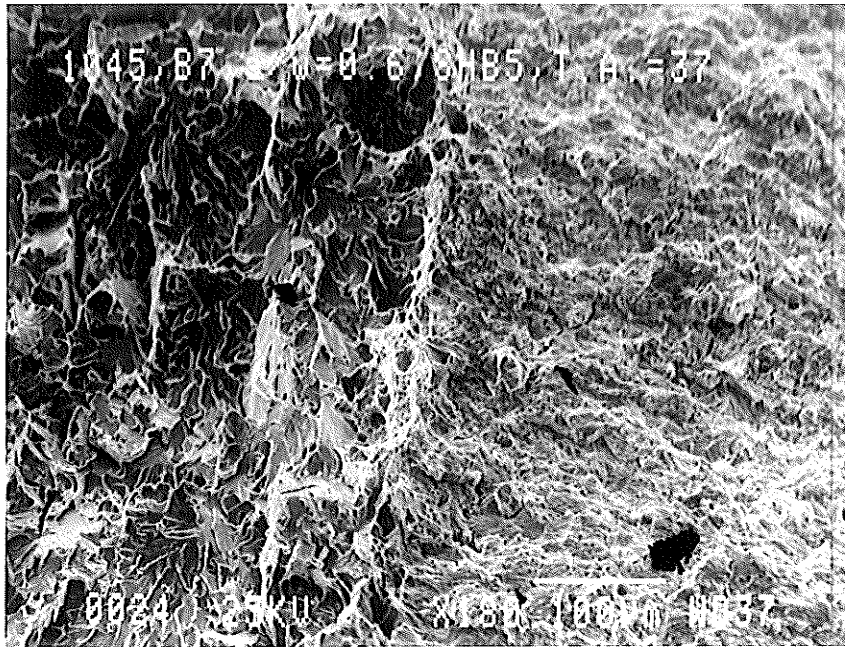
Scanning electron micrographs for test Q.S. #14



Scanning electron micrographs for test #SHB2



Scanning electron micrographs for test #SHB3



Scanning electron micrographs for test #SHB5